New measurements of neutrino oscillation parameters and development of novel interaction uncertainties at current and future long-baseline experiments

Thomas Holvey

St John's College

University of Oxford

A thesis submitted for the degree of

Doctor of Philosophy

Trinity 2024

Abstract

T2K is a long-baseline neutrino oscillation experiment designed to perform precision measurements of the neutrino oscillation parameters $\sin^2\theta_{23}$, $\sin^2\theta_{13}$, and Δm^2_{32}, as well as constrain the CP-violating phase δ_{CP}. It performs these measurements by propagating a neutrino beam of average energy 0.6 GeV, produced at the J-PARC facility in Tokai, along a 295 km baseline to Super-Kamiokande (often referred to as Super-K or SK). The unoscillated beam is measured by a suite of near detectors 280 m downstream of the target, and the oscillated spectra are measured at Super-K.

This thesis details constraints on the oscillation parameters measured by T2K from a joint fit to near and far-detector data using a Bayesian Markov chain Monte Carlo method. The results of two fits are reported, firstly fitting to T2K data only, and then applying an external constraint on $\sin^2\theta_{13}$ from reactor experiments.

When fitting to T2K data only, the best-fit points and 68% credible intervals for the oscillation parameters are: $\sin^2\theta_{23} = 0.488^{+0.057}_{-0.018}$, $\Delta m^2_{32} = 2.51 \times 10^{-3}$ eV^2 with a range of $[2.43, 2.57] \cup [-2.58, -2.51]$, $\sin^2\theta_{13} = 0.0235^{+0.0056}_{-0.0031}$, $\delta_{CP} = -1.92^{+1.17}_{-0.84}$.

When applying an external reactor constraint to $\sin^2\theta_{13}$, the best-fit points and 68% credible intervals are: $\sin^2\theta_{23} = 0.531^{+0.028}_{-0.044}$, $\Delta m^2_{32} = 2.51 \times 10^{-3}$ eV^2 with a range of $[2.42, 2.58] \cup [-2.56, -2.53]$, $\sin^2\theta_{13} = 0.0221 \pm 0.0007$, $\delta_{CP} = -1.84^{+0.83}_{-0.74}$. CP-conserving values of both the CP-violating phase δ_{CP} and the Jarlskog invariant are excluded at the 90% significance level.

Current oscillation parameter measurements are limited by statistical uncertainties. However, future measurements made at next-generation long-baseline experiments are anticipated to be limited by systematic uncertainties. It is therefore vital that work is carried out to better understand neutrino interaction cross sections, which currently represent a significant source of the total systematic uncertainty in oscillation parameter measurements. This thesis presents the development of two sets of novel interaction uncertainties for current and future experiments.

First, parameters were developed at T2K to describe sizeable model differences seen in the low-energy transfer region. These parameters were further motivated by an alternative model study that demonstrated a significant bias

in Δm^2_{32}, which was the largest contribution to the total systematic uncertainty for this parameter. This thesis demonstrates that the newly developed systematic uncertainties significantly reduce this bias and improve the flexibility and robustness of T2K's interaction model.

Finally, this thesis presents new interaction uncertainties that modify the nuclear ground state, developed especially for the Deep Underground Neutrino Experiment (DUNE), a next-generation long-baseline experiment. Benefiting from much higher statistics and improved detector resolution, it is anticipated that DUNE will have a strong sensitivity to nuclear effects, which are currently poorly understood. It is demonstrated that mis-modelling the nuclear ground state may lead to biases in oscillation parameter measurements.

Statement of Originality

This thesis describes my work and the original research that I have performed as part of the T2K and DUNE collaborations. Work completed by my fellow collaborators has been clearly cited and referenced.

Chapters 1 and 2 present a summary and historical overview of the field of neutrino physics, focusing on areas particularly relevant to the work in this thesis. Chapter 3 describes the T2K experiment, the data from which is analysed in later chapters. Chapter 4 presents an overview of Bayesian inference and Markov chain Monte Carlo methods, which provide the statistical framework underpinning most results presented in this thesis. All techniques, results and figures are properly referenced and cited. Internal T2K sources can be made available upon request to the collaboration.

Chapter 5 presents the analysis framework of the oscillation analysis. The near and far-detector selections and systematic uncertainty model were developed by fellow collaborators and have been clearly referenced. The MaCh3 analysis framework has been developed by many people throughout the T2K experiment, and my work involved updating and adapting the existing far-detector specific framework for this current analysis. This involved implementing and validating new systematic uncertainties, validating the oscillation fit with other groups within T2K, and implementing new fitting mechanics into the analysis framework.

Chapter 6 presents the results and interpretations of the oscillation fit, which used data and inputs from the T2K collaboration and are the result of my own work with support from T2K collaborators. Chapter 7 expands upon the oscillation analysis presented in chapter 6 with the addition of new systematic uncertainties to model a specific region of phase space. These parameters were motivated and designed by both myself and Stephen Dolan. The implementation and testing of the new parameters in the MaCh3 framework were performed by myself. Finally, additional systematic parameters designed specifically for the DUNE experiment and other future neutrino experiments are presented in chapter 7. These parameters were motivated by myself, Stephen Dolan and Laura Munteanu and the implementation and testing constitute my own original research.

Acknowledgements

During my DPhil, I've had the opportunity to travel to many wonderful places and meet many equally wonderful people. As such, this section may be rather long, as there are a lot of people to thank without whom this thesis may not have been written. Or maybe it would have been, though the time leading up to writing it wouldn't have been as fun.

First, I'd like to thank Alfons Weber and Kirsty Duffy for being excellent supervisors and supporting me throughout my DPhil. A special thanks to Alfons for not dropping me as his student after accidentally calling him 'Alfonso' in our first email exchange. Additional thanks go to Giles Barr for his helpful supervision, advice and support during my second year, as well as to Dave and Morgan for their support and guidance.

I'd like to thank the entire Oxford group for making the office a great place to work when we all managed to be there at the same time... To Clarance, Luke, Patrick and Dan for their support and always being available to help with my research. To my fellow students in the Oxford neutrino group - Ciaran, Soniya, Federico, John, Weijun, Lars, Abbey and Yiwen - for their friendship and for making the office a fun place to be over the past four years. Ciaran, I especially enjoyed driving around suburban Chicago for several hours in search of a batting cage, only to end up at a Dick's Sporting Goods.

The main topic of this thesis is an oscillation analysis, which is very much a collaboration-wide effort. I owe much to the T2K collaboration for their input and advice, with special thanks to the entire MaCh3 group. I'd like to thank Patrick Dunne for his invaluable support during the busy period of the oscillation analysis. Thanks also to Asher Kaboth, Ed Atkin, Kevin Wood, Clarance Wret and Kamil Skwarczyński for their guidance and support throughout my time working in the MaCh3 group. A Bayesian oscillation analysis would feel rather incomplete without a hybrid-frequentist counterpart, so thanks also go to Kenji Yasutome and Lukas Berns of the PTheta group.

During my DPhil, I had the incredible opportunity to spend six months at CERN with the EP-NU group. I'd like to thank the entire EP-NU group for welcoming me as a visiting researcher. I'd like to especially thank Stephan Dolan and Laura Munteanu for their excellent guidance, support and friendship during

my work on interaction uncertainties at both DUNE and T2K. Stephen, my offer still stands: if you need a Director of Communications, I'm just a phone call away. Thanks also to James Herd and Innes MacKay for being great roommates. James, I'll fondly remember our very intense final few FIFA matches.

Over the course of my nearly ten years living and studying in Oxford, I have had the privilege of meeting so many incredible people beyond my research. First, I'd like to thank Kieran Storer for her encouragement and support throughout my time in Oxford. If it wasn't for you, I never would have considered pursuing a DPhil, and for that, I am eternally grateful. St Peter's College Boat Club was a big part of my time as a DPhil student, and I'd especially like to thank Nils Cwiekala, Sam Heywood, Max Williamson and Marcus Spiegel for their support and friendship. From Summer Torpids blades to spearing dinghies on the Isis at Oriel Regatta, memories of rowing together will always hold a very special place in my heart. Thanks also to Nick Stedman for his friendship and advice, from ORA to Jack Clow Road and beyond, with many impromptu Lord of the Rings reenactments along the way. Special thanks go to Toby Paterson, Nishant Chauhan, and William Blythe at St John's. Our jam sessions were always a highlight of my week, and I'll never forget our one and only live gig. Thanks also to the staff of Popeyes Louisiana Kitchen, Oxford, for the many (perhaps too many) delicious spicy chicken sandwiches that fuelled the writing of this thesis.

Throughout my time spent in Oxford, I've always cherished returning to the green, green grass of home. I'd like to thank Jamie Williams, Cairan Prior, William Harry and Joel Knight for their friendship and support over the years. Thanks also to Kayleigh Poulsom for her valuable friendship. I would still trade this DPhil for your 2013 Haberdasher's Award.

I would like to thank my family for all of the love and support they have given me throughout this DPhil. I'd like to thank my sister, Caitlin, my cousins, Charlie and Joel, and my Uncle Chris and Auntie Rose. I would be remiss not to also mention the vital support of my canine and feline friends: Angel, Pippa, and Penny. Finally, I would like to thank my parents, Darren and Joanne, and my grandmother, Ruth, for their love and encouragement from the very beginning. I wouldn't be where I am today without you.

Dedicated to the memory of my beloved Grancha, Wyndham Thomas.

Contents

List of Figures

List of Tables

1 Introduction

One of the greatest unsolved problems in physics is the origin of the observed matter-antimatter asymmetry. According to our understanding, when the Universe began with the Big Bang, equal amounts of matter and antimatter were expected to have been created. If this were the case, the matter and antimatter would have annihilated into pure energy, and the Universe would be a rather boring place. However, what we observe today is a matter-dominated universe. Where did all of the antimatter go? Stated differently, why are we all here?

In 1967, Andrei Sakharov proposed three necessary conditions that must be met to explain the observed matter-antimatter asymmetry, known as the Sakharov conditions [1]. One of these conditions is the violation of CP symmetry, which can be interpreted as a fundamental distinction in the laws of physics between matter and antimatter.

CP violation is allowed in the Standard Model and indeed has been experimentally observed in the quark sector. However, the *amount* of CP violation that has been measured is far from sufficient in explaining the matter-antimatter asymmetry we observe in the Universe. Therefore, there must be additional sources of CP asymmetry beyond the Standard Model.

Neutrino mixing offers an interesting gateway into investigating CP violation in the leptonic sector. Compared to the hadronic sector, a significantly higher

amount of CP violation is still possible in neutrino mixing. Indeed, if maximal CP violation occurs in neutrino oscillations, the degree of CP violation would be approximately a thousand times greater than that observed in the hadronic sector. Neutrino mixing is typically described using the PMNS parameterisation, where the effect of CP violation is encoded in the CP-violating phase δ_{CP}. The determination of the value of δ_{CP} is perhaps the most important question experimental neutrino physics must address. Furthermore, a measurement of δ_{CP} which violates CP symmetry may have profound implications for understanding the matter-antimatter asymmetry in the Universe[1].

T2K is a current-generation long-baseline neutrino oscillation experiment located in Japan [2]. It was designed to make precision measurements of the PMNS parameters $\sin^2\theta_{23}$ and $\sin^2\theta_{13}$, the mass-squared splitting Δm^2_{32}, and constrain the CP-violating phase δ_{CP}. Using a beam composed predominantly of muon neutrinos (ν_μ) or antineutrinos ($\bar{\nu}_\mu$), it constrains the PMNS parameters by measuring two distinct oscillation channels: the disappearance of muon neutrinos, and the appearance of electron neutrinos. This thesis presents the latest and most robust set of oscillation parameter constraints from the T2K experiment, currently representing a world-leading measurement of the oscillation parameters.

Current neutrino oscillation parameter measurements are limited by statistics. However, next-generation long-baseline experiments such as DUNE [3] and Hyper-K [4] are anticipated to be limited by systematic uncertainties. The modelling of neutrino interactions is likely to be a dominant component of the total systematic uncertainty, therefore improving our understanding of neutrino interactions is of critical importance if future-generation experiments are to achieve their physics goals. This thesis presents the development of novel interaction uncertainties designed for both current and next-generation experiments.

[1] CP violation in left-handed neutrinos may suggest the presence of CP violation in the decays of their heavier right-handed counterparts, which would result in a lepton asymmetry. Through processes far beyond the scope of this thesis, this can be converted into a Baryon asymmetry.

Systematic uncertainty paramterisations were designed and implemented in the T2K oscillation analysis framework to describe sizeable model differences in events where neutrinos transfer relatively small amounts of energy to the target nucleon. Model variations in this kinematic region caused a large bias on T2K's measurement of Δm^2_{32} and was the dominant contribution to its total systematic uncertainty. These parameters utilised regularisation techniques to ensure smooth, physical responses across kinematic bins.

Looking ahead to the DUNE experiment, new systematic parameters were designed to specifically target and model the nuclear ground state. With its utilisation of advanced detector technologies and unprecedented statistics, DUNE is anticipated to have significant constraining power for studying nuclear effects, which are currently poorly understood. Mis-modelling the nuclear ground state can lead to biases in oscillation parameter measurements, therefore introducing appropriate systematic uncertainties that can modify the nuclear ground state will form an important component of future oscillation analyses.

This thesis presents the most robust oscillation parameter constraints made by any oscillation experiment to date, but also looks towards the forthcoming precision era of oscillation physics, and what is required to ensure that next-generation experiments achieve their physics objectives.

Chapter 2 presents an overview of the field of neutrino physics. It discusses the discovery of the neutrino and its position within the Standard Model of particle physics, and details the theory underpinning neutrino oscillations. Furthermore, the chapter explores neutrino interactions and provides an overview of the different types of neutrino experiments. The chapter concludes by presenting the current status of neutrino physics and addresses the significant open questions that remain to be answered in the field.

Chapter 3 describes the T2K experiment, including the neutrino beamline, and the near and far detectors. The simulation techniques used are also briefly discussed, as well as the upcoming T2K near-detector upgrade.

Chapter 4 presents the statistical framework that underpins the primary result of this thesis, which is a Bayesian oscillation analysis. The chapter provides a brief overview of Bayesian inference and Markov chain Monte Carlo methods, as well as detailing how parameter constraints are extracted from the posterior distribution.

Chapter 5 provides an overview of the oscillation analysis strategy, the near and far-detector samples and the systematic uncertainties considered. Monte Carlo predictions at the far detector are presented, and validations performed before proceeding to data fits are also discussed. The final oscillation parameter constraints are then presented in chapter 6.

Chapter 7 presents the development and implementation of novel systematic parameters designed to address the largest component of the systematic uncertainty on the Δm^2_{32} constraint presented in chapter 6. This chapter also describes the implementation of new interaction uncertainties at the DUNE experiment, specifically designed and tailored for the next generation of long-baseline experiments.

To conclude, the results and implications of the work presented in this thesis are discussed in chapter 8. A short outlook on the future of experimental neutrino physics is also given.

2
Neutrino Physics

Soon after postulating the existence of a tiny, neutral particle in 1930 [5], Wolfgang Pauli said: "I have done a terrible thing, I have postulated a particle that cannot be detected". Coined the *neutrino* by Enrico Fermi, Pauli's postulation was finally detected in 1956 by Clyde Cowan and Frederick Reines [6]. Throughout the latter half of the 20th century, there was a signifcant increase in both experimental and theoretical reaearch into the neutrino. The discovery of neutrino oscillations by the Super-Kamiokande collaboration in 1998 [7] further spurred interest in neutrinos as the field advanced into the 21st century. Long predicted and believed to be massless, this result demonstrated the non-zero, finite mass of the neutrino; overnight, the field of neutrino physics ventured beyond the Standard Model.

This chapter provides an overview of key developments in the field of neutrino physics. Section 2.1 will describe the discovery of the neutrino and its representation within the Standard Model of particle physics. Section 2.2 will detail the theoretical description of oscillations, while section 2.3 will discuss neutrino interaction physics and its impact on oscillation measurements. Finally, section 2.4 will provide an overview of neutrino oscillation experiments and the current status and understanding of neutrino oscillations.

2.1 Discovery of The Neutrino

In the early 20th century, the only known fundamental particles were the proton and the electron. Around this time in 1914, James Chadwick was studying the energy spectrum of electrons produced in β decay [8], which was assumed to be a two-body decay in which an isotope X decays into an isotope Y via the emission of an electron:

$$ {}^{A}_{Z}\mathrm{X} \rightarrow {}^{A}_{Z+1}\mathrm{Y} + e^{-} \, . \tag{2.1} $$

For known isotopes X and Y, the energy of the outgoing electron can be calculated exactly using relativistic kinematics and the conservation of energy and momentum. Therefore, the spectra Chadwick expected to measure was a single line at an energy

$$ E_e = \frac{m_{\mathrm{X}}^2 - m_{\mathrm{Y}}^2 + m_e^2}{2m_{\mathrm{X}}} \, , \tag{2.2} $$

where m_{X} and m_{Y} are the masses of isotopes X and Y respectively, and m_e is the mass of the electron. However, Chadwick measured a continuous energy spectrum, with an endpoint of energy given by equation 2.2 [8].

The apparent violation of energy, momentum and angular momentum conservation in β decay led Pauli to postulate the existence of a neutral, spin-1/2 particle with very low mass which he called the 'neutron' [5]. Prospects of discovering such a low-mass particle seemed poor, nevertheless, Pauli's elegant solution was expanded upon by Enrico Fermi, who constructed a theoretical description of β decay assuming the existence of Pauli's new particle [9]. Two years after Pauli predicted the existence of a new particle, James Chadwick discovered the more massive nucleon we are familiar with today: the neutron [10]. This led Fermi to rename Pauli's particle, coining the term neutrino (meaning 'little neutral one'). Fermi's work now described β decay as a three-body process, including the (electron anti)neutrino:

$$ {}^{A}_{Z}\mathrm{X} \rightarrow {}^{A}_{Z+1}\mathrm{Y} + e^{-} + \bar{\nu}_e \, . \tag{2.3} $$

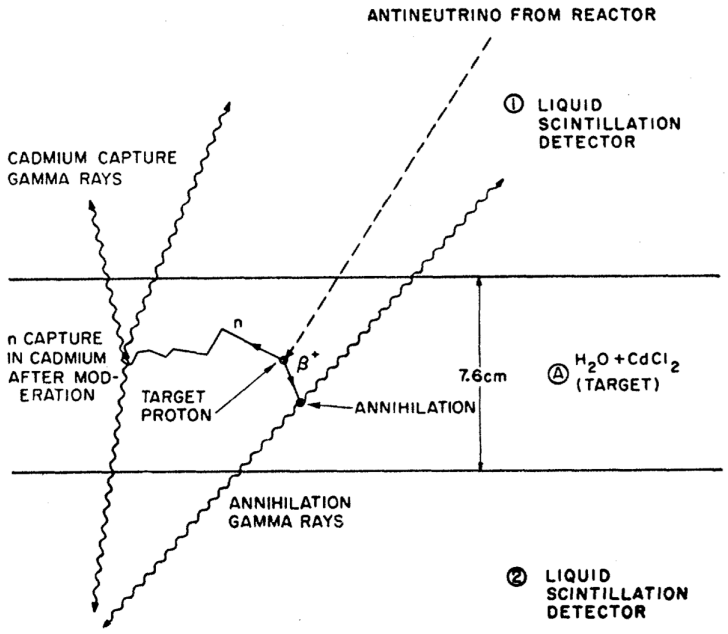

Figure 2.1: A schematic diagram of the experiment performed by Cowan and Reines. Figure from [11].

As well as providing a more accurate description of β decay, Fermi theory also predicted a process known as inverse beta decay (IBD), in which a free (anti)neutrino interacts with a proton, producing a positron and a neutron:

$$\bar{\nu}_e + p \rightarrow e^+ + n \; . \tag{2.4}$$

The likelihood for such an interaction to take place is very small, with a predicted cross section of 10^{-44} cm^2. Still, IBD's unique interaction signature provided optimism to those seeking an indirect detection of Pauli's elusive neutrino.

The neutrino remained long undetected until 1956, when Clyde Cowan and Frederick Reines conducted an experiment aiming to detect the interaction of a (electron anti)neutrino with water molecules, taking advantage of the large antineutrino flux from a nearby nuclear reactor [6, 11]. Their experiment consisted of two water tanks doped with cadmium chloride ($CdCl_2$) sandwiched between three liquid scintillator detectors. A schematic diagram of the experiment is shown in figure 2.1.

The pair were searching for the coincidence of two distinct signals. First, a positron annihilates with an electron in the water, emitting two prompt 0.51

MeV gamma rays. Second, a free neutron is captured by the cadmium nucleus to form an excited state which then decays (after $\sim 5\mu$s) via the emission of a de-excitation gamma ray. The experiment ran for a total of 1371 hours, and the neutrino signal was greater than twenty times the accidental background rate associated with the detector. The existence of Pauli's (anti)neutrino had finally been experimentally verified.

A few years later in 1962, Lederman, Schwartz and Steinberger performed an experiment at Brookhaven National Laboratory measuring neutrino interactions in a 10-ton aluminium spark chamber [12]. They aimed to investigate whether neutrinos emitted from charged-pion decays exhibited differences from those generated in β decays, as had been hypothesised by Bruno Pontecorvo [13]. In what was the world's first conventional accelerator neutrino beam, and highly analogous to the T2K beam described in section 3.1, 15 GeV protons struck a beryllium target producing mostly charged pions. These pions subsequently decayed to form a collimated beam of (muon) neutrinos. The experiment found that when these neutrinos interacted, only muons were produced. This led to the conclusion that ν_μ and ν_e were distinct particles.

After the discovery of the charm quark in 1974 [14, 15], quarks and leptons could be neatly organised into two distinct generations. This was until a series of experiments were performed by Perl et al. between 1974 and 1977 using the SPEAR electron-positron collider at the Stanford Linear Accelerator Center (SLAC). They observed 64 events at centre-of-mass energies of around 4 GeV of the form $e^+ + e^- \rightarrow e^\pm + \mu^\mp$ + missing energy, in which no other charged particles or photons were detected [16]. These events were consistent with the pair production and subsequent decay of a new, heavier lepton: the τ.

Following the trend observed in the preceding two generations, there was an underlying expectation that the τ lepton would be accompanied by its corresponding tau neutrino ν_τ. This recurrent sequence within particle generations found representation within the Standard Model of particle physics.

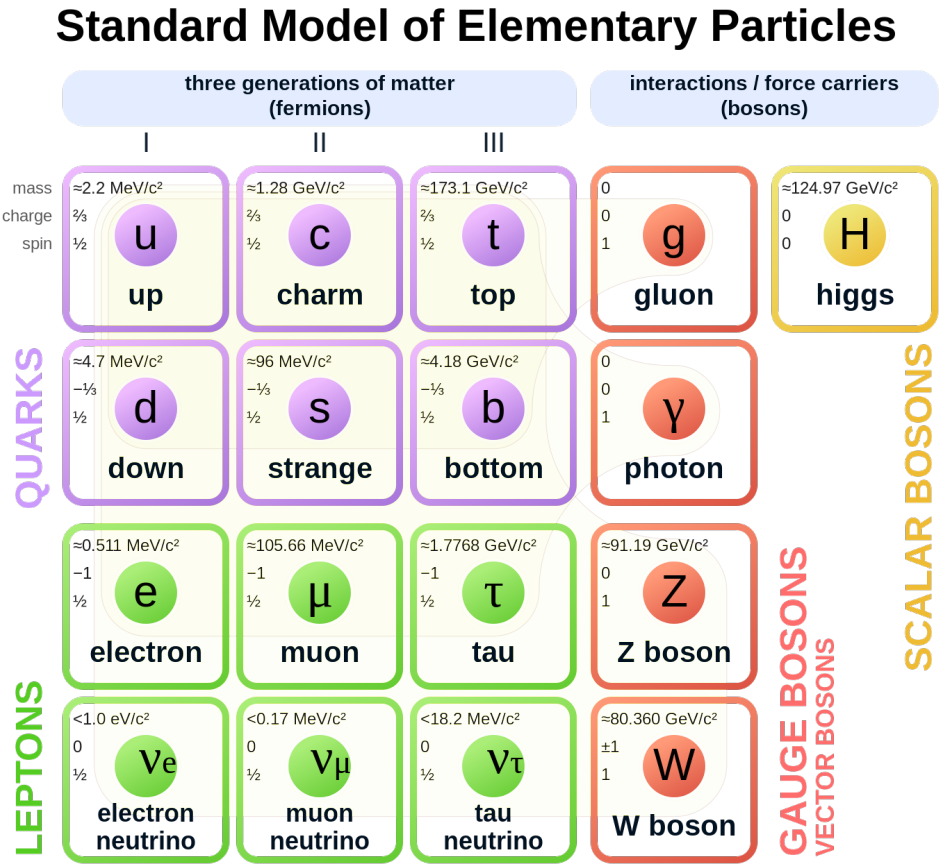

Figure 2.2: The constituent particles of the Standard Model. Figure from [17]

The Standard Model (SM) describes how elementary particles undergo interactions governed by three of the four known fundamental forces of nature, mediated by particles called gauge bosons. The forces and their respective gauge bosons are the strong interaction (gluon, g), the electromagnetic interaction (photon, γ), and the weak interaction ($W^{\pm}/Z^{0}$). Gravity is notably not included within the Standard Model, though on the sub-atomic scale, the effect of gravity compared with the other fundamental forces is negligible. These forces govern the behaviour of fermions, which are spin-1/2 particles that can be further classified into quarks and leptons. There are six quarks paired within three generations: up and down (u, d), charm and strange (c, s) and top and bottom (t, b). The first quark in each pair (u, c, t) carries $+\frac{2}{3}$ charge, while the second quark (d, s, b) carries $-\frac{1}{3}$ charge. Quarks also carry colour charge and therefore feel the

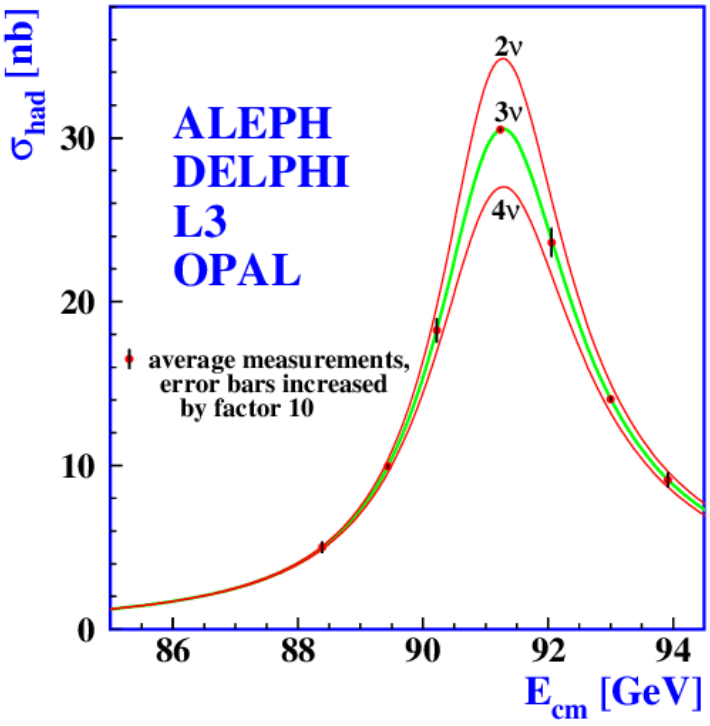

Figure 2.3: Measurements of the hadron production cross section near the Z^0 resonance. Each curve indicates the predicted cross section for two, three and four active neutrino generations compared with combined data from the ALEPH, DELPHI, L3, and OPAL experiments. Figure from [19].

strong interaction. Due to colour confinement, quarks must combine to form colourless objects bound by the strong force, such as baryons (qqq) and mesons ($q\bar{q}$). Similarly, there are three lepton generations (or flavours): electron (e, ν_e), muon (μ, ν_μ), and tau (τ, ν_τ). Leptons possess zero colour charge and therefore do not interact via the strong force. All fundamental particles in the Standard Model receive their mass by interacting with the Higgs field, the simplest manifestation of which is the corresponding Higgs boson, discovered at CERN in 2012 [18]. The constituent particles of the Standard Model are given in figure 2.2.

In the Standard Model, neutrinos are chargeless, colourless and massless leptons, and therefore only interact via the weak force. The tau neutrino had yet to be discovered when the Standard Model was under construction, but its existence was heavily suggested both by symmetry arguments and precision measurements of the decay width of the Z^0 boson. When it decays, the Z^0 boson can produce any SM fermion and its antiparticle (excluding the top), therefore

the total decay width can be written as

$$\Gamma_Z = 3\Gamma_{Z\to l^- l^+} + \sum_q \Gamma_{Z\to q\bar{q}} + N_\nu \Gamma_{Z\to \nu\bar{\nu}} \ , \tag{2.5}$$

where $\Gamma_{Z\to l^- l^+}$, $\Gamma_{Z\to q\bar{q}}$ and $\Gamma_{Z\to \nu\bar{\nu}}$ are the partial widths for decays to charged leptons, hadrons and neutrino-antineutrino pairs respectively, and N_ν is the number of active neutrino generations. Γ_Z, $\Gamma_{Z\to l\bar{l}}$ and $\Gamma_{Z\to q\bar{q}}$ can be obtained directly from experiment, while $\Gamma_{Z\to \nu\bar{\nu}}$ can be predicted using the Standard Model. A combined fit to data from experiments operating at the electron-positron colliders SLC and LEP gives $N_\nu = 2.9840 \pm 0.0082$, consistent with three active neutrino generations, as shown in figure 2.3. It should be noted that this measurement exclusively probes the number of neutrino flavours that couple to the Z^0, so does not include possible sterile or heavy neutrino species. In 2000, the ν_τ was finally discovered by the DONUT collaboration where they observed tracks consistent with τ decays originating from charged-current ν_τ scattering in a nuclear emulsion [20].

2.2 Neutrino Oscillation Theory

Neutrino oscillations are a manifestation of the mixing between a neutrino's flavour and mass eigenstates. Neutrinos are created and interact via the weak force in well-defined flavour eigenstates defined by their charged lepton partner, $|\nu_\alpha\rangle$, where $\alpha \in \{e, \mu, \tau\}$. Since neutrinos possess non-zero mass, there must also exist some set of mass eigenstates, $|\nu_i\rangle$, where $i \in \{1, 2, 3, ...\}$, each with mass m_i. The flavour state $|\nu_\alpha\rangle$ of a neutrino can be expressed as a quantum superposition of its mass eigenstates $|\nu_i\rangle$, related by a leptonic mixing matrix U:

$$|\nu_\alpha\rangle = \sum_i \mathrm{U}^*_{\alpha i} |\nu_i\rangle \ . \tag{2.6}$$

U is commonly referred to as the PMNS (Pontecorvo–Maki–Nakagawa–Sakata) matrix [13, 21], the leptonic equivalent of the CKM quark-mixing matrix. The size and parameterisation of U depends on the system being described. For

example, when considering only two neutrino flavours (as in section 2.2.2), U is a 2×2 matrix parameterised by one mixing angle θ[1]. Analogously, one can move beyond the 3ν framework to investigate potential sterile neutrino states. In this case, U would be a square matrix of size $3 + N$, where N represents the number of sterile neutrino states.

Within the framework of the Standard Model, there are three distinct neutrino flavour eigenstates ν_α. These states must be mutually orthogonal, otherwise, interactions where lepton flavour number is violated would be observed, such as $W^+ \rightarrow \mu^+ \nu_e$. Similarly, the neutrino mass eigenstates ν_i must also be orthogonal as they are eigenstates of the free particle Hamiltonian. If there are only three neutrino mass eigenstates (as our current understanding suggests), it follows that U must be a unitary 3×3 matrix [22]. The work done in this thesis implicity assumes that U fulfils this unitarity condition.

Assuming three neutrino flavour eigenstates, U can be written as

$$\mathrm{U} = \begin{pmatrix} \mathrm{U}_{e1} & \mathrm{U}_{e2} & \mathrm{U}_{e3} \\ \mathrm{U}_{\mu 1} & \mathrm{U}_{\mu 2} & \mathrm{U}_{\mu 3} \\ \mathrm{U}_{\tau 1} & \mathrm{U}_{\tau 2} & \mathrm{U}_{\tau 3} \end{pmatrix} , \tag{2.7}$$

where row α indicates the linear combination of neutrino mass eigenstates ν_i that couples to the charged lepton α, and column i indicates the linear combination of flavour eigenstates ν_α that comprise the mass eigenstate ν_i.

The PMNS matrix can be paramterised in terms of three mixing angles θ_{12}, θ_{13}, and θ_{23} and three complex phases δ_{CP}, α_1 and α_2 [23]:

$$\mathrm{U} = \underbrace{\begin{pmatrix} 1 & 0 & 0 \\ 0 & c_{23} & s_{23} \\ 0 & -s_{23} & c_{23} \end{pmatrix}}_{\text{Atmospheric}} \underbrace{\begin{pmatrix} c_{13} & 0 & s_{13} e^{-i\delta_{\mathrm{CP}}} \\ 0 & 1 & 0 \\ -s_{13} e^{i\delta_{\mathrm{CP}}} & 0 & c_{13} \end{pmatrix}}_{\text{Reactor/Accelerator}} \underbrace{\begin{pmatrix} c_{12} & s_{12} & 0 \\ -s_{12} & c_{12} & 0 \\ 0 & 0 & 1 \end{pmatrix}}_{\text{Solar}} \underbrace{\begin{pmatrix} e^{i\alpha_1/2} & 0 & 0 \\ 0 & e^{i\alpha_2/2} & 0 \\ 0 & 0 & 1 \end{pmatrix}}_{\text{Majorana}} , \tag{2.8}$$

where $c_{ij} \equiv \cos\theta_{ij}$ and $s_{ij} \equiv \sin\theta_{ij}$. The form of U in equation 2.8 is purely a convention. It helpfully separates the oscillation parameters into sub-matrices, each

[1] Assuming U is unitary.

making substantial contributions to different types of oscillation experiments. The first matrix contains only θ_{23}, which dominantly contributes to oscillations seen in atmospheric neutrinos ($\nu_\mu \rightarrow \nu_\tau$). The second matrix includes θ_{13} and δ_{CP}, with the former largely governing short-baseline oscillations observed at reactor experiments, and the latter encoding the level of CP violation present within the neutrino sector, with $\delta_{CP} = 0$ or $\pm\pi$ indicating CP conservation. The third matrix only contains θ_{12}, which dominates oscillations seen in solar neutrinos ($\nu_e \rightarrow \nu_\mu$). If neutrinos are Majorana particles, meaning neutrinos are their own antiparticle, there are also two additional Majorana phases α_1 and α_2, which are included here for completeness. Whether neutrinos are Dirac or Majorana is an open question in neutrino physics and is unable to be answered by oscillation experiments due to the cancellation of the Majorana phases when oscillation probabilities are calculated.

2.2.1 Oscillation Probability Calculation

Neutrino oscillation experiments consist of propagating neutrinos of a known flavour state, denoted as α, over a long distance (or 'baseline') L, and then re-measuring their flavour state, denoted as β. A schematic of such a neutrino oscillation can be found in figure 2.4.

Such experiments make inferences about the PMNS parameters by considering the oscillation probability. To calculate the probability that a neutrino created with flavour α is detected in flavour state β after travelling a distance L, denoted as $P(\nu_\alpha \rightarrow \nu_\beta)$, the eigenstate of the neutrino at $t = 0$ can be written as

$$|\nu_\alpha(0)\rangle = \sum_i U^*_{\alpha i} |\nu_i\rangle \ . \tag{2.9}$$

The time evolution of the mass eigenstate $|\nu_i\rangle$ obeys the Schrödinger equation[2]

$$i\frac{\partial}{\partial t} |\nu_i(t)\rangle = \mathcal{H} |\nu_i(t)\rangle \ . \tag{2.10}$$

[2]Natural units ($\hbar = c = 1$) are used throughout this thesis

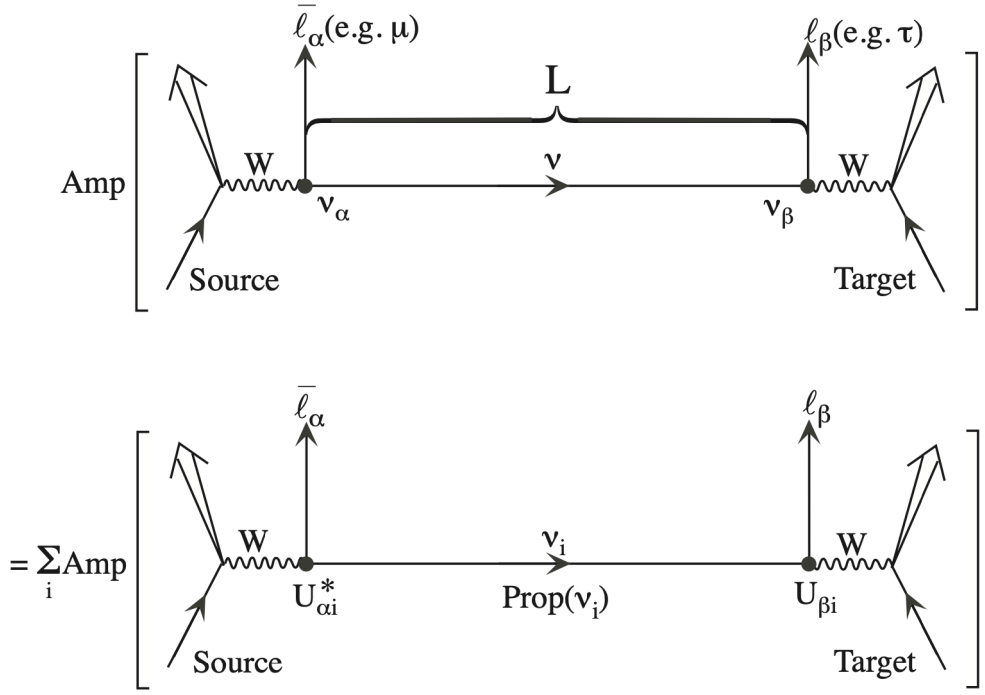

Figure 2.4: Schematic of neutrino oscillaton in vacuum. A neutrino created with flavour α propagates over a distance L and oscillates into flavour β. 'Amp' corresponds the amplitude $\mathcal{A}$, and 'Prop(ν_i)' denotes the propagator. Figure from [23].

Therefore, the neutrino mass eigenstate can be expressed as a plane wave

$$|\nu_i(t)\rangle = e^{-i(E_i t - \vec{p}\cdot\vec{x})} |\nu_i\rangle \ . \tag{2.11}$$

The time evolution of the flavour state of the neutrino can be computed by combining equation 2.9 and 2.11 to give

$$|\nu_\alpha(t)\rangle = \sum_i U^*_{\alpha i} \, e^{-i(E_i t - \vec{p}_i\cdot\vec{x}_i)} |\nu_i\rangle \ , \tag{2.12}$$

where E_i is the energy of neutrino mass eigenstate $|\nu_i\rangle$, and $\vec{p}_i$ and $\vec{x}_i$ are its momentum and position vectors respectively. Next, the Hermitian conjugate of equation 2.6 is used to construct the β flavour state vector

$$\langle\nu_\beta| = \sum_j U_{\beta j} \langle\nu_j| \ . \tag{2.13}$$

By taking the inner product of equation 2.13 with equation 2.12, the amplitude for a neutrino to change flavour from ν_α to ν_β can be calculated, denoted as

$\mathcal{A}(\nu_\alpha \rightarrow \nu_\beta)$, can be calculated as

$$\begin{aligned}\mathcal{A}(\nu_\alpha \rightarrow \nu_\beta) &= \langle \nu_\beta | \nu_\alpha(t) \rangle \\ &= \sum_i \sum_j \mathrm{U}^*_{\alpha i} \mathrm{U}_{\beta j}\, e^{-i(E_i t - \vec{p}_i \cdot \vec{x}_i)} \langle \nu_j | \nu_i \rangle \\ &= \sum_i \mathrm{U}^*_{\alpha i} \mathrm{U}_{\beta i}\, e^{-i(E_i t - \vec{p}_i \cdot \vec{x}_i)} \,,\end{aligned} \tag{2.14}$$

where the mutual orthogonality of the neutrino mass eigenstates has been utlised, $\langle \nu_j | \nu_i \rangle = \delta_{ij}$.

The phase factor in equation 2.14 can be simplified by first evaluating its value in the lab frame as

$$E_i t - \vec{p}_i \cdot \vec{x}_i = E_i t - |\vec{p}_i| L \,, \tag{2.15}$$

where t is the time taken for a neutrino to travel a distance L, and E_i and $\vec{p}_i$ are the energy and momentum of eigenstate $|\nu_i\rangle$ respectively. As neutrino masses are known to be very small ($m_\nu < 0.8$ eV at 90% CL [24]) the momentum can be approximated by

$$|\vec{p}_i| = \sqrt{E_i^2 - m_i^2} \approx E_i - \frac{m_i^2}{2E} \,. \tag{2.16}$$

Therefore equation 2.15 can be re-written as

$$E_i t - \vec{p}_i \cdot \vec{x}_i \approx E(t - L) + \frac{m_i^2}{2E} L \,, \tag{2.17}$$

where each neutrino mass eigenstate is assumed to have a common energy E. Equation 2.17 can be further simplified by ignoring the factor $E(t - L)$ as it's common to all mass eigenstates. Using this result the amplitude given in equation 2.14 can be written as

$$\mathcal{A}(\nu_\alpha \rightarrow \nu_\beta) = \sum_i \mathrm{U}^*_{\alpha i} \mathrm{U}_{\beta i}\, e^{-i m_i^2 \frac{L}{2E}} \,. \tag{2.18}$$

Finally, squaring the amplitude in equation 2.18 gives the oscillation probability $P(\nu_\alpha \rightarrow \nu_\beta)$, expressed as

$$\begin{aligned}P(\nu_\alpha \rightarrow \nu_\beta) = \delta_{\alpha\beta} &- 4 \sum_{i>j} \Re \left(\mathrm{U}^*_{\alpha i} \mathrm{U}_{\beta i} \mathrm{U}_{\alpha j} \mathrm{U}^*_{\beta j} \right) \sin^2 \left(\frac{\Delta m^2_{ij} L}{4E} \right) \\ &+ (-)\, 2 \sum_{i>j} \Im \left(\mathrm{U}^*_{\alpha i} \mathrm{U}_{\beta i} \mathrm{U}_{\alpha j} \mathrm{U}^*_{\beta j} \right) \sin \left(\frac{\Delta m^2_{ij} L}{2E} \right) \,,\end{aligned} \tag{2.19}$$

where $\Delta m^2_{ij} = m^2_i - m^2_j$, and the negative sign is for the case of antineutrino oscillations. This derivation largely followed approaches found in [23] and [25], a more detailed derivation and discussion of neutrino oscillation probabilities can be found in [26].

There are several important consequences worth noting when analysing equation 2.19:[3]

- If neutrinos are massless (as predicted by the Standard Model), $\Delta m^2_{ij} = 0$, meaning the flavour changing (i.e. $\alpha \neq \beta$) probability is zero. Therefore, observation of oscillations both implied and required massive neutrinos.

- Oscillation probabilities are dependent on the mass-squared splitting between mass eigenstates. This means neutrino oscillation experiments have no sensitivity to the absolute mass scale of the neutrino. However, they do have sensitivity to the *ordering* (or hierarchy) of the mass states[4], the two possibilities referred to as normal ($m_3 > m_1$) or inverted ($m_3 < m_1$) ordering. The orderings of the mass eigenstates and their respective flavour contents are shown in figure 2.5.

- Using equation 2.19 and the unitarity of U, one can show that

$$\sum_{\beta} P(\nu_\alpha \to \nu_\beta) = 1 \,, \tag{2.20}$$

  where β sums over all neutrino flavours, including the original flavour α. This demonstrates that total neutrino flux is conserved, with flavour changes causing redistributions of its composite flavours.

- Including the implicit extra factors of $\hbar$ and c, the argument of the $\sin^2$ term of equation 2.19 can be written as

$$\frac{\Delta m^2_{ij} L}{4E} = 1.27 \Delta m^2_{ij}(\mathrm{eV}^2) \frac{L(\mathrm{km})}{E(\mathrm{GeV})} \,. \tag{2.21}$$

[3] List adapted from [23]

[4] Though it is possible to measure the mass ordering using the imaginary part of equation 2.19, most oscillation experiments use matter effects to perform such a measurement. Matter effects are described in section 2.2.3.

For oscillations to be measurable by experiments, $\sin^2(x)$ should be of the order 1, meaning $\mathcal{O}(x) \sim \pi/2$, where $x = 1.27\Delta m^2_{ij}(\text{eV}^2)\frac{L(\text{km})}{E(\text{GeV})}$. Consequently, oscillation experiments need to carefully choose L and E to achieve sensitivity to the desired mass-squared splitting. A given experiment with a baseline L km and energy E GeV will be sensitive to neutrino mass-squared splittings down to $\sim \left(\frac{L(\text{km})}{E(\text{GeV})}\right)^{-1}$. For example, T2K has a baseline of 295 km and a peak neutrino energy of 0.6 GeV, and is therefore sensitive to $\Delta m^2_{ij} \sim \mathcal{O}(10^{-3}\text{eV}^2)$.

- Of particular interest to long-baseline oscillation experiments, the oscillation probability for neutrinos and antineutrinos is different if U is complex. If it was found that $P(\nu_\alpha \to \nu_\beta) \neq P(\bar{\nu}_\alpha \to \bar{\nu}_\beta)$, this would indicate a violation of CP symmetry in the leptonic sector. Such a result would have important consequences and implications for particle physics. So far, CP asymmetry has only been detected in the quark sector [27], and is not large enough to explain the matter-antimatter asymmetry seen in the universe today. Measuring CP violation in neutrino interactions may provide a solution to this problem.

2.2.2 Two Flavour Approximation

There are several scenarios in neutrino oscillation physics where it is both useful and entirely appropriate to approximate only two neutrino mass and flavour eigenstates, denoted as $\{\nu_1, \nu_2\}$ and $\{\nu_\alpha, \nu_\beta\}$ respectively. Notable cases that are dominated by a single oscillation channel include solar ($\nu_e \leftrightarrow \nu_\mu$) and atmospheric ($\nu_\mu \leftrightarrow \nu_\tau$) neutrino oscillations. In this case, there is only one mass-squared splitting, $\Delta m^2 \equiv m^2_2 - m^2_1$, and the mixing matrix is simply a 2×2 rotation matrix

$$\text{U} = \begin{pmatrix} \cos\theta & \sin\theta \\ -\sin\theta & \cos\theta \end{pmatrix} , \tag{2.22}$$

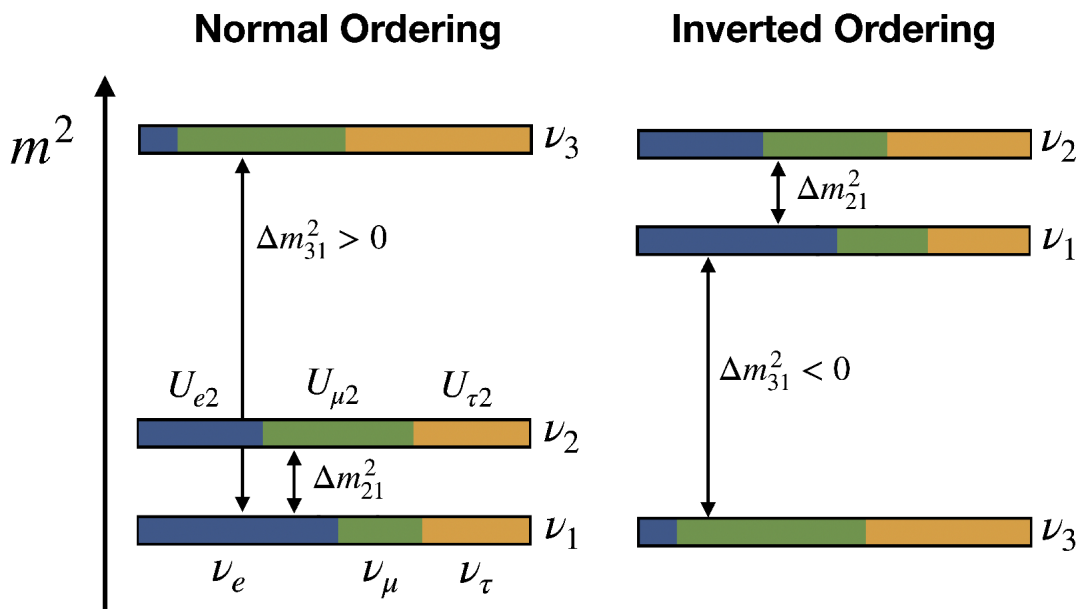

Figure 2.5: Neutrino mass eigenstates and their flavour contents for normal ordering (left) and inverted ordering (right). Figure from [28].

parameterised by a single mixing angle θ. Using this definition for U the oscillation probability in equation 2.19 can be further simplified to

$$P(\nu_\alpha \to \nu_\beta) = \sin^2 2\theta \sin^2 \left(\frac{\Delta m^2 L}{4E} \right) , \tag{2.23}$$

and using the total law of probability, the survival probability can be written as

$$P(\nu_\alpha \to \nu_\alpha) = 1 - \sin^2 2\theta \sin^2 \left(\frac{\Delta m^2 L}{4E} \right) . \tag{2.24}$$

Note, since U is a real matrix, equation 2.23 also applies to antineutrino oscillations. Therefore, CP violation in neutrino oscillations requires three flavour eigenstates.

2.2.3 Matter Effects

So far, our oscillation probability calculations have assumed that neutrinos propagate through a vacuum. However, often in oscillation experiments, neutrinos are travelling in the presence of matter. This alters the Hamiltonian of the system

$$\mathcal{H} = \mathcal{H}_{\text{vac.}} + \mathcal{V} , \tag{2.25}$$

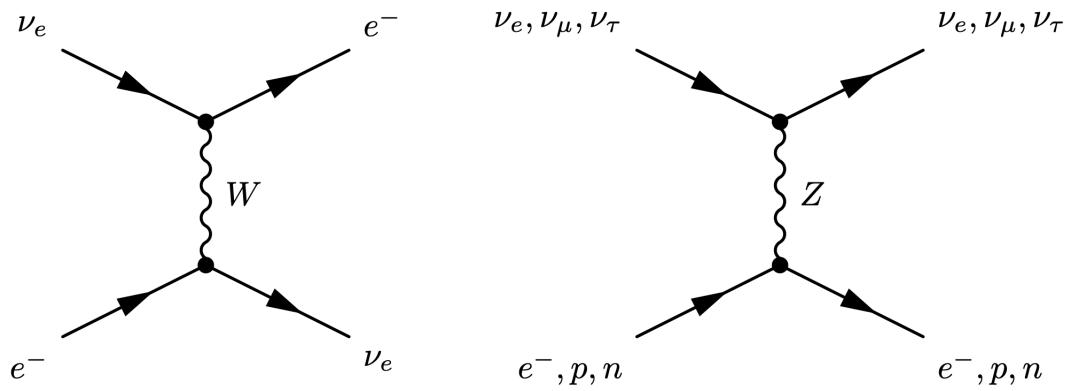

Figure 2.6: Feynman diagram for coherent forward neutrino scattering via charged-current (left) and neutral-current (right) exchange. Figure from [31]

where $\mathcal{H}_{\text{vac.}}$ is the Hamiltonian for oscillations in vacuum, and $\mathcal{V}$ is the added potential due to neutrinos undergoing coherent forward scattering with particles within the matter. In the Standard Model, a neutrino can coherent forward scatter by exchanging either a W or Z boson. In normal matter, only protons, neutrons and electrons are present. Consequently, when interacting within matter, all neutrino flavours can undergo neutral current interactions, while only electron neutrinos can interact via W exchange. Feynman diagrams for these processes are shown in figure 2.6. Because all neutrino flavours experience a potential due to the weak neutral current, the overall oscillation probability is unaffected. Therefore, only the potential due to the charged-current scattering of electron neutrinos needs to be considered when calculating neutrino oscillation probabilities. The impact due to the presence of matter on oscillation probabilities was first considered by L. Wolfenstein [29], and further expanded upon in the context of solar neutrinos by S. Mikheev and A. Smirnov [30].

It can be shown [25] that the additional potential $\mathcal{V}$ experienced by electron neutrinos can be written as

$$\mathcal{V} = \pm\, 2 G_F N_e \,, \tag{2.26}$$

where the positive (negative) sign corresponds to neutrinos (antineutrinos), G_F is the Fermi constant, and N_e is the number of electrons per unit volume. Through

further derivation, detailed in [23], it is possible to show that the Hamiltonian for two-flavour neutrino oscillations in matter can be expressed as

$$\mathcal{H} = \frac{\Delta m^2}{4E} \begin{pmatrix} -(\cos 2\theta - A) & \sin 2\theta \\ \sin 2\theta & (\cos 2\theta - A) \end{pmatrix} , \tag{2.27}$$

where the parameter A quantifies the significance of the matter effect relative to the mass-squared splitting and is defined as

$$A = \frac{2\sqrt{2} G_F N_e E}{\Delta m^2} . \tag{2.28}$$

Matter effects have the following implications on neutrino oscillation probability measurements:

1. The additional potential (see equation 2.26) felt due to the presence of matter is positive for neutrinos but negative for antineutrinos. This means matter effects will create an asymmetry between neutrino and antineutrino oscillations resembling actual CP violation. Consequently, it is important to correctly separate these two effects when attempting to measure true CP violation in neutrinos.

2. The strength of the matter effect (see equation 2.28) is dependent on the sign of the mass splitting Δm^2. It is therefore possible to use the matter effect to identify the normal or inverted ordering of the neutrino mass states.

3. The strength of the matter effect scales with neutrino energy E, and therefore has different impacts on different neutrino oscillation experiments. At T2K's neutrino energies, the matter effect has a very small impact on oscillation probabilities. However, future experiments such as DUNE, which has a much longer baseline of 1300 km and peak neutrino energies of $\sim$ 2.5 GeV, will observe a considerably stronger matter effect [3].

The impact of matter effects on oscillation probabilities, assuming the two-flavour approximation, as well as the impact of the sign of Δm^2, is shown in figure 2.7. The analysis presented in this thesis uses the Prob3++ software package [32] to

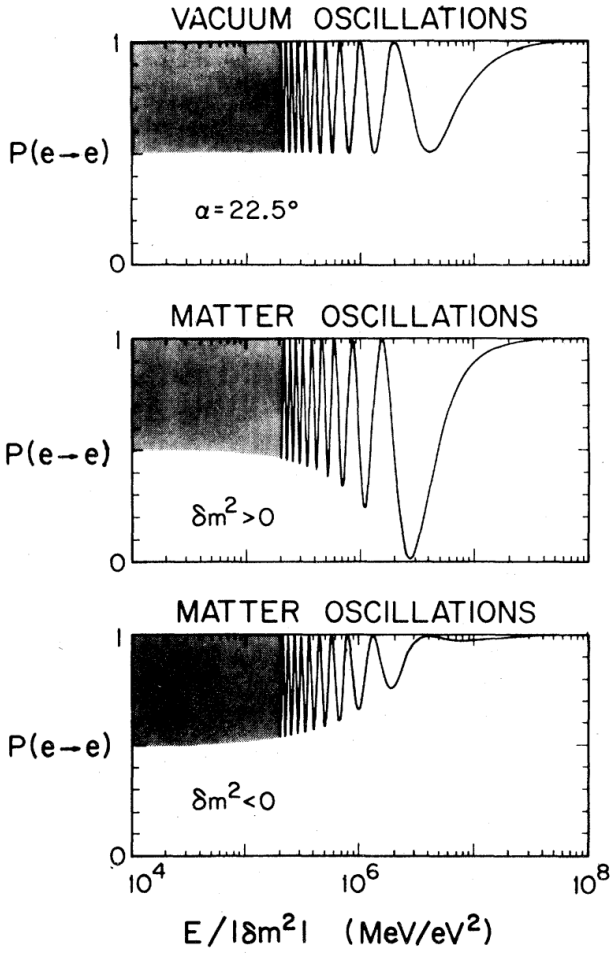

Figure 2.7: Comparison of the two-flavour approximation vacuum and matter survival probability $P(\nu_e \to \nu_e)$, assuming a mixing angle $\alpha = 22.5°$, a baseline $L = 5000$km, and $N_e = 2N_A$. Figure from [34].

calculate oscillation probabilities. The matter effect is fully taken into account, assuming an average matter density of 2.6 gcm^{-3} [33].

2.2.4 Oscillations at T2K

T2K and other long-baseline neutrino experiments look for neutrino oscillations in two main channels: muon (anti)neutrino disappearance and electron (anti)neutrino appearance. Neglecting higher order terms and matter effects, their oscillation probabilities are given by

$$P(\nu_\mu(\bar{\nu}_\mu) \rightarrow \nu_\mu(\bar{\nu}_\mu)) = 1 - 4\cos^2\theta_{13}\sin^2\theta_{23} \times (1 - \cos^2\theta_{13}\sin^2\theta_{23})\sin^2\left(\frac{\Delta m^2_{32}L}{4E}\right), \tag{2.29}$$

$$P(\nu_\mu(\bar{\nu}_\mu) \rightarrow \nu_e(\bar{\nu}_e)) = \sin^2\theta_{13}\sin^2\theta_{23}\sin^2\left(\frac{\Delta m^2_{32}L}{4E}\right) - (+)\frac{1.27\Delta m^2_{21}L}{E}8\mathcal{J}_{\mathrm{CP}}\sin^2\left(\frac{\Delta m^2_{32}L}{4E}\right), \tag{2.30}$$

where negative and positive signs in equation 2.30 are used to denote neutrino and antineutrino oscillation probabilities respectively. Figure 2.8 shows both oscillation probabilities superimposed on the T2K neutrino flux. The disappearance probability, shown in equation 2.29, is identical for neutrino and antineutrino oscillations. In contrast, the appearance probability, shown in equation 2.30, is different for neutrinos and antineutrinos, giving rise to CP violation. The CP-violating term of equation 2.30 contains $\mathcal{J}_{\mathrm{CP}}$, known as the Jarlskog invariant [35]. The Jarlskog invariant, originally used to study CP violation in the quarks, provides a convention-independent measure of CP violation in the neutrino sector. Assuming the PMNS parameterisation, it can be written as

$$\mathcal{J}_{\mathrm{CP}} = s_{13}c^2_{13}s_{12}c_{12}s_{23}c_{23}\sin\delta_{\mathrm{CP}}, \tag{2.31}$$

where $s_{ij} \equiv \sin\theta_{ij}$ and $c_{ij} \equiv \theta_{ij}$.

Assuming values for the PMNS parameters quoted in the latest global fits [27], the current maximum value for the Jarlskog invariant in the neutrino mixing sector is $\mathcal{J}^{\mathrm{Max}}_{\mathrm{CP}} = 0.03$. This is several orders of magnitudes larger than the corresponding value in the quark sector, where $\mathcal{J}^{\mathrm{Quarks}}_{\mathrm{CP}} = (3.00^{+0.15}_{-0.09}) \times 10^{-5}$. An accurate measurement of this quantity would therefore have significant implications for the matter-anti-matter asymmetry problem, where it is well-established that the observed level of CP violation in the hadronic sector is unable to fully explain the asymmetry.

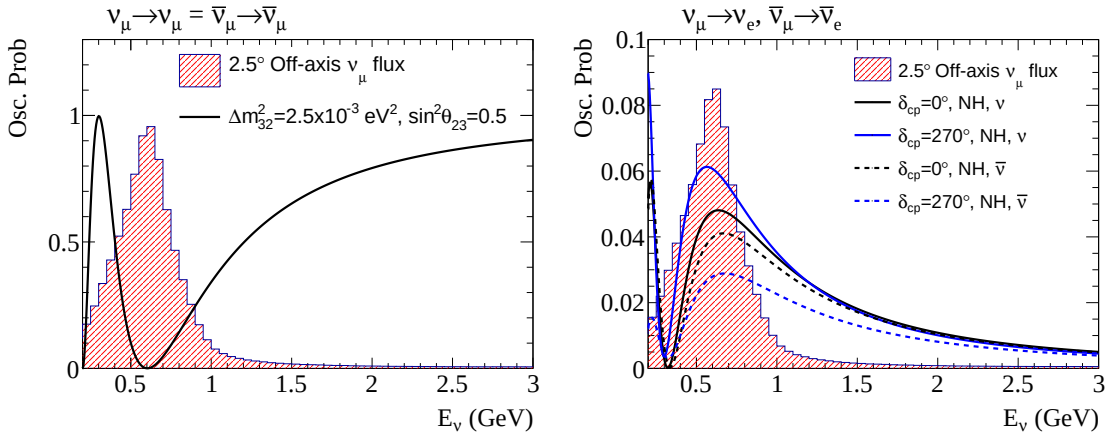

Figure 2.8: Oscillation probabilities with T2K ν_μ flux overlaid for the disappearance (left) and appearance (right) channels. The appearance probability has been calculated for $\delta_{\mathrm{CP}} = 0°, 270°$, and for both neutrinos and antineutrinos, demonstrating the convolution of matter effects and genuine CP violation. Figures from [36].

2.3 Neutrino Interactions

The fundamental calculation involved in a neutrino oscillation analysis is the comparison of the data measured at the far detector with a prediction. This prediction is the output of a detailed analysis of the unoscillated neutrino spectrum at the near detector, and extrapolating this to the far detector. Ideally, an exact measurement of the neutrino flux at the near and far detector could be performed to extract the oscillation probability, but in reality what experiments measure is a complex product of flux, cross-section and detector effects. The near detector can be used to constrain the systematic effects at the far detector. The ratio of the number of electron-like events at the far-detector (N_e^{FD}) to the number of muon-like events at the near detector (N_μ^{ND}) can be written as

$$\frac{N_e^{\mathrm{FD}}(E_{\mathrm{rec}})}{N_\mu^{\mathrm{ND}}(E_{\mathrm{rec}})} = \frac{\int P_{\nu_\mu \to \nu_e}(E_\nu) \cdot \Phi_\mu^{\mathrm{ND}}(E_\nu) \cdot \mathcal{F}_{\mathrm{ND}\to\mathrm{FD}}(E_\nu) \cdot \sigma_e(E_\nu) \cdot \mathcal{S}_e^{\mathrm{FD}}(E_\nu, E_{\mathrm{rec}})\, dE_\nu}{\int \Phi_\mu^{\mathrm{ND}}(E_\nu) \cdot \sigma_\mu(E_\nu) \cdot \mathcal{S}_\mu^{\mathrm{ND}}(E_\nu, E_{\mathrm{rec}})\, dE_\nu}, \quad (2.32)$$

where Φ_μ^{ND} is the flux of muon-neutrinos at the near detector, $\mathcal{F}$ is the near to far detector flux extrapolation, $\sigma_{e/\mu}$ is the electron/muon-neutrino cross section, and $\mathcal{S}_{e/\mu}^{\mathrm{FD/ND}}$ is the relation of reconstructed (E_{rec}) to true (E_ν) neutrino energy and the impact of detector effects. Additionaly, $P_{\nu_\mu \to \nu_e}(E_\nu)$ is the probability

for a ν_μ to oscillate to a ν_e. The quantities in equation 2.32 do not cancel fully, therefore if precision measurements of the neutrino oscillation parameters are to be made, each term must be well understood. Of particular importance to the work presented in this thesis is the understanding of neutrino interaction uncertainties, which currently account for a large proportion of the total uncertainty on measurements of the oscillation parameters [37].

2.3.1 Interaction Types

Standard Model neutrino interactions can be divided into two broad categories: charged current (CC) and neutral current (NC). Example Feynman diagrams for these interactions are shown in figure 2.9. CC interactions involve an incoming neutrino interacting within the nucleus and producing a charged lepton of the same flavour as the incoming neutrino. Conversely, NC interactions result in only a neutrino in the leptonic final state. These interactions can be divided further into their specific interaction modes:

- **Quasi-elastic (QE) scattering** - a neutrino interacts with an individual nucleon inside the nucleus producing a lepton and a single nucleon at the interaction vertex
- **Multinucleon processes (2p2h)** - similar to QE scattering, but instead the neutrino interacts with a correlated pair of nucleons inside the nucleus
- **Resonance production (RES)** - a neutrino interacts with a nucleon and produces a Baryonic resonant state (often a Δ)
- **Deep inelastic scattering (DIS)** - the neutrino interaction resolves quark structure within the struck nucleon

Figure 2.10 shows the predicted cross sections for each interaction mode as a function of neutrino energy, and the Feynman diagrams for CCQE, CCRES and CCDIS interactions are illustrated in figure 2.11. At T2K energies, CCQE and 2p2h interactions are most probable, though there are important contributions at higher

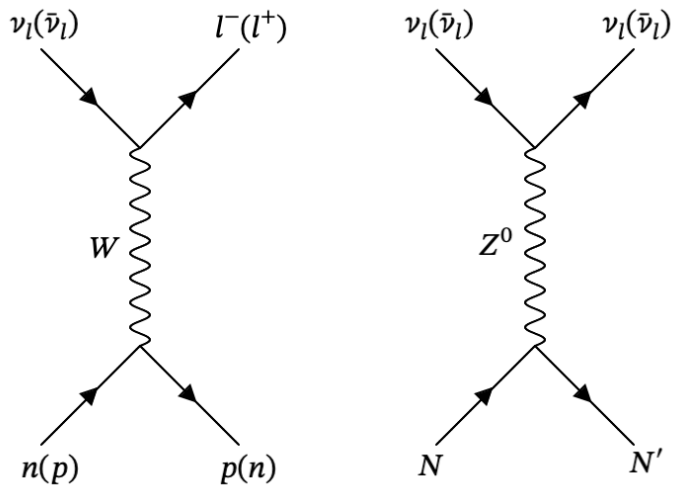

Figure 2.9: Feynman diagrams for charged-current (left) and neutral-current (right) neutrino/antineutrino interactions.

energies from CCRES and CCDIS events. This is somewhat fortunate as CCQE interactions are simpler and much better understood. However, in anticipation of future experiments such as DUNE and its higher energy neutrino beam, achieving a more comprehensive understanding of CCRES and CCDIS interactions will be important for making precise measurements of the oscillation parameters.

2.3.2 Nuclear Effects and Final State Interactions

A neutrino's oscillation probability depends, among other factors, on its true energy, commonly written as E_ν. As neutrino energy cannot be directly measured experimentally, precise calculations of oscillation probabilities rely on the accurate reconstruction of the neutrino energy from final-state particles. This process would be relatively straightforward if neutrinos were interacting with just free nucleon targets, however, all current neutrino oscillation experiments include nuclear targets. This leads to complications when reconstructing the true neutrino energy.

Bound nucleons within a nuclear target are not stationary. Instead, they possess some unknown momenta due to Fermi motion [39]. The initial energy and momenta of nucleons in the nuclear ground state are not experimentally accessible and instead need to be theoretically modelled. Models commonly

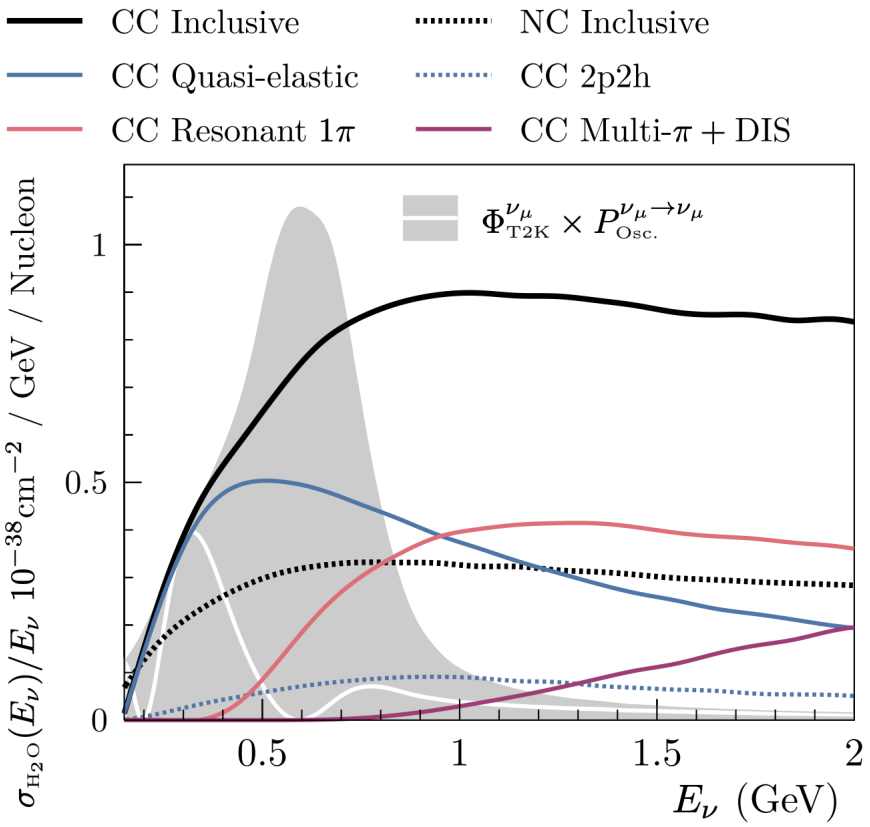

Figure 2.10: Simulated T2K ν_μ cross section on water broken down by interaction mode. The ν_μ flux at the far detector is shown as a white line, and the shaded region shows the unoscillated ν_μ flux seen at the near detector. Figure from [38].

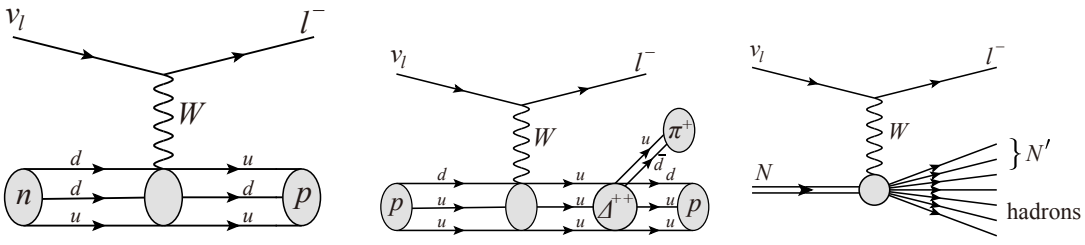

(a) CCQE **(b)** CCRES **(c)** CCDIS

Figure 2.11: Feynman diagrams for CCQE, CCRES and CCDIS neutrino interactions.

chosen by oscillation experiments include Fermi gas-based models, where the nucleus is considered to be a Fermi gas of non-interacting nucleons, and the Benhar spectral function (SF) model, where the energy and momenta of nucleons are distributed in a more realistic shell-like structure [40]. The SF model also incorporates short-range correlations (SRC), which account for around 20% of nucleons in the nuclear ground state [41]. SRCs are strongly-correlated pairs of nucleons with high momentum. When neutrinos interact with these pairs, it results in the presence of two nucleons in the final state [42].

Particles produced during a neutrino interaction at the interaction vertex must then leave the nucleus. During this process, they can undergo further scatters that modify their kinematics or produce additional particles. These processes are known as final state interactions (FSI), and a diagram illustrating such interactions is presented in figure 2.12. Mis-modelling FSI can lead to the mis-reconstruction of events. For example, consider a CCRES event in which a charged pion is produced but then subsequently absorbed within the nucleus. The pion would not escape the nucleus and hence never be detected, leading to the event instead being classified as CCQE. This holds significance in oscillation experiments since it could lead to the inaccurate reconstruction of neutrino energy, which would result in an incorrect calculation of the oscillation probability.

2.4 Neutrino Oscillation Experiments

There are many natural and artificial sources of neutrinos, some of which provide opportunities to study neutrino oscillations and make precision measurements of the PMNS parameters. Experiments studying neutrino oscillations are typically categorised based on the origin of the neutrinos they study. The primary types of experiments include those focusing on solar, reactor, atmospheric and accelerator neutrinos. This section will explore significant experiments and results from each of these categories.

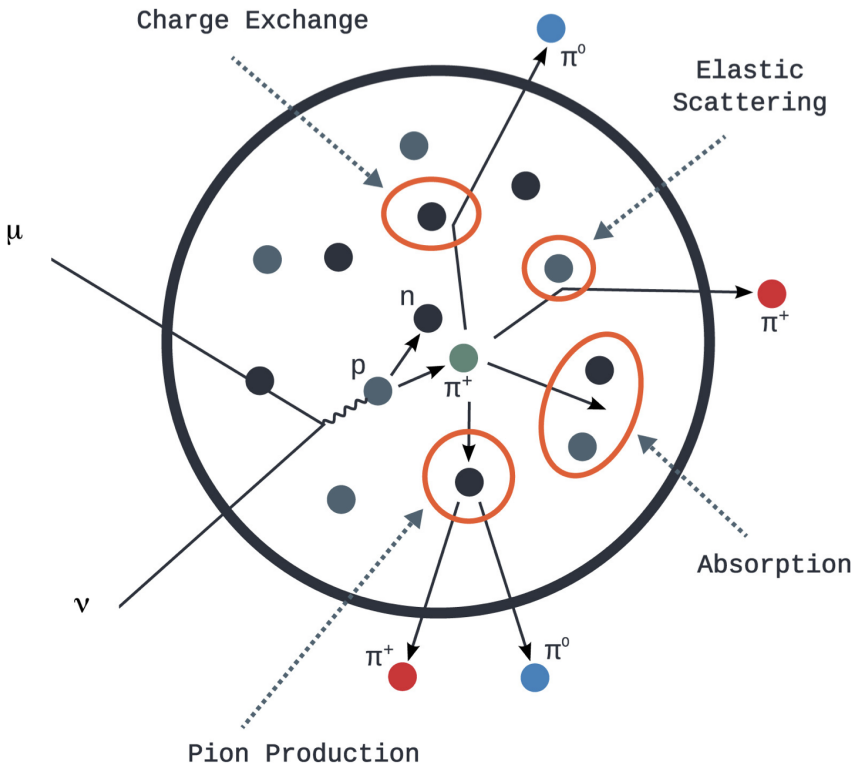

Figure 2.12: Schematic of Final State Interactions (FSI). Figure from [43].

2.4.1 Solar Experiments

Neutrinos are produced in the cores of stars through a variety of nuclear fusion reactions. In the Sun, the proton-proton (pp) chain dominates over other fusion processes, and the energy spectra of the neutrinos from the pp chain are shown in figure 2.13. Standard Solar models (SSMs) are theoretical descriptions of the structure and behaviour of the Sun, and of particular importance to the study of neutrinos are the models developed by Bahcall and collaborators, which were used to compute the expected flux of solar neutrinos at the Earth's surface [44].

The solar neutrino flux was first measured by Ray Davis's groundbreaking Homestake experiment [46]. They utilised the inverse β-decay reaction $\nu_e + {}^{37}\mathrm{Cl} \rightarrow {}^{37}\mathrm{Ar} + e^-$ to detect electron neutrinos originating from within the Sun. The neutrino energy threshold for this interaction to occur is $E_\nu^{\mathrm{th}} = 0.814$ MeV, therefore they mostly detected higher energy neutrinos originating from ${}^{8}\mathrm{B}$ decays. The experiment measured a solar neutrino rate that was approximately three times smaller than predicted by the SSM, a discrepancy of more than

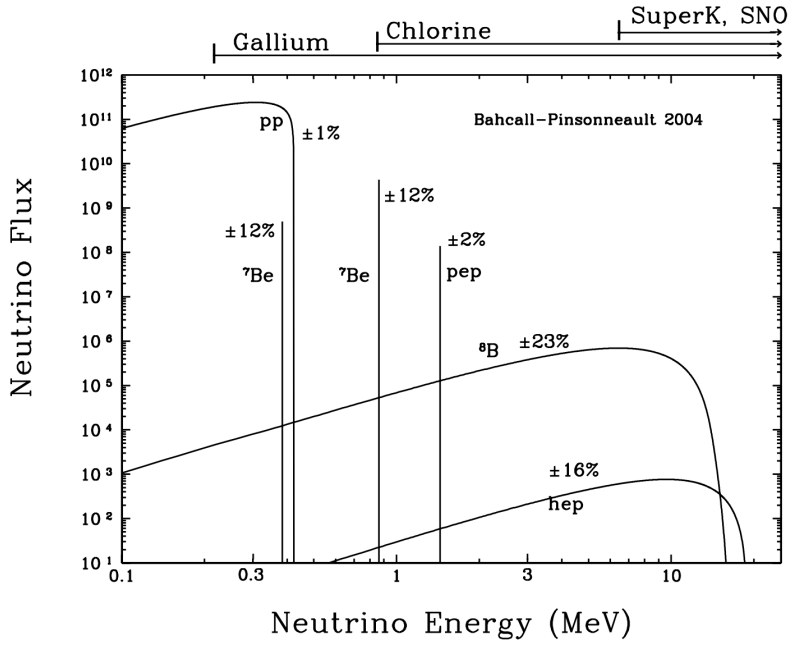

Figure 2.13: Energy spectra of neutrino fluxes from the pp chain, as predicted by the standard solar model. The energy ranges explored by different solar neutrino experiments are specified. For continuous sources, the differential flux is measured in $\mathrm{cm}^{-2}\mathrm{s}^{-1}\mathrm{MeV}^{-1}$, while for line sources, the flux is in $\mathrm{cm}^{-2}\mathrm{s}^{-1}$. The percentages represent theoretical uncertainties in the flux values. Figure from [45].

3σ [31]. This disagreement between experimental observations and theoretical predictions became known as the 'solar neutrino problem'.

This discrepancy was reinforced in the years that followed, first by the Kamiokande-II experiment in 1989 [47], then by the gallium-based experiments GALLEX [48] and SAGE [49] in the 1990s, all of which measured a solar neutrino flux of around half the rate predicted by the SSM. The gallium-based results were especially significant due to their much lower neutrino energy threshold of $E_\nu^{\mathrm{th}} = 0.233$ MeV, therefore allowing them to probe lower energy pp chain neutrinos which had lower flux uncertainties.

By the late 1990s, the solar neutrino problem had been firmly established. Early efforts to reconcile the inconsistency between theory and experiment proposed that the SSM might be inaccurate, though progress in helioseismology raised doubts about this proposition [50]. An alternative explanation had been proposed a year prior to Davis' Homestake experiment by Pontecorvo, who

postulated that solar electron neutrinos were undergoing oscillations into muon neutrinos [51].

The resolution to the solar neutrino problem was provided by the Sudbury Neutrino Observatory (SNO) experiment in 2002 [52]. In contrast to previous experiments, SNO was able to measure both the total flux of solar neutrinos across all flavours as well as the flux of electron neutrinos. SNO observed ^{8}B solar neutrinos through the reactions

$$\begin{aligned} \text{CC:} \quad & \nu_e + d \rightarrow p + p + e^- \\ \text{NC:} \quad & \nu_\alpha + d \rightarrow p + n + \nu_\alpha \\ \text{ES:} \quad & \nu_\alpha + e^- \rightarrow \nu_\alpha + e^- \ , \end{aligned} \tag{2.33}$$

where d is deuterium and $\alpha = \{e, \mu, \tau\}$. The CC reaction is sensitive only to ν_e, while the NC reaction is equally sensitive to all active neutrino flavours. While elastic scattering (ES) is sensitive to all neutrino flavours, its sensitivity is significantly enhanced for ν_e as $\nu_e + e^-$ can proceed either via W or Z exchange, whereas only the latter is possible for ν_μ and ν_τ. SNO was able to confirm the deficit of electron neutrinos observed in previous experiments and also measured a total solar neutrino flux that was consistent with the standard solar model. SNO's results, shown in Figure 2.14, demonstrated that the solar neutrino problem arose due to ν_e oscillations.

2.4.2 Reactor Experiments

Reactor neutrinos are produced from the β decays of neutron-rich isotopes formed in nuclear fission reactors. Reactor neutrinos are exclusively electron antineutrinos and possess a relatively low mean energy of around 3 MeV. $\bar{\nu}_e$ can be detected through inverse β decay, detailed in equation 2.4. Reactor experiments can only search for the disappearance of $\bar{\nu}_e$; they cannot search for an appearance signal since the neutrino energy is insufficient to produce μ or τ leptons. The survival probability for a reactor $\bar{\nu}_e$ can be written as [54]

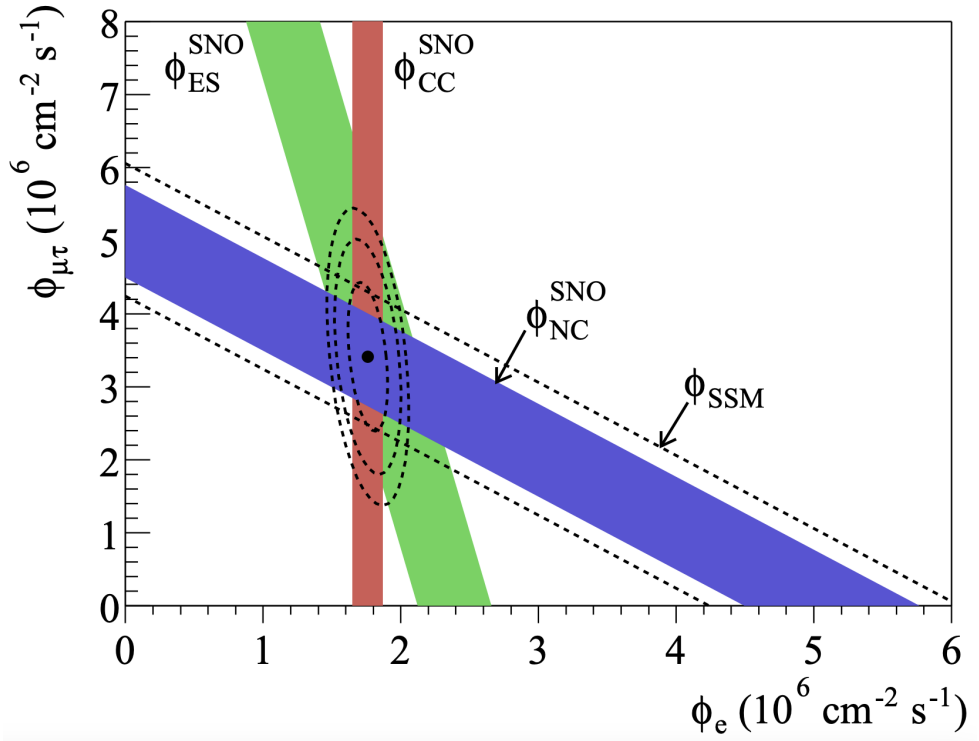

Figure 2.14: SNO's measurements of the ν_e flux (ϕ_e) and the combined ν_μ and ν_τ flux ($\phi_{\mu\tau}$) from the three neutrino reactions outlined in equation 2.33. The SNO measurements are shown by each solid band, and the intersections of these bands with the axes indicate the $\pm 1\sigma$ errors. The dashed diagonal band represents the total ^{8}B flux predicted by the standard solar model [53]. Figure from [52].

$$P(\bar{\nu}_e \to \bar{\nu}_e) = 1 - \cos^4\theta_{13}\sin^2 2\theta_{12}\sin^2\left(\frac{\Delta m^2_{21}L}{4E}\right) - \sin^2 2\theta_{13}\sin^2\left(\frac{\Delta m^2_{32}L}{4E}\right). \tag{2.34}$$

By examining equation 2.34, it can be observed that reactor neutrino oscillations happen on two different distance scales. Measurements of reactor neutrino oscillations over distances of $\mathcal{O}(100)$ km are sensitive to the solar parameters θ_{12} and Δm^2_{21}, while over distances of $\mathcal{O}(1)$ km they are sensitive to the mixing angle θ_{13}. The $\bar{\nu}_e$ survival probability is shown in figure 2.15.

KamLAND is a reactor neutrino experiment located at the Kamioka Observatory in Japan [55]. It was designed to detect $\bar{\nu}_e$ from several nuclear reactors across Japan, with a flux-weighted average distance of 180 km and an energy spectrum peaking at ~ 4 MeV. Together, this meant that KamLAND was mostly sensitive

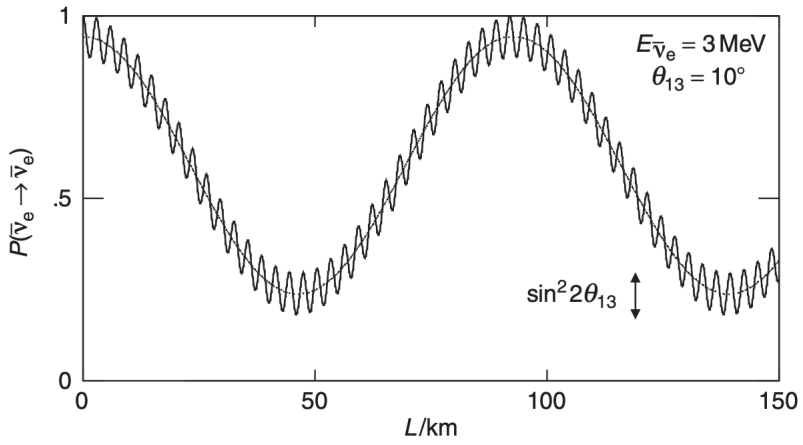

Figure 2.15: The $\bar{\nu}_e$ survival probability as a function of the baseline L, assuming 3 MeV antineutrinos and $\theta_{13} = 10°$. Figure from [54].

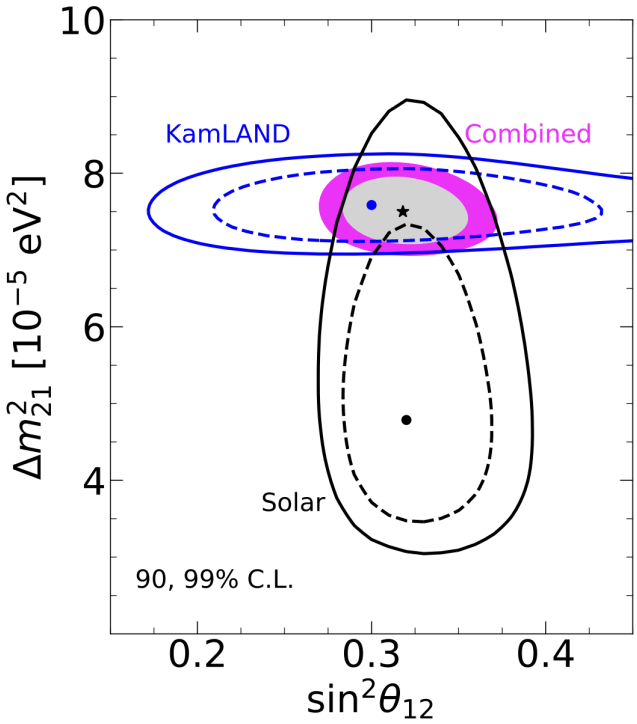

Figure 2.16: The 90% and 99% confidence regions for the solar parameters obtained from solar neutrino experiments (black lines), KamLAND (blue lines), and a combined analysis (coloured regions). Figure from [56].

to the solar oscillation parameters θ_{12} and Δm^2_{21}. Combining KamLAND's measurements with constraints from solar neutrino experiments yields the most precise determination of the solar oscillation parameters, illustrated in figure 2.16.

The mixing angle θ_{13} remained largely unknown throughout the 2000s, and a

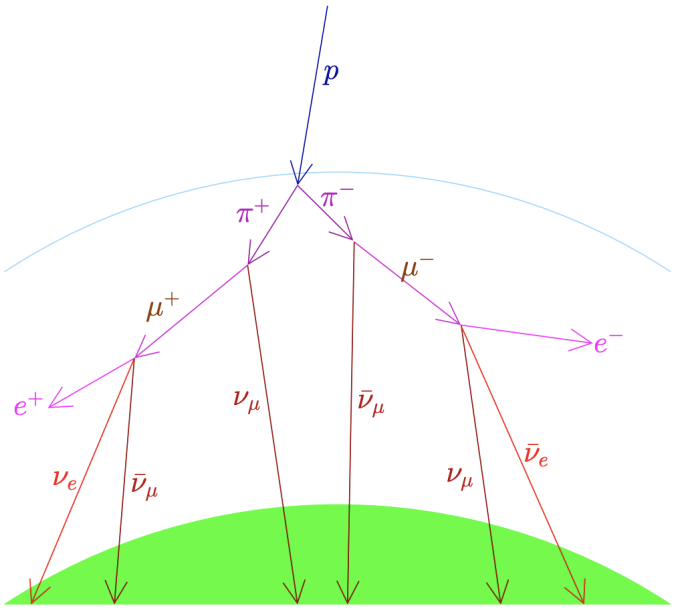

Figure 2.17: A primary cosmic ray interacts in the atmosphere to produce pions, which subsequently decay to produce muons and neutrinos. Figure from [31].

range of new reactor experiments with shorter baselines had been proposed to precisely determine its value. The value of θ_{13} had significant consequences for the future direction of neutrino physics, as CP violation in neutrino oscillations would only be detectable if θ_{13} was measured to be non-zero. The Daya Bay [57], Double Chooz [58], and RENO [59] experiments were constructed and relied upon the cancellation of systematic uncertainties at their respective near and far detectors to achieve sub-percent-level systematics [60]. Most recently, Daya Bay measured $\sin^2 2\theta_{13} = 0.0851 \pm 0.0024$, which is currently the most precise measurement of θ_{13} [57]. Interestingly, despite being the last mixing angle to be determined, θ_{13} is now the most precisely known. Due to their superior sensitivity, constraints on θ_{13} from reactor experiments are often used by long-baseline experiments to improve their measurements of δ_{CP}.

2.4.3 Atmospheric Experiments

Atmospheric neutrinos are created via interactions of cosmic rays with nuclei in the Earth's atmosphere. These interactions, illustrated in figure 2.17, produce mesons (mostly pions) which subsequently decay to produce neutrinos:

$$\begin{aligned} \pi^+ &\to \mu^+ \nu_\mu \,, \quad \pi^- \to \mu^- \bar{\nu}_\mu \,, \\ \mu^+ &\to e^+ \nu_e \bar{\nu}_\mu \,, \quad \mu^- \to e^- \bar{\nu}_e \nu_\mu \,. \end{aligned} \tag{2.35}$$

From observing the multiplicities of neutrinos in the interactions in equation 2.35, one would expect the total muon neutrino flux to be double the total electron neutrino flux. However, measurements from the IMB [61] and Kamiokande [62] experiments implied a ratio significantly smaller than predicted. This disagreement became known as the atmospheric neutrino anomaly.

The anomaly would later be resolved in 1998 by the Super-Kamiokande collaboration [7]. Their results confirmed the deficit seen in prior experiments and further demonstrated that the presence of neutrino oscillations provided an excellent description of the data. Measurements of the muon-to-electron flavour ratio from multiple atmospheric neutrino experiments are shown in figure 2.18. Super-Kamiokande's result was jointly awarded the 2015 Nobel Prize in Physics alongside the SNO collaboration for confirming the existence of neutrino oscillations and demonstrating the non-zero mass of the neutrino. Oscillation parameter constraints from atmospheric neutrino experiments are shown alongside accelerator neutrino experiments in section 2.4.4.

2.4.4 Accelerator Experiments

Accelerator neutrino experiments were designed and constructed to make precision measurements of the neutrino mixing parameters, most notably the CP-violating phase δ_{CP}. Accelerator experiments use artificial neutrino sources produced by impinging accelerated protons onto a target, which produces charged mesons that subsequently decay into mostly muon-type neutrinos. A predominantly ν_μ or $\bar{\nu}_\mu$ beam can be attained by focusing positive or negatively charged mesons, respectively.

Accelerator neutrino experiments can be categorised according to their baseline. Short-baseline experiments ($L \sim 1$ km), such as the SBND programme at Fermilab [64], often make dedicated measurements of neutrino cross sections

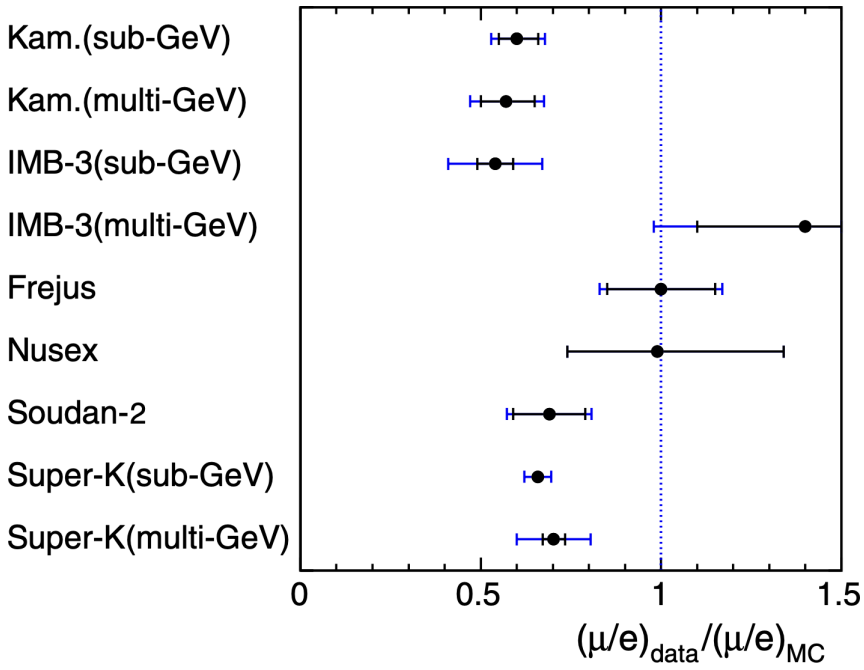

Figure 2.18: Measurements of the double muon-to-electron flavour ratio comparing data to MC prediction from several atmospheric neutrino experiments. The inner and outer error bars signify statistical and statistical + systematic errors respectively. Figure from [63].

and search for oscillations beyond the standard 3ν framework. Long-baseline experiments ($L \sim 10^{2-3}$ km), such as the T2K [37] and NOvA [65] experiments, are primarily dedicated to making precision measurements of the neutrino mixing parameters. Long-baseline experiments typically consist of a near and far detector. The near detector measures the unoscillated neutrino beam, helping to constrain neutrino interaction and flux uncertainties. The far detector measures the oscillated neutrino flux and, combined with near-detector predictions, is used to obtain oscillation parameter constraints.

Long-baseline experiments are sensitive to the oscillation parameters Δm^2_{32}, $\sin^2\theta_{23}$, $\sin^2\theta_{13}$ and δ_{CP}. Constraints from past and present accelerator and atmospheric neutrino experiments are shown in figures 2.19 and 2.20. Notably, all experiments find similar constraints for the disappearance parameters $\sin^2\theta_{23}$ and Δm^2_{32}, but there is a small tension between T2K and NOvA's δ_{CP} constraint, assuming normal ordering.

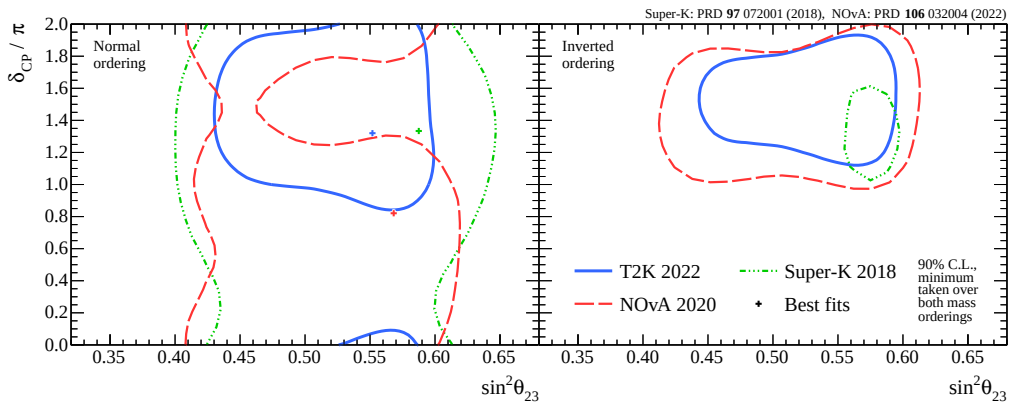

Figure 2.19: Comparison of δ_{CP} and $\sin^2\theta_{23}$ constraints assuming normal (left) and inverted (right) ordering from the Super-K [66], T2K [67] and NOvA [65] collaborations. Figure from [67].

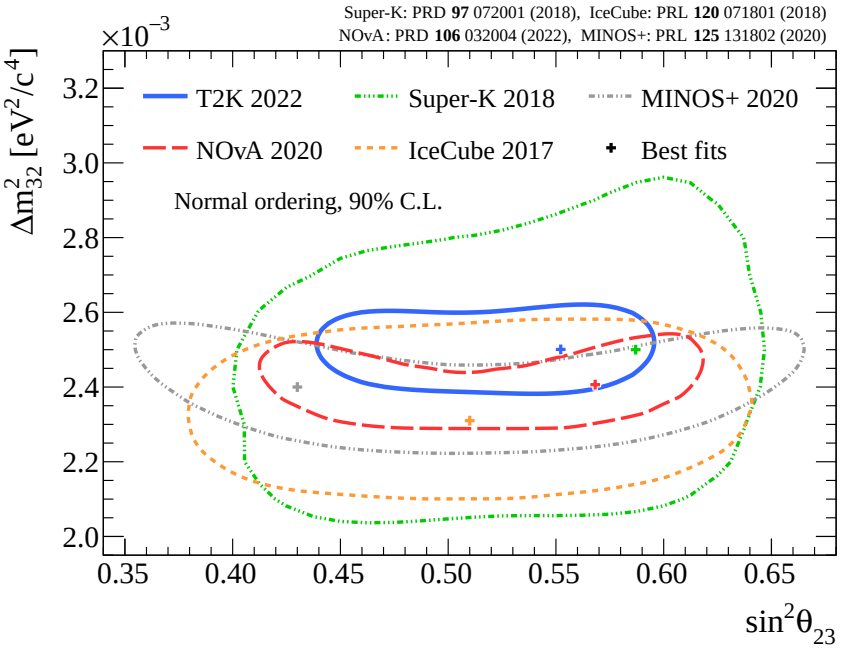

Figure 2.20: Comparison of Δm^2_{32} and $\sin^2\theta_{23}$ constraints in normal ordering from the Super-K [66], IceCube [68], MINOS [69], T2K [67] and NOvA [65] collaborations. Figure from [67].

	Normal Ordering		Inverted Ordering	
	Best fit $\pm 1\sigma$	3σ range	Best fit $\pm 1\sigma$	3σ range
$\sin^2\theta_{12}$	$0.303^{+0.012}_{-0.012}$	0.270 – 0.341	$0.303^{+0.012}_{-0.012}$	0.270 – 0.341
$\sin^2\theta_{13}$ [$\times 10^{-3}$]	$22.25^{+0.56}_{-0.59}$	20.52 – 23.98	$22.23^{+0.58}_{-0.58}$	20.48 – 24.16
$\sin^2\theta_{23}$	$0.451^{+0.019}_{-0.016}$	0.408 – 0.603	$0.569^{+0.016}_{-0.021}$	0.412 – 0.613
δ_{CP} [°]	232^{+36}_{-26}	144 – 350	276^{+22}_{-29}	194 – 344
Δm^2_{21} [$\times 10^{-5}$ eV^2]	$7.41^{+0.21}_{-0.20}$	6.82 – 8.03	$7.41^{+0.21}_{-0.20}$	6.82 – 8.03
Δm^2_{32} [$\times 10^{-3}$ eV^2]	$2.507^{+0.026}_{-0.027}$	2.427 – 2.590	$-2.486^{+0.025}_{-0.028}$	-2.570 – -2.406

Table 2.1: PMNS parameter constraints from a fit to global data as of November 2022. Table adapted from [71, 72].

Current measurements of the oscillation parameters, particularly δ_{CP}, are largely dominated by statistical uncertainties. Next-generation experiments, such as Hyper-K [4] and DUNE [70], will be able to make much more precise measurements of the PMNS parameters, benefiting from much greater statistics.

2.5 Current Status and Open Questions

The neutrino mixing parameters have been measured to varying levels of precision by many different types of neutrino experiments. A global fit to available data, including the best-fit points and the $1/3\sigma$ errors, is shown in table 2.1. Parameters measured by solar and reactor experiments, namely θ_{12}, θ_{13} and Δm^2_{21}, as well as the atmospheric mass-squared splitting Δm^2_{32}, are relatively well-constrained. However, despite the rapid development within the field of neutrino physics, many significant questions remain unanswered. Several of these are discussed below.

1. Are neutrinos Dirac or Majorana particles? The answer to this question would have significant implications for the origin and mechanism of neutrino masses. Neutrino oscillation experiments are not sensitive to the

Majorana phases of the PMNS matrix, so this question is being researched by neutrinoless double beta decay experiments.

2. In most oscillation analyses, it is assumed that there are only three neutrino flavour and mass eigenstates, related through the unitary PMNS matrix. Measurements that suggested the PMNS matrix to be non-unitary would provide indirect evidence of additional neutrino flavour and mass eigenstates, which would have implications for neutrino mass mechanisms and dark matter searches.

3. Both the absolute neutrino mass scale and the ordering of the neutrino mass eigenstates are undetermined. The KATRIN experiment has been able to place an upper limit of 0.8 eV on the neutrino mass by precisely measuring the end-point of the tritium β-decay spectrum [24]. The neutrino mass ordering is expected to be determined by next-generation reactor and long-baseline experiments.

4. Constraints from current oscillation experiments [37, 65] indicate two statistically degenerate solutions for $\sin^2\theta_{23}$, which deviate from the maximal mixing value of 0.5. These two solutions are referred to as upper-octant ($\sin^2\theta_{23} > 0.5$) and lower-octant ($\sin^2\theta_{23} < 0.5$) respectively. Next-generation long-baseline experiments are anticipated to resolve the octant. This is an important question to answer as it carries significant implications for neutrino mass and mixing models [73].

5. Most relevant for this thesis is the determination of the CP-violating phase δ_{CP}. A statistically significant measurement of CP violation in the leptonic sector could have significant consequences that help to understand and explain the matter-anti-matter asymmetry observed in the Universe. The primary physics goal of next-generation long-baseline experiments is the precise determination of δ_{CP}.

3
The T2K Experiment

The Tokai-to-Kamioka (T2K) experiment is a long-baseline neutrino oscillation experiment located in Japan [2]. T2K's neutrino beam is created at the Japan Proton Accelerator Research Complex (J-PARC) by impinging 30 GeV protons on a graphite target. The resulting charged mesons are focused by a series of magnetic horns to produce a predominantly muon neutrino or antineutrino beam. The neutrino beam is measured 280 m downstream of the target by a suite of near detectors, and again at 295 km by the far detector, Super-Kamiokande. T2K measures neutrino oscillations via two channels: muon (anti)neutrino disappearance, and electron (anti)neutrino appearance. A schematic of the T2K experiment is shown in figure 3.1.

T2K's physics goals include the precise determination of the oscillation parameters θ_{23}, θ_{13} and Δm^2_{32}, and to constrain the CP-violating phase δ_{CP}. Using

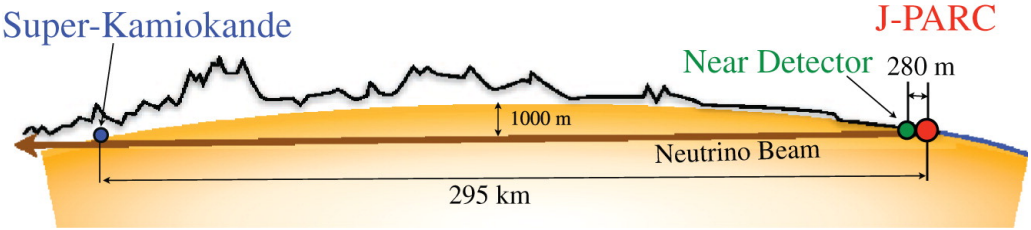

Figure 3.1: Schematic of the T2K experiment. Figure from [2].

its suite of near detectors, T2K also performs world-leading neutrino cross-section measurements.

This chapter discusses aspects of T2K's experimental setup that are most relevant for oscillation and interaction physics. Section 3.1 describes the production of the neutrino beam. Sections 3.2.1 and 3.2.2 describe the near detectors INGRID and ND280 respectively, while section 3.2.3 briefly discusses the upcoming ND280 upgrade. Section 3.3 describes the far detector, Super-Kamiokande. Finally, section 3.4 provides a brief overview of the simulation packages employed at the near and far detectors.

3.1 The T2K Beam

The J-PARC facility consists of three accelerators: a linear accelerator (LINAC), a rapid-cycling synchrotron (RSC) and a main ring (MR) synchrotron [2]. To produce the proton beam, H^- ions are accelerated to 400 MeV and converted into H^+ ions by charge-stripping foils. These protons are further accelerated to 3 GeV in the RSC, before being injected into the MR where they are accelerated to kinetic energies of 30 GeV.

Proton spills accelerated in the MR are then extracted into the T2K beamline, with each beam spill consisting of eight proton bunches. The neutrino beamline consists of a primary and secondary beamline, as illustrated in figure 3.2. First, the primary beamline is used to direct the extracted proton beam toward Kamioka (Super-K), and a series of magnets are used to tune the proton beam to minimise beam loss and ensure stable neutrino beam production.

Upon entry into the secondary beamline, illustrated in figure 3.3, the proton beam impinges on a graphite target, producing charged mesons (mostly pions and kaons). These charged mesons are focused by three magnetic horns [74] and enter the decay volume, where they decay to produce neutrinos. The target is a 91.4 cm (1.9 interaction lengths) long, 2.6 cm diameter graphite rod. The proton beam produces a large amount of heat when interacting with the target, so helium gas is used to provide cooling.

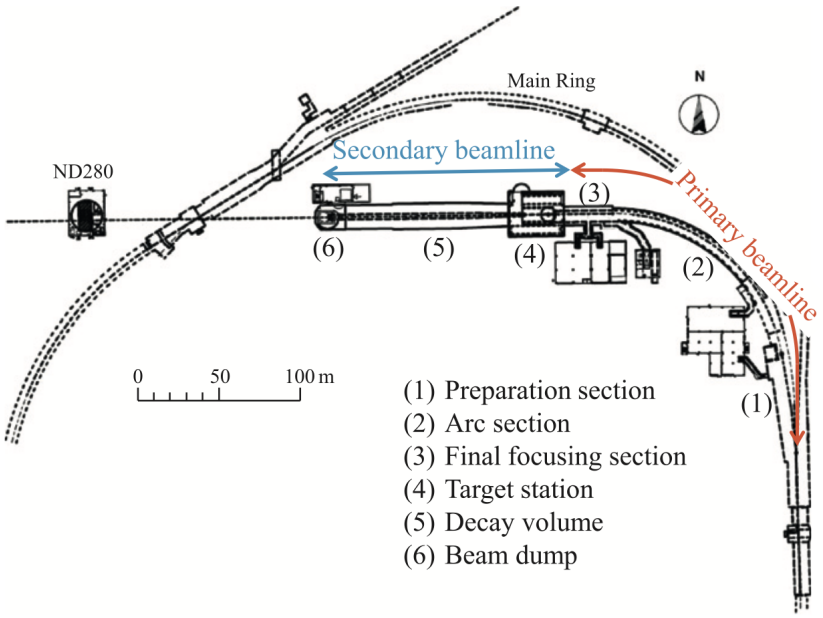

Figure 3.2: Schematic of the T2K primary and secondary beamlines and their respective components. Figure from [2].

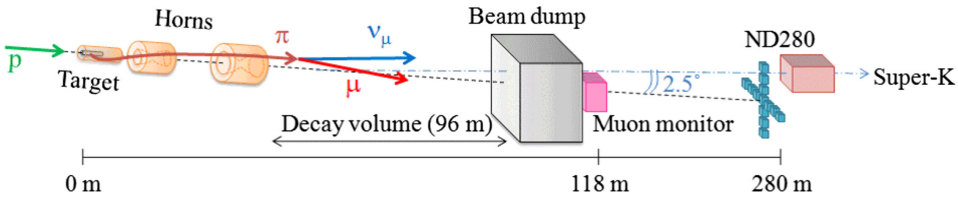

Figure 3.3: Schematic of the secondary beamline. Figure from [75].

The first magnetic horn, in which the target sits, collects the charged mesons produced at the target, and the second and third horns focus the mesons into a beam. The focused mesons then enter a decay volume, where they decay to produce muon neutrinos and antineutrinos:

$$\pi^+ \to \mu^+ \nu_\mu \,, \qquad K^+ \to \mu^+ \nu_\mu \,, \qquad (\nu - \text{mode})$$
$$\pi^- \to \mu^- \bar{\nu}_\mu \,, \qquad K^- \to \mu^- \bar{\nu}_\mu \,. \qquad (\bar{\nu} - \text{mode})$$

Other flavours of neutrinos are also produced, albeit far less often, via the following processes:

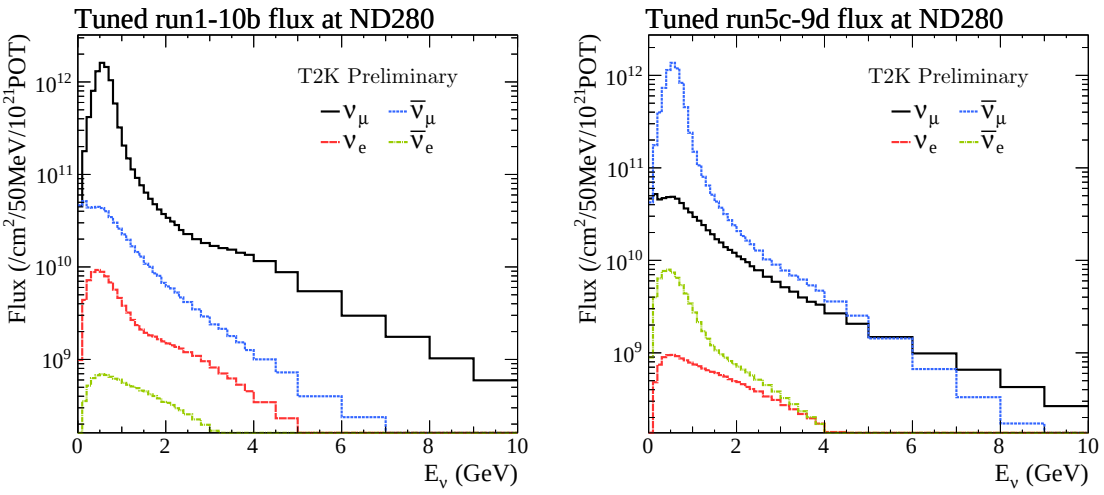

(a) ν-mode **(b)** $\bar{\nu}$-mode

Figure 3.4: Neutrino flux prediction at the far detector split by neutrino flavour. Figure from [76].

$$K^+ \to \pi^0 e^+ \nu_e \,, \qquad \mu^+ \to e^+ \nu_e \bar{\nu}_\mu \,.$$

The magnetic horns can be configured in such a way as to focus positively (negatively) charged mesons, yielding a neutrino (antineutrino) enhanced beam. These running modes are called 'forward horn current' (FHC, +250 kA) and 'reverse horn current' (RHC, -250 kA) respectively. In this thesis, the terms 'neutrino mode' and FHC, as well as 'antineutrino mode' and RHC, will be used interchangeably.

Whether running in neutrino or antineutrino mode there will be some level of wrong-sign contamination (ν in $\bar{\nu}$ or $\bar{\nu}$ in ν); neither beam mode will result in a purely neutrino or antineutrino beam. The neutrino flavour components of each beam mode are shown in figure 3.4. It can be observed that the wrong-sign background is much larger in RHC beam mode than in FHC beam mode.

At the end of the decay volume sits the beam dump, which consists of 75 tons of graphite. This stops and absorbs all hadrons and muons below $\sim$5 GeV. Muons above this threshold are detected by the muon monitor which consists of two different detector arrays: ionisation chambers and silicon photodiodes.

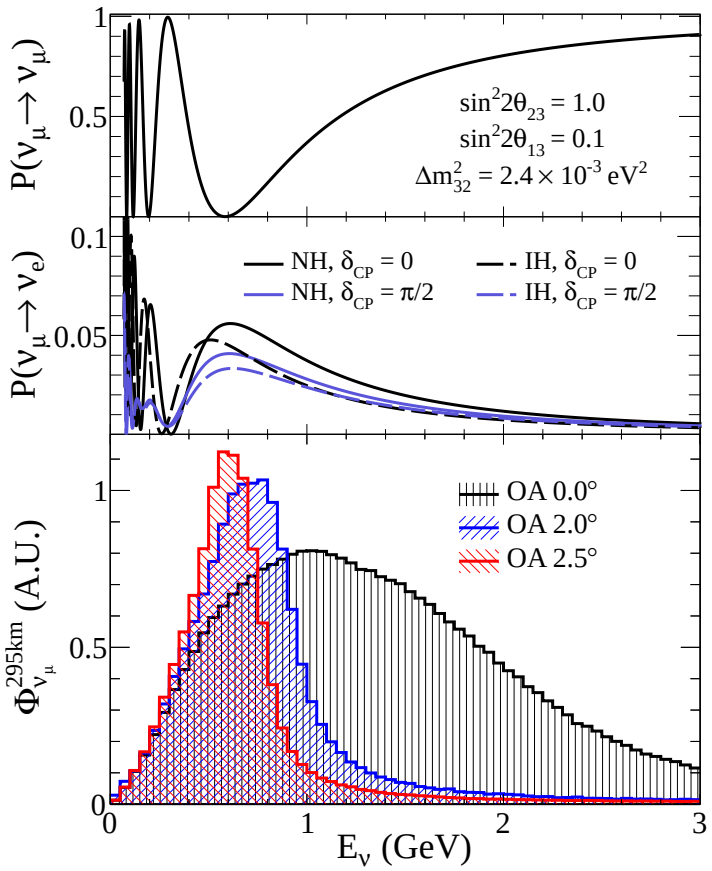

Figure 3.5: ν_μ survival probability (top), ν_e appearance probability (middle), and total ν_μ flux prediction at the far detector for different off-axis angles (bottom). It can be observed that the neutrino energy spectrum narrows as the off-axis angle increases. Figure from [76].

The muon monitor is used to monitor and constrain the neutrino beam intensity and direction on a bunch-by-bunch basis.

One of T2K's near detectors and the far detector are positioned at a 2.5° off-axis angle relative to the neutrino beam, taking advantage of the kinematics of two-body decays. As the vast majority of neutrinos in the beam originate from the two-body decays of charged pions ($\pi \rightarrow \mu\nu$), the neutrino energy can be calculated to be

$$E_\nu = \frac{m_\pi^2 - m_\mu^2}{2(E_\pi - p_\pi \cos\theta_{\nu\pi})}, \tag{3.1}$$

where E_ν is the neutrino energy, E_π, p_π and m_π are the pion's energy, momentum and mass respectively, m_μ is the muon mass, and $\theta_{\nu\pi}$ is the angle of the emitted neutrino with respect to the pion direction. As $\theta_{\nu\pi}$ increases, the neutrino energy

spectrum narrows, as shown in figure 3.5. An off-axis angle of 2.5° results in a peak neutrino energy of 0.6 GeV, which is directly aligned with the muon-neutrino oscillation probability maximum. This yields several advantages, including reduced high-energy backgrounds and an increased likelihood of CCQE interactions occurring, which are considerably better understood theoretically.

3.2 The T2K Near Detectors

The unoscillated neutrino beam is measured by a suite of near detectors 280 metres downstream of the target. The near detectors are primarily used to monitor the neutrino beam, make precision neutrino cross-section measurements and predict the number of neutrinos that will be observed at the far detector. T2K uses two near detectors: INGRID and ND280.

3.2.1 INGRID

The Interactive Neutrino GRID (INGRID) is a neutrino detector that lies on axis, and is used to monitor the neutrino beam direction and profile [77]. The detector samples the beam spill-by-spill and consists of fourteen identical modules arranged as a cross, the centre of which corresponds to the centre of the neutrino beam. INGRID's configuration and an exploded view of an individual INGRID module are shown in figure 3.6.

Each INGRID module consists of a sandwich structure of nine iron plates of 6.5 cm thickness and eleven tracking scintillator planes of 1 cm thickness. These are surrounded by veto scintillator planes that reject interactions that occur outside of the module. Each module's fiducial mass is 7.1 tonnes and exposes a 1.24×1.24 m^2 area facing the beam [37]. Additionally, a proton module is used to efficiently detect muons together with protons generated from neutrino interactions within the module, enabling the measurement of the charged-current quasi-elastic cross section on carbon. The proton module is placed at the centre of the INGRID configuration.

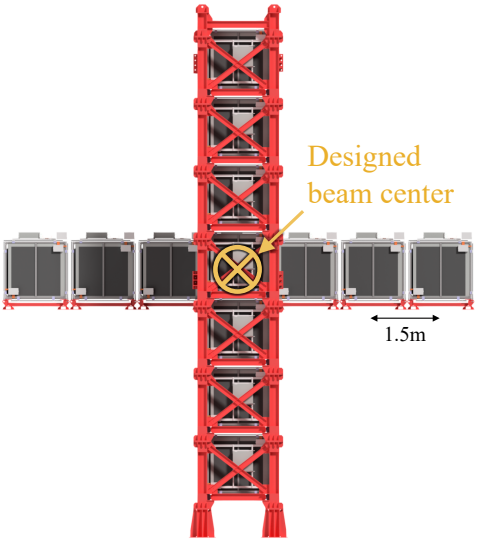

(a) INGRID. Figure from [76].

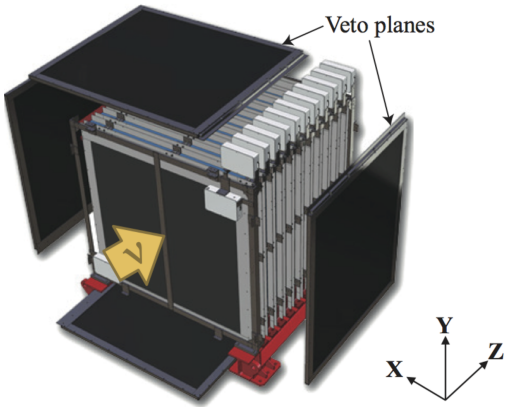

(b) An exploded view of an INGRID detector module. The veto planes (black) are shown surrounding the iron and and tracking planes. Figure from [2].

Figure 3.6: The INGRID near detector.

INGRID's measurement of the neutrino beam direction is of significant importance to the determination of the off-axis angle, and consequently, the energy of the neutrino beam at the far detector. A 1 mrad deviation in the beam direction corresponds to a 2% shift in the peak neutrino energy at the far detector [78]. INGRID can measure the beam direction with an accuracy exceeding 0.4 mrad, well within the design goal of 1 mrad.

3.2.2 ND280

The unoscillated neutrino flux (primarily $\nu_\mu/\bar{\nu}_\mu$) is measured by ND280, the off-axis near detector situated 280 m from the target. ND280 measures the neutrino energy spectrum, flavour components and interaction rates of the unoscillated beam, all of which are used to reduce flux and cross-section uncertainties, as well as predict the oscillated spectra at the far detector [2]. ND280 is a magnetised, composite detector composed of several sub-detectors, as shown in figure 3.7. The technologies and design purpose of each sub-detector are discussed in the subsequent sections.

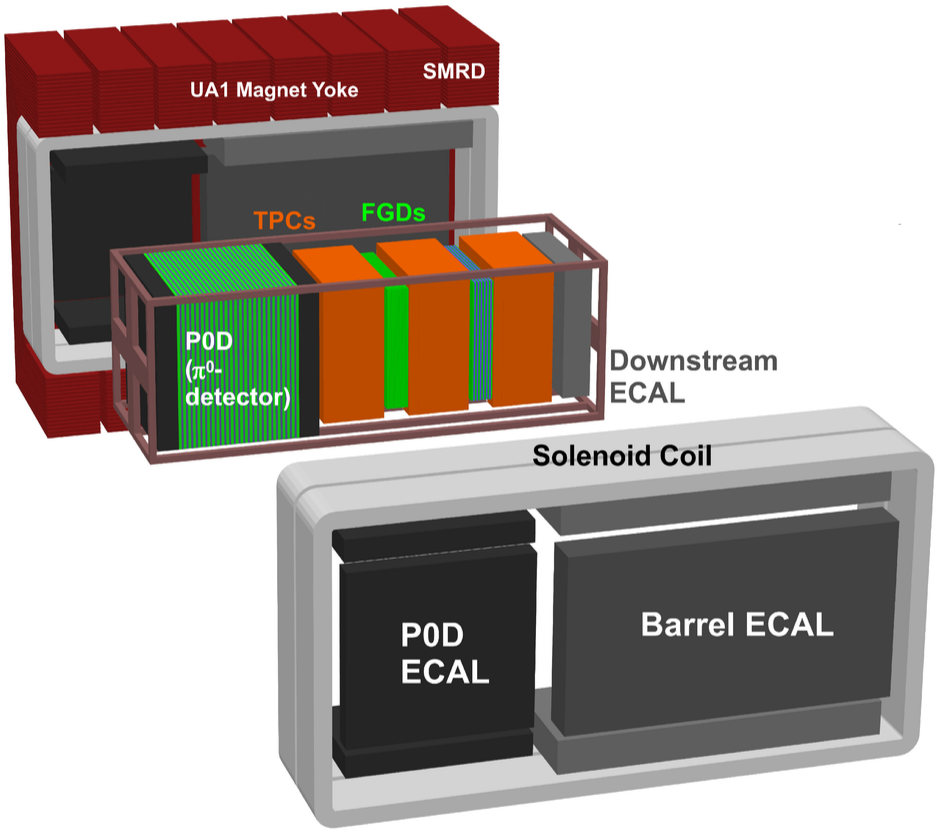

Figure 3.7: An exploded view of ND280 and its sub-detectors. Figure from [2].

3.2.2.1 The π^0 Detector

The most upstream sub-detector in ND280 is the π^0 detector (PØD), designed to measure neutral current interactions of the form $\nu_\mu + N \rightarrow \nu_\mu + N + \pi^0$ on a water target [79]. Neutral current interactions with a π^0 in the final state (NC1π^0) are a dominant background to ν_e appearance, therefore to make accurate measurements of the CP-violating phase δ_{CP}, it is important to measure this background at the near detector.

The PØD's water target is divided into an upstream and central section which comprise alternating scintillator planes, water bags and brass sheets. At the front and rear sections of the PØD sit the upstream and central electromagnetic calorimeters (ECals) respectively, both consisting of alternating scintillator planes and lead sheets. The ECals allow for better containment of electromagnetic

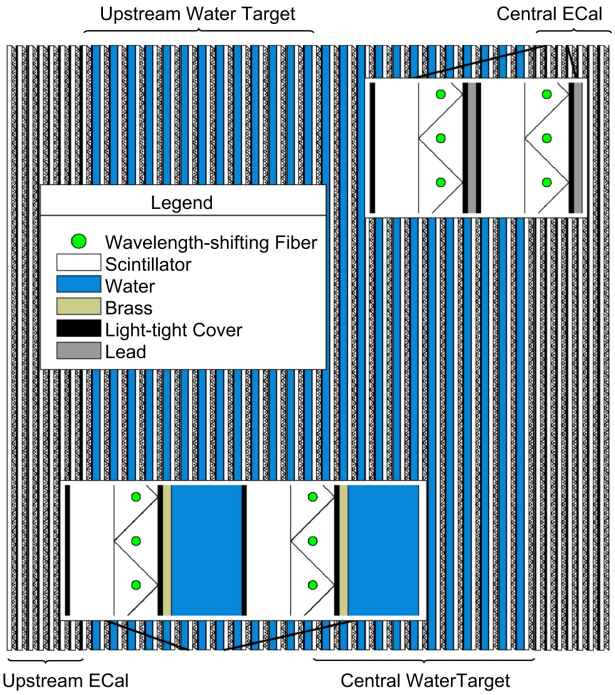

Figure 3.8: Schematic of the PØD. In the orientation, the neutrino beam traverses left to right. Figure from [79].

showers and serve as a veto region to reject particles originating from interactions outside the PØD. A schematic of the PØD is shown in figure 3.8.

3.2.2.2 Fine-Grained Detectors

The tracking region of ND280 consists of two fine-grained detectors (FGDs) positioned between three time projection chambers (TPCs). The FGDs [80] provide target mass for neutrinos interacting within ND280, as well as the capability to track charged particles close to the interaction vertex. The dimensions of each FGD are 2300 mm $\times$ 2400 mm $\times$ 365 mm (width $\times$ height $\times$ depth), and each contains a target mass of 1.1 tonnes.

The most upstream FGD, referred to as FGD1, consists of 30 layers of 192 scintillator bars orientated sequentially in the horizontal and vertical directions. A reflective coating covers each scintillator bar, and a wavelength shifting (WLS) fibre passes through its centre and is read out from one end by a multi-pixel photon counter (MPPC).

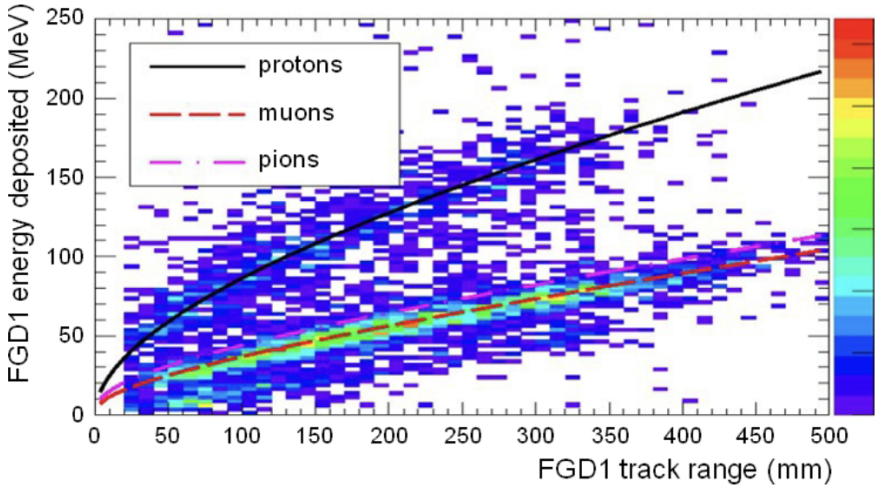

Figure 3.9: The total deposited energy plotted against track range for particles stopping in FGD1. The 2D plot shows stopping particles from neutrino beam data, and the curves show the MC predictions for protons, muons and pions. Figure from [80].

Downstream of FGD1 sits FGD2, which contains seven plastic scintillator layers (identical to those found in FGD1) separated by six 2.5 cm thick layers of water. A water target at the near detector aids in constraining the predicted event rate at the far detector, which also utilises a water target.

The FGDs are also able to reconstruct particle tracks and perform particle identification (PID). Tracks that are fully contained within the FGD are primarily lower momentum particles, and the total deposited energy and track length can be used to distinguish between protons, pions and muons. This method is demonstrated in figure 3.9, which illustrates the total deposited energy as a function of track length for different charged particles. Furthermore, TPC tracks must be matched with FGD tracks to determine the primary interaction vertex.

3.2.2.3 Time Projection Chambers

ND280's three TPCs [81], which alternate with the two FGDs, have identical designs and fulfil three essential roles at the near detector [2]. Firstly, the TPC's excellent 3D imaging capabilities can be utilised to construct high-purity samples targeting different types of neutrino interactions. Secondly, as ND280 is embedded within a magnetic field, it is possible to measure the momenta of

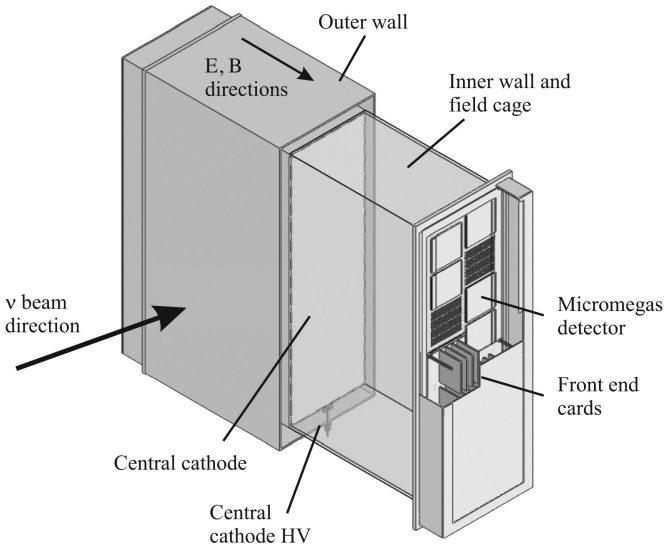

Figure 3.10: A simplified schematic of ND280 TPC design. Figure from [81].

charged particles, allowing for the calculation of the event rate of the unoscillated neutrino flux at the near detector as a function of reconstructed neutrino energy. Lastly, particle identification can be performed by utilising measurements of charged particle's momenta and ionisation loss.

Each TPC consists of an inner box that contains an argon-based drift gas and an outer box that contains CO_2, which acts as an insulator. The outer box is grounded, while the panels of the inner box have a copper strip pattern, which combined with a central cathode panel provides a uniform electric field aligned with the magnetic field. A simplified design of an individual TPC can be found in figure 3.10.

When a charged particle travels through a TPC, they ionise electrons in the gas that drift away from the central cathode towards the readout planes of the inner box, where the electrons are multiplied and sampled with bulk micromegas detectors [82]. 3D particle paths can be reconstructed using the arrival time and positions of the signals.

Particle identification can be performed in the TPCs by measuring the energy loss per unit distance, dE/dx. The energy loss as a function of momentum is shown for positively and negatively charged particles in figure 3.11. Measurements of dE/dx have a resolution of $7.8 \pm 0.2\%$, meaning the probability

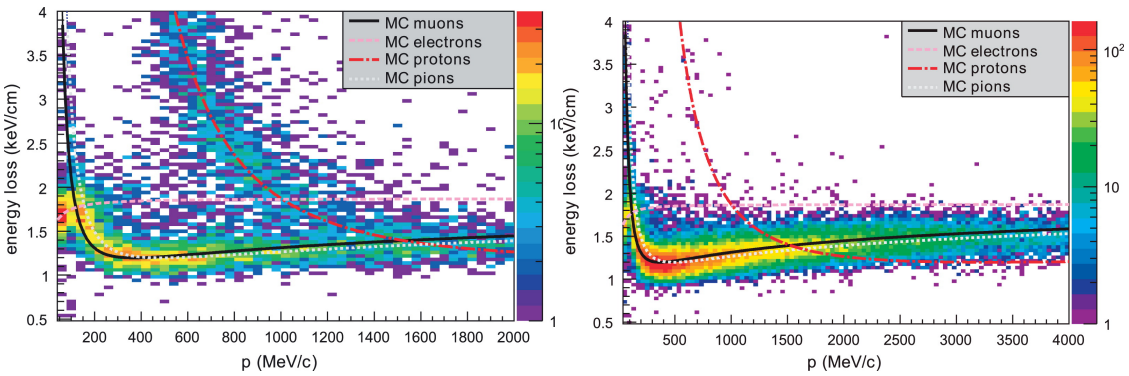

(a) Positive particles **(b)** Negative particles

Figure 3.11: Energy loss in one of T2K's TPCs as a function of particle momentum for (a) positive and (b) negative particles. Data, plotted as a 2D histogram, is shown alongside MC predictions for muons, electrons, protons and pions. Figures from [81].

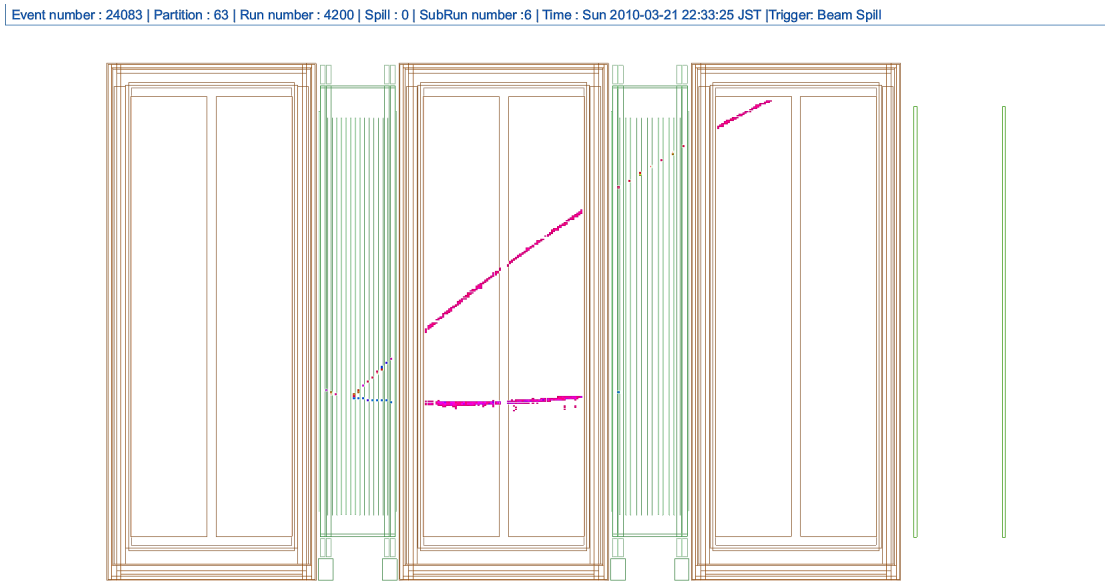

Figure 3.12: An ND280 event display of a CC interaction in FGD1. Figure from [76].

of misidentifying a muon as an electron is 0.2% for muons with a momentum below 1 GeV. This resolution exceeds the prior design requirement of 10%. A typical event display that utlises information from both the FGDs and TPCs can be seen in figure 3.12.

3.2.2.4 Electromagnetic Calorimeter

The inner detectors (PØD, TPCs, FGDs) of ND280 are surrounded by the electromagnetic calorimeter (ECal) [83]. It was designed to complement the inner

detectors in full event reconstruction, utilising its near-hermetic coverage of the inner detector volume. A photon showers' energy and directionality can be determined, which aids in electron-muon-pion separation and the reconstruction of π^0s produced outside of the PØD. The ECal consists of three sections: the PØD ECal, the barrel ECal, and the downstream ECal. The PØD ECal is used to tag particles exiting the PØD, while the barrel and downstream (tracker) ECals complement the inner tracking detectors in fully reconstructing tracks and showers that exit the region.

3.2.2.5 The Magnet and Side Muon Range Detectors

ND280's sub-detectors sit within the refurbished CERN UA1/NOMAD dipole magnet. The magnet, which operates at a current of 2.7 kA, generates a uniform magnetic field of 0.2 T. The presence of a magnetic field allows for precision measurements of charged particle's momenta, as well as being able to determine the sign of charged particles. The former is important for reconstructing the neutrino energy, while the latter allows for the discrimination of neutrino and antineutrino events.

The outermost component of ND280 is the side muon range detector (SMRD), which consists of 440 scintillator modules and is situated in the air gaps of the magnet's return yoke [84]. The SMRD can measure the momentum of high-angle muons generated from neutrino interactions within the detector and also operates as a cosmic trigger signal, which is important for the calibration of the ND280 detector.

3.2.3 T2K Near Detector Upgrade

As part of the second phase of the T2K experiment, the ND280 detector is undergoing extensive upgrades. As part of the upgrade, the PØD is being replaced by a new scintillator detector, the Super-FGD (SFGD), sandwiched between two High-Angle TPCs (HA-TPCs). Both the SFGD and HA-TPCs will be surrounded by six time of flight (TOF) planes to determine track direction

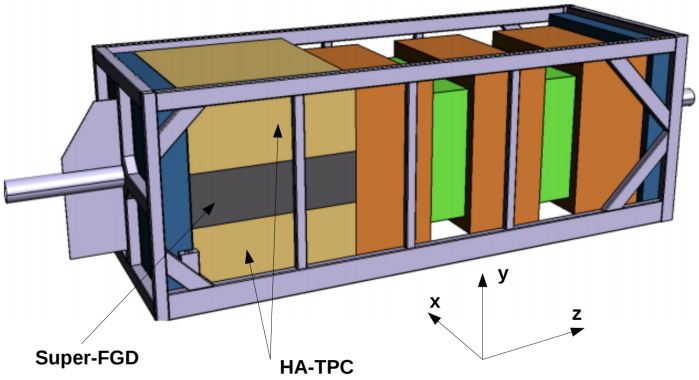

Figure 3.13: Schematic of the upgraded ND280 detector. The new Super-FGD (grey) and High-Angle TPCs (brown) sit in the upstream portion of the detector. The downstream portion contains the existing FGDs (green) and TPCs (orange). Figure from [85].

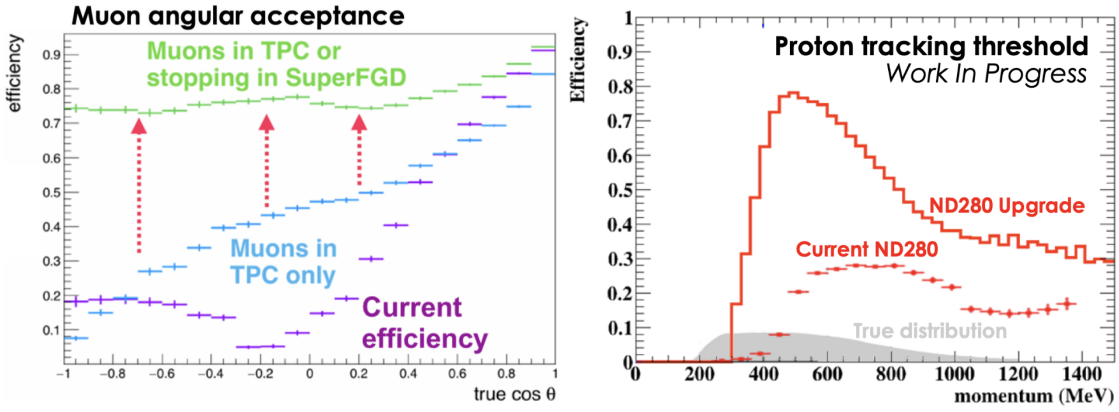

Figure 3.14: Muon angular acceptance (left) and proton tracking efficiency (right) for the current and upgraded ND280 detector.

and improve PID [85]. A schematic of the upgraded ND280 detector is shown in figure 3.13.

Several analysis improvements are expected as a result of the near-detector upgrade. First, with the SFGD's high granularity, much lower proton tracking thresholds and higher tracking efficiency are anticipated. The HA-TPCs will also greatly improve the angle coverage for muons produced in CC events, with nearly 4π coverage expected for muons detected in the TPC or stopping in the SFGD. Furthermore, the overall target mass will increase by a factor of two with the addition of the SFGD. The upgraded detector's performance is compared to the current ND280 detector in figure 3.14.

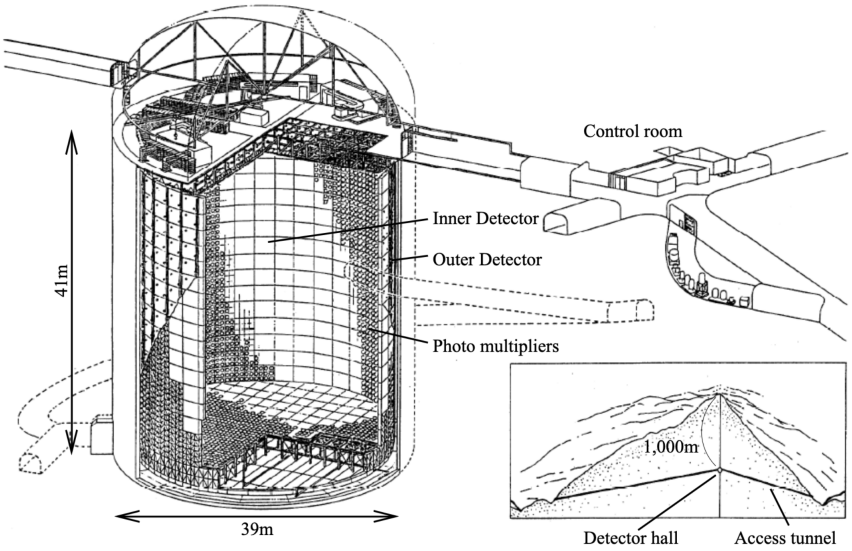

Figure 3.15: The Super-Kamiokande detector. Figure from [87].

3.3 The T2K Far Detector - Super Kamiokande

T2K uses Super-Kamiokande (SK) [86] as its far detector, located 295 km away from the near detectors. SK is a 50 kton water Cherenkov detector and measures the oscillated neutrino flux, specifically looking for the appearance of electron (anti)neutrinos and the disappearance of muon (anti)neutrinos. The SK detector comprises a cylindrical tank (39 m in diameter, 42 m tall), divided into an inner (ID) and outer (OD) detector. The ID is equipped with 11,129 inward-facing photo-multiplier tubes (PMTs), each with a diameter of 50 cm, yielding around 40% photo coverage. The OD, which primarily acts as a cosmic-ray veto, has 1,885 20 cm-diameter outward-facing PMTs.

SK can detect neutrino interactions by measuring the Cherenkov light produced by charged particles that are above the Cherenkov threshold. Separation between muon/electron (anti)neutrino events is primarily determined by the 'fuzziness' of the Cherenkov ring. Muons produce sharp, well-defined rings in the detector, while electrons largely create fuzzy rings due to their tendency to produce electromagnetic showers. An example of a muon and electron event is shown in figure 3.16. Tau leptons are not observed at SK as the neutrino beam energy is well below the threshold for tau production.

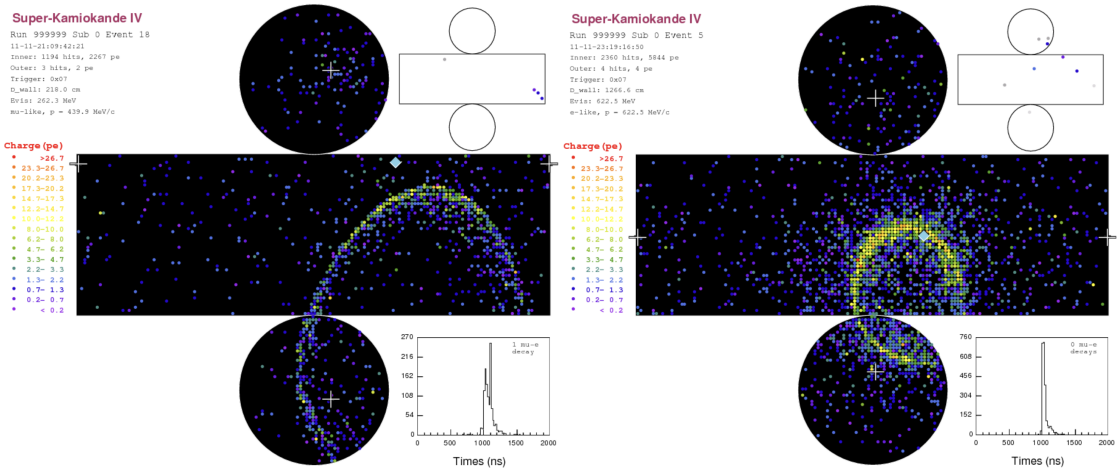

(a) μ-like event **(b)** e-like event

Figure 3.16: SK event displays. Figures from [76].

At T2K energies, CCQE events dominate and SK's excellent e/μ separation allows for signal events to be separated into muon-like and electron-like samples. However, it is important to be cautious of potential backgrounds caused by other types of neutrino interactions. One example is resonant pion production, where a neutrino interacting with a nucleus causes a resonance (normally a Δ baryon) to be formed which subsequently decays into a pion-nucleon pair. However, if the charged pion produced is below Cherenkov threshold, it will not be reconstructed at the far detector, and the event topology will be identical to a CCQE event. These events form an irreducible background to CCQE interactions in single-ring events at the far detector. Additionally, NC interactions at the far detector may produce neutral pions, which subsequently decay into two photons which Compton scatter and produce electron-positron pairs. If one of Cherenkov rings from the photons are not fully reconstructed or they overlap, these events may imitate electron-like CCQE events. These types of events are especially important to measuring the CP-violating phase, δ_{CP}. Extensive work is performed at ND280 to measure the cross sections of the aforementioned interaction modes, and ND280 data is used directly in the oscillation analysis to update the far detector prediction and better understand the potential backgrounds to the signal events.

3.4 Simulation

Neutrino interactions at both the near and far detectors are simulated using the NEUT neutrino interaction generator, described in detail in [38]. CCQE interactions are modelled using a spectral function [40], which provides a realistic shell-model-based description of the nuclear ground state based largely on electron-scattering measurements. 2p2h interactions are described using the Valencia model [88], with the nuclear ground state for such interactions modelled as a local Fermi gas. Single-pion production events in NEUT are described using the Rein-Seghal model [89], but with improvements to the nucleon axial form factors [90, 91]. Multi-pion production and DIS interactions use the Bodek-Yang model [92, 93], and Pion FSI are described by a semi-classical intranuclear cascade model [94], tuned to $\pi - A$ scattering data.

The neutrino flux is simulated using several software packages. Hadronic interactions inside the target and baffle are simulated using FLUKA 2011.2 [95, 96], and these particles are then propogated through to their eventual decay into neutrinos using JNUBEAM (based on GEANT3 [97]). Hadronic re-interactions are simulated using GCALOR [98], which shows good consistency with external hadron production data. ND280 and INGRID are simulated using GEANT4 [99], while the electronics are simulated using elecSim, a custom-written software package. The SK detector simulation uses the SKDETSIM package, based on GEANT3.

4

Bayesian Inference and Markov Chain Monte Carlo

The oscillation parameter constraints presented in this thesis are calculated assuming a Bayesian view of statistics. A Markov chain Monte Carlo (MCMC) method is used to explore the parameter space, construct a probability distribution of the model parameters, and extract parameter estimations and uncertainties. This chapter will provide an overview of Bayesian inference and a theoretical description of the relevant MCMC methods.

Section 4.1 will provide an introduction to Bayesian statistics, while section 4.2 will detail the MCMC method employed in this analysis. Section 4.3 will discuss how it is ensured Markov chains used in this analysis have converged and are well-behaved. Finally, section 4.4 will describe how information about the model parameters is extracted from the posterior distribution.

4.1 Bayesian Inference

The fundamental objective of any experiment is to constrain a set of model parameters, $\vec{\theta}$, using the data it collects, D. In a Bayesian framework, a full probability model of the data and model parameters can be constructed, known

as the joint probability distribution. The joint probability distribution, $\mathcal{P}(D, \vec{\theta})$, can be written as

$$\mathcal{P}(D, \vec{\theta}) = \mathcal{L}(D|\vec{\theta}) \cdot \pi(\vec{\theta}) \,, \tag{4.1}$$

where $\mathcal{L}(D|\vec{\theta})$ represents the likelihood of measuring the data given a set of model parameter values, and $\pi(\vec{\theta})$ is the prior term, which encodes all previous knowledge, including external constraints, about the model parameters.

To extract parameter estimations and uncertainties in a Bayesian analysis, it is first necessary to construct the posterior distribution, labelled as $\mathcal{P}(\vec{\theta}|D)$. Using Bayes' theorem, the posterior distribution can be calculated from the joint probability distribution

$$\mathcal{P}(\vec{\theta}|D) = \frac{\mathcal{L}(D|\vec{\theta}) \cdot \pi(\vec{\theta})}{\int \mathcal{L}(D|\vec{\theta}) \cdot \pi(\vec{\theta}) \, d\vec{\theta}} \,. \tag{4.2}$$

Once the posterior is calculated, estimates and uncertainties for all model parameters can be extracted from it. The denominator of equation 4.2 is often quite complex to evaluate[1], therefore its calculation is omitted in this analysis and the posterior is calculated up to some normalisation constant. This is entirely sufficient as all posterior distributions presented in this thesis have been normalised to area one.

4.2 Markov Chain Monte Carlo

MCMC methods are a widely used and effective way of building up a set of points proportional to the posterior distribution. A Markov chain carries out a semi-random walk through the parameter space, building up a set of discrete points whose density is proportional to the posterior distribution. The chain starts in a region of parameter space where each parameter is assigned a random value drawn from its prior distribution. Following this, the chain will start to explore the parameter space. As the starting position of the chain is drawn randomly

[1] For the oscillation analysis presented in chapter 6, this would be a 791-dimensional integral.

from the prior distribution, the chain will likely start in a low-probability region of parameter space. But, as the chain progresses, it will eventually converge upon the stationary distribution. This means the chain has converged upon the posterior distribution, and at each step after this point, it is sampling from the true posterior distribution. For a Markov chain to have a stationary distribution, it needs to satisfy the three 'regularity' conditions:

1. **Irreducibility** - the chain has a non-zero probability of reaching all other potential states

2. **Recurrence** - once the stationary distribution has been reached, all subsequent samples are drawn from this distribution

3. **Aperiodicity** - the chain must not be periodic

A more detailed discussion of Markov chains can be found in [100, 101].

To ensure the Markov chains satisfy the above conditions, the well-established Metropolis-Hastings algorithm [102, 103] is used to explore the parameter space and sample the posterior. The Metropolis-Hastings algorithm is as follows:

1. **Initlisation** - Following step n, the Markov chain is at a specific point in parameter space, denoted as current step $\vec{\theta_n}$

2. **Step proposal** - A new step $\vec{\theta_{n+1}}$ is generated from a symmetric proposal function centered on current step $\vec{\theta_n}$, labelled as $q(\vec{\theta_{n+1}}|\vec{\theta_n})$

3. **Acceptance probability** - The acceptance probability α is calculated using the formula

$$\alpha(\vec{\theta_n}, \vec{\theta_{n+1}}) = \min\left(1, \frac{\mathcal{P}(\vec{\theta_{n+1}}|D)q(\vec{\theta_n}|\vec{\theta_{n+1}})}{\mathcal{P}(\vec{\theta_n}|D)q(\vec{\theta_{n+1}}|\vec{\theta_n})}\right) . \tag{4.3}$$

As the proposal function is symmetric, $q(\vec{\theta_{n+1}}|\vec{\theta_n}) = q(\vec{\theta_n}|\vec{\theta_{n+1}})$, the acceptance probability can be simplified to the minimum of one or the ratio of the

posterior probabilities at the current and proposed step. Therfore, equation 4.3 can be rewritten as

$$\alpha(\vec{\theta_n}, \vec{\theta_{n+1}}) = \min\left(1, \frac{\mathcal{P}(\vec{\theta_{n+1}}|D)}{\mathcal{P}(\vec{\theta_n}|D)}\right). \tag{4.4}$$

4. **Accept or reject** - A random number r is generated from a uniform distribution between 0 and 1. If $r < \alpha$, the step is accepted and the chain is now at point $\vec{\theta_{n+1}}$ in parameter space. Otherwise, the step is rejected and the chain remains at $\vec{\theta_n}$.

5. **Repeat** - this process repeats until the desired number of steps is reached

The Metropolis-Hastings algorithm ensures that steps within regions of higher probability are always accepted, but due to the semi-random nature of step four, steps with lower probabilities can also be accepted. For results presented in this thesis, several hundred Markov chains are run in parallel. As each Markov chain is statistically independent (assuming they have reached the stationary distribution), they can be combined to reduce the MC statistical error and improve parameter estimates.

4.3 Diagnostics

The Metropolis-Hastings algorithm ensures a Markov chain satisfies the three regularity conditions, and therefore will eventually converge upon the stationary distribution. However, it does not necessarily guarantee that this convergence will occur quickly or efficiently. Markov chains used in this analysis have undergone tuning and several diagnostics tests to ensure that they are behaving as expected and converging in a reasonable amount of time.

4.3.1 Step Size Tuning

Every Markov chain starts at a random point in parameter space, often far away from the desired stationary distribution. A new step is proposed using the

proposal function $q(\vec{\theta_{n+1}}|\vec{\theta_n})$, which is a Gaussian distribution centred on the current step. The width of the proposal function, commonly referred to as the 'step size', can be tuned to increase the speed at which the chain reaches the stationary distribution. These step sizes need to be carefully chosen as their values can drastically impact the behaviour of the Markov chain.

The potential consequences of untuned step sizes are illustrated in figure 4.1, which shows three Markov chains with step sizes of 0.5, 0.1 and 10 respectively. Despite sharing the same stationary distribution - a standard normal distribution $N(0,1)$ - their behaviours vary significantly. In case (a), the chain quickly converges upon the stationary distribution and explores a wide area of the parameter space. In case (b), the step size is far too small, and while the rate of acceptance is very high, it would take a very long time to adequately explore the parameter space. Conversely, case (c) hasfar too large a step size and a very low acceptance due to the proposition of steps far outside of the high likelihood region of parameter space. Similarly to case (b), the chain in case (c) would also require a large number of steps to reliably explore the parameter space.

Figure 4.1 illustrates the importance of tuning parameter step sizes to ensure the chains converge as quickly and efficiently as possible.

4.3.2 Autocorrelations

Although step sizes can be easily tuned to achieve an optimal acceptance probability, it is also important to consider step-to-step correlations by measuring a quantity known as autocorrelation. Autocorrelation is a measure of how correlated a step is with another step in the chain and acts as a metric for how many independent samples the chain is drawing from the stationary distribution. The autocorrelation r_l for parameter Y can be calculated using the the function

$$r_l = \frac{\sum_{i=1}^{N-l}(Y_i - \hat{Y})(Y_{i+l} - \hat{Y})}{\sum_i^N (Y_i - \hat{Y})^2}, \tag{4.5}$$

where Y_i is the value of parameter Y at step i, $\hat{Y}$ is the mean of parameter Y and N is the total number of steps in the Markov chain. The lag, denoted as l, is the

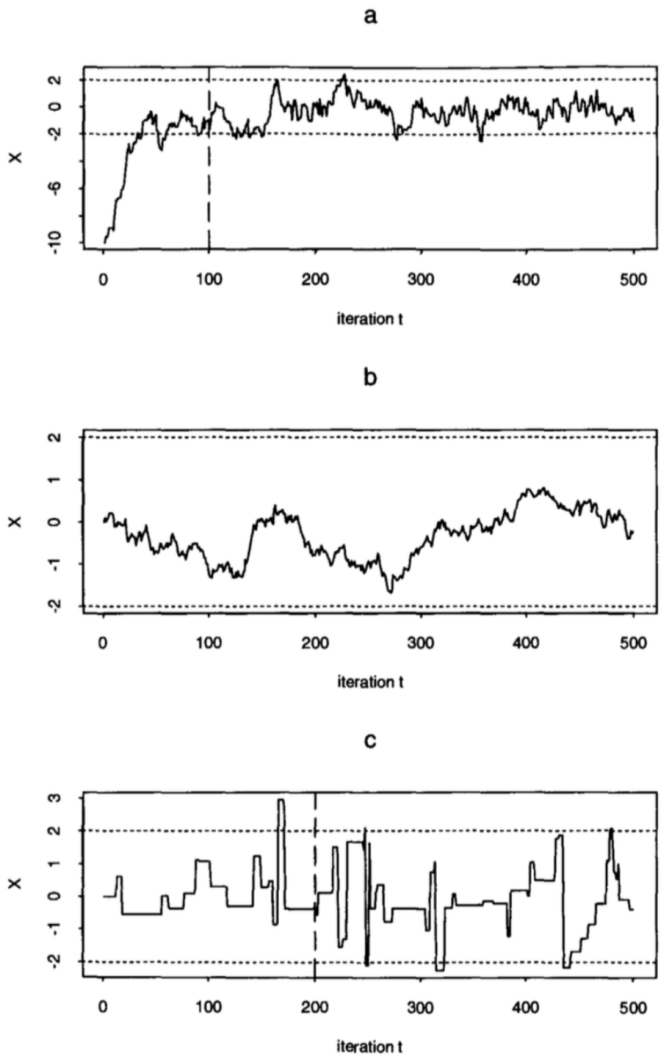

Figure 4.1: 500 iterations from Markov chains with stationary distribution $N(0,1)$ and Gaussian proposal functions with step sizes (a) 0.5, (b) 0.1, and (c) 10. Figure from [100].

number of steps beyond the current step i that is considered when computing the autocorrelation. Stated differently, equation 4.5 measures the correlation between step i and step $i+l$.

In T2K oscillation analyses, the a priori objective is to achieve an autocorrelation of below 0.2 after a lag of 30,000 steps for all fit parameters, and the step sizes are tuned accordingly to fulfil this condition. Figure 4.2 shows the autocorrelation function for a cross-section and flux parameter. The cross-section and flux parameters are described in section 5.3.

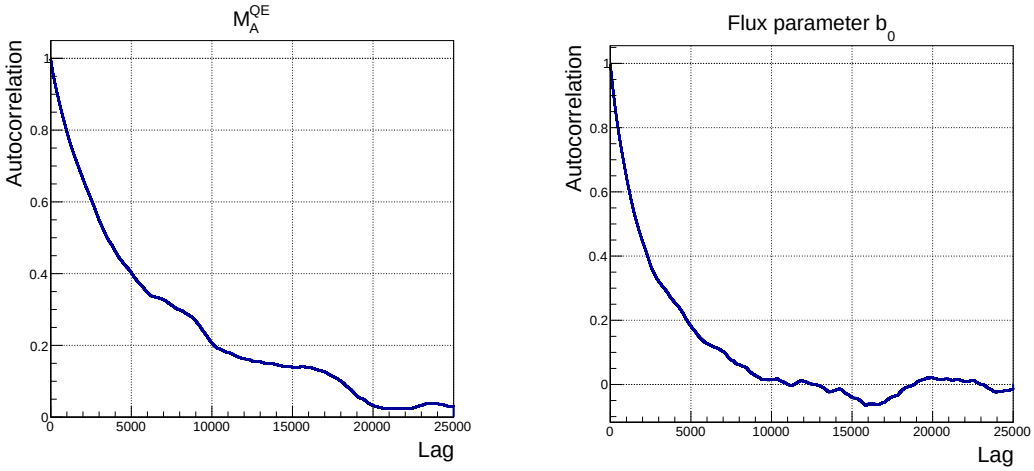

(a) Cross-section parameter M_A^{QE} **(b)** Flux parameter b_0

Figure 4.2: The autocorrelation function for two oscillation analysis fit parameters up to a lag of 25,000.

4.3.3 Burn-in

Markov chains often start far away from the high probability density regions of parameter space, therefore it typically requires some time for the chain to converge upon the stationary distribution. This period of exploration is commonly referred to as the 'burn-in' period. These steps must be discarded before making parameter estimations since they do not represent samples from the posterior distribution. Figure 4.3 illustrates the burn-in period for a typical Bayesian oscillation analysis fit. It can be observed that the log-likelihood function changes rapidly during the first 80,000 steps, but soon stabilises, indicating the chain has reached the stationary distribution. A burn-in cut of 60,000 was found to be sufficient for the data fits presented in chapter 6.

4.4 The Posterior Distribution

The fundamental outcome of a Bayesian analysis is the posterior probability distribution, which contains information about all of the model parameters. In this analysis, the posterior is a 791-dimensional distribution, which is problematic to visualise or meaningfully interpret. To construct best-fit point estimates and

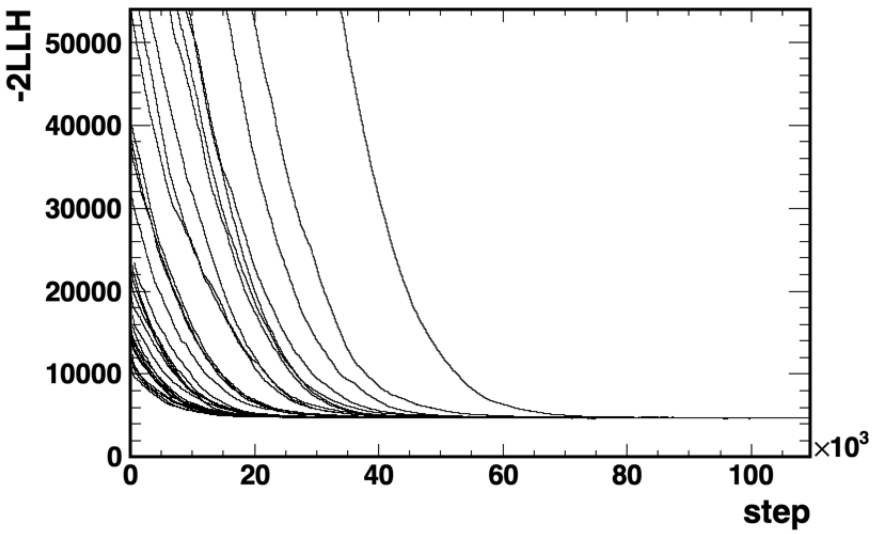

Figure 4.3: The negative log-likelihood (LLH) of several Markov chains from an Asimov fit plotted against the number of steps. The burn-in cut was chosen to be 80,000 steps.

uncertainties of the parameters of interest - $\sin^2\theta_{23}$, $\sin^2\theta_{13}$, Δm^2_{32} and δ_{CP} - it is necessary to construct the marginal posterior distribution.

4.4.1 Marginalisation of Nuisance Parameters

Marginalisation allows for the posterior to be projected onto fewer dimensions whilst retaining the uncertainty introduced by nuisance parameters. In this analysis, nuisance parameters include cross-section, flux and detector uncertainties, as well as the solar oscillation parameters, to which T2K has very little sensitivity. Whilst these parameters are important in their own right, from the point of view of an oscillation analysis, there is little interest in making statistical statements about each of these nuisance parameters. However, their correlations with the oscillation parameters and their uncertainties must be taken into account when making statistical statements about the oscillation parameters. Marginalisation ensures the effects of nuisance parameters are properly handled.

The posterior distribution is often marginalised to one or two dimensions to make statistical statements about the oscillation parameters. Consider parameters of interest $\vec{\beta}$ and all other parameters $\vec{\theta}$, then the marginalised posterior distribution is given by

$$\mathcal{P}(\vec{\beta}|D) = \int \mathcal{P}(\vec{\beta}|\vec{\theta})\mathcal{P}(\vec{\theta}|D)d\vec{\theta}\,. \tag{4.6}$$

The marginalised posterior distribution can then be used to make best-fit point estimates and construct credible intervals for the parameters of interest.

4.4.2 Best-fit Point Estimates and Uncertainties

After computing the marginal posterior distribution, best-fit point estimations and uncertainties for the parameters of interest can be calculated. The mode of the marginal posterior distribution is used as the best-fit point, commonly referred to as the highest posterior density (HPD) point. Uncertainties on parameters are given by constructing Bayesian credible intervals from the marginalised posterior distribution. The α% credible interval will satisfy the integral

$$\int_{\beta_1}^{\beta_2} \mathcal{P}(\beta|D)d\beta = \alpha\,, \tag{4.7}$$

where $\mathcal{P}(\beta|D)$ is the marginal posterior distribution for parameter of interest β. Credible intervals presented in this thesis are defined such that the α% credible interval contains the most probable points that represent α% of the marginal posterior probability. In this thesis, the 68%, 90% and 99% credible intervals for the oscillation parameters are typically presented. An example of the 1D and 2D marginal posterior distributions for $\sin^2\theta_{23}$ and the cross-section parameter M_A^{QE}[2] is shown in figure 4.4. The 68% credible intervals are also drawn overlaid on the 1D marginal posterior distributions.

The binned marginal posterior probability can be interpreted as a likelihood function to calculate Frequentist-style confidence intervals. The point of maximum likelihood is defined to be the maximum of the posterior distribution, $\mathcal{L}_{\text{max}}$, and each bin of the marginal posterior also has a likelihood $\mathcal{L}_{\text{bin}}$. These likelihoods are simply the value of the posterior distribution in a specific bin. A $\Delta\chi^2$ curve can then be computed by iterating through each bin and calculating

[2] M_A^{QE} is the axial mass term in the axial form factor, and is the dominant interaction parameter for CCQE interactions.

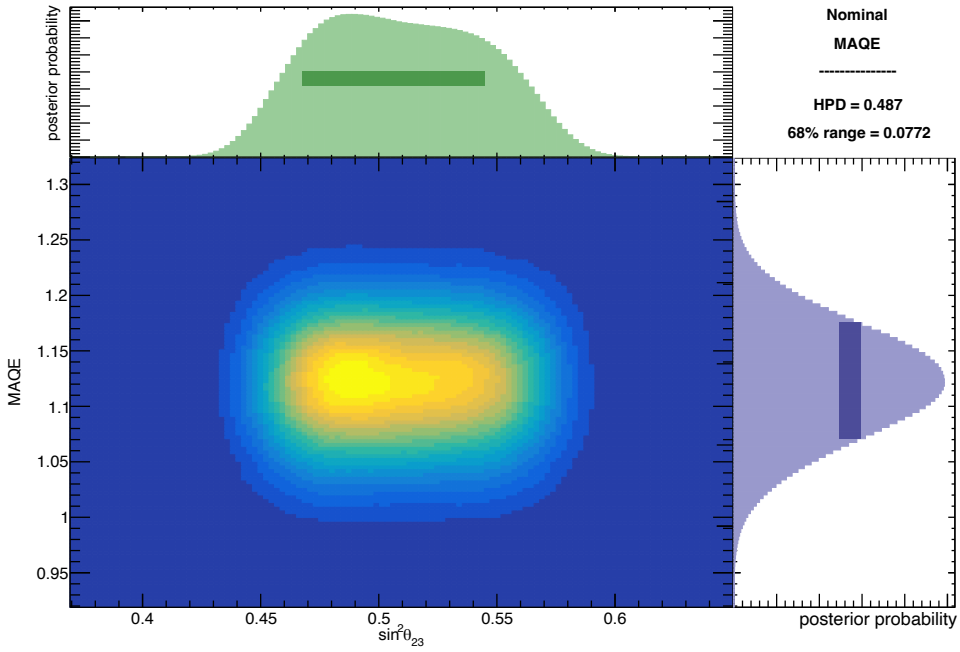

Figure 4.4: The 1D and 2D marginal posterior distributions for the parameters $\sin^2\theta_{23}$ and M_A^{QE}. The 68% credible intervals are drawn on the 1D distributions.

$$\Delta\chi^2 = -2\ln\left(\frac{\mathcal{L}_{\text{bin}}}{\mathcal{L}_{\text{max}}}\right) . \tag{4.8}$$

After converting the posterior to a $\Delta\chi^2$ distribution, confidence intervals can be extracted and compared to other T2K oscillation analysis groups as a validation exercise.

Best-fit point estimations and uncertainties for parameters of interest can differ depending on the number of dimensions over which the posterior is marginalised. This phenomenon, known as marginalisation effects, is illustrated in figure 4.5. It can be observed that the best-fit point for the δ_{CP} parameter is different depending on whether the posterior is marginalised onto one or two dimensions. This is very likely to happen in oscillation fits due to the non-Gaussian nature of many of the model parameters. For example, both δ_{CP} and $\sin^2\theta_{23}$ exhibit non-Gaussian behaviour, and many cross-section parameters have physical boundaries they are forbidden from entering, causing asymmetries in their marginal posterior distributions. Although these effects may seem to resemble biases in the fit, it's

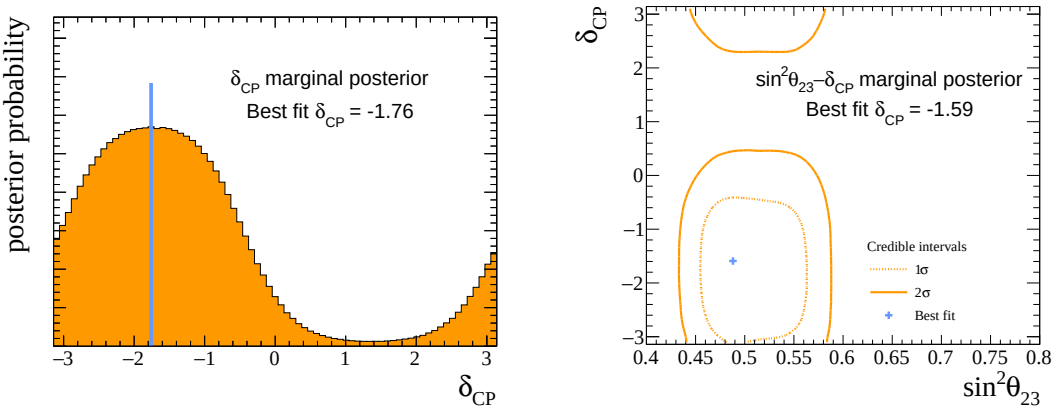

(a) δ_{CP} marginal posterior distribution **(b)** $\sin^2\theta_{23}$-δ_{CP} marginal posterior distribution

Figure 4.5: An example of how the point estimation for a parameter can change due to marginalisation effects. In (a), the posterior distribution is marginalised onto one dimension, where a best-fit point δ_{CP} = -1.76 is extracted. In (b), the posterior is instead marginalised onto two dimensions, and a best-fit point of δ_{CP} = -1.59 is found.

important to recognise that they are genuine manifestations of the marginal posterior distribution.

In this thesis, the best-fit points for the oscillation parameters are calculated using the 2D disappearance ($\sin^2\theta_{23}$, Δm^2_{32}) and appearance ($\sin^2\theta_{13}$, δ_{CP}) marginal posterior distributions, and the credible intervals are constructed from the 1D marginal posterior distributions.

4.4.3 Alternative Priors

The posterior distribution is proportional to the likelihood function $\mathcal{L}(D|\vec{\theta})$ multiplied by a prior $\pi(\vec{\theta})$. The prior term contains all presumed/past knowledge about a parameter. For the oscillation analysis presented later in this thesis, flat (uninformative) priors are assumed on all the oscillation parameters T2K has sensitivity to, namely: $\sin^2\theta_{23}$, $\sin^2\theta_{13}$, Δm^2_{32} and δ_{CP}.

An advantageous feature of Markov chains and Bayesian analyses is that because the posterior probability is proportional to a prior multiplied by the likelihood, it is possible to simply reweight the original posterior according to a different prior. The method to reweight a Markov chain is as follows: consider a probability function $P(x)$, and an equivalent probability function with

a different parameterisation $Q(y)$. There must exist a variable transformation $y = y(x)$ where $P(x)$ and $Q(y)$ are equivalent probability distributions, which is equivalent to writing

$$Q(y) = P(x(y))\frac{dx}{dy}. \tag{4.9}$$

If $P(x)$ is a uniform distribution, such as a flat prior, equation 4.9 can be simplified to

$$Q(y) \propto \frac{dx}{dy}, \tag{4.10}$$

up to a normalisation constant. In equation 4.10, y is the original parametrisation of the prior, and x represents the new parameterisation that is to be tested. As the posterior is proportional to the prior, $Q(y)$ must be evaluated for every accepted step in the Markov chain and the posterior is then reweighted by the value of this function.

For a statistical statement about the oscillation parameters to be significant, it must be robust to alternative prior testing. The impact of alternative prior testing on the results of this thesis is shown in section 6.5.

4.4.4 Bayes Factors

As well as constructing point estimates and credible intervals, it is also possible to quantify the data's preference for one model over another. This is encapsulated in a quantity known as the Bayes factor. The Bayes factor can be derived by considering the posterior odds ratio of one model M_i over another model M_j:

$$\frac{\mathcal{P}(M_i|D)}{\mathcal{P}(M_j|D)} = \frac{\mathcal{L}(D|M_i)}{\mathcal{L}(D|M_j)}\frac{\pi(M_i)}{\pi(M_j)} = B_{ij}\frac{\pi(M_i)}{\pi(M_j)}. \tag{4.11}$$

The Bayes factor B_{ij} can therefore be interpreted as the relative likelihood of two models given the observed data. In the case of equal prior probabilities, the Bayes factor is equal to the posterior odds. Bayes factors can be interpreted using table 4.1, developed by Kass and Raftery [104] based on work completed by Jeffreys [105].

$\log_{10} B_{ij}$	B_{ij}	Strength of evidence
0 to 0.5	1 to 3.2	Not worth more than a bare mention
0.5 to 1	3.2 to 10	Substantial
1 to 2	10 to 100	Strong
>2	>100	Decisive

Table 4.1: The Kass-Raferty scale [104] for interpreting Bayes factors, based on work completed by Jeffreys [105]

5 Oscillation Analysis: Framework

This chapter will describe the MaCh3 analysis framework that underpins all oscillation results presented in this thesis. T2K's oscillation analysis is naturally quite developed and mature due to the runtime of the experiment, therefore this work is both adapted from and builds upon previous results presented in internal technical notes and past theses [106, 107].

Section 5.1 will describe the broad analysis strategy, and section 5.2 will describe the event selection and samples at the near and far detector. Section 5.3 will discuss the systematic uncertainties that enter the oscillation fit, while section 5.4 will present pre-fit MC predictions for each far detector sample. Finally, the results of fitter validation studies will be presented in section 5.5.

5.1 Analysis Strategy

Oscillation parameter constraints are obtained by performing a binned joint fit of ND280 and SK data using a Bayesian Markov chain Monte Carlo method. Using protons-on-target (POT) as a metric for the amount of data collected, the SK data comprises 19.7×10^{20} POT in neutrino (FHC) beam mode and 16.3×10^{20} POT in antineutrino (RHC) beam mode. The near-detector fit is performed using ND280 data corresponding to 11.5×10^{20} POT in FHC and 8.3×10^{20} POT in RHC

beam modes respectively. The data and Monte Carlo prediction are compared bin-by-bin using the likelihood and prior terms

$$
\begin{aligned}
-\ln(\mathcal{L}) = & \sum_{i}^{\text{ND280bins}} N_i^{\text{ND},p}(\vec{b},\vec{x},\vec{d}) - N_i^{\text{ND},d} + N_i^{\text{ND},d} \ln\left(N_i^{\text{ND},d}/N_i^{\text{ND},p}(\vec{b},\vec{x},\vec{d})\right) + \frac{(\beta_i-1)^2}{2\sigma_{\beta_i}^2} \\
& + \sum_{i}^{\text{SKbins}} N_i^{\text{SK},p}(\vec{b},\vec{x},s\vec{k}d,\vec{o}) - N_i^{\text{SK},d} + N_i^{\text{SK},d} \ln\left(N_i^{\text{SK},d}/N_i^{\text{SK},p}(\vec{b},\vec{x},s\vec{k}d,\vec{o})\right) \\
& + \frac{1}{2}\sum_{i}^{\text{osc osc}}\sum_{j} \Delta o_i (V_o^{-1})_{i,j} \Delta o_j + \frac{1}{2}\sum_{i}^{\text{fluxpars fluxpars}}\sum_{j} \Delta b_i (V_b^{-1})_{i,j} \Delta b_j \\
& + \frac{1}{2}\sum_{i}^{\text{xsecpars xsecpars}}\sum_{j} \Delta x_i (V_x^{-1})_{i,j} \Delta x_j + \frac{1}{2}\sum_{i}^{\text{ND280det ND280det}}\sum_{j} \Delta d_i (V_d^{-1})_{i,j} \Delta d_j \\
& + \frac{1}{2}\sum_{i}^{\text{SKdet SKdet}}\sum_{j} \Delta skd_i (V_{skd}^{-1})_{i,j} \Delta skd_j \,,
\end{aligned}
\tag{5.1}
$$

where $V_{i,j}$ are the covariance matrices acting as constraints on the systematic parameters, with labels b for the ND280 and SK flux parameters (split by horn current and neutrino flavour at production), x for cross section, d and skd for ND280 and SK detector systematics respectively, and o for the oscillation parameters. $N_i^{\text{ND},p}$ and $N_i^{\text{SK},p}$ denotes the number of predicted events from the Monte Carlo in bin i for ND280 or SK respectively, given the values of the systematic parameters. $N_i^{\text{ND},d}$ and $N_i^{\text{SK},d}$ denotes the number of observed data events in bin i at ND280 and SK respectively. Furthermore, as MC generation is inherently a random process, there is an underlying uncertainty in the MC prediction. Therefore, β_i and σ_{β_i} are parameters that correct the likelihood expression to account for the effects of MC statistical uncertainties. This correction only applies to ND samples, as the low number of data events at the far detector is expected to result in small MC statistical uncertainties. This method is fully described in [108].

The likelihood expression in equation 5.1 is calculated at each step in the Markov chain during the Metropolis-Hastings algorithm calculation, and the prior terms encode external constraints and enter through the values assigned in the covariance matrices.

As in any Bayesian analysis, it is necessary to choose well-informed priors for all model parameters. A prior encodes all previous and assumed knowledge

about a parameter. Gaussian priors are used for all systematic parameters, and for the oscillation parameters $\sin^2\theta_{12}$ and Δm^2_{21}, to which T2K has little sensitivity. Flat priors are assigned bounded by their physically allowed values to $\sin^2\theta_{23}$, Δm^2_{32} and δ_{CP}, meaning no prior knowledge is assumed regarding these parameters. For $\sin^2\theta_{13}$, the prior may be flat (referred to as 'T2K-only') or Gaussian according to the measurement of this parameter by reactor neutrino experiments in the latest PDG release [109]: $\sin^2\theta_{13} = 0.0220 \pm 0.0007$ (referred to as 'T2K + reactor' or 'T2K + RC'). Additionally, a prior is used for the mass ordering, where the probabilities for normal (NO) and inverted (IO) ordering are equal: $P(\mathrm{NO}) = P(\mathrm{IO}) = 0.5$. This is encoded as the sign of Δm^2_{32}, where in each step of the Markov chain there is a 50% probability for the proposal function to switch sign/ordering.

Further, to ensure the Markov chain properly samples each octant of $\sin^2\theta_{23}$ efficiently, an explicit octant flipping mechanism was implemented. At each step of the chain there is a 50% probability to switch to the opposite octant, mirrored around the point of maximal disappearance. This point can be determined by differentiating the disappearance oscillation probability formula written in equation 2.29 with respect to $\sin^2\theta_{23}$:

$$\begin{aligned}\frac{\partial}{\partial \sin^2\theta_{23}} P(\nu_\mu(\bar{\nu}_\mu) \to \nu_\mu(\bar{\nu}_\mu)) &= -4\cos^2\theta_{13} + 8\cos^4\theta_{13}\sin^2\theta_{23} \\ 0 &= -4\cos^2\theta_{13} + 8\cos^4\theta_{13}\sin^2\theta_{23} \\ \Rightarrow \sin^2\theta_{23} &= \frac{1}{2(1-\sin^2\theta_{13})}\,.\end{aligned} \tag{5.2}$$

Evaluating equation 5.2 using the PDG constraint for $\sin^2\theta_{13}$ yields a point of maximal disappearance of $\sin^2\theta_{23} = 0.5112$[1]. It is necessary to switch octant about this point to ensure that the chain moves to an area of parameter space with equal neutrino mixing probability. This technique is necessary due to the non-Gaussian nature of the posterior probability of $\sin^2\theta_{23}$, and the region of

[1]Note that the exact value of maximal disappearance will vary depending on the assumptions made in its calculation, which may vary across long-baseline oscillation experiments.

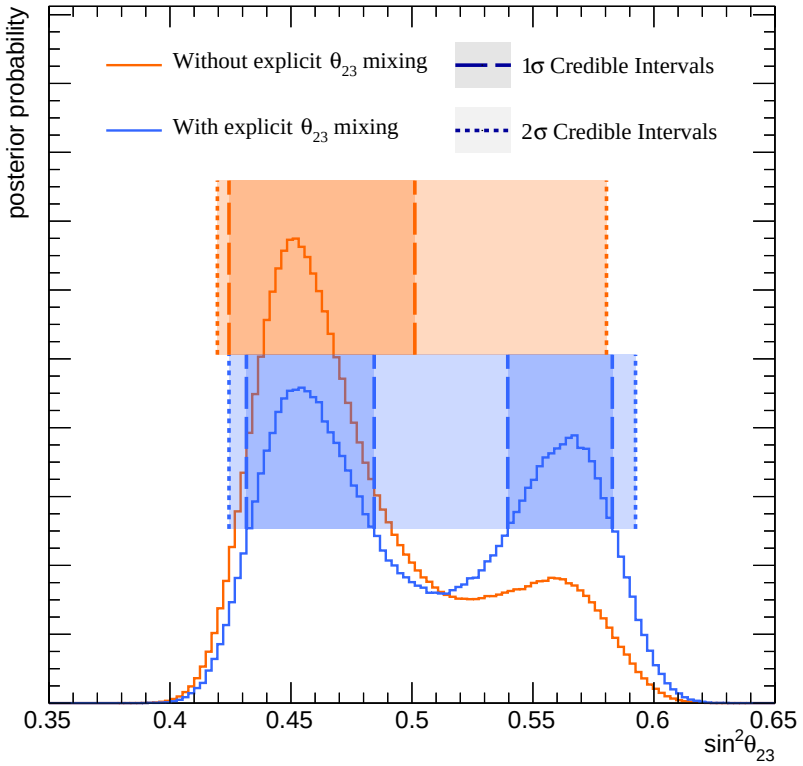

Figure 5.1: A comparison of two Asimov fits performed where the Asimov point is set to $\sin^2\theta_{23} = 0.45$. It can be seen that when θ_{23} mixing is enabled (blue) the chain more thoroughly explores each octant.

low probability which separates the two octants. This makes it difficult for the Markov chain to regularly cross this point of parameter space, therefore an explicit mechanism was implemented to counter this. The effect of this mixing mechanism on the $\sin^2\theta_{23}$ marginal posterior is shown in figure 5.1. All fits presented in this thesis have the octant flipping mechanism enabled.

5.2 Event Selection

5.2.1 ND280

The ND280 samples are designed to target charged-current ν_μ or $\bar{\nu}_\mu$ events originating in the fiducial volume of FGD1 or FDG2 that produce interaction products that are measured in at least one of the TPCs. Detailed information

regarding the ND280 data selections can be found in [110, 111], and the selections are summarised below.

To enter the broad CC-inclusive selection, each event must fulfil the following general selection criteria[2]:

- **Event quality** – only events that occur within the timeframe of a beam spill are selected.
- **Total multiplicity** – the event contains at least one reconstructed track crossing one of the TPCs.
- **Track quality and fiducial volume** – the event's reconstructed vertex is within the FGD's fiducial volume (FV). The FV is chosen to minimise the number of events where the reconstructed vertex lies within the FGDs, but the true interaction vertex is located outside. Furthermore, only tracks with more than 18 clusters are selected to reject short tracks, which are less reliably reconstructed in the TPCs.
- **Upstream background veto** – an event is rejected if the second highest momentum track has a start position of at least 150 mm upstream of the muon candidate. This cut is designed to prevent a single track with a large scatter from being mis-reconstructed as two separate tracks.
- **Broken track** – If an event contains at least one reconstructed FGD-only track, the initial position of the muon candidate track must be less than 425 mm from the upstream edge of the FGD. This cut vetos events in which a single track has been erroneously split into two separate tracks due to mis-reconstruction.
- **Muon PID** – The highest momentum (positive or negative) track in the TPC is classified as a muon.

[2] List adapted from [111]

The CC-inclusive selection can then be further divided into samples based on the multiplicity of final state particles.

FHC samples are constructed by considering the presence of photons, protons and pions in the final state. Proton-tagged samples help to better probe CCQE and 2p2h interactions, while photon-tagged samples aid in measuring neutral pion production. Photon and proton tagging is a recent addition to T2K analyses and is fully described in [111]. Charged pions are identified via secondary tracks which are distinct from the muon candidate, after which TPC or FGD PID information is utilised to distinguish them. The secondary tracks are required to occur within the same time as the muon candidate, and must originate from the same FGD FV. Candidate pions tracks in the TPC are identified by measuring the dE/dx of the track. If the candidate pion was contained within the FGD, FGD information can be utilised to perform PID. Additionally, for pion tracks that are too short to register hits in the FGDs, Michel electron tagging can serve as an alternative method of PID. It should be noted that photon and proton tagging is only used in the FHC samples. A summary of the ND280 samples used in this analysis is shown in table 5.1.

The selection process for RHC samples is largely similar to FHC samples, and further details can be found in [110]. Due to the increased wrong-sign component in the RHC beam mode, additional RHC ν_μ samples are included which are specifically aimed at this component. These samples are important to include in near-detector analyses due to the far detector's inability to distinguish between neutrino and antineutrino events.

5.2.2 Super-Kamiokande

Selections at the far detector are made based on the topology of the Cherenkov rings produced when a neutrino interacts inside the detector. Both the data and MC are divided into six samples, detailed in table 5.2.

The ν_μCC1π sample is a recent addition to T2K analyses, which yields a statistical increase of 38% in FHC μ-like data. However, it should be noted that

All Reconstructed Events		
↙	↓	↘
FHC ν_μ CC-Inclusive (FGD1 & FGD2)	RHC $\bar{\nu}_\mu$ CC-Inclusive (FGD1 & FGD2)	RHC ν_μ CC-Inclusive (FGD1 & FGD2)
↓	↓	↓
CC0π-0p-0γ CC0π-Np-0γ CC1π^+-0γ CC-Other-0γ CC-Photon	CC0π CC1π^- CC-Other	CC0π CC1π^+ CC-Other

Table 5.1: ND280 samples. Table adapted from [112].

SK sample	Ring topology
FHC 1Rμ	single muon-like ring with fewer than two decay electrons in FHC mode
FHC ν_μCC1π	one muon-like ring and a delayed electron-like ring, along with up to two further rings from a charged pion, depending on its final state and secondary interactions
FHC 1Re	single electron-like ring with zero decay electrons in FHC mode
FHC 1Re1de	single electron-like ring and a further electron-like ring originating from an invisible (below Cherenkov threshold) charged pion decay
RHC 1Rμ	single muon-like ring with fewer than two decay electrons in RHC mode
RHC 1Re	single electron-like ring with zero decay electrons in RHC mode

Table 5.2: The six SK samples and their respective Cherenkov ring topologies.

due to the relatively high reconstructed neutrino energy of this sample, which predominantly sits above the oscillation maximum, significant improvements to oscillation parameter measurements are not expected. Despite this, the addition of this sample provides an opportunity to test the consistency of the cross-section and flux model at higher neutrino energies.

Interactions within the SK detector are reconstructed using the fiTQun algorithm [113]. FiTQun employs a maximum-likelihood approach to reconstruct particle IDs and kinematics using PMT hit charge and time information. Fol-

lowing reconstruction, distinct event selection criteria need to be met for each of the far-detector samples. These differ based on topology but are identical for FHC and RHC events. Detailed information and motivation regarding the selection criteria for each far-detector sample can be found in [114, 115] and the criteria are summarised below.

For the 1Rμ samples, the selection criteria are:

- **Fully contained** – the event must be fully reconstructed within the fiducial volume.
- **Ring topology** – fiTQun must find only one ring in the first sub-event[3] and identify it as muon-like.
- **Momentum** – the reconstructed muon momentum must be greater than 200 MeV.
- **Decay electrons** – fewer than two decay electrons are observed.
- **2D π^+ cut** – the event must pass the cut $\ln(L_\pi/L_\mu) < 0.15 \times p_\mu$ which is designed to reduce the background from NC1π^+ events.

For the 1Re samples, the selection criteria are:

- **Fully contained** – the event must be fully reconstructed within the fiducial volume.
- **Ring topology** – fiTQun must find only one ring in the first sub-event and identify it as electron-like.
- **Visible energy** – the visible energy (E_{vis}) is greater than 100 MeV.
- **Decay electrons** – zero decay electrons are detected.
- **Neutrino energy** – reconstructed neutrino energy (E_ν^{rec}) is less than 1250 MeV

[3] A sub-event refers to particle interactions within the detector that occur within a short time window of $\mathcal{O}(10\mu\text{s})$.

- π^0 **rejection** – the event must pass the cut $\ln(L_{\pi^0}/L_e) < 175 - 0.875 \times m_{\gamma\gamma}$ which is designed to reduce the background from NC1π^0 events.

The selection criteria for the FHC 1Re1de sample is largely identical to FHC 1Re but with the modified requirement of detecting one decay electron instead of zero.

The new ν_μCC1π sample has the following selection criteria:

- **Fully contained** – the event must be fully reconstructed within the fiducial volume.
- **Ring topology** – fiTQun must find greater than one ring in the first sub-event, **or** the number of decay electrons in the event is greater than one.
- **Decay electrons** – one or two decay electrons are detected, depending on the number of rings found by fiTQun.
- **2D likelihood cuts** – the two primary rings must not be identified as electron-like. This is done by applying 2D likelihood cuts comparing the nominal particle hypothesis (e.g. $\pi\pi$) to alternative particle hypotheses (e.g. $e\pi^+$ or ee).
- **Energy loss** – for events where only one decay electron is identified, the sum of the energy loss must be greater than 300 MeV. This rejects a significant proportion of the NC1π^+ background which suffers from large interaction and detector systematic uncertainties.

A schematic of a ν_μCC1π event is shown in figure 5.2.

Oscillation probabilities depend on the true neutrino energy, which must be reconstructed from detector measurements. The topology of the event and the kinematics of the outgoing lepton determine the reconstructed neutrino energy for each sample. For the FHC and RHC 1Rμ and 1Re events, it is assumed that the event was a CCQE interaction on a stationary bound nucleon. The reconstructed neutrino energy for a neutrino interacting with a bound neutron is given by

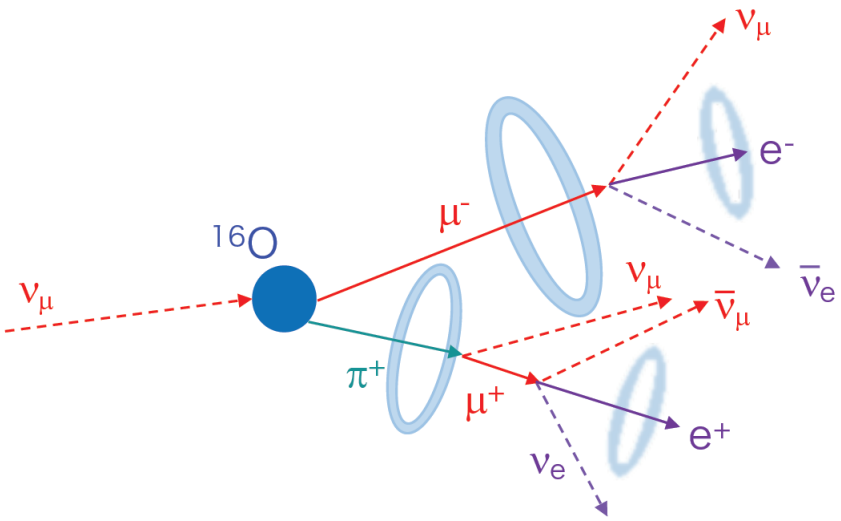

Figure 5.2: Schematic illustration of a ν_μCC1π event at SK. Figure from [116].

$$E_\nu^{\text{rec}} = \frac{(m_n - E_b)E_l - m_l^2/2 + m_n E_b - E_b^2/2 + (m_p^2 - m_n^2)/2}{m_n - E_b - E_l + p_l \cos\theta_{\text{beam}}}, \tag{5.3}$$

where m_p, m_n, and m_l are the proton, neutron, and lepton masses respectively. E_b is the binding energy of the neutron, E_l, is the outgoing lepton energy, p_l is the lepton momentum, and $\cos\theta_{\text{beam}}$ is the cosine of the angle of the outgoing lepton with respect to the incoming neutrino beam direction.

The quasi-elastic assumption is no longer valid for both the FHC ν_μCC1π and FHC 1Re1de samples. In this case, the outgoing baryon is assumed to be a Δ^{++} rather than a proton. The formula for the reconstructed neutrino energy becomes

$$E_\nu^{\text{rec}} = \frac{2m_p E_l + m_{\Delta^{++}}^2 - m_p^2 - m_l^2}{2(m_p - E_l + p_l \cos\theta_{\text{beam}})}, \tag{5.4}$$

where $m_{\Delta^{++}}$ is the Δ^{++} resonance mass.

Additionally, a correction is applied to p_l for MC events to account for the effect of Coulomb interactions between the outgoing charged lepton and the charged nucleus [117].

The muon-like samples are fitted in reconstructed neutrino energy, while the electron-like samples are fitted in both reconstructed neutrino energy and the angle between the outgoing lepton and the incoming neutrino, θ. This is to allow

for better discrimination between electron neutrinos and antineutrinos, with the cross section for antineutrinos creating a more forward distribution for the outgoing lepton. The binning for each sample is as follows:

- μ-like samples: 50 MeV-width bins from 0 to 3 GeV, after which the bin edges are: 3.25, 3.5, 3.75, 4, 4.5, 5.0, 5.5, 6.0, 7.0, 8.0, 9.0, 10.0 and 30 GeV.

- e-like samples: uniform 50 MeV-width bins with a reconstructed energy cut at 1.25 GeV. The θ binning has uniform binning of 10°-width bins from 0° to 140° and one bin for 140°–180°.

During an oscillation fit, MC events are subject to momentum shifts due to binding energy and Coulomb corrections, which are described in section 5.3. This may cause events that initially pass the selection cuts to migrate out of selection, or conversely, events above these kinematic boundaries may migrate into selection. In previous analyses, events were only able to shift out of selection, and events that initially fell outside of the kinematic selections were not included in the fit. In this analysis, a small number of events above/below the aforementioned sample kinematic cuts are included in the MC and are therefore able to enter the selection. To ensure these events receive the correct cross-section responses, they also enter the spline calculation, described in section 5.3.2. This method of handling events around kinematic boundaries is a new addition to this analysis and was found to have no significant impact on the oscillation results, as was anticipated. Nevertheless, the capacity for events to migrate across kinematic boundaries provides a more sophisticated description of events within these regions of phase space.

The total number of data events in each far-detector sample is given in table 5.3. Additionally, figure 5.3 shows the number of events plotted against reconstructed neutrino energy for each sample.

Selection	POT	Number of data events
FHC 1Rμ	19.644×10^{20}	318
FHC ν_μCC1π		135
FHC 1Re		94
FHC 1Re1d.e		14
RHC 1Rμ	16.34556×10^{20}	137
RHC 1Re		16

Table 5.3: The total number of data events in each SK sample.

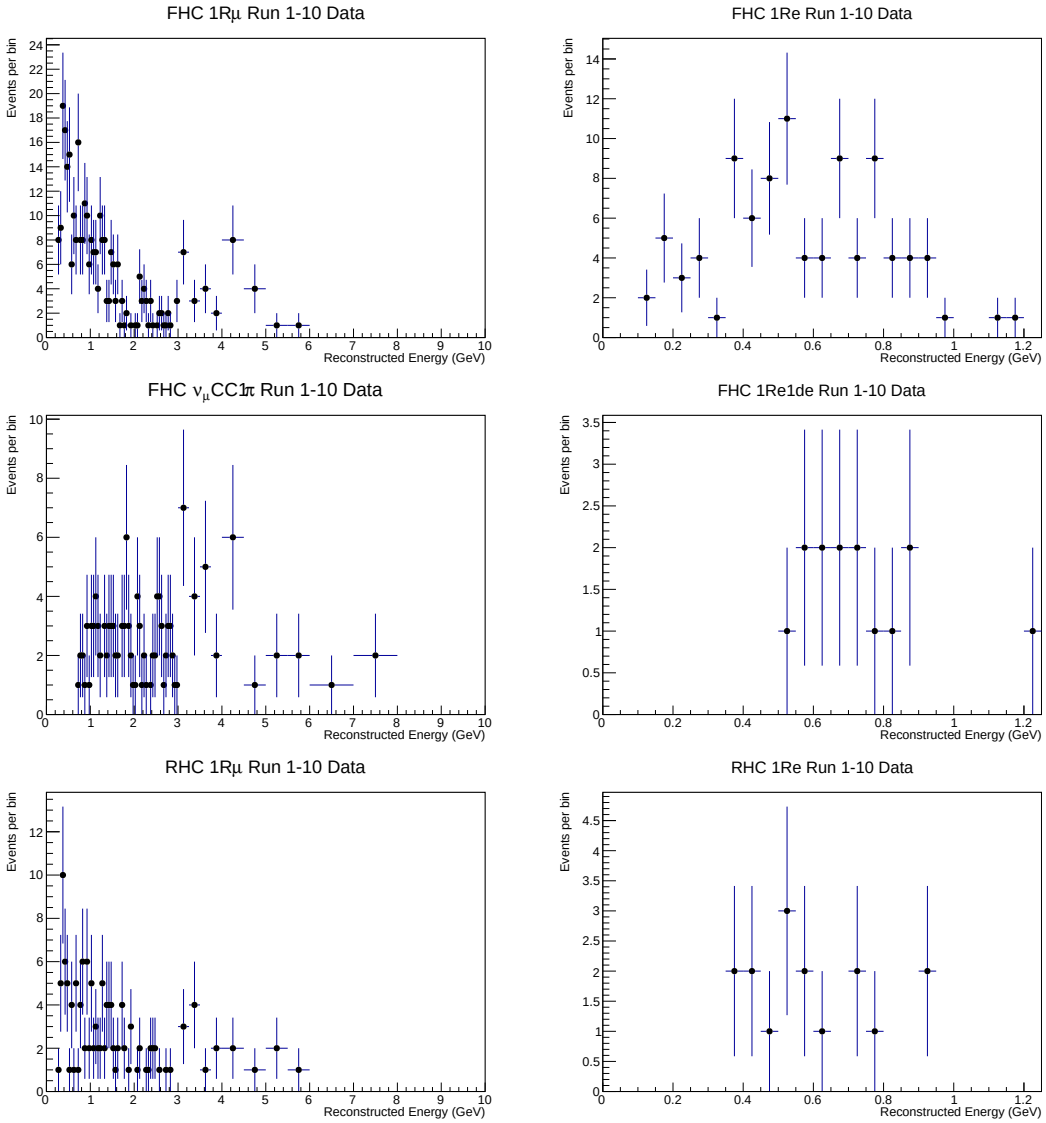

Figure 5.3: The number of data events per bin plotted against reconstructed neutrino energy for each SK sample.

5.3 Systematic Errors

5.3.1 Flux

A robust prediction of the neutrino flux is essential to making precision measurements of the oscillation parameters. The flux model used in the oscillation analysis presented in this thesis is described in detail in [118] and will be summarised below.

The leading source of uncertainty on the neutrino flux is the modelling of hadronic interactions of protons impinging on the neutrino production target. Other sources of uncertainty include the proton beam profile and off-axis angle, the horn current and magnetic field, the beamline alignment, modelling of the graphite target, and the number of protons in the proton beam. A recent update to the flux tuning includes the use of NA61/SHINE T2K replica target data [119], which resulted in a significant decrease in the flux uncertainty due to hadronic interactions, especially at higher energies ($1 \sim 2$ GeV) where kaons start to dominate. The total flux uncertainty and its individual contributions for muon neutrinos and antineutrinos at ND280 and SK for a neutrino-mode and antineutrino-mode beam respectively are shown in figure 5.4.

The flux uncertainty parameters in the oscillation analysis are implemented as bin-content normalisations that can vary the flux prediction in each bin of true neutrino energy. There are separate parameters for each beam mode (FHC or RHC), neutrino flavour (ν_μ, ν_e, $\bar{\nu}_\mu$, $\bar{\nu}_e$) and detector (SK or ND280). This results in a total of 100 flux parameters: 50 for ND280 and 50 for SK. The prior (pre-fit) covariance matrix for the flux parameters is shown in figure 5.5.

5.3.2 Cross Section

A key component of the oscillation analysis is the oscillation probability calculation, which depends on the true neutrino energy. Detectors can reconstruct quantities such as neutrino energy and lepton momentum, but this reconstruction assumes an interaction model. If the model is incorrect, event kinematics will be

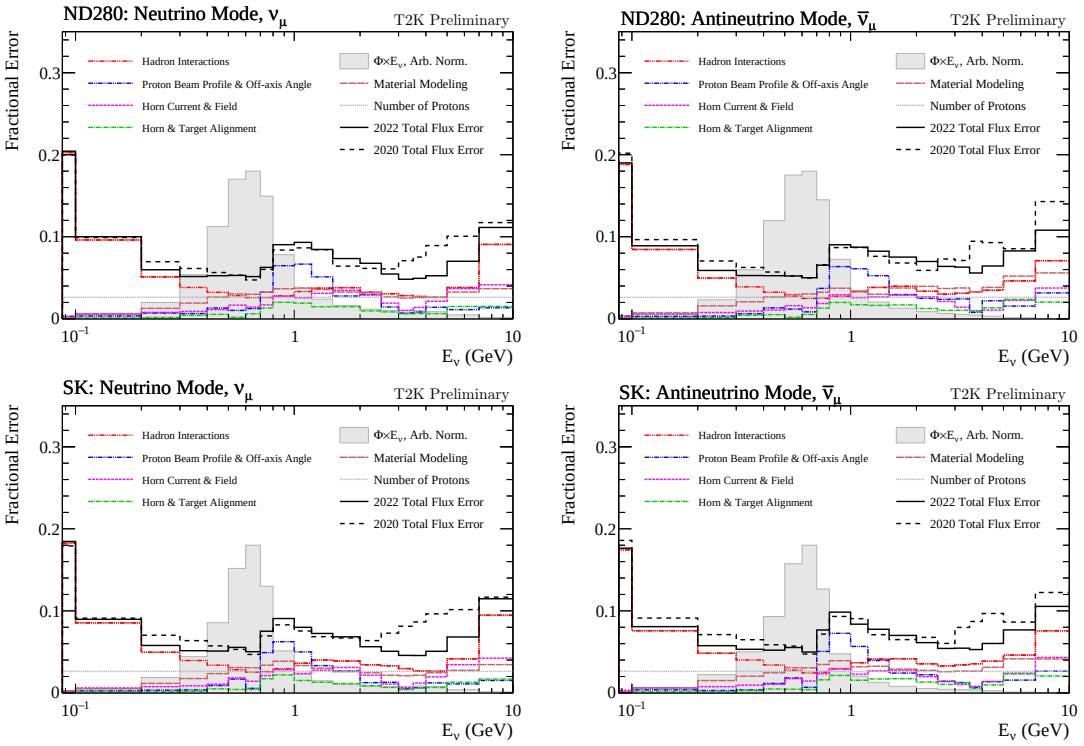

Figure 5.4: Total flux uncertainty for FHC ν_μ and RHC $\bar{\nu}_\mu$ at ND280 (top row) and SK (bottom row). Individual sources of uncertainty are also plotted. $\Phi \times E_\nu$ (grey shaded region) represents the unoscillated nominal flux. Figure from [118].

incorrectly reconstructed, which may lead to biases in the oscillation measurements. Therefore, as discussed in section 2.3, a thorough and well-understood neutrino interaction model is of critical importance to the oscillation analysis.

In the oscillation analysis presented here, there are 74 cross-section systematic parameters (dials) which can be broadly categorised into three main types:

- **Normalisation** – parameters that impact all events of a particular interaction channel or neutrino flavour in the same way, independent of energy; each event is weighted by the same value.

- **Shape** – parameters that affect events with different energies and kinematics differently. To construct an event's response to these parameters, weights are pre-calculated at discrete parameter positions and interpolated between using a spline (a cubic function).

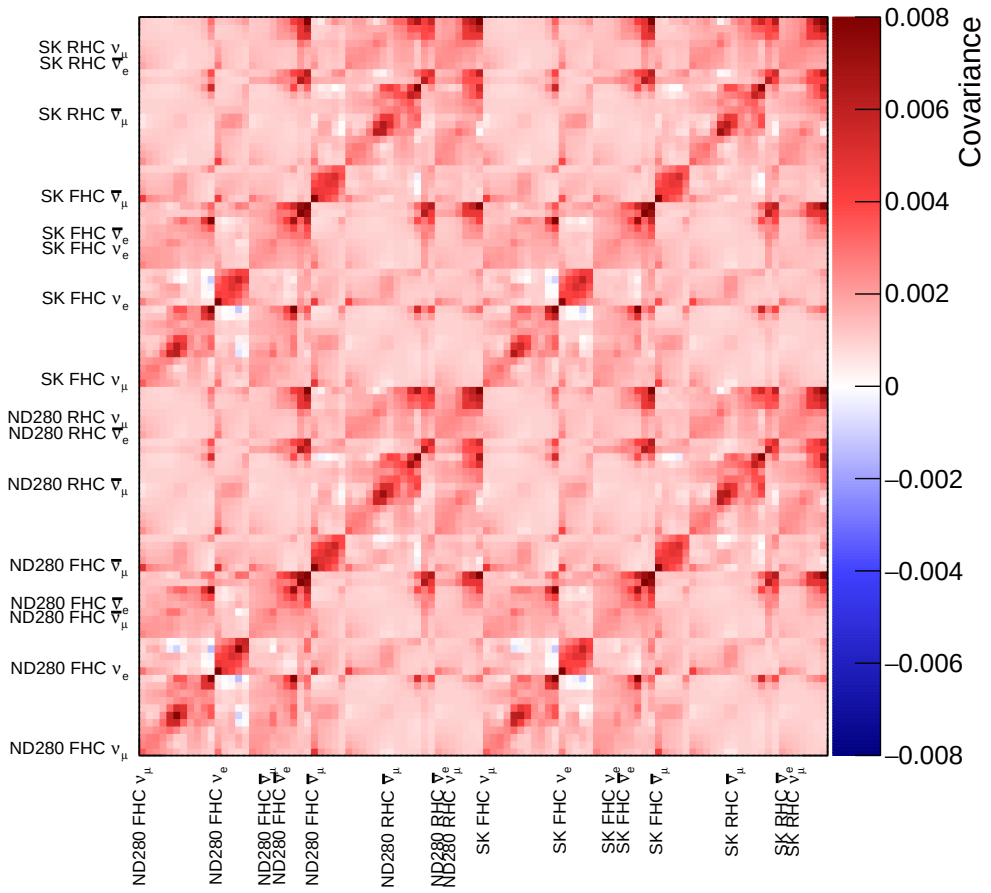

Figure 5.5: The flux covariance matrix used in the oscillation analysis. The axis labels indicate the detector, horn current and neutrino flavour each parameter corresponds to.

- **Functional shift** – parameters that cause shifts in an event's kinematic variables. These are calculated event-by-event during the fit.

The implementation of shape parameters differs between the near and far detector. At ND280, each event receives a spline for each cross-section parameter that impacts the event. At SK, events are binned in true and reconstructed neutrino energy (and θ for e-like samples), and splines are calculated from the average cross-section weight for each parameter in every kinematic bin.

The neutrino interaction model used in the oscillation analysis is built and recommended by T2K's Neutrino Interactions Working Group (NIWG). A full description of the motivation, design and implementation of the interaction model can be found in [120]. The cross-section parameters that are used in

the oscillation analysis are listed in table 5.4, and the pre-fit covariance matrix is shown in figure 5.7. The cross-section model will be described below, with parameters categorised according to the specific areas of the interaction model they were developed for. There is a focus on parameters affecting charged-current quasi-elastic (CCQE) interactions, where newly developed uncertainty parameters to describe such interactions are further discussed in chapter 7.

CCQE interactions and nuclear ground state

- **Axial mass** – neutrino-nucleon CCQE interactions are governed by three nucleon form factors: electric, magnetic and axial. The electric and magnetic components are well-constrained by electron-scattering experiments [121]. The axial form factor dominates neutrino-nucleon interactions and is commonly parameterised as a dipole form

$$F_{\mathrm{A}}(Q^2) = \frac{g_{\mathrm{A}}}{\left(1 + \frac{Q^2}{M_A^{QE2}}\right)^2}, \tag{5.5}$$

  where F_{A} is the axial form factor, Q^2 is the squared four-momentum transfer, and g_{A} is the overall normalisation which is well-known from β-decay experiments [31]. Thus, the only uncertainty in the axial form factor is the axial mass: $M_{\mathrm{A}}^{\mathrm{QE}}$. The prior value of 1.03 GeV is chosen to be consistent with bubble chamber experimental data [122].

- **Spectral function** – an interaction model is built on top of the nuclear ground state, which describes the initial energy and momenta of nucleons within the nucleus. For CCQE interactions, this is a spectral function, introduced in section 2.3.2. The spectral function is a 2D distribution that encodes the probability of finding a nucleon with some particular momentum and removal energy (E_{rmv}), which is the energy required to remove the nucleon from the nuclear potential. It should be noted that removal energy may also be referred to interchangeably as 'missing energy'

(E_{miss})[4]. The 2D spectral function distributions for both carbon and oxygen are shown in figure 5.6. There are 12 parameters in total to modify the shape of the spectral function: 5 for carbon and 7 for oxygen. These can modify both the mean-field (MF) region of the spectral function in which the shells are located, as well as the short-range correlations (SRC) contribution, which accounts for pairs of correlated nucleons with momentum higher than the Fermi momentum.

- **Pauli blocking** – when neutrinos interact with nucleons within the nucleus, it transfers energy and momentum to the nucleon with which it interacts. The struck nucleon may then transition to a higher energy state, but as nucleons are fermions, these states may already be occupied, rendering them inaccessible. This phenomenon is known as Pauli blocking. Four parameters are included to modify the Fermi surface, which is a Fermi gas-inspired approach to modelling the effect of Pauli blocking. These parameters are split by neutrino or antineutrino and target nucleus (carbon or oxygen).

- **Optical potential** – as the spectral function model is built on top of the plane wave impulse approximation (PWIA), parameters are included to account for FSI effects that distort the outgoing wave function. This effect is most prominent at low energy and momentum transfer (q_0 and q_3).

- **Binding energy** – during a CCQE interaction, struck nucleons are liberated from the nuclear potential in which they sit. The energy required to do this is referred to as the binding energy. Accurately describing the binding energy is important for oscillation analyses as it directly impacts the reconstructed neutrino energy. The correction due to binding energy is applied directly to an event's reconstructed energy and is calculated as

$$(\Delta E_{\text{rmv}})_{\nu,T} = \delta_{\nu,T} + \alpha(mq_3 + c) \,, \tag{5.6}$$

[4]Though used interchangeably, there is a subtle difference between the two. Removal energy is the physical quantity related to the nuclear ground state, while missing energy is the physical observable, which is not identical to removal energy due to the effects of FSI.

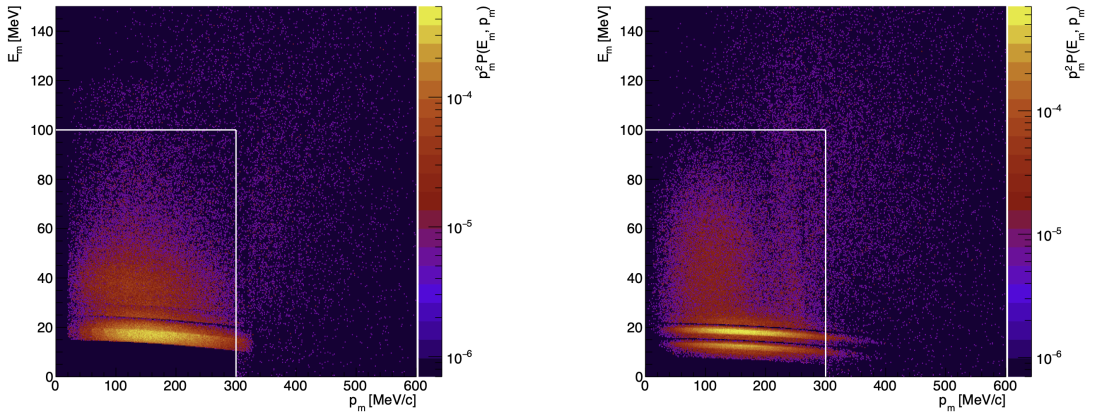

Figure 5.6: The 2D spectral function for carbon (left) and oxygen (right) in NEUT. The shell-like structure of the nucleus can be observed in the dark regions indicating a higher probability of finding a nucleon. The white lines indicate the separation between the mean-field ($E_\mathrm{m} < 100$ MeV & $p_\mathrm{m} < 300$ MeV) and short-range correlations ($E_\mathrm{m} > 100$ MeV & $p_\mathrm{m} > 300$ MeV) regions. Figure from [120].

where $(\Delta E_\mathrm{rmv})_{\nu,\mathrm{T}}$ is the binding energy correction for neutrinos or antineutrinos on target nucleus T (carbon or oxygen), $\delta_{\nu,\mathrm{T}}$ is the value of one of the four binding energy parameters, and m and c are constants derived from a fit to external data [120]. α controls the strength of the q_3-dependent part of the binding energy correction. Along with Coulomb corrections, binding energy corrections may cause events to migrate between analysis bins.

2p2h/Multi-nucleon Interactions

- **Normalisation** – two normalisation parameters modify the 2p2h cross section separately for neutrinos and antineutrinos. An additional normalisation parameter models the uncertainty on the extrapolation of carbon to oxygen nuclei.

- **Pair fraction** – 2p2h interactions can involve either nn or pn pairs, and a dial is implemented to modify the ratio of pn to nn pairs. This dial was motivated by the addition of new proton-tagged samples at the near detector, which may bring sensitivity to the ratio of nn to pn pairs.

- **Shape** – four dials separated by nucleon pair type and neutrino or antineutrino interactions alter the shape of the 2p2h cross section by modifying the ratio of events between two regions of $q_0 - q_3$ phase space. This is motivated by theoretical uncertainties relating to the Valencia model [88].

- **Energy dependence** – energy-dependent parameters are added to account for the shape differences between different 2p2h models. There are four parameters in total, one for each low/high (below or above 600 MeV) and neutrino/antineutrino combination.

Resonant Interactions

- **Axial mass** – analogously to CCQE interactions, $M_{\mathrm{A}}^{\mathrm{RES}}$ is the axial mass for resonant interactions. C_{A}^{5} is the normalisation of the axial form factor.

- **Non-resonant background** – two dials control the uncertainty due to non-resonant backgrounds to the CCRES cross section. The low p_π parameter models the uncertainty due to low-momentum pions below Cherenkov threshold at SK.

- **RS Δ decay** – this parameter interpolates between two different model predictions for the outgoing pion and nucleon kinematics. Lepton kinematics are unaffected.

- **Neutral pion production** – motivated by photon-tagged samples at the near detector, two normalisation parameters were introduced to model π^0 production in resonant interactions.

- **Binding energy** – four parameters are implemented to model binding energy for resonant interactions on carbon or oxygen and for neutrino or antineutrino interactions.

Final State Interactions

- **FSI dials** – six parameters modify the probabilities of different pion-FSI processes occuring, examples of which include charge exchange and absorption. A semi-classical intranuclear cascade model is used to describe pion FSI, tuned to $\pi - A$ scattering data [123]. A parameter to model nucleon FSI is also included.

Miscellaneous

- **DIS** – four parameters model multi-pion production, including the Bodek-Yang (BY) parameterisation [93] and pion multiplicity. There is also BY correction dial for DIS events, and two normalisation parameters for DIS neutrino and antineutrino events. Lastly, a parameter is implemented to model rarer interactions such as CC1K, CC1γ and CC1η.

- **Coherent** – there are two normalisation parameters for coherent interactions on oxygen and carbon. Coherent interactions are when a neutrino scatters on the nucleus as a whole rather than individual nucleons.

- **Neutral current** – three normalisation parameters model the uncertainty of NC events at both the near and far detectors, with a specific dial to describe NC1γ events, which are the dominant background to electron neutrino appearance measurements at SK.

- **Coulomb corrections** – the momentum of negatively (positively) charged leptons produced in CC interactions will be increased (decreased) due to the electrostatic repulsion (attraction) between the charged lepton and the remnant nucleus. This momentum shift is applied on an event-by-event basis to MC events and varies depending on whether the neutrino interacts with a carbon or oxygen nucleus.

- **CC normalisation** – coulomb interactions involving the outgoing lepton and nucleus can modify the total CC cross section, therefore two normalisation

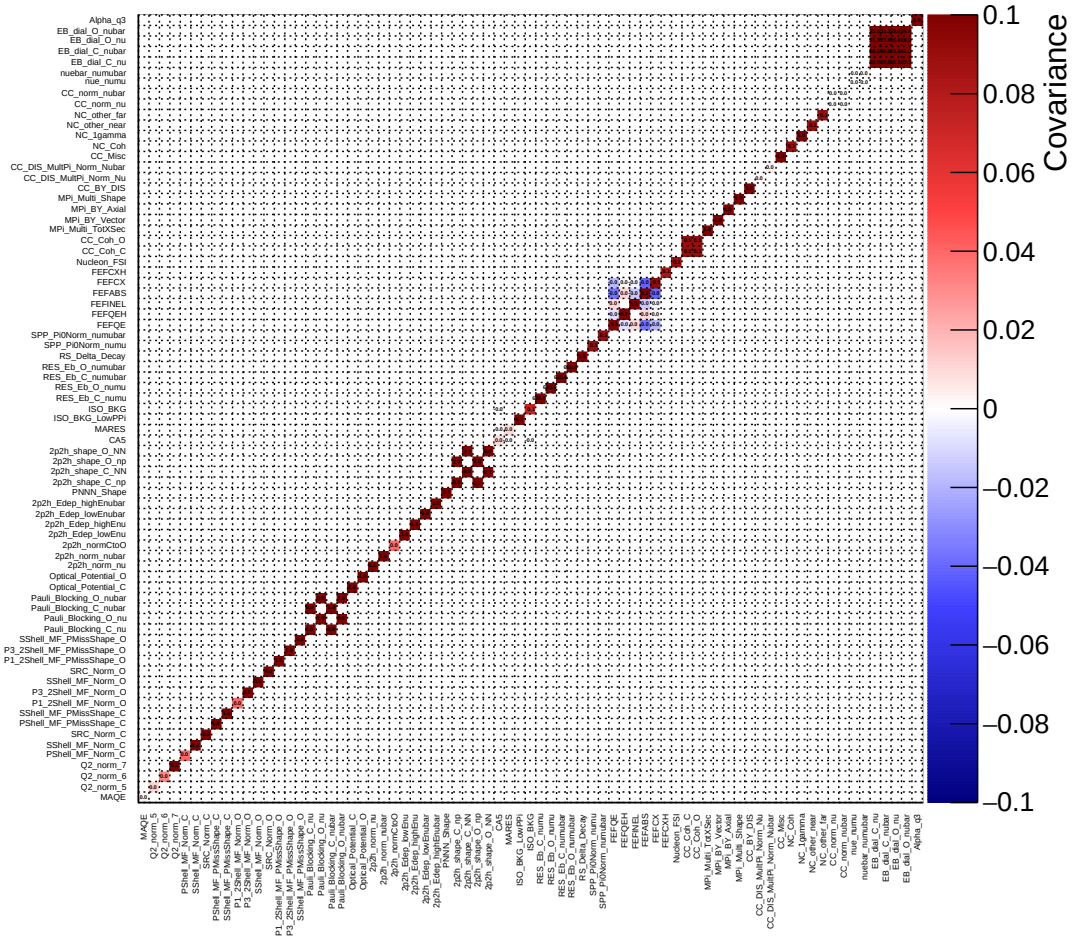

Figure 5.7: The cross-section prior uncertainty covariance matrix used in the oscillation analysis.

dials are implemented to cover this uncertainty for CC events in the region of 300 – 600 MeV.

- $\nu_e/\bar{\nu}_e$ **cross section** – two normalisation parameters model the uncertaintiy for the difference between ν_e ($\bar{\nu}_e$) and ν_μ ($\bar{\nu}_\mu$) cross sections. This is important as only ν_μ measurements at ND280 are used to predict the expected event rate at SK, which includes ν_e interactions.

5.3.3 Near Detector Systematics

ND280 detector systematics account for the uncertainties introduced by, for example, the detection efficiency of each sub-detector, kinematic reconstruc-

Parameter	Validity Range	Generated Value	Prior Value	Prior Error	Type	Unit
M_A^{QE}	all	1.21	1.03	0.06	shape	GeV
Q^2 norm 0.25-0.50 GeV^2	all	1	1	0.11	norm.	—
Q^2 norm 0.50-1.00 GeV^2	all	1	1	0.18	norm.	—
Q^2 norm $>$ 1.00 GeV^2	all	1	1	0.4	norm.	—
PShell MF Norm C	all	0	0	0.2	shape	—
SShell MF Norm C	all	0	0	0.35	shape	—
SRC Norm C	all	1	1	2	shape	—
PShell MF PMiss C	all	0	0	1	shape	—
SShell MF PMiss C	all	0	0	1	shape	—
P1 2Shell MF Norm O	all	0	0	0.2	shape	—
P3 2Shell MF Norm O	all	0	0	0.45	shape	—
SShell MF Norm O	all	0	0	0.75	shape	—
SRC Norm O	all	1	1	2	shape	—
P1 2Shell MF PMiss O	all	0	0	1	shape	—
P3 2Shell MF PMiss O	all	0	0	1	shape	—
SShell MF PMiss O	all	0	0	1	shape	—
Pauli Blocking C ν	all	0	0	1	shape	—
Pauli Blocking O ν	all	0	0	1	shape	—
Pauli Blocking C $\bar{\nu}$	all	0	0	1	shape	—
Pauli Blocking O $\bar{\nu}$	all	0	0	1	shape	—
Optical Potential C	0–1	0	0	1	shape	—
Optical Potential O	0–1	0	0	1	shape	—
E_b C ν	-10–15	0	2	6	function	MeV
E_b C $\bar{\nu}$	-10–15	0	0	6	function	MeV
E_b O ν	-10–15	0	4	6	function	MeV
E_b O $\bar{\nu}$	-10–15	0	0	6	function	MeV
α q3	0–1	0	0	1	function	—
2p2h norm ν	>0	1	1	1	norm.	—
2p2h norm $\bar{\nu}$	>0	1	1	1	norm.	—
2p2h norm CtoO	>0	1	1	0.2	norm.	—
2p2h Edep low E_ν	0–1	1	1	1	shape	—
2p2h Edep high E_ν	0–1	1	1	1	shape	—
2p2h Edep low $E_{\bar{\nu}}$	0–1	1	1	1	shape	—
2p2h Edep high $E_{\bar{\nu}}$	0–1	1	1	1	shape	—
PN-NN Shape	-1–1	0	0	0.33	shape	—
2p2h shape C np	-1–1	0	0	1	shape	—
2p2h shape C NN	-1–1	0	0	1	shape	—
2p2h shape O np	-1–1	0	0	1	shape	—
2p2h shape O NN	-1–1	0	0	1	shape	—
C_A^5	all	1.01	0.96	0.15	shape	—
M_A^{RES}	all	0.95	1.07	0.15	shape	—
I-$\frac{1}{2}$ bkg. low p_π	all	1.3	0.96	1.3	shape	—
I-$\frac{1}{2}$ bkg.	all	1.3	0.96	0.27	shape	—
RES Eb C ν_μ	0–25	0	25	25	shape	—
RES Eb 0 ν_μ	0–25	0	25	25	shape	—
RES Eb C $\bar{\nu_\mu}$	0–25	0	25	25	shape	—
RES Eb O $\bar{\nu_\mu}$	0–25	0	25	25	shape	—
RS Delta Decay	0–1	1	1	1	shape	—
SPP Pi0 numu	all	1	1	0.3	norm	—
SPP Pi0 numubar	all	1	1	0.3	norm	—
π-FSI QE low E	all	1.069	1.069	0.313	shape	—
π-FSI QE high E	all	1.824	1.824	0.859	shape	—
π-FSI Hadron production	all	1.002	1.002	1.101	shape	—
π-FSI Absoprtion	all	1.404	1.404	0.432	shape	—
π-FSI Charge Exchange low E	all	0.697	0.697	0.305	shape	—
π-FSI Charge Exchange high E	all	1.8	1.8	0.288	shape	—
Nucleon FSI	-1–1	0	0	0.3	shape	—
MPi Multi TotXsec	all	0	0	1	shape	—
MPi BY Vector	all	0	0	1	shape	—
MPi BY Axial	all	0	0	1	shape	—
MPi Multiplicity shape	all	0	0	1	shape	—
CC BY DIS	all	0	0	1	shape	—
CC DIS MultiPi ν	>0	1	1	0.035	norm	—
CC DIS MultiPi $\bar{\nu}$	>0	1	1	0.065	norm	—
CC Misc.	>0	1	1	1	norm.	—
CC Coh. C	>0	1	1	0.3	norm.	—
CC Coh. O	>0	1	1	0.3	norm.	—
NC Coh.	>0	1	1	0.3	norm.	—
NC 1γ	>0	1	1	1	norm.	—
NC other near	>0	1	1	0.3	norm.	—
NC other far	>0	1	1	0.3	norm.	—
CC norm ν	>0	1	1	0.02	norm.	—
CC norm $\bar{\nu}$	>0	1	1	0.01	norm.	—
ν_e ν_μ	>0	1	1	0.0282843	norm.	—
$\bar{\nu}_e$ $\bar{\nu}_\mu$	>0	1	1	0.0282843	norm.	—

Table 5.4: A summary of the cross-section parameters used in this analysis.

tion and magnetic field distortions in the TPCs. ND280 detector systematics are included in the fit via a covariance matrix, where each row and column corresponds to a specific analysis bin for each data sample. The matrix is calculated by simultaneously varying all parameters across 2000 simulations, which results in an event distribution for each analysis bin. Initially, there are 4952 bins/parameters, which would be computationally inefficient to include in a full oscillation analysis fit. Therefore, neighbouring bins with similar distributions are merged, reducing the size of the covariance matrix to 552. Thus, there are 552 bin-content normalisation parameters in that oscillation fit that model the ND280 systematic. Detailed information on the ND280 detector systematics can be found in [110, 111].

5.3.4 Far Detector Systematics

SK detector systematics model the uncertainty due to the mis-reconstruction of events at the far detector. To calculate the detector systematics, SK's large atmospheric neutrino dataset is utilised and compared to MC predictions using a Markov chain Monte Carlo. SK detector uncertainties enter the oscillation fit in the form of a covariance matrix, which contains 57 bin-content normalisation parameters, with each parameter representing a reconstructed energy bin for a specific far-detector topology. A momentum-scale uncertainty of 2.13% is also included in the covariance matrix. The SK detector matrix is provided by the T2K-SK working group, and detailed information on the procedure for calculating SK detector uncertainties can be found in [124].

Uncertainties due to pion secondary interactions (SI) and photo-nuclear (PN) effects are also included in the total SK detector covariance matrix. The uncertainties due to SI+PN are calculated by measuring the change in the predicted events in each bin when considering different amounts of SI and PN. The uncertainty due to PN effects is only applied to 1Re samples as they may cause π^0s to be mid-identified as ν_e appearance signal events. A 100% uncertainty is assumed on the absorption of photons produced from π^0 decays. The procedure of calculating

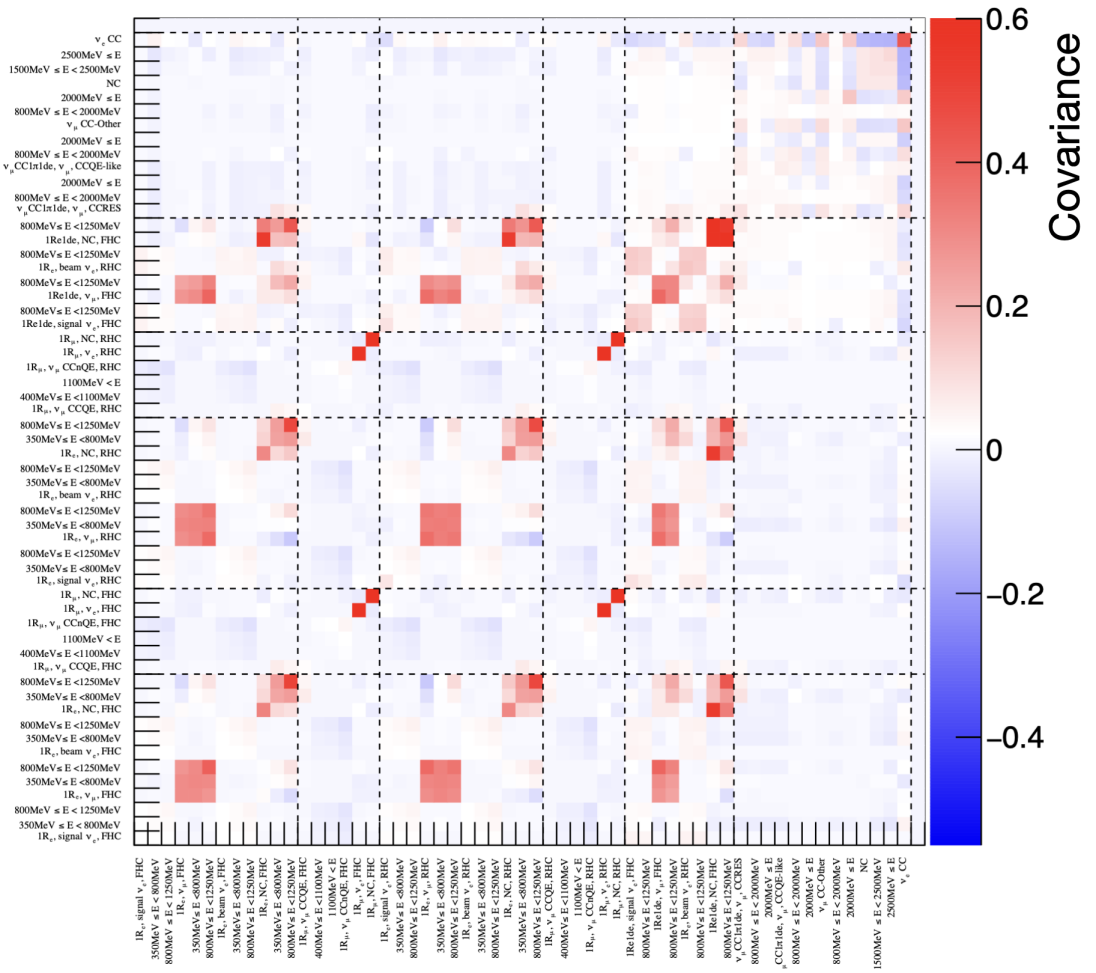

Figure 5.8: The full SK detector covariance matrix used in the oscillation analysis. The dashed lines separate parameters for different SK samples. The momentum-scale parameter is appended to this matrix and has a value of 2.13%.

the SI+PN error matrix is fully described in [117]. Further, it's important to note that pion FSI errors are absent from the SI+PN matrix. This is because parameters exist within the cross-section model that specifically address this uncertainty. These parameters are constrained at ND280 and propagated to SK.

The full SK detector matrix, including uncertainties from SI+PN effects, is shown in figure 5.8.

5.4 Far Detector Monte Carlo Predictions

The raw SK Monte Carlo production files used in this analysis are provided by the T2K-SK group. To calculate the predicted event rate and spectra at the far detector,

several weights need to be applied to the MC. These weights are as follows:

- **POT** – weights are applied to scale the MC production to the amount of collected data. This weight is applied before the fit and is provided by the T2K-SK working group.
- **Flux** – weights are applied at the pre-fit stage to tune the MC to the flux prediction [118]. These weights are provided by the beam group in histograms binned in true neutrino energy. Flux weights can also be applied event-by-event during the fit via the flux covariance matrix.
- **Cross section** – each event receives a weight related to the cross-section model. Cross-section weights are also applied during the fit via the cross-section covariance matrix.
- **SK detector** – events receive weights related to SK detector systematics. These can vary during the fit and enter through the SK detector covariance matrix.
- **Oscillation** – oscillation weights are applied on an event-by-event basis to generate the predicted spectra at SK.

By applying all of the above weights it is then possible to calculate the predicted oscillated and unoscillated pre-fit spectra at the far detector. During the re-weighting of the MC, the cross-section and flux parameters take their best-fit values from a standalone near-detector fit performed by *Beam And ND280 Flux extrapolation task Force* (BANFF) group. This is an analysis choice made to provide consistency between the multiple oscillation fitters within T2K. Furthermore, when calculating the pre-fit spectra at SK, a set of oscillation parameters must be chosen to calculate oscillation weights. This assumed set of parameters is known as the 'Asimov A22' set and is based on T2K's previous best-fit values for the oscillation parameters and further inputs from the Particle Data Group [27]. The Asimov A22 set is given in table 5.5.

Osc. parameter	Asimov A22 value
$\sin^2\theta_{12}$	0.307
$\sin^2\theta_{23}$	0.561
$\sin^2\theta_{13}$	0.0220
Δm^2_{12}	7.53×10^{-5}
Δm^2_{23}	2.494×10^{-3}
δ_{CP}	-1.601

Table 5.5: The Asimov A22 oscillation parameter set.

The unoscillated and oscillated event rates and far-detector spectra are shown in table 5.6 and figure 5.9 respectively. Additionally, figure 5.10 displays each predicted μ-like far-detector sample's oscillated spectra broken down by interaction mode, and figure 5.11 shows the equivalent for the e-like samples.

SK sample	Unosc. event rate	Osc. event rate	Data
FHC 1Rμ	1670.14	378.73	318
RHC 1Rμ	465.10	144.75	137
FHC 1Re	20.43	102.54	94
RHC 1Re	6.45	17.33	16
FHC ν_μCC1π	245.82	116.49	135
FHC 1Re1de	3.15	10.02	14

Table 5.6: Predicted unoscillated and oscillated event rates for each SK sample compared with the number of data events.

5.4.1 Systematic Errors on SK Prediction

The post-fit systematic uncertainty introduced on the predictions at SK for the μ-like and e-like samples can be seen in tables 5.7 and 5.8 respectively. The distribution is computed by randomly sampling steps from a Markov chain and reweighting the nominal event prediction based on the parameter values at the chosen step. The uncertainty is then calculated to be the RMS of the event rate distribution. Uncertainties introduced from each part of the model are calculated by varying individual subsets of parameters while fixing other parameters to

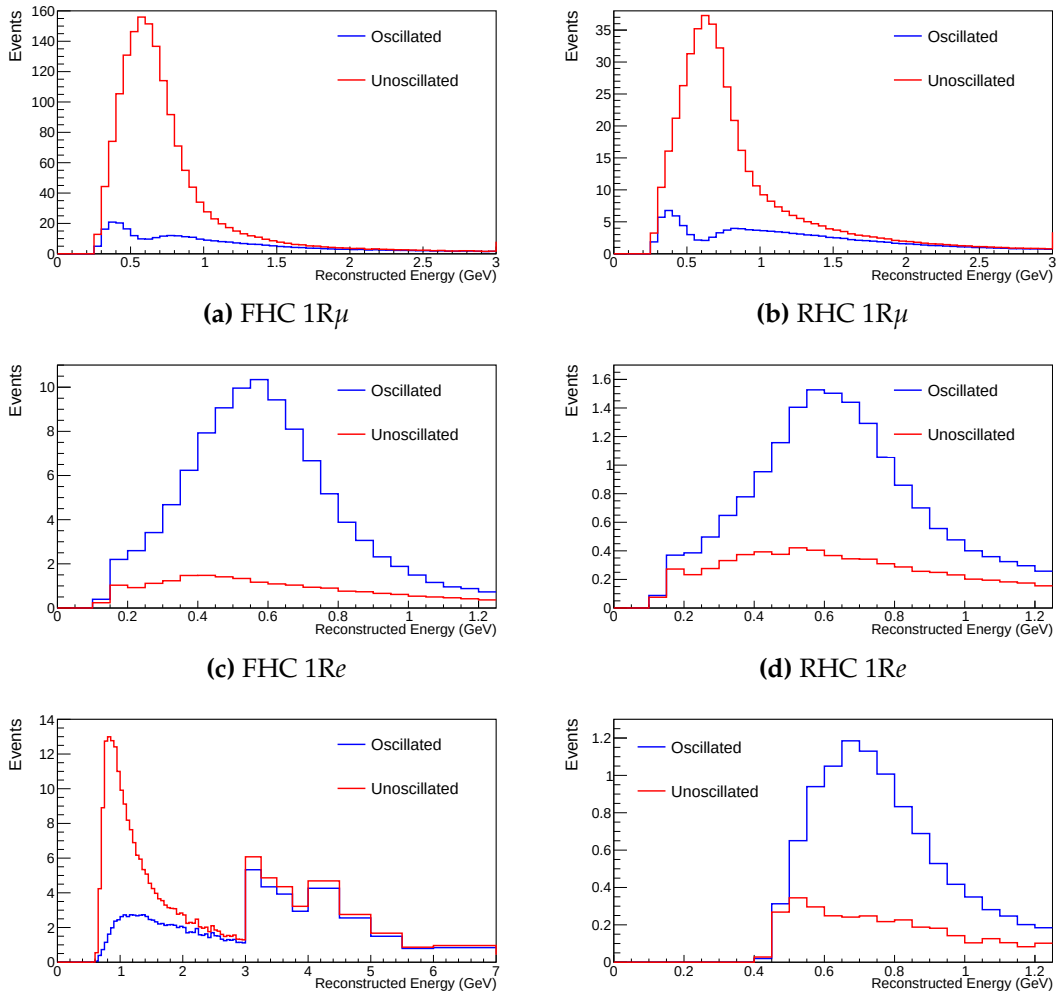

(a) FHC 1Rμ **(b)** RHC 1Rμ

(c) FHC 1Re **(d)** RHC 1Re

(e) FHC ν_μCC1π **(f)** FHC 1Re1de

Figure 5.9: The oscillated (blue) and unoscillated (red) predicted spectra for each SK sample binned in reconstructed neutrino energy.

their prior values. When performing this procedure, correlations between the varied and fixed parameters are removed. Therefore it is not expected that the sum of the individual components in quadrature will be equal to the total error. Parameters that are unconstrained at the near detector are given separately, which are the energy-dependent 2p2h parameters, the non-resonant low-momentum pion background parameter and the neutral-current far-detector parameters. The total systematic uncertainty is given with and without oscillations. It can be seen that the oscillation parameters introduce a significant uncertainty on the expected rate of the e-like samples.

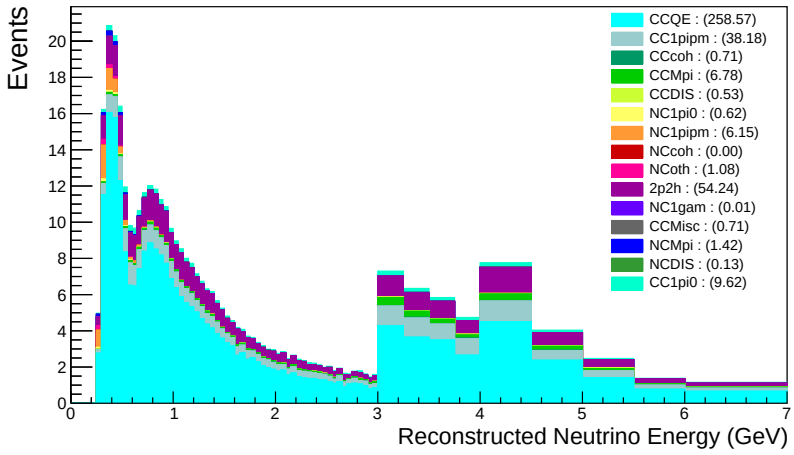

(a) FHC 1Rμ

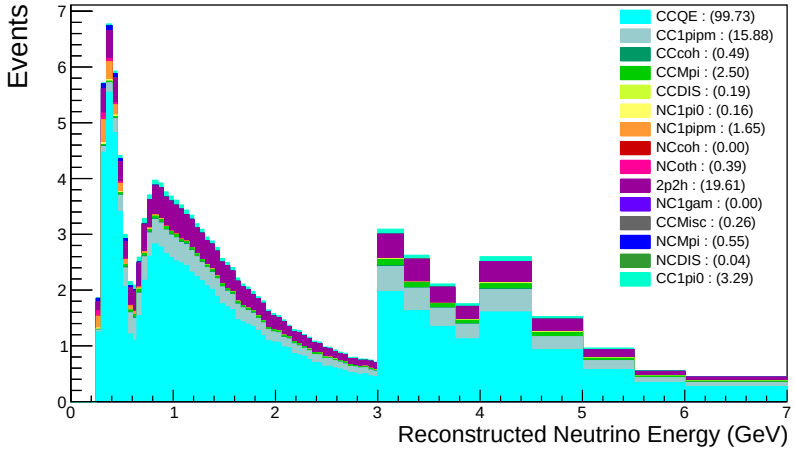

(b) RHC 1Rμ

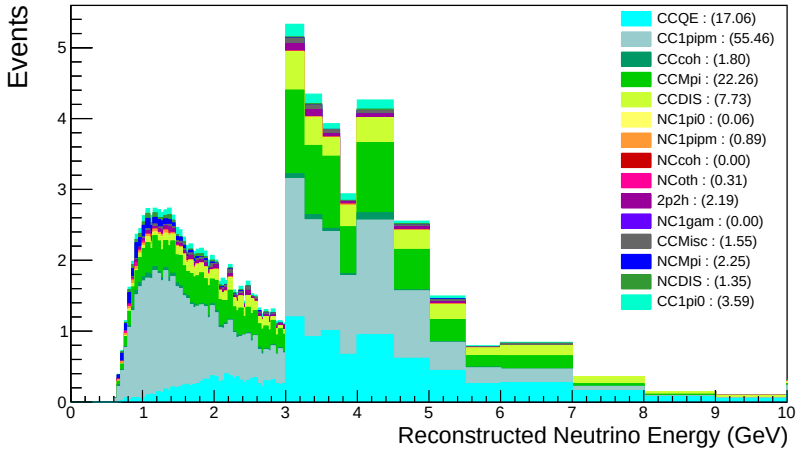

(c) FHC ν_μCC1π

Figure 5.10: Predicted oscillated spectra for the μ-like far-detector samples broken down by interaction mode.

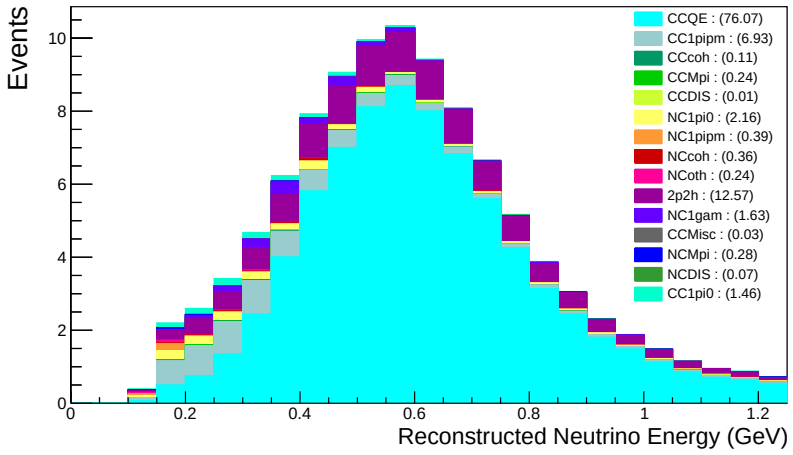

(a) FHC 1Re

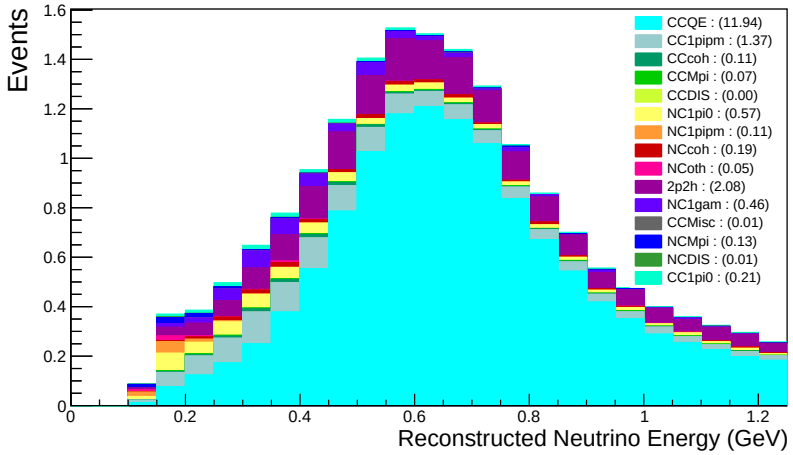

(b) RHC 1Re

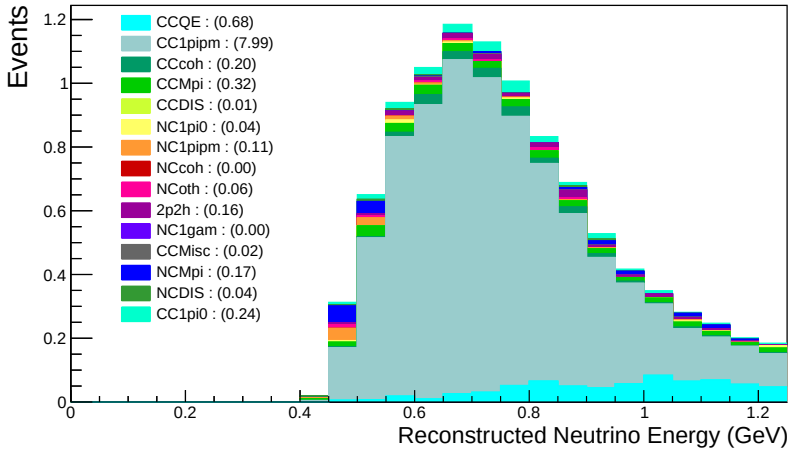

(c) FHC 1Re1de

Figure 5.11: Predicted oscillated spectra for the e-like far-detector samples broken down by interaction mode.

Error source	FHC 1Rμ	RHC 1Rμ	FHC ν_μCC1π
Flux	2.45%	2.81%	2.65%
Cross section	3.34%	4.53%	3.29%
Cross section (ND const.)	2.45%	2.35%	2.14%
2p2h Edep	0.46%	0.47%	0.06%
IsoBkg Low-p$_\pi$	0.45%	3.20%	1.28%
$\sigma(\nu_e)$, $\sigma(\bar{\nu}_e)$	0.00%	0.00%	0.00%
NC γ	0.00%	0.00%	0.00%
NC Other SK	0.21%	0.20%	1.00%
Flux $\times$ cross-section	2.40%	3.77%	2.57%
Flux $\times$ cross-section (ND const.)	2.45%	2.34%	2.14%
SK det	1.84%	1.59%	3.61%
Total Syst.	2.79%	3.84%	4.14%
Total Inc. Osc.	3.02%	3.85%	4.27%

Table 5.7: Systematic error contributions on the event rates for the SK μ-like samples.

Error source	FHC 1Re	RHC 1Re	FHC 1Re1de
Flux	2.70%	3.00%	2.73%
Cross section	4.44%	5.08%	4.58%
Cross section (ND const.)	3.75%	3.55%	4.01%
2p2h Edep	0.20%	0.22%	0.03%
IsoBkg Low-p$_\pi$	0.08%	2.79%	0.08%
$\sigma(\nu_e)$, $\sigma(\bar{\nu}_e)$	2.56%	1.48%	2.58%
NC γ	1.24%	2.08%	0.00%
NC Other SK	0.17%	0.34%	0.77%
Flux $\times$ cross-section	3.73%	4.50%	4.04%
Flux $\times$ cross-section (ND const.)	3.75%	3.55%	4.01%
SK det	2.97%	3.52%	11.38%
Total Syst.	4.81%	5.80%	12.09%
Total Inc. Osc.	9.04%	14.60%	13.72%

Table 5.8: Systematic error contributions on the event rates for the SK e-like samples.

Sample	MaCh3	PTheta	% Difference
FHC 1Rμ	378.725	378.693	0.01
RHC 1Rμ	144.749	144.913	0.11
FHC ν_μCC1π	116.486	116.617	0.11
FHC 1Re	102.543	102.612	0.07
RHC 1Re	17.330	17.331	0.00
FHC 1Re1de	10.024	10.010	0.14

Table 5.9: A comparison of the predicted oscillated event rate for each SK sample between MaCh3 and PTheta.

5.5 Fitter Validations and Asimov Fits

Several validation tests are performed before analysing data fits to ensure the systematic parameters and associated fitter machinery have been implemented as intended. MaCh3 compares its results with PTheta [67], the other primary oscillation parameter fitter on T2K. MaCh3 and PTheta differ in many ways, including choice of sample binning, treatment of the near detector, overall statistical approach and primary results. Therefore, a comparison of our results (when appropriate) at each stage of the analysis is a useful tool for ensuring each fitter is behaving as expected.

5.5.1 Pre-fit Validations

Before running any fits, the two primary methods of validating the fitter are event rates and systematic variation comparisons. Table 5.9 shows a comparison of the predicted far-detector event rates between MaCh3 and PTheta, with both fitters using the BANFF near-detector fit for the cross-section and flux parameters. The agreement between MaCh3 and PTheta is better than 0.14%.

The effect of varying individual systematic parameters is studied by looking at systematic variations. All far-detector parameters are varied by $\pm1\sigma$ and $\pm3\sigma$ (or other specified points where appropriate) separately to see the effect on each SK selection. Figure 5.12 shows an example of such a comparison between MaCh3 and PTheta for the $M_{\mathrm{A}}^{\mathrm{QE}}$ and $M_{\mathrm{A}}^{\mathrm{RES}}$ cross-section parameters.

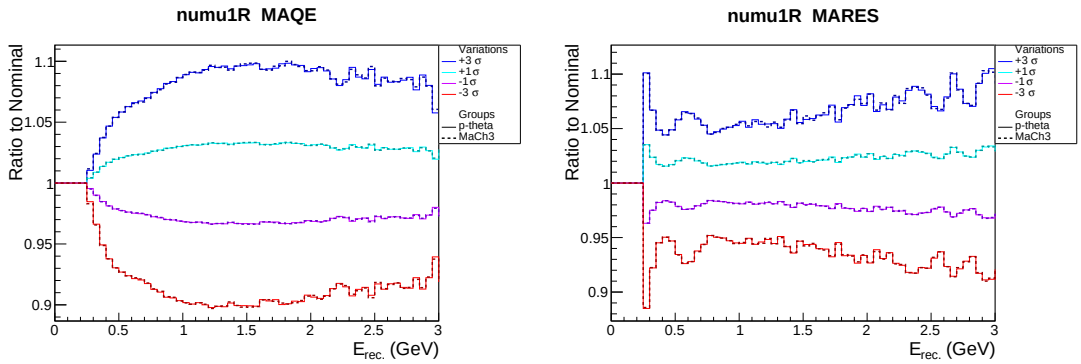

Figure 5.12: A comparison between MaCh3 and PTheta of the ratio of the resulting spectra when varying $M_{\mathrm{A}}^{\mathrm{QE}}$ (left) and $M_{\mathrm{A}}^{\mathrm{RES}}$ (right) relative to the nominal spectra for the FHC 1Rμ sample.

Additionally, a scan was conducted to examine the behaviour of the log-likelihood (LLH) function around key values of the oscillation parameters $\sin^2\theta_{23}$, $\sin^2\theta_{13}$, Δm^2_{32}, and δ_{CP}. As the negative of the LLH function is minimised during a data fit, valuable insights can be gleaned when analysing the LLH function around the expected best-fit points. To perform the scan, first, an Asimov fake far-detector dataset is constructed by setting the oscillation parameters to their Asimov A22 values and fixing the systematic parameters at their prior values. The content of every bin in the Asimov dataset is set exactly equal to the PMNS prediction, with no statistical fluctuations. In other words, the far-detector MC prediction *is* the 'data'. Therefore, if the output of the fit is not what was input, this indicates a potential problem with the fitter and cannot be attributed to statistical fluctuations. To perform the LLH scan, one must iterate over bins in the 2D oscillation parameter space, with the oscillation parameters in the MC set to the central values of each bin. The LLH function is then computed for this Asimov 'data' and MC combination and the result is plotted as 2D histograms in oscillation parameter space.

The outcomes of each LLH scan are shown in figures 5.13 and 5.14 for the parameter spaces of $\sin^2\theta_{13} - \delta_{\mathrm{CP}}$ and $\sin^2\theta_{23} - \Delta m^2_{32}$, respectively. In both figures, a red cross signifies the input oscillation parameter values, while a white triangle marks the minimum bin, denoted as 'MaCh3 best fit'. Both figures show

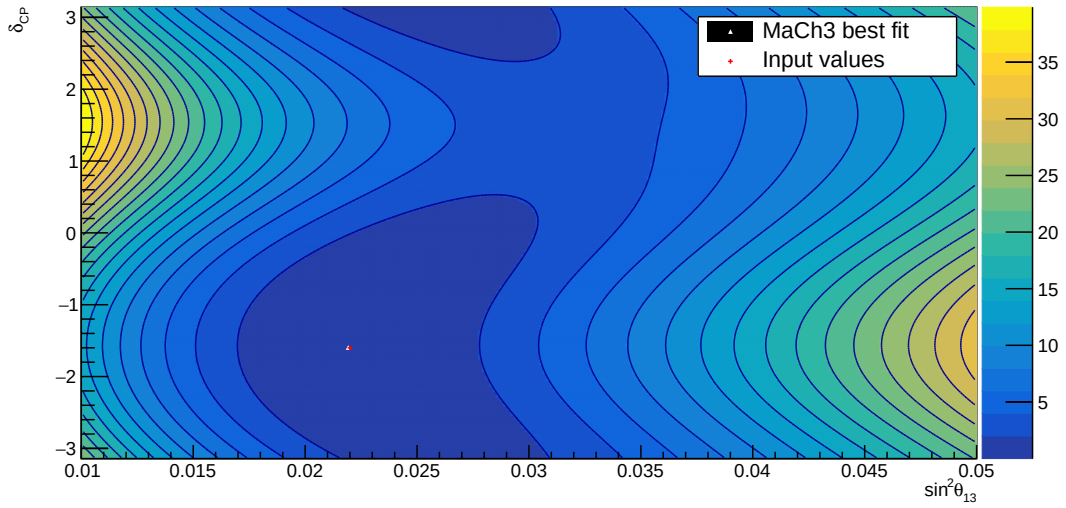

Figure 5.13: Asimov LLH scan in $\sin^2\theta_{13} - \delta_{CP}$. The point of the minimum LLH is the same as the input values, as expected.

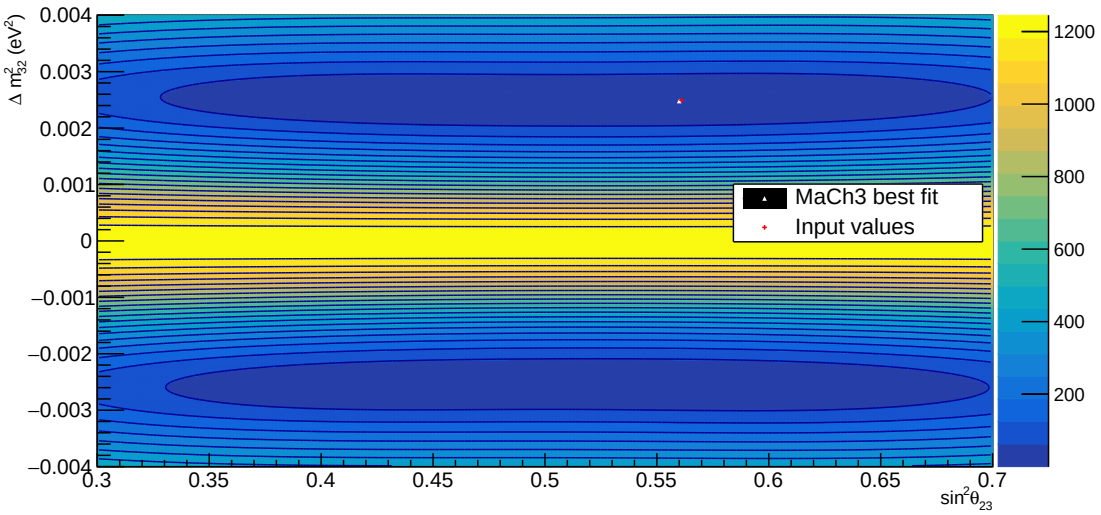

Figure 5.14: Asimov LLH scan in $\sin^2\theta_{23} - \Delta m^2_{32}$. The point of the minimum LLH is the same as the input values, as expected.

the input and minimum LLH points are positioned identically, indicating the correct identification of the best-fit point by the likelihood calculation. This suggests there is no bias in the oscillation parameters in the fit.

5.5.2 Asimov Fits

The main purpose of performing Asimov fits is to test a fitter's robustness and sensitivity. Both MaCh3 and PTheta construct the far-detector Asimov data using cross-section and flux parameter best-fit values from the BANFF near-detector fit. However, each fitter's handling of the near detector does differ. In a PTheta Asimov fit, the near-detector constraint *is* the BANFF constraint. However, MaCh3 performs a joint fit to ND280 data and SK Asimov data, where the MaCh3 near-detector machinery fits the near-detector parameters. This may lead to apparent biases if the MaCh3 ND-only fit and BANFF do not predict the same far-detector spectra. The Asimov fits presented in this section were performed with the oscillation parameters set to their Asimov A22 values.

In each MaCh3-PTheta comparison, two different PTheta results are shown. Contours labelled 'PTheta' are PTheta's nominal result, while those labelled 'PTheta, MaCh3-like' are results from a PTheta fit using identical SK sample binning to MaCh3, and applying constraints from a MaCh3 near-detector fit.

Figure 5.15 shows 2D contour comparisons between MaCh3 and PTheta Asimov fits for both normal and inverted ordering, without applying the reactor constraint. When comparing the disappearance contours, MaCh3 finds a more maximal constraint in $\sin^2\theta_{23}$ when compared to PTheta, but this difference is resolved when PTheta performs a 'MaCh3-like' fit. The appearance results are in good agreement, with small differences observed at large values of $\sin^2\theta_{13}$, which are again resolved when PTheta performs a 'MaCh3-like' fit.

Figure 5.16 shows a comparison of the 1D $\Delta\chi^2$ distribution for $\sin^2\theta_{23}$. Here it can be seen that the MaCh3 and 'PTheta, MaCh3-like' fits deviate away from the best-fit point found by the nominal PTheta fit, and also do not reach a local minimum at the Asimov point of $\sin^2\theta_{23} = 0.561$. This is due to MaCh3 fitting BANFF-predicted far-detector spectra with a MaCh3 ND-only constraint. As anticipated, if the BANFF and MaCh3 near-detector fitters do not predict the same far-detector spectra, this difference will be absorbed in the far-detector side of the fit, usually by shifting the oscillation parameters. However, it is

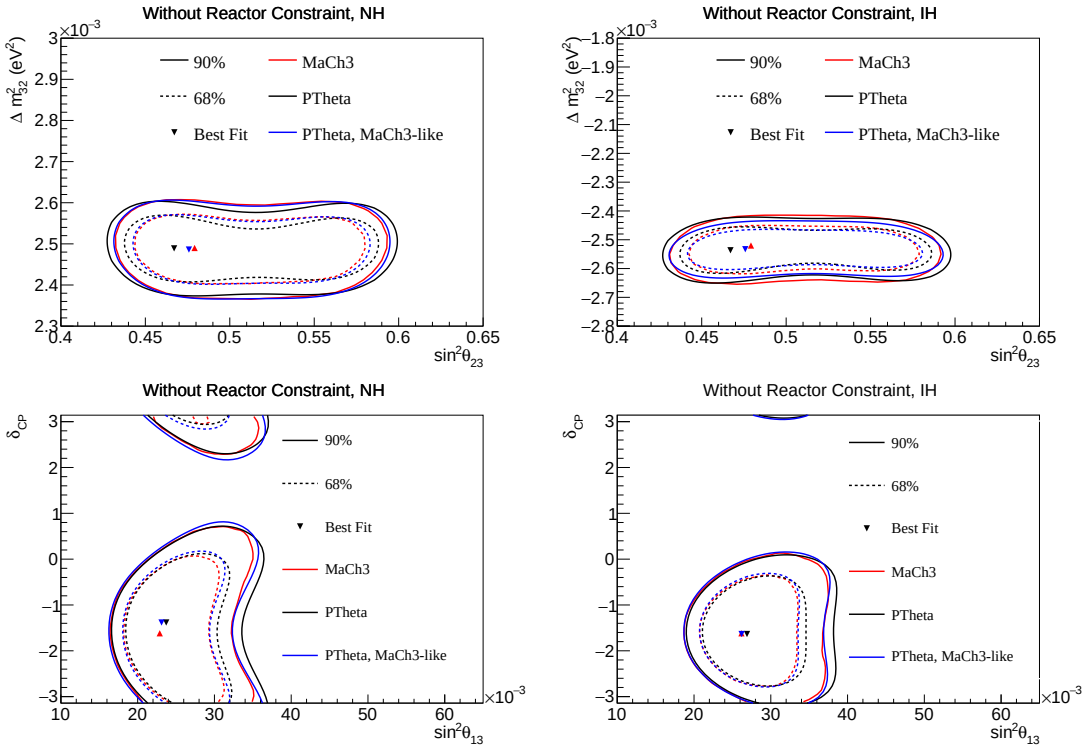

Figure 5.15: Comparison of the Asimov A22 oscillation parameter contours between MaCh3 and PTheta, without applying the reactor constraint. Disappearance and appearance results are displayed in the top and bottom rows, respectively, while normal and inverted orderings are depicted in the left and right columns.

worth highlighting that a potential weakness of the BANFF near-detector fit is that it assumes all parameters are Gaussian. This is required to propagate constraints via a covariance matrix. This assumption can be problematic as some nuisance parameters are known to be non-Gaussian, for example, due to physical boundaries in parameter space. Therefore, a MaCh3 near-detector data fit is likely to be more accurate as it does not rely on this assumption.

To be satisfied that deviations from the Asimov point seen in figure 5.16 are due to differences in the far-detector predictions, Asimov fits were performed in MaCh3 with the far-detector 'data' set to prediction made by a MaCh3 ND-only fit. This is then compared with the standard Asimov fit in figure 5.17. It can be seen that when the Asimov data is set to the MaCh3 ND's prediction, the fitter can successfully output the input Asimov point.

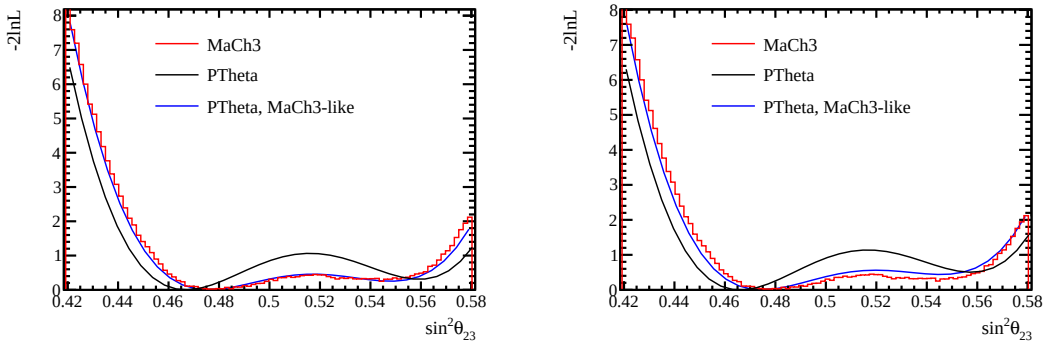

Figure 5.16: Comparison of the Asimov A22 1D $\sin^2\theta_{23}$ $\Delta\chi^2$ between MaCh3 and PTheta, without applying the reactor constraint. The Asimov A22 value for $\sin^2\theta_{23}$ is 0.561. Normal and inverted orderings are depicted in the left and right columns.

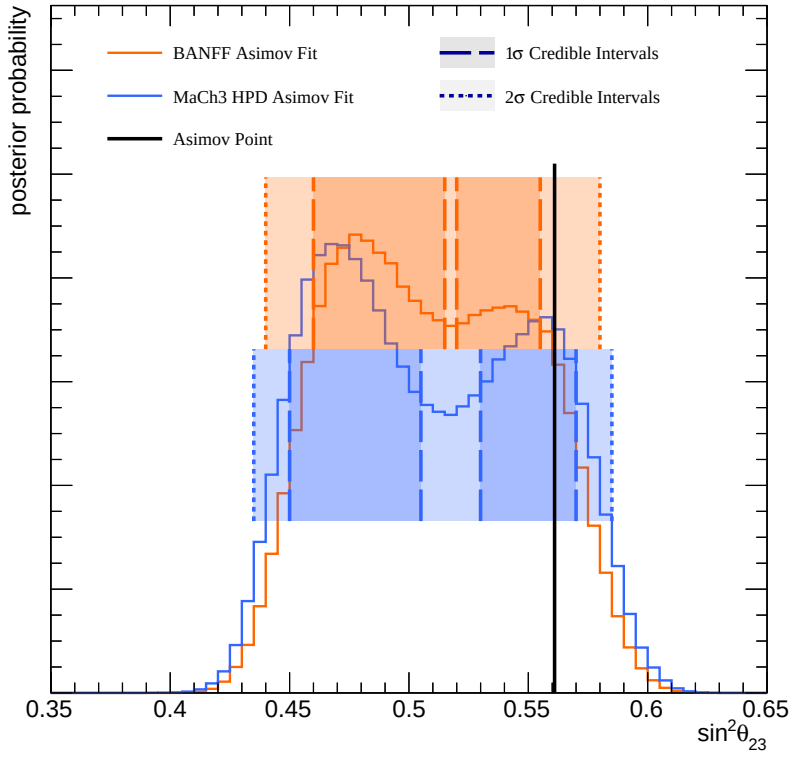

Figure 5.17: Comparing the 1D posterior distributions of $\sin^2\theta_{23}$ for Asimov A22 fits using BANFF (orange) and MaCh3 (blue) far-detector predictions.

6
Oscillation Analysis: Results

This chapter presents the results of a joint fit to ND280 and SK data using the analysis framework described in chapter 5. Two sets of results are presented: one using T2K data only (denoted 'T2K-only'), and another utilising an additional constraint on $\sin^2\theta_{13}$ from reactor neutrino experiments (denoted 'T2K + reactor' or 'T2K + RC'). Only a T2K-only fit is performed, with the resulting posterior distribution reweighted to apply the external reactor constraint from the PDG: $\sin^2\theta_{13} = 0.0220 \pm 0.0007$ [109]. The results presented in this thesis are T2K's latest and most robust oscillation result and were first presented at the Neutrino 2022 conference [125]. The analysis utilises all near and far-detector data that was available at the time and includes several analysis improvements including updated near-detector selections, a new far-detector sample, and a more sophisticated flux and cross-section model. The accumulated POT and beam power for each data run is shown in figure 6.1. All parameter constraints are calculated from a Markov chain with 188 million steps.

Goodness-of-fit tests are described in section 6.1, with constraints on the oscillation parameters and the Jarlskog invariant in sections 6.2 and 6.3. A comparison to the previous T2K result is presented in section 6.4, while alternative oscillation parameter priors are tested in section 6.5. Finally, alternative model

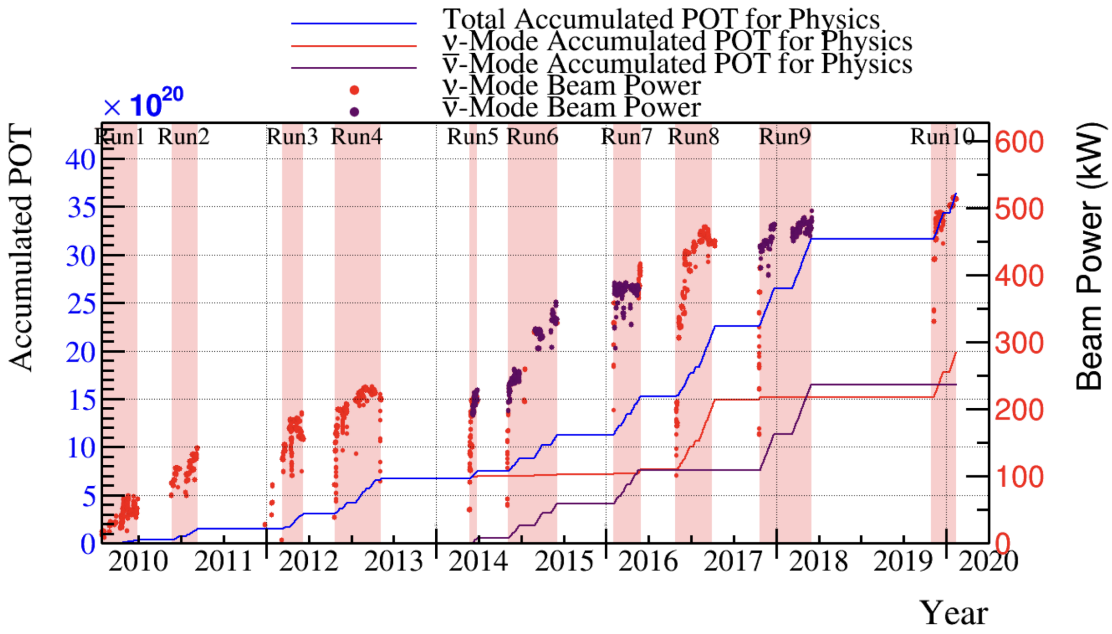

Figure 6.1: The accumulated POT, beam power and time for each data run. Whether the beam was configured to run in neutrino or antineutrino mode is also illustrated. Figure from [76].

studies are discussed in section 6.6, and a summary of the oscillation results is presented in section 6.7.

6.1 Goodness-of-fit Tests

6.1.1 Posterior Predictive Method

A useful metric to gauge how well the fit describes the data is to calculate the posterior distribution as a function of reconstructed neutrino energy for each far-detector sample. This prediction can then easily be compared to the data. This is done using the posterior predictive method, which generates a far-detector predicted spectrum as a function of reconstructed neutrino energy by sampling directly from the posterior distribution. The method is as follows:

1. Choose a suitable number of samples (or 'throws'), N to draw from the Markov chain. In this analysis, $N = 2500$.

2. For each bin in the energy spectrum, calculate a prediction for the event rate assuming a set of parameter values from each of the N throws. This

results in an event rate distribution in each bin.

3. Fit a Gaussian to the distribution in each bin. The mean of the Gaussian is the predicted event rate in that bin, and the 1σ error is calculated by taking the RMS of the distribution in each bin.

The posterior predicted spectra for each SK sample using a T2K + reactor fit are shown in figure 6.2.

6.1.2 Goodness-of-fit Metrics

Once the oscillation fit has been performed it is useful and necessary to quantify how well the fit describes the data by performing a goodness-of-fit test. This is done by calculating a posterior predictive p-value. The significance level was set to 5% prior to the analysis being performed, meaning that any model with a p-value higher than 5% is considered to provide a good fit to the data. The method to calculate the posterior predictive p-value, outlined fully in [126], is as follows[1]:

1. For each of the 2500 points sampled from the posterior, construct a far-detector fake data set by reweighting the MC according to the parameter values drawn from the Markov chain

2. Apply a Poisson fluctuation to each MC bin in the far detector fake data prediction according to its bin contents

3. Calculate the χ^2 test statistic between the Poisson fluctuated prediction and the far-detector fake data, denoted as $\chi^2(\text{fake data})$

4. Calculate the χ^2 test statistic between the observed data and the far-detector fake data, denoted as $\chi^2(\text{data})$

5. Plot the two test statistics in a 2D histogram and calculate the p-value, which will be the proportion of samples for which $\chi^2(\text{data}) < \chi^2(\text{fake data})$

[1] List adapted from [127]

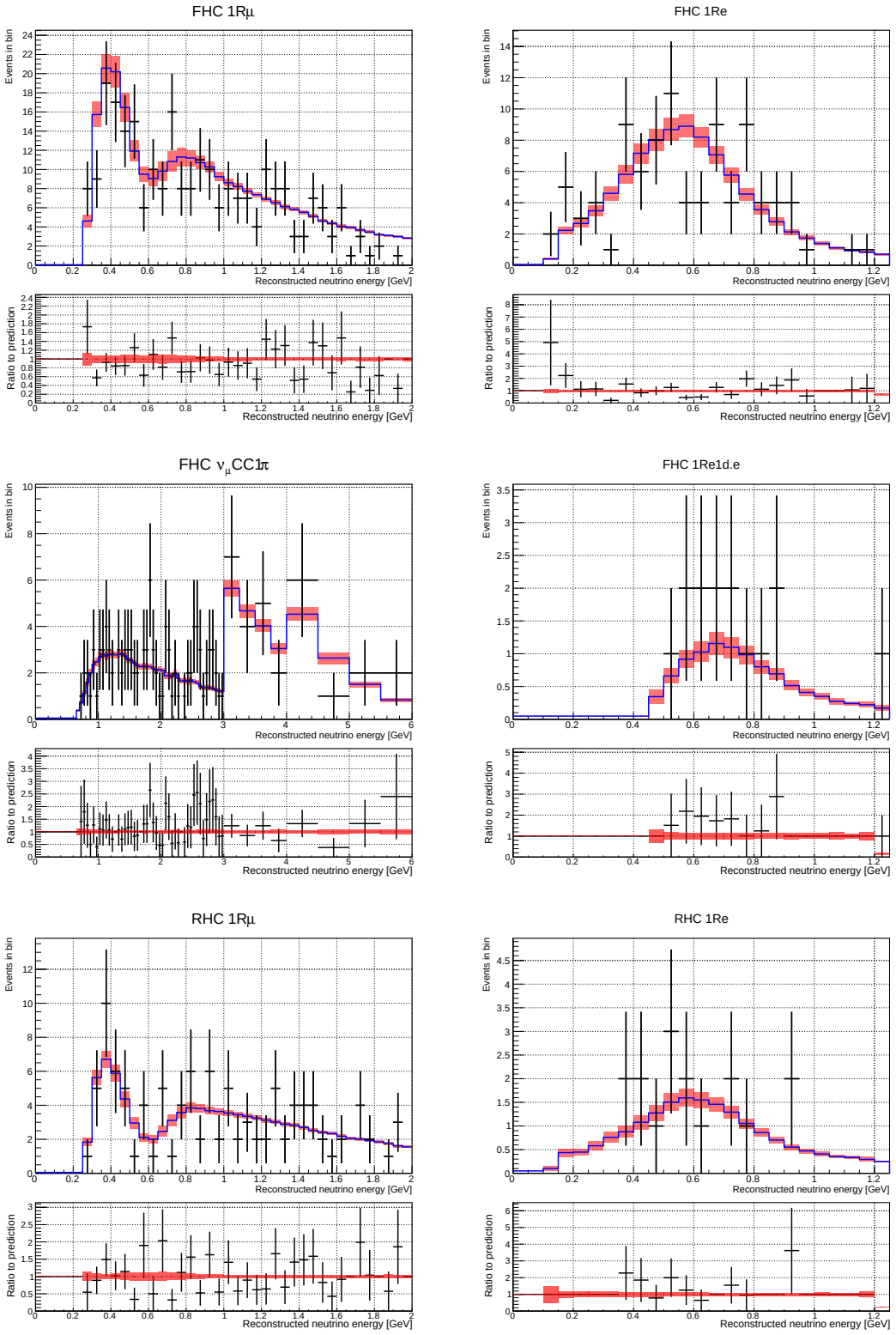

Figure 6.2: Posterior predictive spectra for all SK samples. Each plot shows the best fit of the event rate distribution in each bin (blue), the 1σ error band (red), with data (black) overlaid.

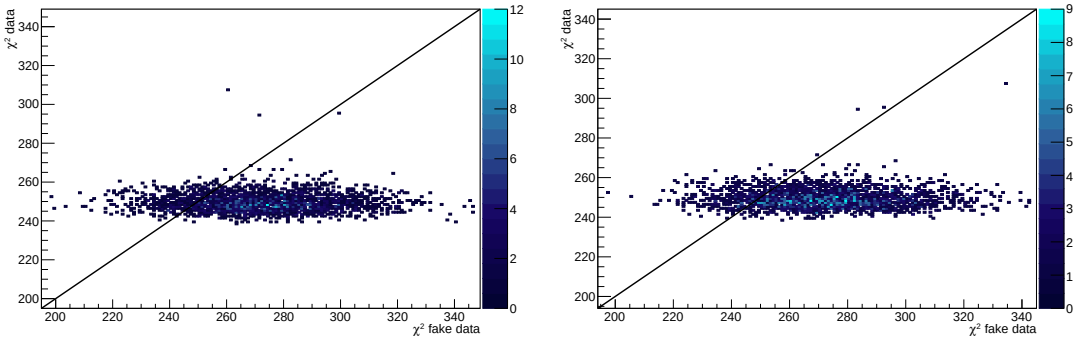

Figure 6.3: The χ^2 between the data and each MC sample (χ^2data) plotted against the χ^2 between the fake data set and the MC sample (χ^2fake data), for a T2K-only data fit (left) and a T2K + reactor fit (right).

The χ^2 test statistic for a sample with observed events n_i and predicted events λ_i is defined as

$$\chi^2 = -2\ln\mathcal{L} = -2\sum_i^N \left[n_i \ln\frac{n_i}{\lambda_i} + \lambda_i - n_i \right], \tag{6.1}$$

where the sum runs over every bin in each of the six SK samples. This method is referred to as a 'shape-based' test as it compares data to an MC prediction bin-by-bin, rather than considering just the total number of events. Figure 6.3 shows the distribution of the χ^2(fake data) and χ^2(data) for each of the 2500 Markov chain samples for both a T2K-only and T2K + reactor fit. As discussed, the p-value is the number of samples for which $\chi^2(\text{data}) < \chi^2(\text{fake data})$, which corresponds to the total number of points below the diagonal $y = x$ line in figure 6.3.

In a Bayesian framework, the posterior predictive p-value is more broadly defined as the probability that, given the data, a future observation is as or more extreme (as measured by some test variable, in this case, the p-value) than the data [128]. In general, a higher posterior predictive p-value indicates better agreement between the model and data. This method yields a p-value of 84% for a T2K-only fit and 86% for a T2K + reactor fit.

In addition to the method outlined above, a p-value calculation is also performed where each 'bin' is the total number of events in each SK sample, referred to as the 'rate-based' p-value. This approach treats the data and MC as a set of

	T2K-only		T2K + reactor	
Sample	Shape-based	Rate-based	Shape-based	Rate-based
FHC 1Rμ	0.30	0.02	0.32	0.02
FHC 1Re	0.12	0.51	0.13	0.52
FHC ν_μCC1π	0.96	0.30	0.96	0.31
FHC 1Re1de	0.89	0.26	0.88	0.27
RHC 1Rμ	0.84	0.66	0.84	0.65
RHC 1Re	0.66	0.39	0.64	0.39
Total	0.84	0.10	0.86	0.09

Table 6.1: Posterior predictive p-values calculated from both a T2K-only and T2K + reactor fit for each far-detector sample, quoted separately for a bin-by-bin (shape-based) and total rate (rate-based) χ^2 calculation.

counting measurements. The test statistic is of an identical form to equation 6.1, except that each SK sample is treated as one bin. This method yields a p-value of 10% for a T2K-only fit and 9% for a T2K + reactor fit. Further, the shape and rate-based p-values are quoted separately for each SK sample for a T2K-only and T2K + reactor fit in table 6.1.

When computing the p-values for individual samples, the FHC 1Rμ sample yields a p-value of 0.02 when using the rate-based method, which is below the pre-defined significance level of 0.05. However, when performing multiple hypothesis tests, it is important to take into account the 'Look Elsewhere Effect'. This is a phenomenon where an apparently statistically significant observation may have appeared by chance due to the large size of the parameter space being explored and the high number of statistical tests being performed[2]. The look elsewhere effect is more generally known in statistics as the 'Many comparisons problem'. A more detailed discussion about this effect can be found in Ref. [129].

When performing multiple statistical tests, the family-wise error-rate (FWER) (the probability of wrongly rejecting the null hypothesis) increases. If m statistical tests are performed, with a pre-defined statistical significance level of α (5% in

[2]Often, these two factors are interconnected as a large parameter space normally requires a higher number of statistical tests.

this analysis), the FWER is written as

$$FWER = 1 - (1 - \alpha)^m \,. \tag{6.2}$$

For a fixed statistical significance level, it can be seen from Equation 6.2 that the FWER increases with the number of statistical tests being performed. In the case of the goodness-of-fit tests presented here, when the by-sample p-values are computed, six statistical tests are performed. This gives a FWER of 26.5%. To account for the look elsewhere effect, a p-value is considered to represent disagreement between a model and the data sample only if it is below the Bonferroni-corrected significance level, given by

$$\alpha_B = \frac{\alpha}{m} = \frac{0.05}{6} = 0.008 \,. \tag{6.3}$$

Comparing the sample p-values in Table 6.1 with the Bonferroni-corrected statistical significance level, it is concluded that all samples, both individually and collectively, demonstrate no indication of any disagreement between the model predictions and the data.

6.2 Oscillation Parameter Constrains

This section presents constraints on the oscillation parameters that T2K has sensitivity to: $\sin^2\theta_{23}$, Δm^2_{32}, $\sin^2\theta_{13}$ and δ_{CP}. $\sin^2\theta_{23}$ and Δm^2_{32} are known and referred to as 'disappearance' parameters, as they are mostly constrained by the observation of an absence of muon neutrinos at the far detector. Analogously, $\sin^2\theta_{13}$ and δ_{CP} are known as 'appearance' parameters, as they are (mostly) constrained by the observation of electron neutrinos. The 68/90/99% credible intervals are presented for both the one and two-dimensional marginalised posterior distributions. Disappearance and appearance parameter constraints are analysed separately in sections 6.2.1 and 6.2.2 respectively. All one-dimensional posterior probability distributions have been normalised to 1.

6.2.1 Disappearance parameters

Figure 6.4 shows the 2D marginal posterior distribution for the disappearance parameters, with and without applying the external reactor constraint. Figure 6.5 shows their corresponding 1D marginal posteriors. Additionally, the best-fit points and credible intervals for each disappearance parameter for a T2K-only and T2K + reactor fit are shown in tables 6.2 and 6.3 respectively. In the T2K-only fit, a lower-octant best-fit point for $\sin^2\theta_{23}$ is found, though both octants are within the 68% credible interval. A small preference for normal ordering is also found. When applying the reactor constraint, the fit now prefers the upper octant and has an increased preference for normal ordering.

The posterior probabilities for mass ordering and octant preference can be found in tables 6.4 and 6.5 for the T2K-only and T2K + reactor fits respectively. Model preference can be quantified by calculating the Bayes factor, as introduced in section 4.4.4. In this analysis, it is simply the ratio of the total posterior probability of one model over another. Performing this calculation for a T2K-only fit yields Bayes factors of $\mathfrak{B}(\text{NO/IO}) = 1.70$, indicating a slight preference for normal ordering, and for octant preference, it found that $\mathfrak{B}(\text{UO/LO}) = 1.38$. Repeating the procedure for the T2K + reactor fit yields $\mathfrak{B}(\text{NO/IO}) = 2.70$ and $\mathfrak{B}(\text{UO/LO}) = 2.23$. Fitting with the reactor constraint increases the preference for normal ordering and upper octant, though it should be noted that when comparing to the Kass-Raferty scale in table 4.1, these Bayes factors are not statistically significant.

T2K-only	$\sin^2\theta_{23}$	Δm^2_{32} $[\times 10^{-3}\text{eV}^2]$
2D best fit	0.488	2.51
68% C.I. (1σ) range	0.470 – 0.545	-2.58 – -2.51 $\cup$ 2.43 – 2.57
90% C.I. range	0.455 – 0.564	-2.62 – -2.47 $\cup$ 2.40 – 2.60
95.4% (2σ) C.I. range	0.448 – 0.575	-2.65 – -2.45 $\cup$ 2.38 – 2.62

Table 6.2: Best-fit values and 1D credible interval ranges for the disappearance parameters from a T2K-only data fit. The 2D best-fit values are taken from the mode of the 2D $\sin^2\theta_{23} - \Delta m^2_{32}$ marginal posterior distribution.

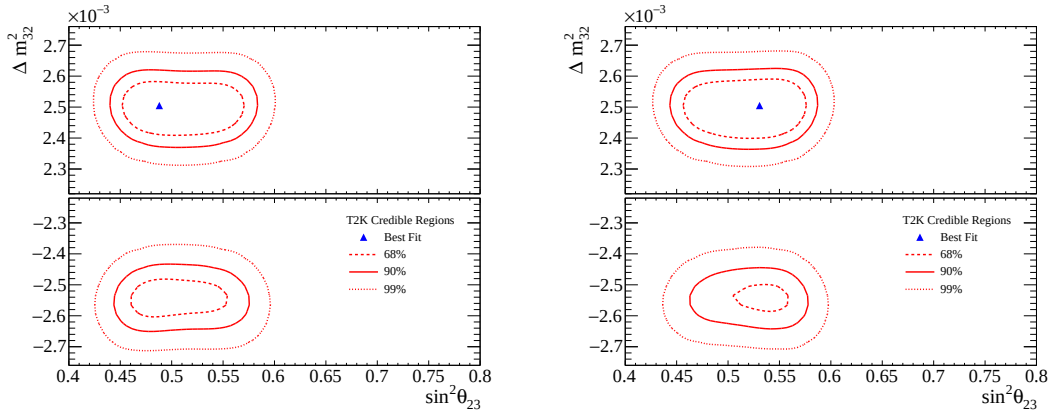

Figure 6.4: 2D $\sin^2\theta_{23}$-Δm^2_{32} marginal posterior distribution and credible intervals, from a T2K-only data fit (left) and a T2K + reactor data fit (right).

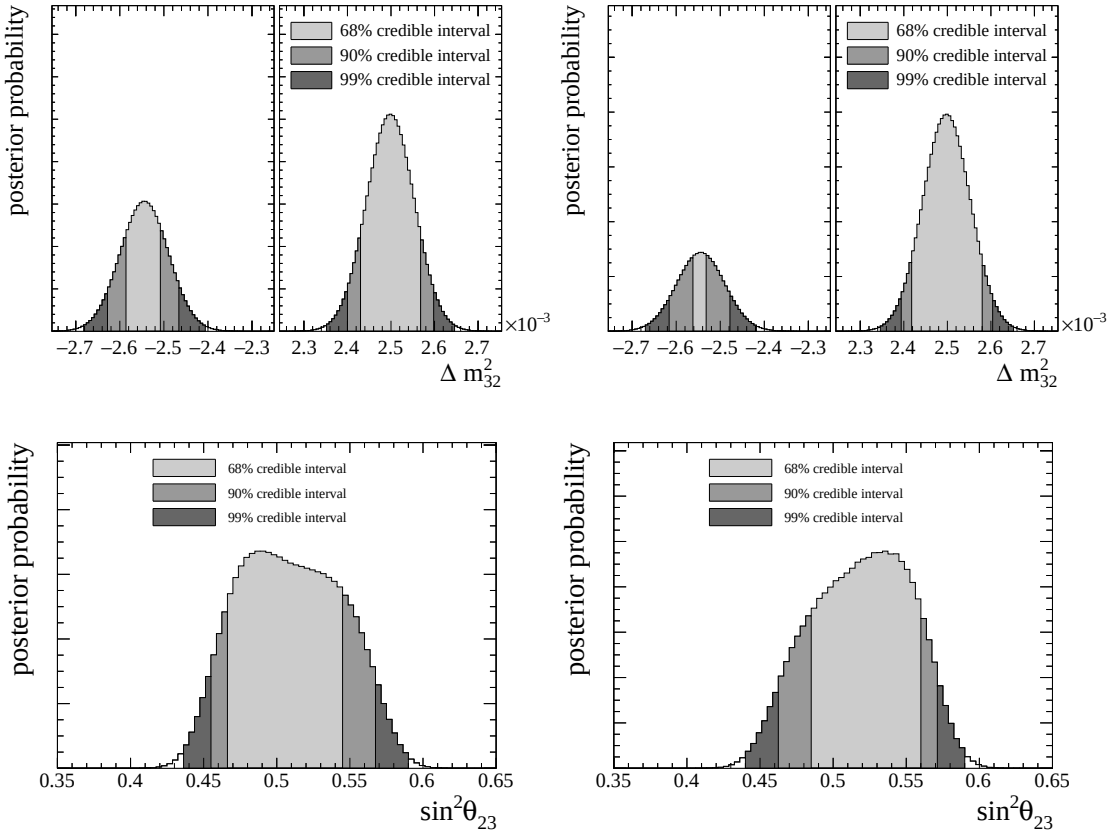

Figure 6.5: 1D marginal posterior distribution and credible intervals for the disappearance parameters from a T2K-only data fit (left) and a T2K + reactor (right) data fit. Both mass orderings are marginalised.

T2K-only	$\sin^2\theta_{23} < 0.5$	$\sin^2\theta_{23} > 0.5$	Sum
NO ($\Delta m^2_{32} > 0$)	0.26	0.37	0.63
IO ($\Delta m^2_{32} < 0$)	0.16	0.21	0.37
Sum	0.42	0.58	1.00

Table 6.4: Total posterior probabilities for normal and inverted mass orderings, as well as upper and lower octants, extracted from a T2K-only data fit.

T2K + reactor	$\sin^2\theta_{23} < 0.5$	$\sin^2\theta_{23} > 0.5$	Sum
NO ($\Delta m^2_{32} > 0$)	0.24	0.49	0.73
IO ($\Delta m^2_{32} < 0$)	0.07	0.20	0.27
Sum	0.31	0.69	1.00

Table 6.5: Total posterior probabilities for normal and inverted mass orderings, as well as upper and lower octants, extracted from a T2K + reactor data fit.

T2K + reactor	$\sin^2\theta_{23}$	Δm^2_{32} $[\times 10^{-3}\text{eV}^2]$
2D best fit	0.531	2.51
68% C.I. (1σ) range	0.489 – 0.560	-2.56 – -2.53 $\cup$ 2.42 – 2.58
90% C.I. range	0.466 – 0.571	-2.61 – -2.48 $\cup$ 2.39 – 2.60
95.4% (2σ) C.I. range	0.455 – 0.579	-2.63 – -2.45 $\cup$ 2.38 – 2.62

Table 6.3: Best-fit values and 1D credible interval ranges for the disappearance parameters from a T2K + reactor data fit. The 2D best-fit values are taken from the mode of the 2D $\sin^2\theta_{23} - \Delta m^2_{32}$ marginal posterior distributions.

6.2.2 Appearance parameters

Figure 6.6 shows the 2D marginal posterior distribution for the appearance parameters, with and without applying the external reactor constraint. Figure 6.7 shows their corresponding 1D marginal posteriors. Additionally, the best-fit points and credible intervals for each appearance parameter for a T2K-only and T2K + reactor fit are shown in tables 6.6 and 6.7 respectively. Good agreement is found between T2K's constraint on $\sin^2\theta_{13}$ and the external constraint from reactor experiments. An increase in sensitivity to δ_{CP} is observed when applying the reactor constraint, where the T2K + reactor fit excludes CP-conserving

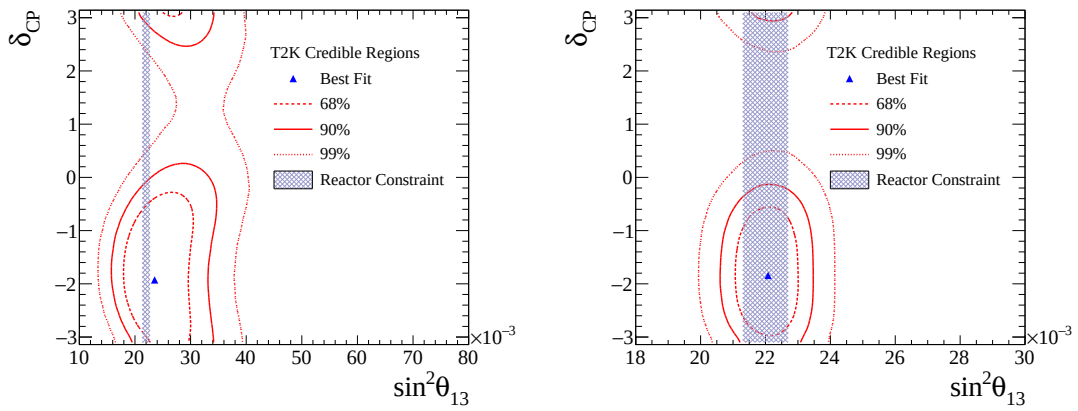

Figure 6.6: 2D $\sin^2\theta_{13}$-δ_{CP} marginal posterior distribution and credible intervals, from a T2K-only data fit (left) and a T2K + reactor data fit (right). The PDG reactor constraint 1σ region is shown as a shaded region. Both mass orderings are marginalised.

values of δ_{CP} from the 90% credible interval. Note the log scale on the 1D posterior probability distributions for δ_{CP} shown in Figure 6.7. This is to aid visualisation of the disfavoured regions of parameter space around $\delta_{CP} \sim \pi/2$. Further, the irregularities in the posterior distribution in this region are due to the reweighting procedure. A useful property of Markov chains is that the final posterior distribution can be reweighted to apply different priors; this procedure is entirely equivalent to running a new fit. However, doing so results in weights close to 0 in highly disfavoured regions of parameter space, meaning a smaller number of accepted steps and larger statistical fluctuations. This problem would be mitigated with a longer Markov chain, however for this analysis, only parameter constraints up to 3σ are desired. As is the case for all marginal posteriors presented in this report, the distributions are stable enough to make parameter conclusions at this level.

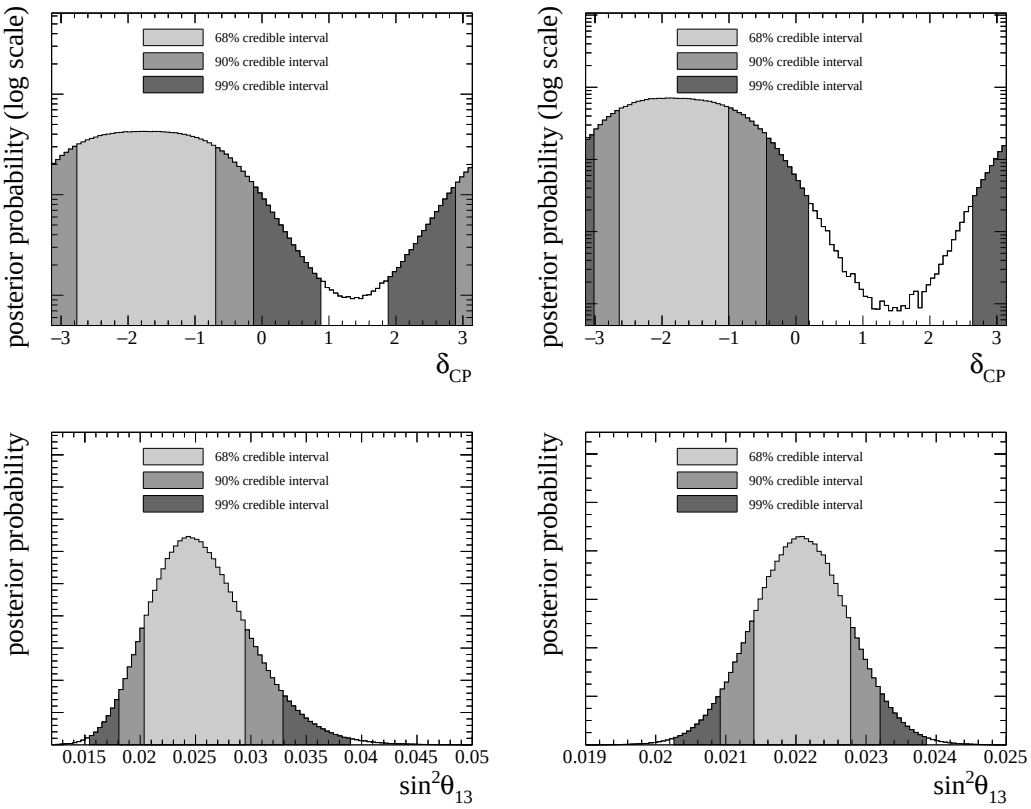

Figure 6.7: 1D marginal posterior distribution and credible intervals for the appearance parameters from a T2K-only data fit (left) and a T2K + reactor (right) data fit. Both mass orderings are marginalised.

T2K-only	$\sin^2\theta_{13}$	δ_{CP}
2D best fit	0.0235	-1.92
68% C.I. (1σ) range	0.0204 – 0.0291	-2.76 – -0.75
90% C.I. range	0.0181 – 0.0325	$-\pi$ – -0.13 & 2.95 – π
95.4% (2σ) C.I. range	0.0173 – 0.0348	$-\pi$ – 0.19 & 2.58 – π

Table 6.6: Best-fit values and 1D credible interval ranges for the appearance parameters from the T2K-only data fit. The 2D best-fit values are taken from the mode of the 2D $\sin^2\theta_{13} - \delta_{CP}$ marginal posterior distribution.

T2K + reactor	$\sin^2\theta_{13}$	δ_{CP}
2D best fit	0.0221	-1.84
68% C.I. (1σ) range	0.0214 – 0.0227	-2.58 – -1.01
90% C.I. range	0.0210 – 0.0232	-3.02 – -0.50
95.4% (2σ) C.I. range	0.0207 – 0.0234	$-\pi$ – -0.25 & 3.08 – π

Table 6.7: Best-fit values and 1D credible interval ranges for the appearance parameters from the T2K + reactor data fit. The 2D best-fit values are taken from the mode of the 2D $\sin^2\theta_{13} - \delta_{CP}$ marginal posterior distribution.

6.3 Jarlskog Invariant

As discussed in section 2.2.4, the Jarlskog invariant [35], $\mathcal{J}_{CP}$, can be calculated to quantify the amount of CP violation in the neutrino sector. Non-zero values for $\mathcal{J}_{CP}$ indicate CP violation and $\mathcal{J}_{CP} = 0$ indicates CP conservation. Assuming the PMNS parameterisation for the neutrino mixing matrix as in equation 2.31, the Jarlskog invariant can be written as $\mathcal{J}_{CP} = s_{13}c_{13}^2 s_{12}c_{12}s_{23}c_{23}\sin\delta_{CP}$, where $s_{ij} \equiv \sin\theta_{ij}$ and $c_{ij} \equiv \theta_{ij}$.

A constraint for $\mathcal{J}_{CP}$ can be extracted by calculating the Jarlskog invariant for each accepted step in the Markov chain. Figure 6.8 shows the 1D marginalised posterior distribution for the Jarlskog invariant when imposing a flat prior in δ_{CP}, or a flat prior in $\sin\delta_{CP}$. Notably $\mathcal{J}_{CP} = 0$, implying CP-conservation, is excluded at the 90% significance level in both cases. This is a conservative statement as $\mathcal{J}_{CP} > 0$ would also indicate CP violation.

6.4 Comparison to Previous T2K Results

As discussed, there have been a number of improvements made to the entire oscillation analysis framework since the previous T2K result [37]. These include a new far-detector sample, updated near-detector selections, and a new neutrino flux and cross-section model. Figure 6.9 shows the 2D disappearance and appearance credible interval contours for a T2K-only and T2K + reactor fit compared with T2K's previous results. A slight shift in the best-fit point for Δm^2_{32}

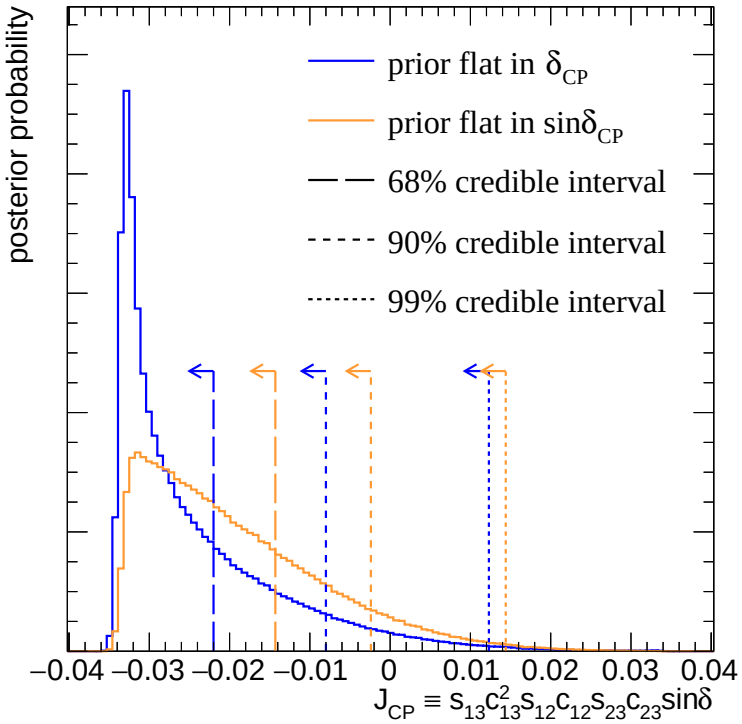

Figure 6.8: Comparison of the 1D marginalised posterior distribution for the Jarlskog invariant using either a prior flat in δ_{CP} (blue), or a prior flat in $\sin\delta_{CP}$ (orange).

is observed, moving towards a slightly higher value. The best-fit point of $\sin^2\theta_{23}$ also moves towards the point of maximal mixing. For the appearance contours, the constraint on δ_{CP} remains largely unchanged, and $\sin^2\theta_{13}$ is observed to move closer to the PDG reactor constraint. Both sets of results are highly consistent with each other, as expected.

6.5 Effect of Alternative Priors

As discussed in section 4.4.3, the posterior probability is proportional to the likelihood multiplied by a prior. In this analysis, flat priors are chosen for all of the oscillation parameters T2K has sensitivity to. The next natural question to ask is, how should a particular prior be *parameterised*? For example, one could choose a prior flat in $\sin^2\theta_{13}$, or just θ_{13} itself[3].

[3]This may be viewed as an exciting flexibility or infuriating shortcoming of Bayesian analyses, depending on your overall outlook on life.

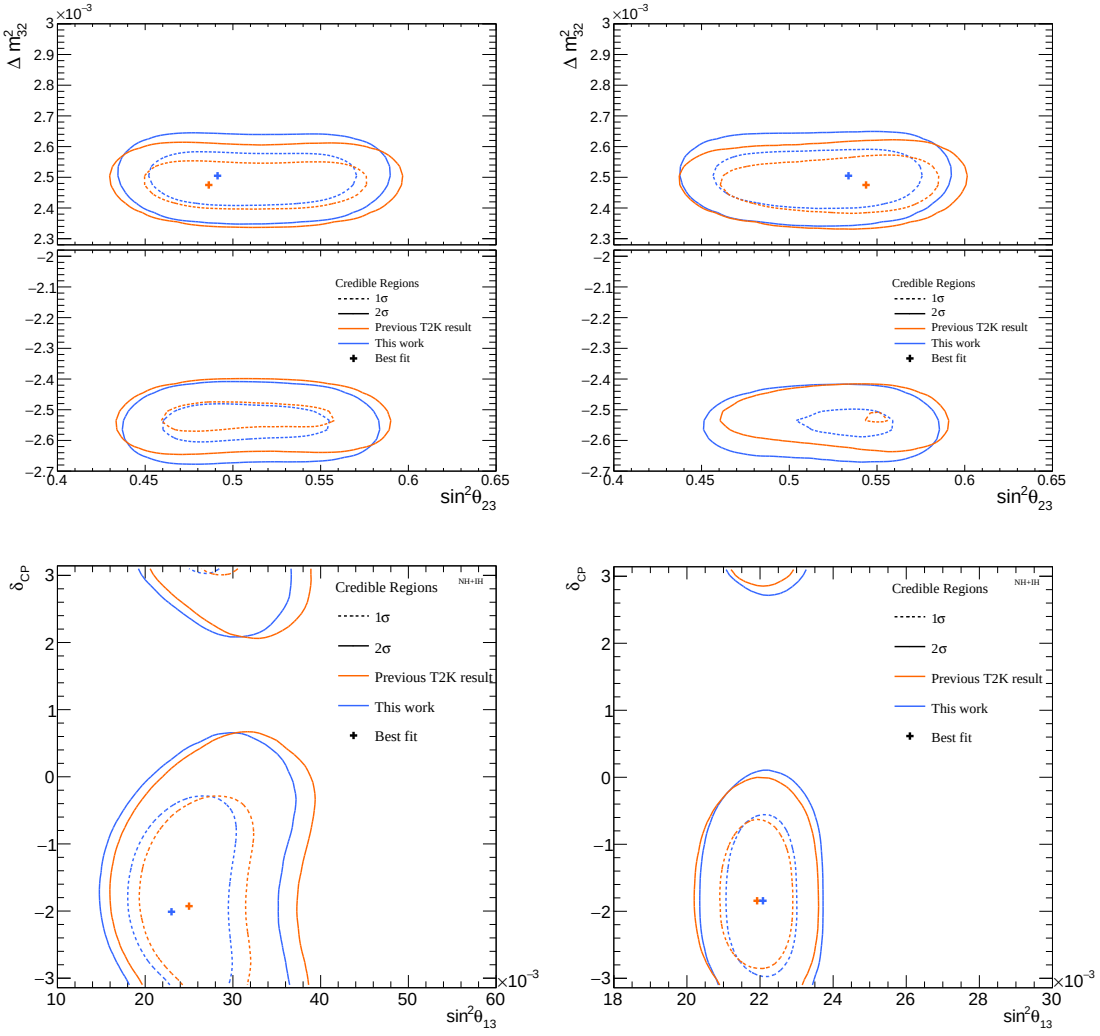

Figure 6.9: 2D disappearance (top row) and apperance (bottom row) marginal posterior distribution and credible intervals for the previous T2K result (orange) and this thesis (blue). Both T2K-only (left column) and T2K + reactor (right column) data fits are shown. Both mass orderings are marginalised.

It is important to test alternative parameterisations of priors as they may alter the statistical statements that can be made about the oscillation parameters. If the constraint from the data is strong, the choice of prior is expected to have little effect on the outcome of the analysis. However, for parameters that suffer from weaker constraints from the data, the choice of prior is expected to have a larger effect. It is therefore important to test that statistical statements made about the oscillation parameters are robust to changes in priors.

The CP-violating phase δ_{CP} is an important parameter to investigate alter-

native priors as the data constraint is weaker compared to the other oscillation parameters, and its measurement has significant consequences for the wider particle physics community. Alternative priors can be tested by simply reweighting the posterior distribution, the method for which is outlined in equations 4.9 and 4.10. To illustrate this method further, consider the case in which a prior that is flat in $x = \sin\delta_{CP}$ is to be applied instead of $y = \delta_{CP}$. Following the established method, each step in the Markov chain must reweighted according to the function

$$Q(y) \propto \frac{dx}{dy} = \frac{d}{dy}(\sin(y)) = \cos(y)\,. \tag{6.4}$$

Figure 6.10 shows a comparison of the 1D marginal posterior distribution for δ_{CP} using the standard prior (flat in δ_{CP}), and the alternative flat priors in $\sin\delta_{CP}$ (6.10a) and $\cos\delta_{CP}$ (6.10b). The posterior probability is clearly affected by the choice of prior, and a striking difference is seen when applying a prior flat in $\sin\delta_{CP}$, with the heavily-favoured region of δ_{CP} parameter space now acquiring a posterior probability of zero. This is fundamentally a consequence of reweighting to the alternative prior, where at $\delta_{CP} = -\pi/2$ the reweighting function, $\cos(\delta_{CP})$, is exactly 0. This apparent inconsistency can be resolved when plotting the posterior as a function of $\sin\delta_{CP}$, as shown in figure 6.11. Here, $\sin\delta_{CP} = -1$, corresponding to $\delta_{CP} = -\pi/2$, is highly favoured and 0 is excluded at the 90% credible interval. Therefore, it can be concluded that CP violation is observed at the 90% significance level independent of the choice of prior. It can be further concluded that the difference seen in figure 6.10a is just a consequence of the prior reweighting procedure, and plotting the posterior with an alternative prior in an unsuitable convention.

An investigation into the impact of alternative priors is a critical component of any sound Bayesian analysis; parameter inferences should be robust to alternative, suitable prior parameterisations. If there are significant changes in results when testing a new prior, this is an indication of a weak data constraint. In this analysis, alternative priors have a non-significant impact on the conclusions made about the oscillation parameters.

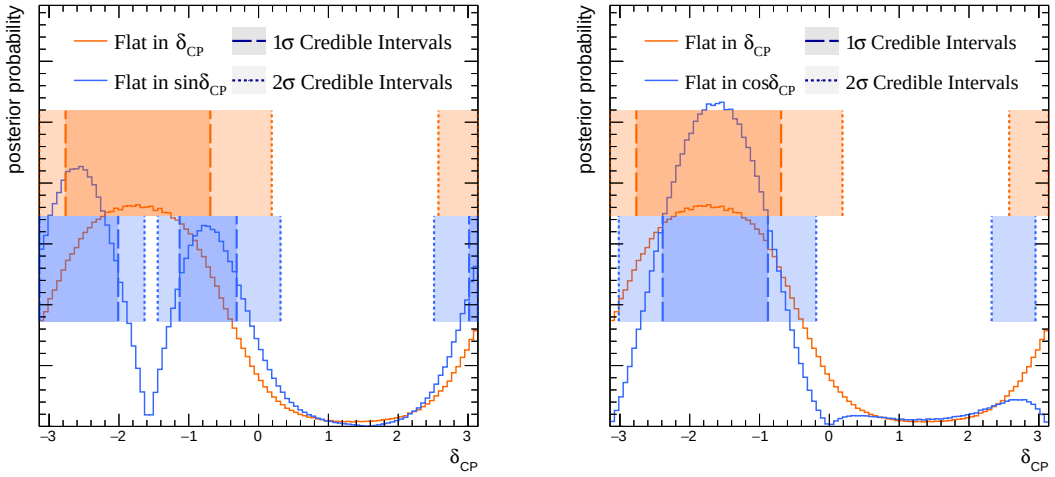

(a) Alternative flat prior in $\sin\delta_{CP}$ **(b)** Alternative flat prior in $\cos\delta_{CP}$

Figure 6.10: The effect of reweighting to an alternate prior parameterisation on the 1D marginal posterior distributions and $1/2\sigma$ credible intervals for the δ_{CP} parameter.

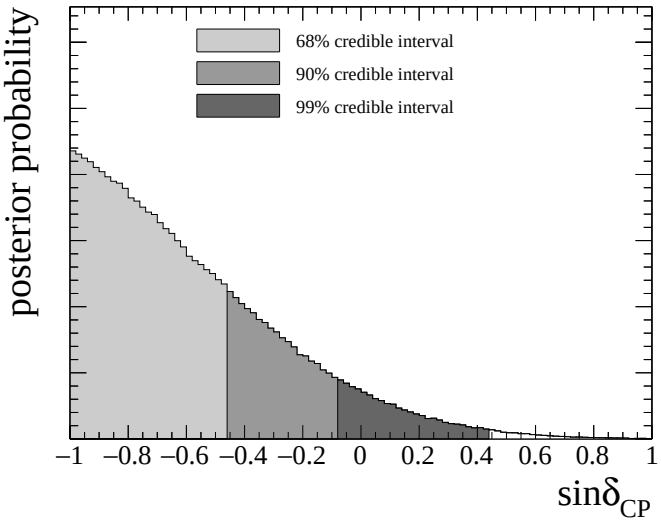

Figure 6.11: 1D marginal posterior distribution and credible intervals from a T2K + reactor constraint fit with a flat prior in $\sin\delta_{CP}$ imposed, plotted against the value of $\sin\delta_{CP}$.

6.6 Alternative Model Studies

An important aspect of the oscillation analysis is the testing of alternative cross-section models beyond the recommendations made by the NIWG [120]. This process is referred to within T2K as 'fake data studies' (FDS). Many different models exist that provide a good description of neutrino interactions, but no one model can adequately describe all neutrino cross-section data. Therefore, such studies aim to test the robustness of the analysis and identify any biases that may have been introduced by the choice of interaction model. Fake data studies performed for this analysis are fully described in [130] and parts relevant to the work in this thesis will be summarised below.

There are several steps in performing a fake data study, which are as follows:

1. **Motivation** – First, a set of alternative models of interest must be decided upon. These are primarily motivated by new additions made to the analysis. For example, with the addition of the new far-detector ν_μCC1π sample, extra pion-production-focused studies were added to gauge the potential impact of mis-modelling this sample.

2. **Define a metric** – Next, a metric needs to be defined to assess the impact of an alternative model study. In T2K FDS, the primary bias metric is defined as the fractional change in the centre of the 2σ intervals between an Asimov fit and the fake data fit, $\Delta^{2\sigma} = \bar{x}^{2\sigma}_{\text{Asimov}} - \bar{x}^{2\sigma}_{\text{FDS}}$, compared to the Asimov fit 1σ systematic interval, $1\sigma_{\text{syst.}}$ [130]. This metric can be written as

$$B_x^{\text{syst.}} = \frac{\Delta^{2\sigma}}{1\sigma_{\text{syst.}}}. \tag{6.5}$$

3. **Specify criteria** – Once a metric has been defined, it's necessary to define a criterion that, if met, suitable action needs to be taken. For the Δm^2_{32} parameter, which is the main parameter of interest for the FDS described in chapter 7, the criterion for further action is

$$|B_x^{\text{syst.}}| > 0.5\,, \tag{6.6}$$

which can be interpreted as the alternative model introducing a bias in Δm^2_{32} that is greater than 50% of the size of the 1σ systematic interval.

4. **Construct fake data** – Next, the fake data sets at the near and far detectors need to be constructed. This is done by generating the predicted spectra at ND280 and SK when fixing all cross-section parameters at their prior means (see table 5.4), and on top of this applying a correction for the alternative model prediction. Alternative models are encoded as separate parameters within the NIWG framework.

5. **Oscillation fit** – Finally, a full oscillation fit is run using the constructed fake data sets. Oscillation parameter constraints can then be calculated and compared to the nominal Asimov fit, and the metric defined in equation 6.5 can be evaluated to check for any significant biases.

Historically, the modelling of nuclear effects in CCQE interactions has constituted one of the largest contributions to the systematic uncertainty in past T2K oscillation analyses. A particular alternative model of interest is the Hartree-Fock Continuum Random Phase Approximation (HF-CRPA) [131, 132], which has been highly successful in describing electron scattering data and produces significantly different predictions for the neutrino cross section in regions of low-energy transfer (ω) [133, 134].

A fake data study was performed to assess the impact of the alternative HF-CRPA model prediction on the oscillation analysis results presented here. In this study, the criterion in equation 6.6 was met, with HF-CRPA introducing a bias of 85% on Δm^2_{32}, or in terms of the metric defined in equation 6.5, $|B^{syst.}_{\Delta m^2_{32}}| = 0.85$. Figure 6.12 illustrates this bias by comparing the nominal Asimov contour for Δm^2_{32} to the result of the fake data study. To account for this potential bias, the Δm^2_{32} posterior (which fortunately is rather Gaussian-like) was manually

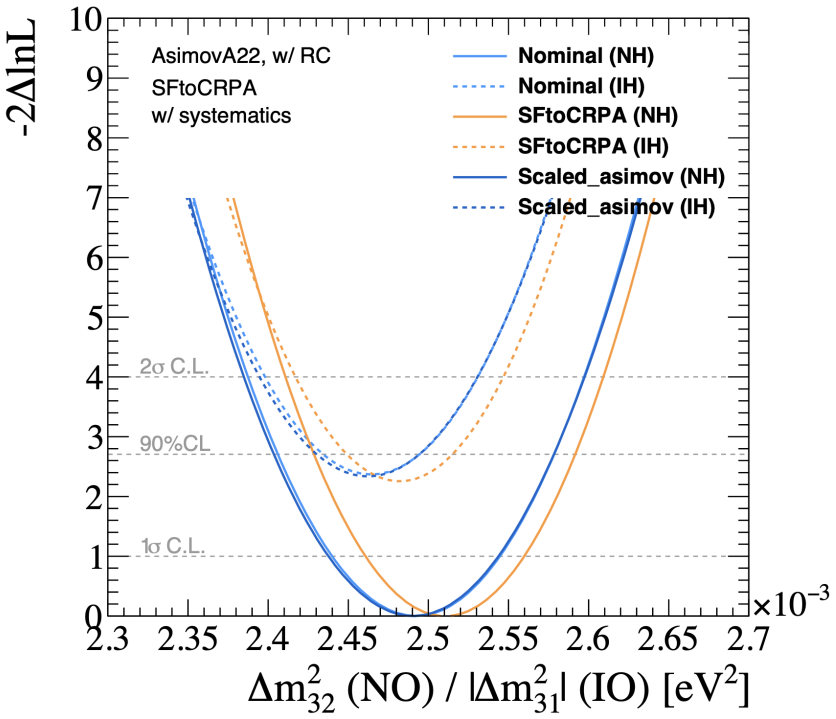

Figure 6.12: 1D likelihood surface for Δm^2_{32} for normal (solid line) and inverted (dashed) ordering for the HF-CRPA FDS (orange) and nominal Asimov A22 fit (blue). The scaled Asimov contour (dark blue) can be safely ignored for the context of this thesis.

smeared to include the effects of this potential mis-modelling. This smearing involves manually increasing the width of the posterior distribution of Δm^2_{32} so that the bias is now contained within the 68% interval. This effect on the Δm^2_{32} posterior is shown in figure 6.13. All oscillation results presented in this chapter include this smearing of Δm^2_{32}.

Though smearing the Δm^2_{32} posterior ensures the bias introduced when using the HF-CRPA model is correctly accounted for, it would be far more ideal if the uncertainty model was able to correctly account for this without the need for smearing. This motivates the work presented in chapter 7, where new systematic parameters were designed and implemented into the interaction model to introduce more freedom in the low-energy transfer region, where the HF-CRPA model prediction varies most significantly when compared to the NEUT SF.

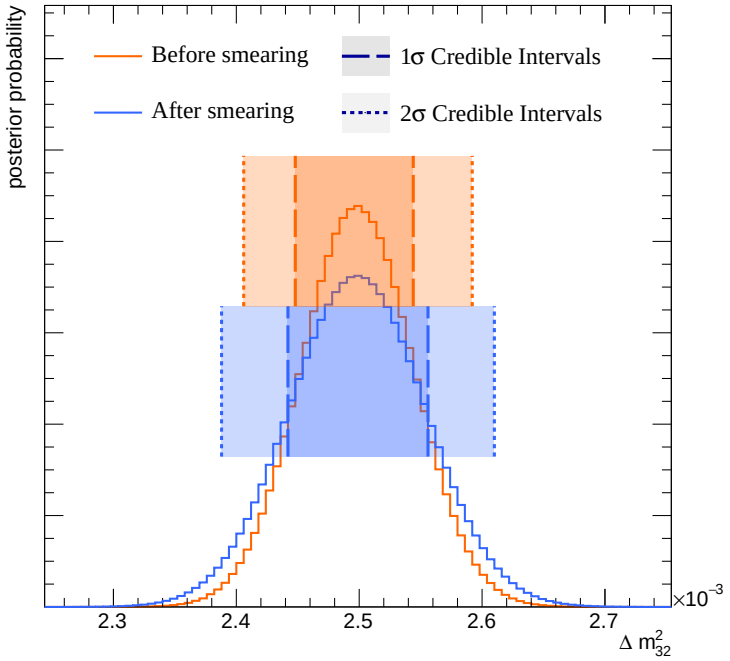

Figure 6.13: 1D marginal posterior for Δm^2_{32} before (orange) and after (blue) smearing due to alternative model studies.

6.7 Summary of Oscillation Results

The results presented in this chapter represent T2K's most accurate and robust measurement of the oscillation parameters to date. A number of notable improvements were made compared to T2K's previous results [37], including the addition of a new far-detector sample [115], updated near-detector selections [111], enhancements to the neutrino interaction uncertainty model [120], and improved flux constraints from replica target NA61/SHINE data [112]. New additions to the MaCh3 analysis framework include allowing events to migrate in and out of samples, and the explicit θ_{23} octant-mixing mechanism.

A summary of the best-fit points and credible intervals for the oscillation parameters can be found in tables 6.8 and 6.9 for a T2K-only and T2K + reactor fit respectively. The best-fit points for each parameter are calculated from the 2D disappearance and appearance marginal posteriors, and the credible intervals are extracted from the 1D marginal posteriors. Flat/uninformative priors are

T2K-only	$\sin^2\theta_{23}$	$\Delta m^2_{32}[\times 10^{-3}\text{eV}^2]$	$\sin^2\theta_{13}$	δ_{CP}
Best-fit	0.488	2.51	0.0235	-1.92
68% C.I.	0.470 – 0.545	-2.58 – -2.51 ∪ 2.43 – 2.57	0.0204 – 0.0291	-2.76 – -0.75
90% C.I.	0.455 – 0.564	-2.62 – -2.47 ∪ 2.40 – 2.60	0.0181 – 0.0325	$-\pi$ – -0.13 ∪ 2.95 – π

Table 6.8: Best-fit points and credible intervals for the oscillation parameters extracted from a T2K-only data fit.

T2K + RC	$\sin^2\theta_{23}$	$\Delta m^2_{32}[\times 10^{-3}\text{eV}^2]$	$\sin^2\theta_{13}$	δ_{CP}
Best-fit	0.531	2.51	0.0221	-1.84
68% C.I.	0.489 – 0.560	-2.56 – -2.53 ∪ 2.42 – 2.58	0.0214 – 0.0227	-2.58 – -1.01
90% C.I.	0.466 – 0.571	-2.61 – -2.48 ∪ 2.39 – 2.60	0.0210 – 0.0232	-3.02 – -0.50

Table 6.9: Best-fit points and credible intervals for the oscillation parameters extracted from a T2K + reactor data fit.

applied in the form of the fitted parameter (e.g. flat in δ_{CP}). Alternative sets of priors have been tested and the constraints are robust.

Analysing the disappearance parameters, a slight preference for the upper octant of $\sin^2\theta_{23}$ and normal mass ordering is found, with Bayes factors of $\mathfrak{B}(\text{UO/LO}) = 2.23$ and $\mathfrak{B}(\text{NO/IO}) = 2.70$ respectively. These Bayes factors are deemed not to be statistically significant when compared to the Kass-Raferty scale given in table 4.1.

When applying the external constraint on $\sin^2\theta_{13}$ from reactor experiments [109], CP-conserving values of δ_{CP} are excluded from the 90% credible interval. Additionally, a Jarlskog invariant $\mathcal{J}_{\text{CP}} = 0$ (implying CP-conservation) is excluded from the 90% credible interval.

7

Novel Interaction Uncertainties at T2K and DUNE

This chapter extends upon the oscillation results presented in chapter 6 with the addition of new systematic parameters to address oscillation parameter biases found during alternative model studies. New parameters were motivated and designed to introduce more freedom in the region of low-energy transfer, where models produce largely different predictions for the neutrino cross section. These new parameters were then implemented into the MaCh3 framework to isolate their effects on the oscillation fit. It is hoped that the introduction of additional freedoms will alleviate the bias seen in Δm^2_{32} during the CRPA alternative model study. As this was the dominant contribution to the systematic uncertainty for Δm^2_{32}, the cross-section model must be suitably expanded to resolve this bias.

The motivation and design of the new parameters will be discussed in section 7.1, and their implementation into MaCh3 and the subsequent impact on the HF-CRPA alternative model study will be presented in section 7.2. Finally, new systematic parameters designed for the next-generation neutrino experiment, DUNE, will be presented in section 7.3.

7.1 Low-Energy Transfer Systematics at T2K

7.1.1 Motivation

As discussed in section 3.4, NEUT uses the Benhar spectral function to model the nuclear ground state. This relies on the plane wave impulse approximation (PWIA), which assumes the incoming neutrino interacts with a single, non-relativistic nucleon, and the outgoing nucleon wavefunction does not experience the nuclear potential. Therefore, the PWIA does not include the effects of nucleon-nucleon correlations, nor does it model the impact of FSI on the cross section of the primary scatter[1]. These shortcomings are most impactful for interactions with low-energy transfer (ω) for two primary reasons. Firstly, for low-ω interactions, the W boson has an effectively longer wavelength, meaning it is more sensitive to nucleon-nucleon correlations and lower energy nuclear physics processes. Furthermore, during such interactions, the energy of the outgoing nucleon is more likely to be affected by the nuclear potential due to their respective comparable values.

Often, corrections are applied to PWIA models to account for these shortcomings, including random phase approximation (RPA) [135] and optical potential corrections [136]. RPA correlations are built on top of a local Fermi gas (LFG) model and account for the effect of nucleon-nucleon correlations on the single-particle wavefunction. Optical potential corrections take into account the effects of final-state interactions between the struck nucleon and residual nucleus.

There are alternative nuclear ground state models that include the necessary physics that is lacking in the PWIA. The HF-CRPA model [131, 132] is expected to be a more robust method of describing the nuclear ground state due to its foundations in a realistic nuclear model (Hartree-Fock), and its success in reproducing giant nuclear resonances at low-energy transfer, as well as being well-validated against electron scattering data [132]. The foundation of the HF-CRPA model is the Hatree-Fock method, which utilises a self-consistent

[1] It may be expected that such secondary processes are quantum mechanically coupled to the primary process.

mean-field approach to calculate the bound-state wavefunctions of the nucleus assuming a realistic nuclear potential [137]. CRPA corrections are then applied to the HF model predictions to account for long-range correlations between nucleons. Furthermore, the CRPA model uses the same nuclear potential as the HF model, making the entire calculation self-consistent. Due to its strong physics foundation and success in describing electron scattering data, the HF-CRPA model is highly relevant to T2K analyses.

As discussed in section 6.6, the HF-CRPA alternative model study demonstrated a significant bias in Δm^2_{32}, approaching 100% of the systematic error budget on this measurement. This motivated the introduction of additional freedoms that can describe the sizeable model variations observed in the low-energy transfer region. Figure 7.1 shows the predictions for the T2K ν_μ flux-averaged cross section from several models binned in ω. Large model differences are observed in the two lowest ω bins, and good model agreement is seen at higher ω, where the assumptions made in the PWIA are more valid.

7.1.2 Parameter Design

As discussed, the PWIA does not account for nucleon-nucleon correlations and it contains no description of the impact of FSI on the primary scattering cross section. Therefore, two sets of parameters were designed to address the limitations of the PWIA, modelling an 'RPA-like' effect and an 'FSI-like' effect. Each parameter is designed to interpolate between two models. For model interpolation parameters, if the parameter value is 0, an event receives a weight of 1, whereas if the parameter value is 1, an event receives a weight equal to the ratio of the two model predictions. For parameter values between 0 and 1 or greater than 1, linear interpolation is used to calculate the cross-section weight. The models used for each parameter set are outlined below:

1. **RPA** – the 'RPA-like' parameters interpolate between the Hartree-Fock plane wave (HF-PW) model and the CRPA-PW model. This applies a CRPA

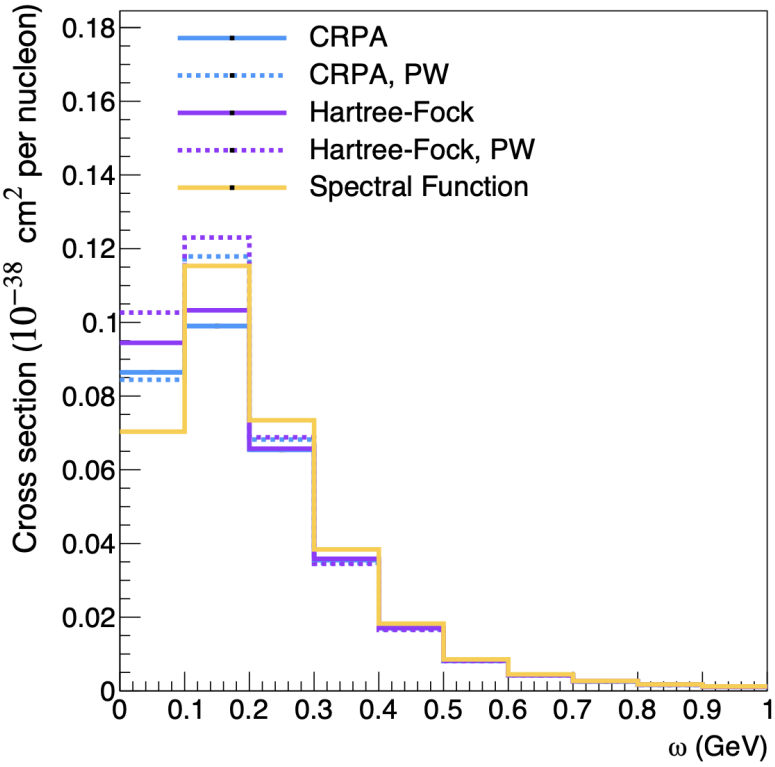

Figure 7.1: Predictions of the differential cross section for the CRPA (blue), Hartree-Fock (purple) and spectral function (yellow) models. The dashed lines indicate the plane-wave assumption being used. Differences between the models are most significant at low ω.

correction to the HF-PW model and contains no description of FSI as both models assume a plane wave for the outgoing nucleon wavefunction.

2. **FSI** – the 'FSI-like' parameters interpolate between the HF-PW model and the HF model. This applies an FSI correction to the HF-PW model by distorting the outgoing nucleon wavefunction.

The ratios between each respective set of models for both the RPA and FSI parameters are shown in figure 7.2.

The dials are then granulated by the region of energy transfer (ω) they affect. Three bins of ω were chosen: $0.05 - 0.1$ GeV, $0.1 - 0.2$ GeV, and > 0.2 GeV. The number of bins was chosen to be three to limit the total number of new parameters being added to the oscillation analysis. During the implementation of these new parameters, it was observed that areas of phase space at higher four-momentum transfer squared (Q^2) were receiving enhancements to the cross

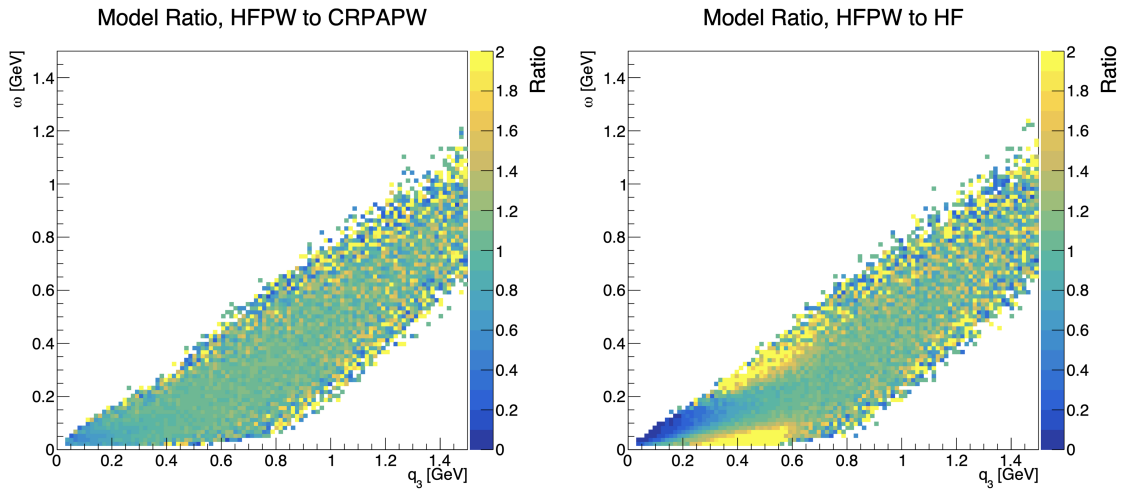

(a) RPA parameters **(b)** FSI parameters

Figure 7.2: The ratio between the predicted cross section for each model for the RPA parameters (left) and the FSI parameters (right). The predictions are binned in energy transfer ω and momentum transfer q_3.

section. As these parameters are purposely designed to suppress the cross section, all weights were capped at 1. This unexpected enhancement at higher values of Q^2 was found to be due to an error in the reweighting code. Once this error had been fixed, the parameters behaved as expected. Due to the time constraints of this analysis, the fits presented here include the *ad hoc* weight cap. However, studies within T2K demonstrate that fixing the reweighting code error removes the unexpected enhancements. Therefore, the fits presented here are expected to be largely similar to fits run without the weight cap. Furthermore, weights calculated at higher values of Q^2 may be less accurate as the non-relativistic approximations made in the HF and CRPA models would start to break down. Finally, the parameters are split by neutrino flavour (neutrino or antineutrino) and target nucleus (carbon or oxygen). This results in 24 new parameters.

Since separate parameters vary the cross section in different regions of ω, it is important to ensure parameter variations are smooth on a bin-by-bin basis. It would be unphysical to have no correction in the lowest ω bin and a full model correction in the neighbouring bin. Following the method outlined in [138], this smoothness condition can be implemented in the form of correlations between the individual parameters by adding a regularisation term to the (inverted)

covariance matrix

$$\tilde{C}^{-1}(\tau) = \tilde{C}_d^{-1} + \tilde{C}_\tau^{-1} = \begin{pmatrix} 1 & 0 & 0 \\ 0 & 1 & 0 \\ 0 & 0 & 1 \end{pmatrix} + \tau \begin{pmatrix} 1 & -1 & 0 \\ -1 & 2 & -1 \\ 0 & -1 & 1 \end{pmatrix}, \tag{7.1}$$

where $\tilde{C}_d^{-1}$ represents each parameter's prior 1σ uncertainties (which are all set to one) and $\tilde{C}_\tau^{-1}$ is a smoothness matrix with regularisation strength τ which penalises large differences in the parameter variations between neighbouring bins. Values of $\tau \gtrsim 20$ would apply strong bin-to-bin correlations, while $\tau \lesssim 0.1$ would yield very weak correlations. Methods employed to inform a suitable choice of τ are described in section 7.1.3.

The covariance matrix in equation 7.1 needs to be inverted and later used in the MaCh3 framework to ensure the parameter correlations are taken into account during the oscillation fit. However, performing this inversion for a general value of τ leads to the parameter's prior uncertainties being less than one. For example, if $\tau = 1$, the covariance matrix is

$$\tilde{C}(\tau = 1) = \begin{pmatrix} 0.63 & 0.25 & 0.13 \\ 0.25 & 0.5 & 0.25 \\ 0.13 & 0.25 & 0.63 \end{pmatrix}. \tag{7.2}$$

Whatever the value of τ, it is desired to cover the models involved in both the RPA and FSI dials at 1σ. Therefore a correction is applied to the covariance matrix that fixes the diagonal elements to 1 and alters the off-diagonal elements accordingly to retain the same correlations between bins. This means the prior uncertainties of the parameters are independent of τ, but their respective correlations very much are impacted by τ. This was deemed acceptable as the physical motivation for smoothness in the variations between bins is encoded in the *correlations*, which are retained. This correction simply allows for the parameters to contain the full model variation within their 1σ uncertainty band at any value of τ.

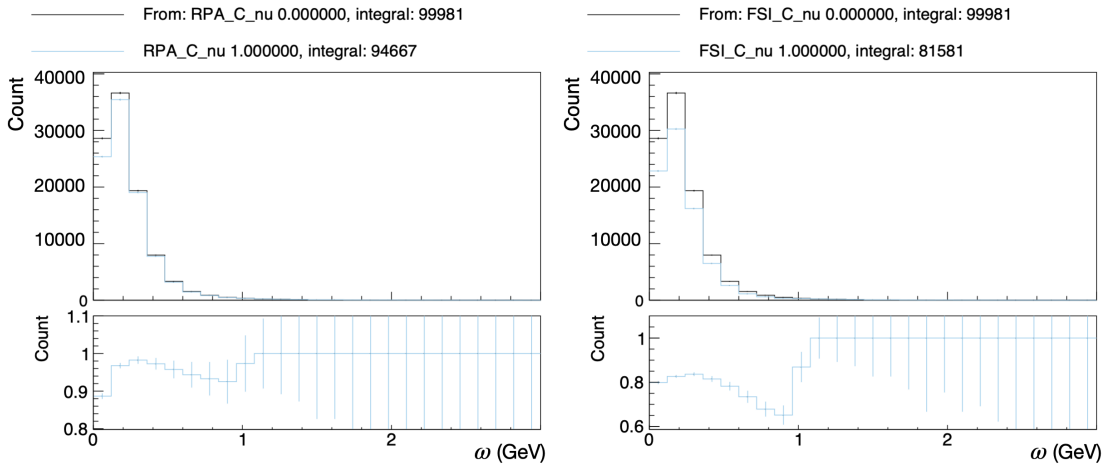

Figure 7.3: Nominal (black) and reweighted (blue) NEUT-generated event rate distributions binned in ω for the RPA-C-ν (left) and FSI-C-ν (right) parameters. Both sets of parameters cause a suppression at low ω, as anticipated.

7.1.3 Parameter Behaviour

Before performing studies to decide upon the optimal regularisation strength it is first necessary to confirm the new parameters are affecting the relevant kinematic distributions as expected. The dials were originally motivated by the strong suppression seen in the cross section at low ω for the HF-CRPA model. A suppression is expected when comparing the model predictions of CPRA-PW to HF-PW and HF to HF-PW, and indeed observing the ratios of the models in figure 7.2, strong suppressions are observed at low ω and q_3, with more suppression expected for the FSI dials. This was tested at the NEUT level by applying weights to NEUT-generated events with all dials set to 1 for a specific physics effect and target-flavour combination. As expected, suppression in the overall generated event rate was observed at low ω. For example, figure 7.3 shows the effects of the RPA and FSI carbon-target neutrino-interaction parameters on the generated event rate binned in ω.

As an initial test to inform a choice of τ, a large number of toy parameter variations were generated by throwing from the covariance matrix for a specified τ. NEUT was then used to generate events and predict the ω distribution for each variation, and the distribution of ω predictions was plotted for multiple

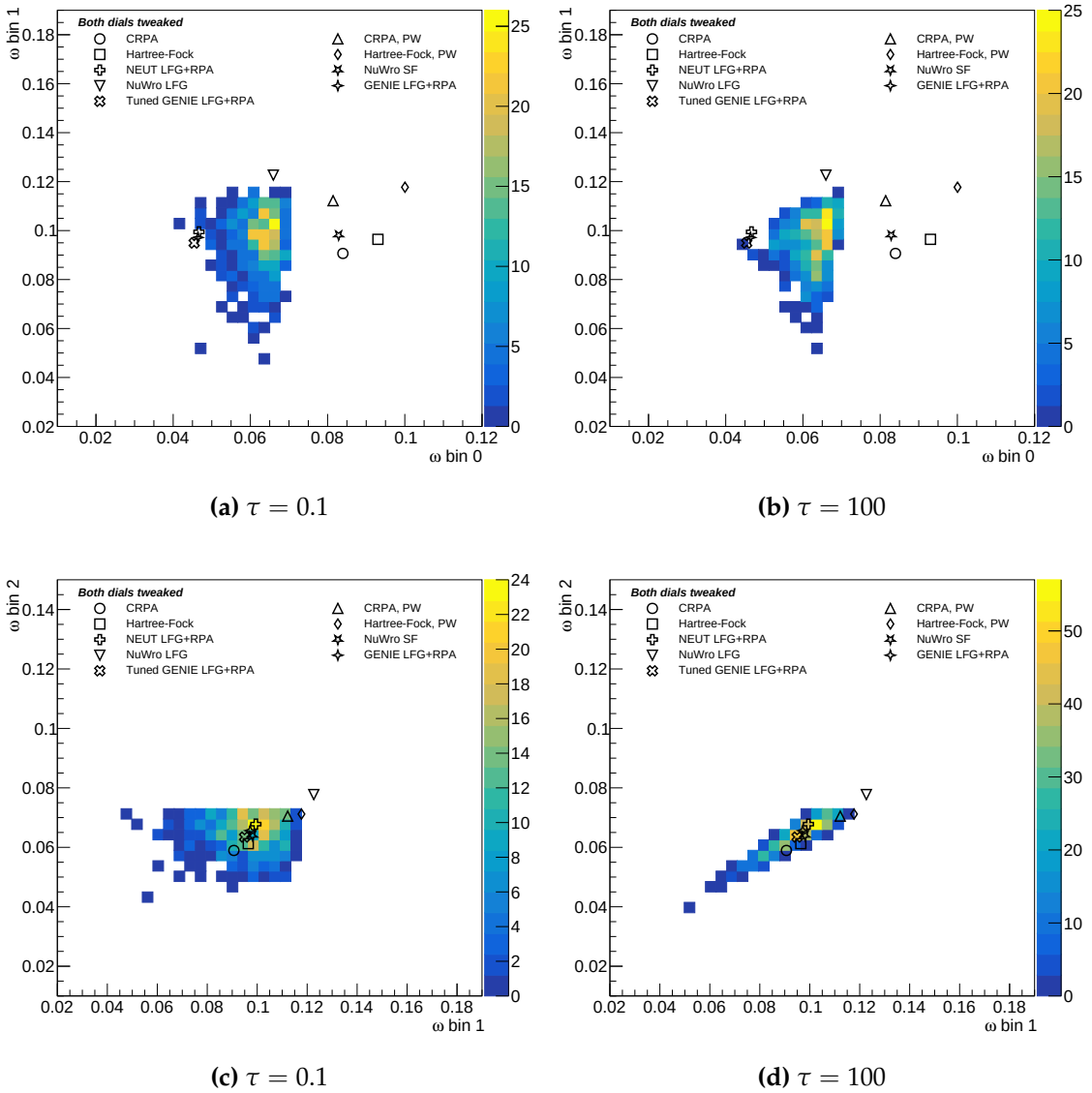

(a) $\tau = 0.1$ **(b)** $\tau = 100$

(c) $\tau = 0.1$ **(d)** $\tau = 100$

Figure 7.4: 2D distribution of ω bin predictions from all toy dial variations for low and high regularisation strengths. Various models of interest are overlaid.

values of τ and compared to a set of well-motivated models. The results of performing this procedure for two extreme values of the regularisation strength τ are the distributions shown in figure 7.4.

The impacts of regularisation become evident when examining the 2D ω distributions in figures 7.4c and 7.4d. These distributions indicate that a high regularisation would be preferable to provide good coverage of the models, but without resulting in over-coverage. However, when viewing the lower ω

bin distributions in figures 7.4a and 7.4b, the effects of regularisation are less evident, and indeed the distributions suggest a very low regularisation would be needed to provide coverage of the models. This was to be expected as the model predictions exhibit more significant divergence at very low-energy transfers.

This test ultimately proved unhelpful when deciding on a specific value for τ. It was therefore decided to investigate the impact of the regularisation within the MaCh3 framework, and these studies are described in section 7.2.1. Nevertheless, it is evident that neither extremely low nor extremely high values of τ are beneficial for all regions of ω. Therefore, more moderate values of τ (2, 5 and 10) were tested within MaCh3.

7.2 Impact on Oscillation Analysis

7.2.1 Validations and Regularisation Strength

Once the parameters had been implemented into the MaCh3 framework, studies were performed to validate that the dials were behaving as expected. First, the parameters were varied individually to test their impact on the near-detector samples. An example of several parameter variations on a few of the ND samples is shown in figure 7.5. As expected, suppression is seen mostly in the low-momentum, forward-going region, which corresponds to events with low ω.

Next, log-likelihood scans were performed for each parameter at several regularisation strengths: $\tau = \{2, 5, 10\}$. The scans performed at the near detector follow an identical method to the LLH scans outlined in section 5.5.1. Two Asimov data sets are constructed with all fit parameters set to their prior values. Then, in one of the Asimov data sets, each parameter is modified and the resulting change in the LLH (-2LLH) between the two sets is computed. The impact of the regularisation can be seen in the penalty term contribution to the total LLH, as shown in figure 7.6. It is observed that for the most well-constrained parameters (e.g. FSI-C-ν-0), the penalty term does not affect the total LLH, as expected

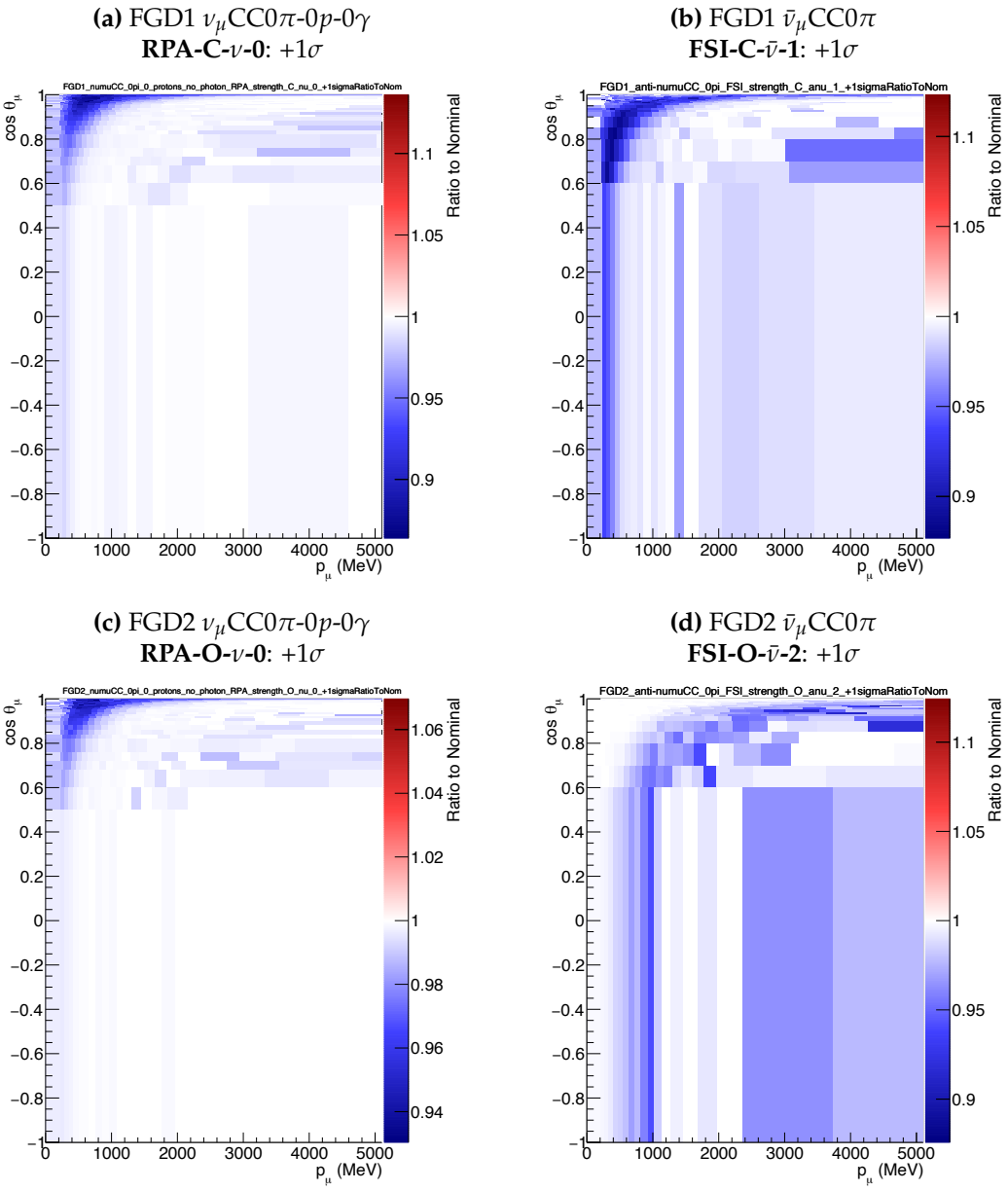

Figure 7.5: Ratio of the nominal and reweighted near-detector sample spectra when varying several of the new low-ω parameters. The samples are binned in 2D $p_\mu - \cos\theta_\mu$ phase space. All parameter variations are a $+1\sigma$ shift, meaning the parameters are set to 1. Suppression of the cross section is observed as expected.

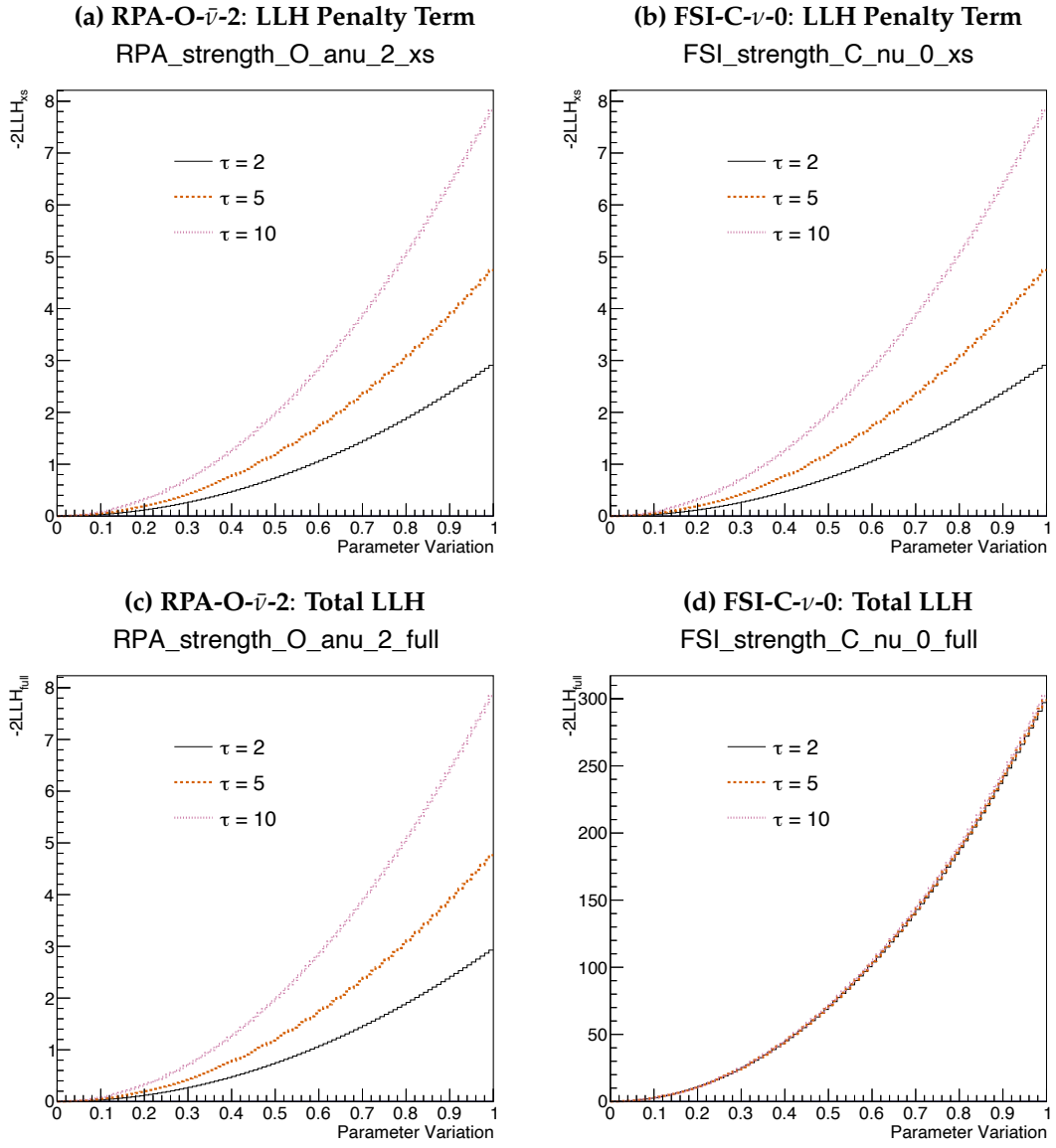

Figure 7.6: LLH scans for the RPA-O-$\bar{\nu}$-2 and FSI-C-ν-0 parameters. These parameters illustrate the extreme cases of the impact of regularisation. Both the penalty term and total LLH are shown for each regularisation strength tested.

when the constraint from the Asimov data is so strong. However, for less well-constrained parameters (e.g. RPA-O-$\bar{\nu}$-2), the effect of the regularisation does impact the total LLH as the penalty term is of comparable size to the sample LLH.

To further investigate the impact of regularisation strengths on parameter behaviour during the fitting process, a near-detector data fit was run for each regularisation strength tested. The parameter constraints and LLH were then compared.

The posterior distributions extracted from the near-detector data fits for each regularisation strength are shown in figures 7.7 and 7.8 for the RPA and FSI parameters respectively. Overall, the behaviour of the parameters across the tested values of τ is similar, with the largest differences between $\tau = 2$ and $\tau = \{5, 10\}$. The posterior distributions for parameters with strong constraints from Asimov data (e.g. RPA-C-ν-0 and FSI-C-ν-0) show minimal differences between each fit, as expected.

Finally, figure 7.9 shows a comparison of the LLH from each fit. Again, very small differences were observed when comparing the LLH from each fit. It was therefore concluded that the exact choice of τ is unlikely to have a tangible effect on the full oscillation analysis.

After establishing that the exact value of τ has a minimal effect on parameter behaviour and constraints, Markov chain diagnostics were used to inform a choice for τ. The autocorrelations were found to be largely similar for all parameters across the three fits, but the acceptance probability for the $\tau = 2$ fit was found to be 15%, while for $\tau = \{5, 10\}$ the acceptance probability is only 9%. Therefore, $\tau = 2$ was chosen as the regularisation strength for the subsequent oscillation fits. This τ will be used for the alternative model study presented in section 7.2.2 as well as T2K's next full oscillation analysis, where these parameters are the main addition to the updated interaction model. The prior correlation matrix for the parameters is shown in figure 7.10. There are zero correlations between the RPA and FSI parameters as they represent very different physical effects. Within the RPA and FSI parameter groups, correlations from the regularisation are included and extrapolated from individual target-flavour groups by assuming a correlation of 0.6 for carbon/oxygen and neutrino/antineutrino interactions. 0.6 was chosen as correlations are expected between carbon and oxygen interactions, and the addition of four nucleons should not drastically impact the effect of RPA and FSI corrections. Further studies should be carried out in future analyses to calculate a more physically-motivated calculation for the target-flavour correlation.

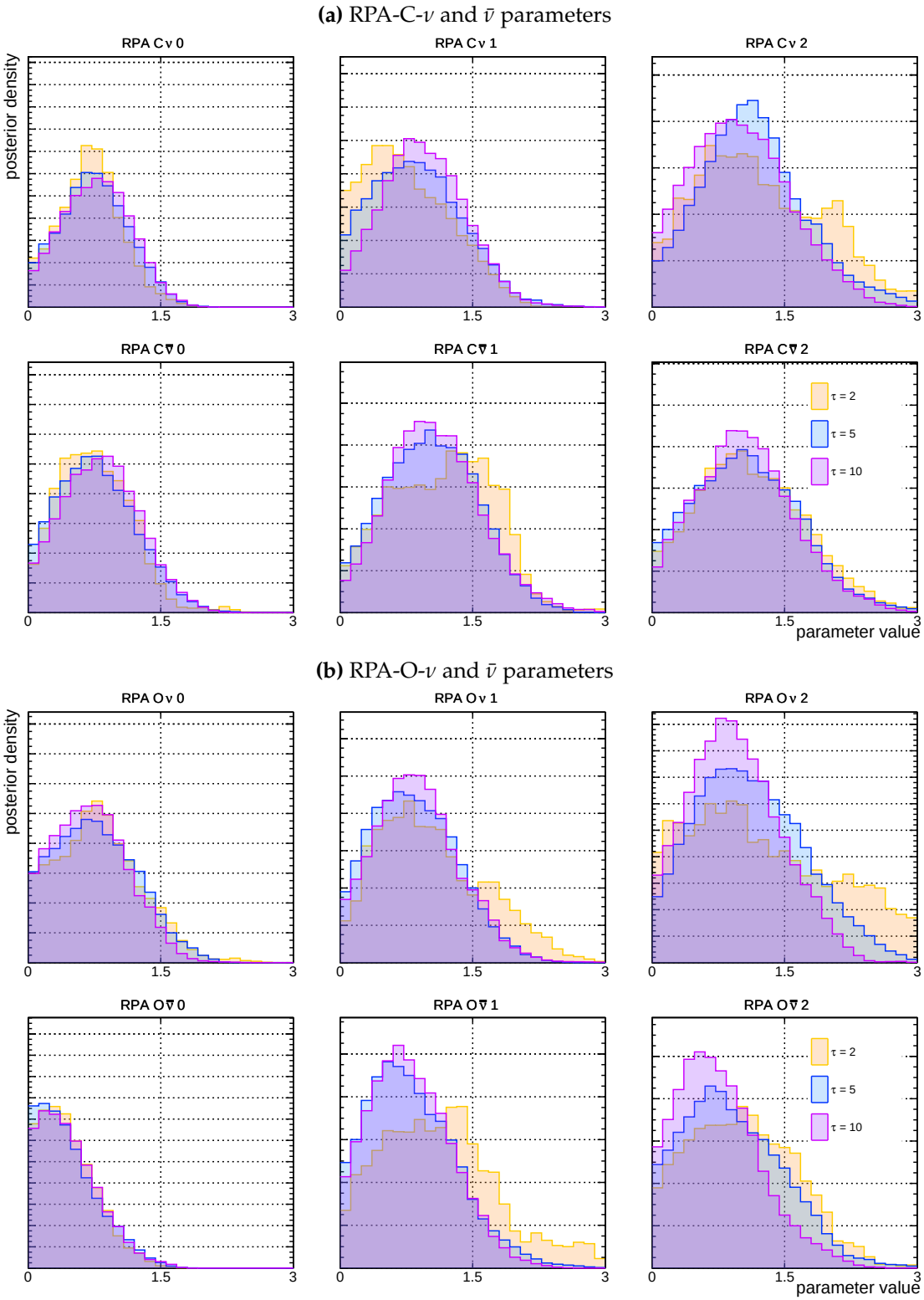

Figure 7.7: The posterior distributions for each RPA parameter for regularisation strengths 2 (orange), 5 (blue) and 10 (violet).

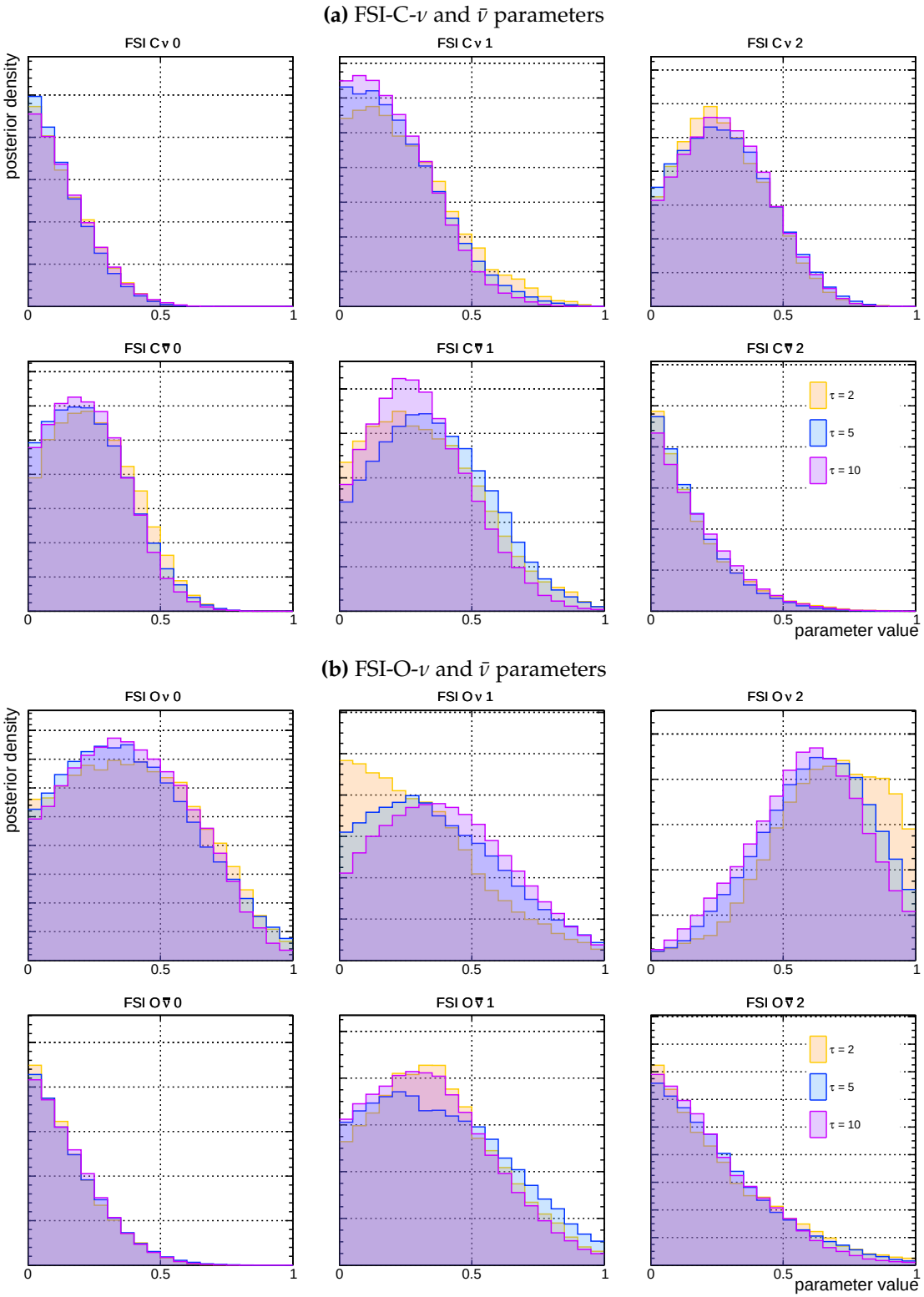

Figure 7.8: The posterior distributions for each FSI parameter for regularisation strengths 2 (orange), 5 (blue) and 10 (violet).

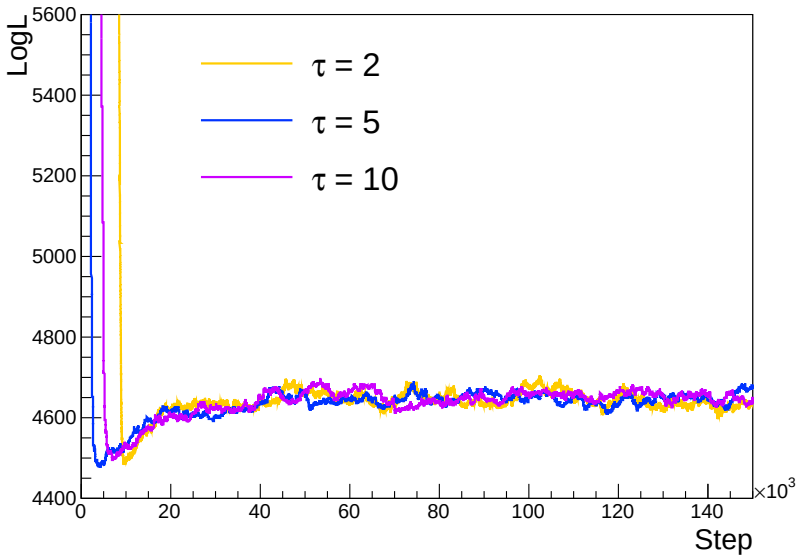

Figure 7.9: The LLH for each near-detector data fit for regularisation strengths 2 (orange), 5 (blue) and 10 (violet).

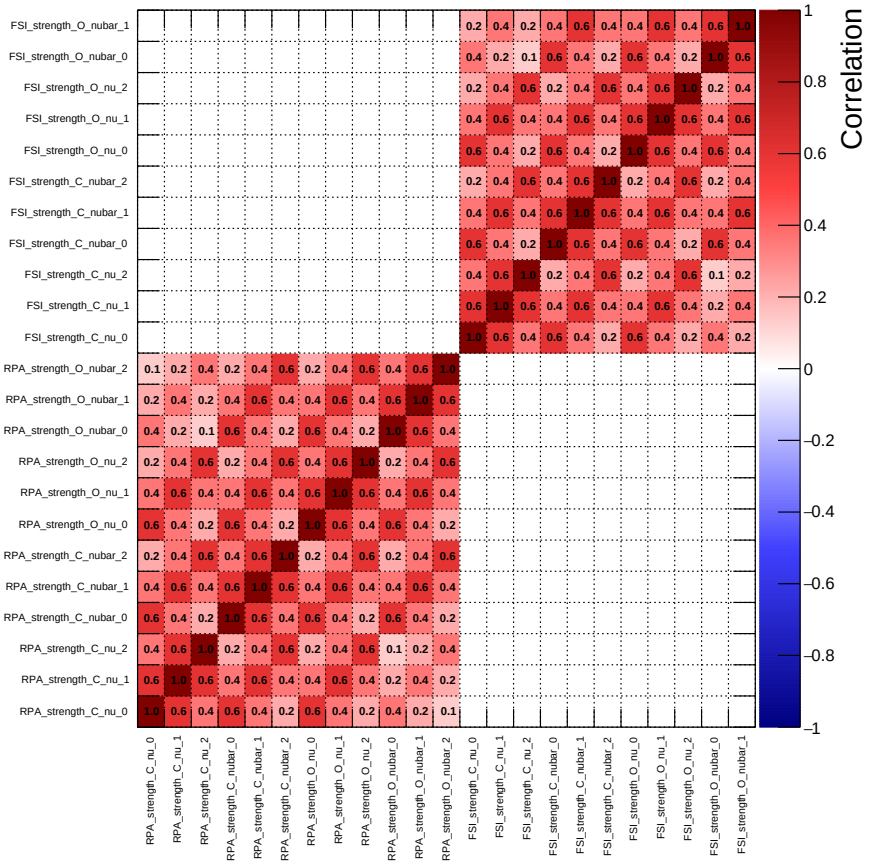

Figure 7.10: The prior correlation matrix for the RPA/FSI parameters for a regularisation strength $\tau = 2$.

7.2.2 Effect on HF-CRPA Fake Data Study Bias

The parameters described in this chapter were designed to introduce appropriate freedom to the interaction model to cover the wide model variations seen in the low-energy transfer region. They were motivated by the near 100% bias seen in the systematic uncertainty budget for Δm^2_{32} when performing the HF-CRPA alternative model study for T2K's latest oscillation analysis. To test whether these parameters help to resolve this bias, the alternative model study must be re-run.

Following the steps outlined in section 6.6, fake data sets were constructed for the near and far detectors using the HF-CRPA model prediction. These fake data sets were then used as inputs for a near and far-detector joint Asimov fit. Also, the optical potential parameters from the 2022 interaction model were removed as they share largely similar physics motivations to the new FSI parameters presented here. If the new parameters introduce the necessary freedom to the interaction model as was intended, there should be little differences between the constraints of a nominal Asimov fit[2] and the HF-CRPA fake-data fit. This would mean the interaction model has sufficient flexibility and robustness to describe the predictions of the HF-CRPA model.

Figure 7.11 compares the constraints on Δm^2_{32} from a nominal Asimov fit and the HF-CRPA fake-data fit. Comparing the posteriors, a small shift in the best-fit value for Δm^2_{32} is observed, but the credible intervals exhibit considerable overlap. This suggests the addition of new systematic parameters has added the necessary flexibility to the interaction model, allowing it to describe the model differences seen in the low-energy transfer region. This can be confirmed by re-calculating the fake-data study metric $B^{\text{syst.}}_{\Delta m^2_{32}}$ given in equation 6.5 and comparing it to the criterion in equation 6.6. When performing this calculation, it is found that $|B^{\text{syst.}}_{\Delta m^2_{32}}| = 0.44$, which is below the criterion for further action, such as smearing, to be taken.

[2]Here, a nominal Asimov fit refers to fitting near and far-detector Asimov data that was constructed using the parameter prior values specified in table 5.4.

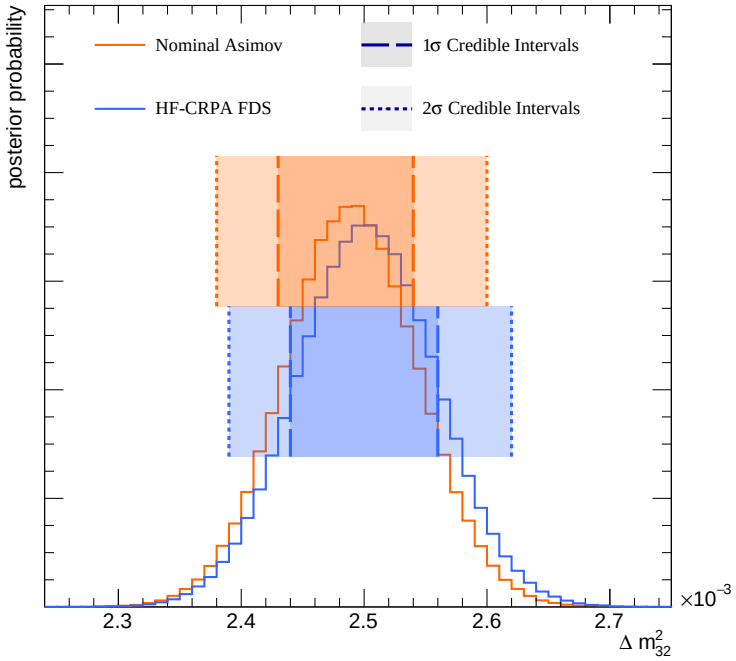

Figure 7.11: A comparison of the constraint on Δm^2_{32} between a nominal Asimov fit (orange) and the HF-CRPA fake data study (blue).

Additionally, the posterior distributions for the RPA and FSI parameters from both fits are shown in figures 7.12 and 7.13 respectively. The constraints on the RPA parameters are largely similar between the two fits. However, the FSI parameters shift to higher values in the HF-CRPA fake-data fit. This is good as it means the oscillation fit uses the new parameters to describe the HF-CRPA model prediction rather than shifting the oscillation parameters.

This work has demonstrated that the addition of novel, physically-motivated parameters, specifically designed to address large model differences at low-energy transfer, has successfully resolved the bias observed in the HF-CRPA fake data study. This bias constituted the largest contribution to the total systematic uncertainty in the measurement of Δm^2_{32} presented in chapter 6. These parameters will be utilised in subsequent T2K analyses and will form an important part of the interaction uncertainty model. It is important to mention that alternative model studies are typically performed using the PTheta fitting framework rather than MaCh3. However, due to the extensive validations carried out between the two

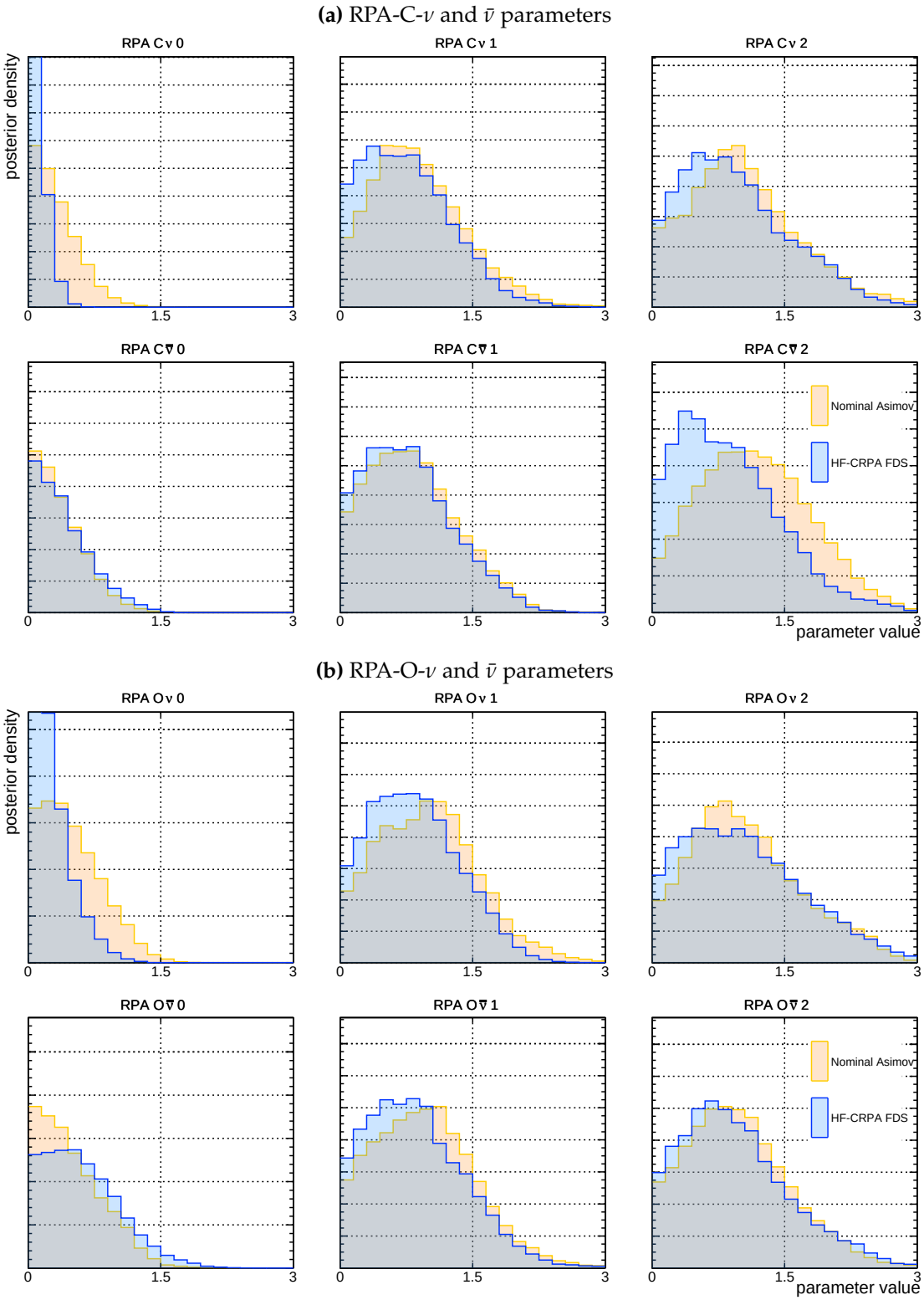

Figure 7.12: The posterior distributions for each RPA parameter from the nominal Asimov fit (orange) and HF-CRPA fake-data fit (blue).

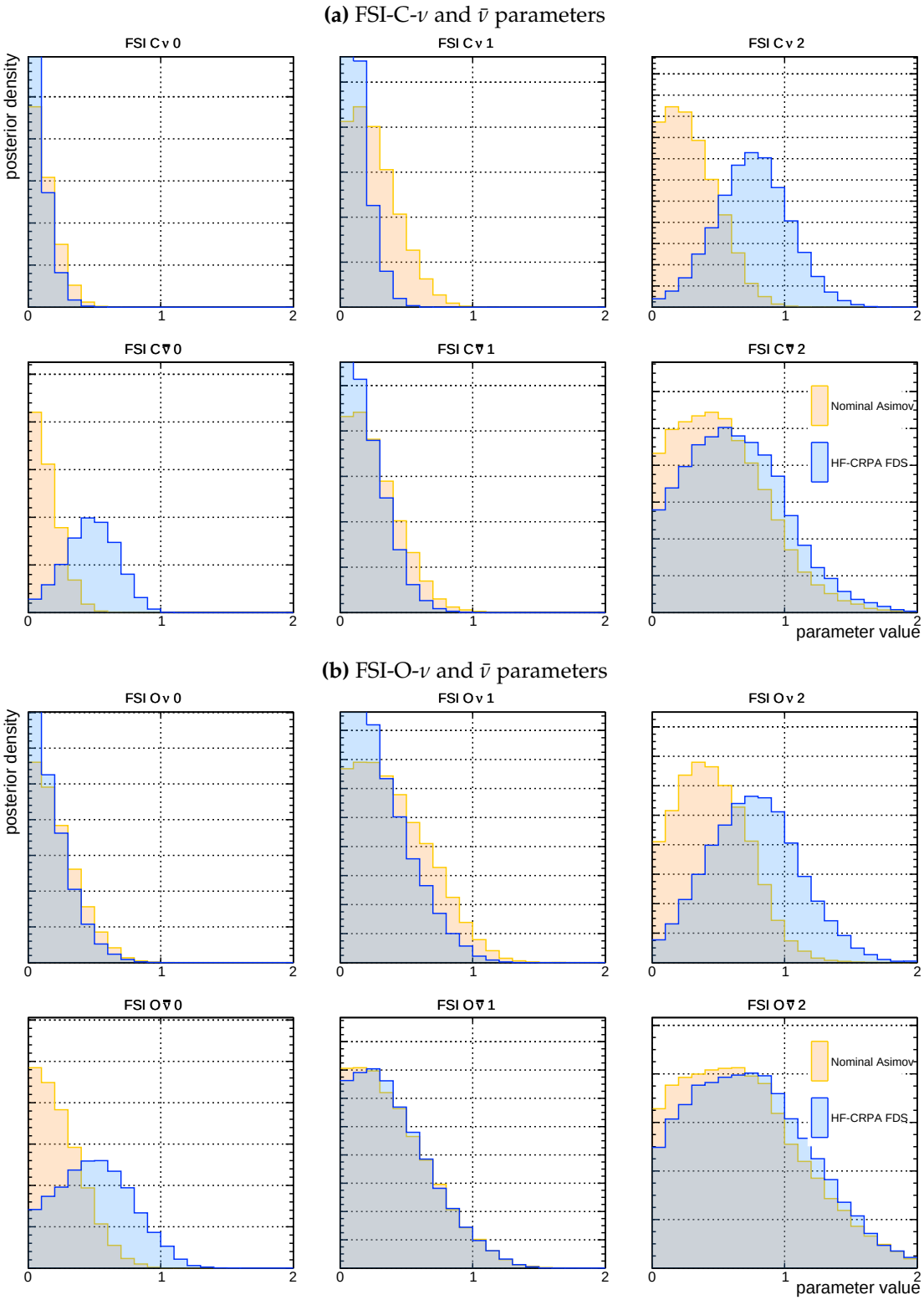

Figure 7.13: The posterior distributions for each FSI parameter from the nominal Asimov fit (orange) and HF-CRPA fake-data fit (blue).

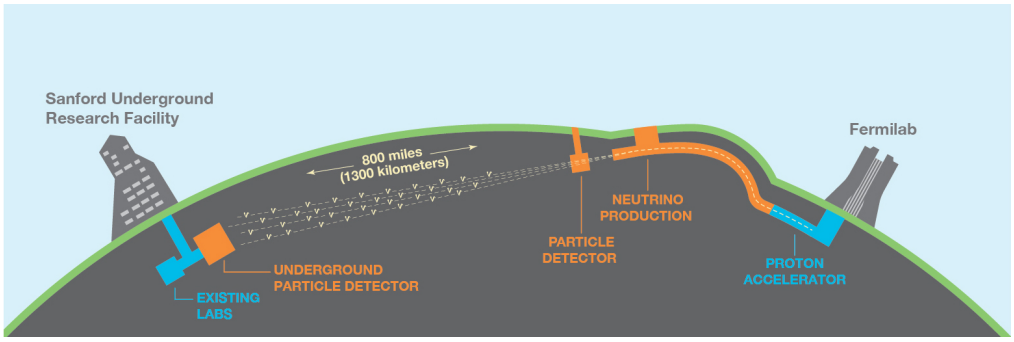

Figure 7.14: Schematic of the DUNE experiment. Figure from [3].

fitting groups, it is anticipated that the resolution demonstrated here will also apply to future T2K studies conducted using PTheta. For further refinement of these parameters, potential improvements include establishing a more physically motivated correlation between targets and flavours and conducting further investigations into the impact of the regularisation condition.

7.3 Removal Energy Systematics at DUNE

The Deep Underground Neutrino Experiment (DUNE) is a next-generation long-baseline neutrino oscillation experiment [3]. A schematic of the DUNE experiment setup is shown in figure 7.14. It has a broad physics programme, including high-precision measurements of the oscillation parameters, determination of the mass ordering, broader tests of the PMNS parameterisation and searching for BSM physics.

7.3.1 The DUNE Experiment

DUNE will utilise liquid argon time projection chamber (LArTPC) technology and a high-intensity broadband neutrino beam to achieve its physics aims. Compared to T2K, DUNE will operate at much higher energies, with average neutrino energies of around 2.5 GeV, and has a much longer baseline of 1285 km. The experimental setup for a typical LArTPC is shown in figure 7.15.

When a neutrino interacts with an argon atom in the TPC, secondary charged particles are produced which cause ionisation electrons to be emitted. These

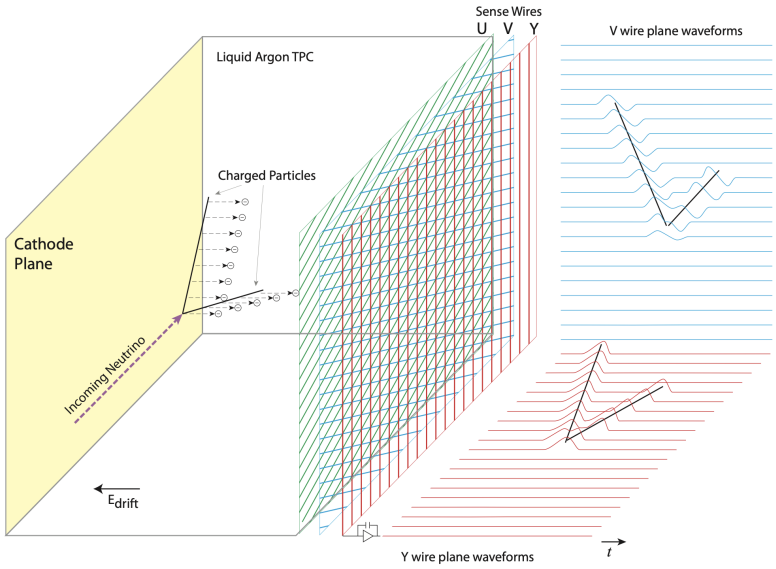

Figure 7.15: Schematic diagram of a LArTPC detector. Figure from [139].

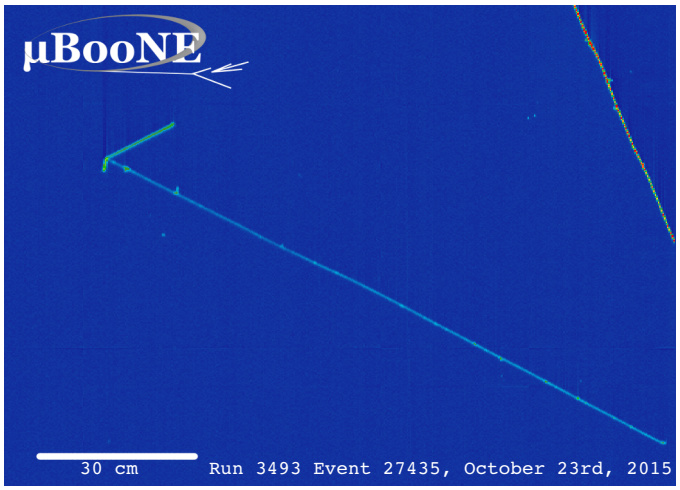

Figure 7.16: LArTPC event display from the MicroBooNE experiment. This event is likely to be a CCQE interaction, with the longest track being a muon, and the short track being a proton. Figure from [140].

electrons are then drifted toward the wire readout planes by a uniform electric field. Therefore, as charged particles propagate through the chamber, they create ionisation tracks which are recorded by the readout planes. As well as ionisation electrons, scintillation light is also emitted during the excitation and ionisation of argon atoms. This light can be used to trigger the start of an event. As such, LArTPCs can produce high-resolution images of neutrino interactions, an example of which can be seen in figure 7.16.

7.3.2 Motivation

With its utilisation of LArTPC detectors and unprecedented statistics[3], DUNE holds great promise for advancing our understanding of neutrino interactions. In addition, the DUNE near detectors will be able to exploit calorimetric information to accurately reconstruct the neutrino energy and also benefit from low tracking thresholds for charged hadrons. As a result, the DUNE near detectors possess significant constraining power for studying nuclear effects.

Modelling neutrino interactions involves estimating the struck nucleon's initial energy and momentum, which will be referred to throughout this section as the removal energy (E_{miss}) and momentum (p_{miss}). These estimations originate from nuclear models, which all predict different energy-momenta distributions. Choosing a suitable nuclear model is critically important for experiments as the entire interaction uncertainty model is built around this base model. The ideal nuclear model for DUNE's physics requirements needs to be physically motivated, capable of predicting lepton and hadron kinematics, easily reweightable, and perhaps most importantly, available in neutrino interaction generators. Taking into account these requirements, a local Fermi gas (LFG) model was chosen as the nuclear ground state model, with two physically-motivated modifications. First, the LFG as implemented in GENIE [141] had a fixed nucleon removal energy, which drastically limits the amount of phase space available. This was expanded by re-calculating the removal energy for a fixed nucleon momentum using energy-momentum conservation. Second, a correlated tail region was added to extend phase space coverage to the short-range correlations (SRC) region. SRC accounts for pairs of correlated nucleons with momentum higher than the Fermi momentum. This is an important region to have sufficient coverage as it possesses a high level of model disagreement. The nuclear ground state $E_{\text{miss}} - p_{\text{miss}}$ distributions after each modification are shown in figure 7.17.

[3]To provide further context, there are just 700 events across all T2K far-detector samples, whereas the DUNE far detectors are expected to observe 10,000 events over seven years.

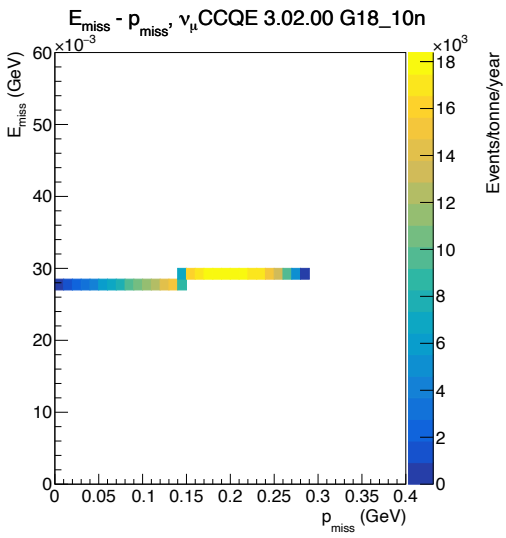

(a) Base GENIE tune

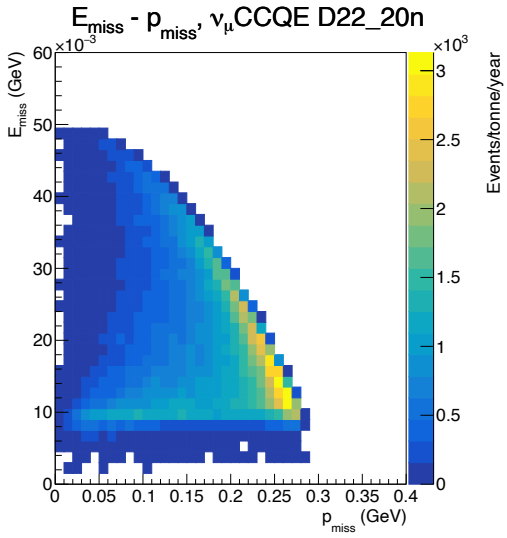

(b) Expand E_{miss} phase space

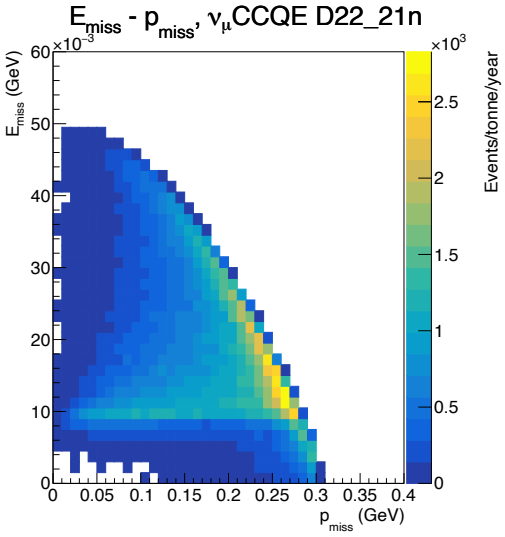

(c) Add correlated tail region

Figure 7.17: $E_{\text{misss}} - p_{\text{miss}}$ distributions for (a) the base GENIE LFG model, (b) recalculating E_{miss}, and (c) adding the correlated tail region ($E_{\text{miss}} < 10$ MeV). There are no FSI effects present in these distributions.

As the nuclear ground state model provides values for the struck nucleon's energy and momentum, the choice of the nuclear model directly impacts neutrino energy reconstruction. If an interaction model does not possess sufficient freedom to alter the chosen ground state model, it may lead to biases in the oscillation parameter measurements[4].

[4]Of course, if you choose the correct nuclear ground state model, you need not worry. However, I'm not sure this exists yet.

7.3.3 New Systematic Parameters

To introduce appropriate freedom for the interaction uncertainty model to modify the nuclear ground state, several new systematic parameters were developed that affect different regions of the removal energy spectrum. Three systematic parameters were implemented into DUNE's cross-section reweighting tools, and are described below.

1. $x_{\text{corr. tail}}$ – this parameter modifies the strength of the correlated tail region, which is defined as events with $E_{\text{miss}} < 10$ MeV. Events in this region receive a weight (w) that either enhances ($w > 1$) or suppresses ($w < 1$) the correlated tail. The parameter has range $x_{\text{corr. tail}} > 0$, and the weight is equal to the value of the parameter, $w = x_{\text{corr. tail}}$.

2. x_{mean} – this parameter increases or decreases the mean of the removal energy spectrum, and only affects events with $E_{\text{miss}} > 10$ MeV. The weight for each event is given by the formula $w = 1 + x_{\text{mean}} \cdot E_{\text{miss}}[GeV]$. Any negative weights are capped at 0. x_{mean} can be positive or negative, corresponding to an increase or decrease in the mean of the removal energy distribution.

3. $x_{\text{shift peak}}$ – this parameter shifts the peak of the removal energy distribution and introduces more physically-motivated, shell-like behaviour. Each event receives a weight $w = 1 + x_{\text{shift peak}} \cdot \cos(0.1\pi \cdot E_{\text{miss}}[MeV])$, where $x_{\text{shift peak}} \geq 0$. Weights cannot be negative and are capped at 0.2 to avoid discontinuities in the removal energy spectrum at $E_{\text{miss}} \sim 10$ MeV. The parameter only affects events with $E_{\text{miss}} > 10$ MeV.

To investigate the impact of each parameter, events were generated using the GENIE event generator and weights were calculated when varying each parameter through a reasonable range. The nominal and reweighted removal energy spectra were then plotted for each parameter variation, as shown in figure 7.18. Each parameter has the desired effect on the removal energy distribution.

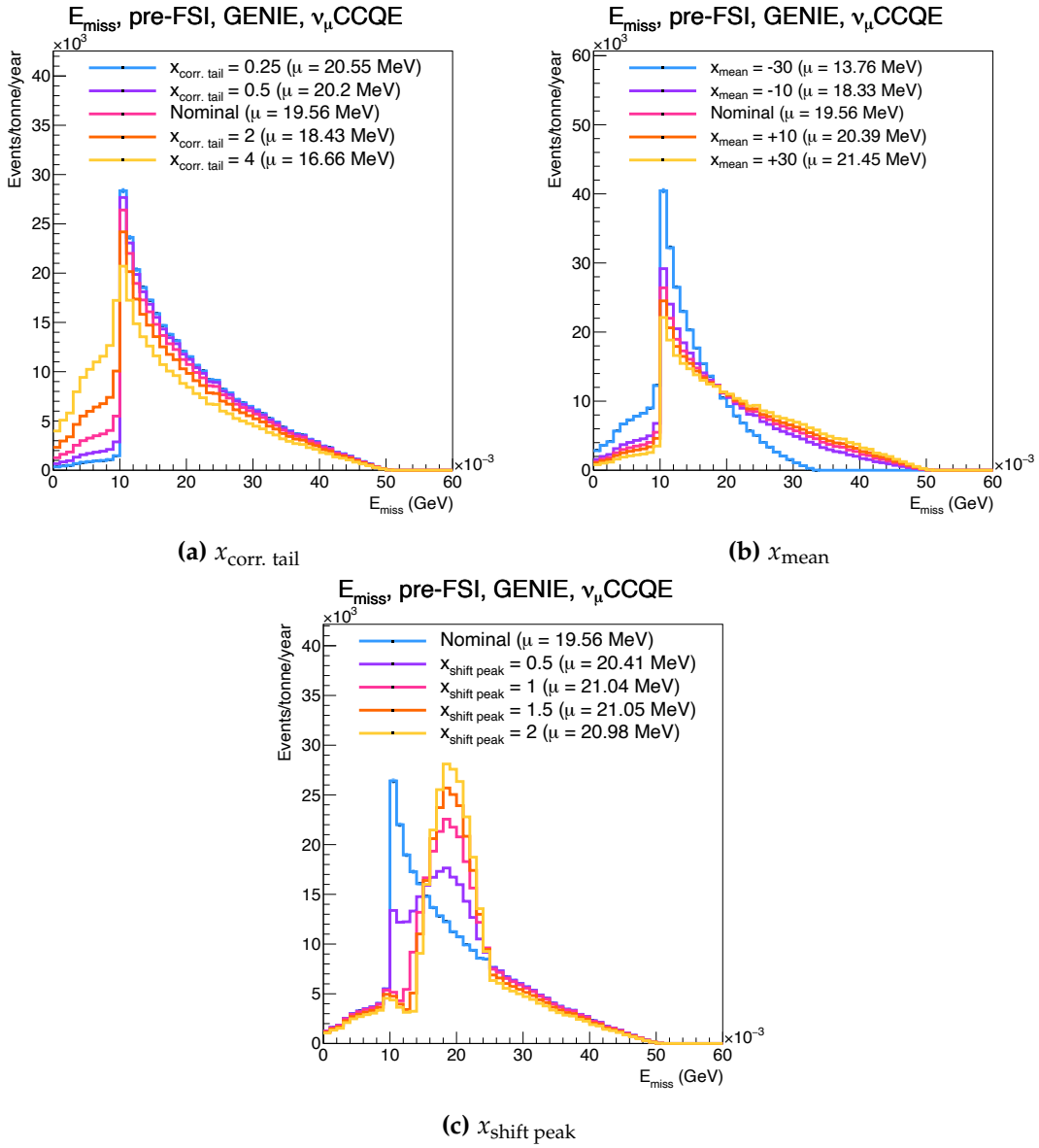

(a) $x_{\text{corr. tail}}$ **(b)** x_{mean}

(c) $x_{\text{shift peak}}$

Figure 7.18: The removal energy distribution after varying each of the missing energy parameters. The means of the distributions are also listed, and each distribution is renormalised to conserve the total cross section. The expected effects are observed in the distributions.

7.3.4 Impact on Oscillation Analyses

After validating the effects of the new parameters on the nuclear ground state, their impact on typical oscillation analysis observables was investigated.

First, given our choice of nuclear ground state model, the expected changes are observed in the transverse momentum imbalance distribution, shown in figure 7.19a. The transverse momentum imbalance, dp_{T}, is the momentum imbalance in

the transverse plane[5], and is one of the single-transverse kinematic imbalance variables [39]. In the absence of nuclear effects, dp_{T} would be zero. Therefore, modifying the nuclear ground state *should* cause measurable distortions in the dp_{T} spectrum, and indeed that is seen. Further, 7.19b shows that when shifting the mean of the removal energy spectrum by approximately 10 MeV, a direct impact on the neutrino energy reconstruction bias of a similar magnitude is observed. On the scale of DUNE neutrino energies, this may seem small, but DUNE's LAr detectors *will* be able to resolve such small energy differences. It is therefore important that such biases are correctly accounted for in the interaction model. Additionally, as the neutrino energy reconstruction is affected, mis-modelling the nuclear ground state will also impact oscillation parameter measurements. This may have an especially noticeable effect at DUNE's second oscillation maximum, which sits at a much lower neutrino energy of $0.8 - 1$ GeV.

Figure 7.20 shows the effect of varying the $x_{\text{corr. tail}}$ and x_{mean} parameters on the reconstructed inelasticity (y_{rec}) and reconstructed neutrino energy (E_{rec}) distributions respectively. Inelasticity is defined as the fraction of the reconstructed neutrino energy attributed to the hadronic system. E_{rec} and y_{rec} are of particular importance as they were the kinematic variables used for the previous DUNE oscillation analysis. As illustrated in figures 7.20a and 7.20b, modifications to the nuclear ground state have no impact on these distributions. Therefore, no obvious biases would be detected during an oscillation fit when observing more traditional 'fit' variables, despite a clear bias being present, as shown in figure 7.19b.

The development of physically motivated and appropriate interaction uncertainties to describe the ground state nuclear model will therefore be critically important as oscillation parameter measurements move into the precision era. The parameters presented here have been developed especially for DUNE-era statistics and measurements and will form an important part of the interaction uncertainty model for the next DUNE oscillation analysis.

[5]Wow, who would have thought it?

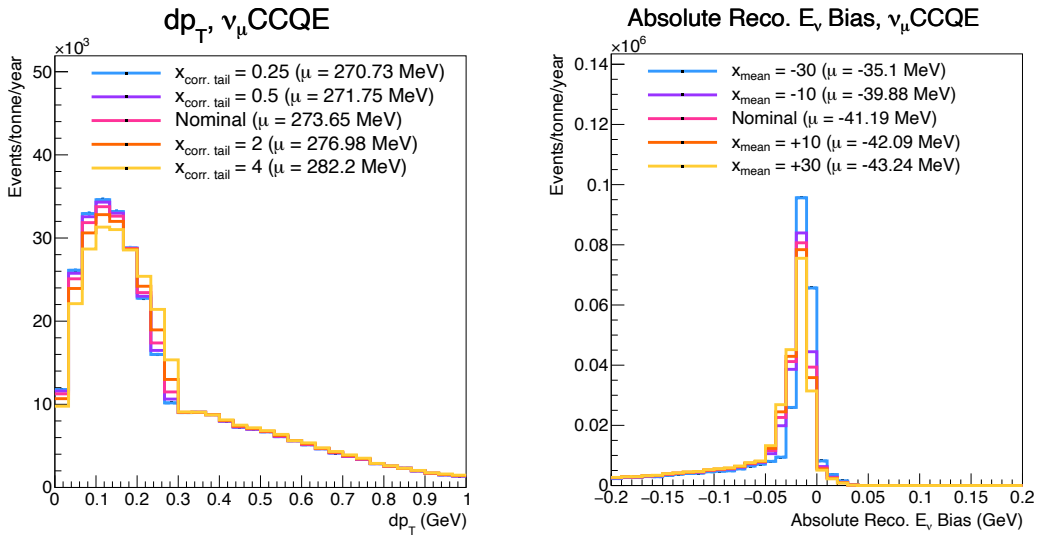

(a) dp_{T} **(b)** $\delta E_{\nu}^{\mathrm{bias}} = E_{\mathrm{rec}}^{\nu} - E_{\mathrm{true}}^{\nu}$

Figure 7.19: The impact of $x_{\text{corr. tail}}$ and x_{mean} variations on the transverse momentum imbalance (left) and reconstructed neutrino energy bias (right) distributions respectively.

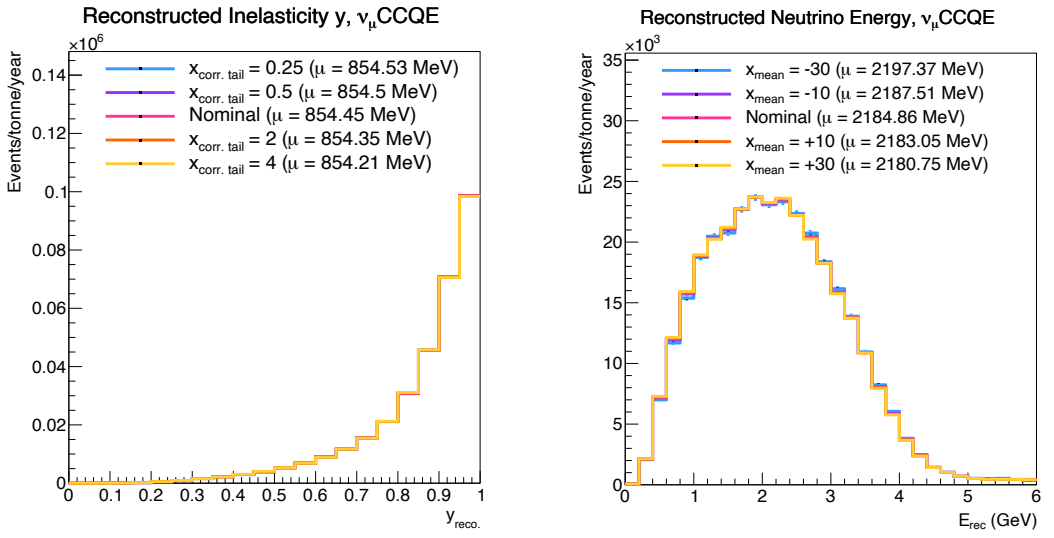

(a) $y_{reco.} = 1 - E_{\mathrm{lep}}/E_{\mathrm{rec}}^{\nu}$ **(b)** E_{rec}^{ν}

Figure 7.20: The impact of $x_{\text{corr. tail}}$ and x_{mean} variations on the reconstructed inelasticity (left) and reconstructed neutrino energy (right) distributions respectively.

8
Conclusions and Outlook

This thesis has presented the latest oscillation parameter constraints from the T2K experiment and has also described the development and implementation of novel neutrino interaction uncertainties at current and future-generation long-baseline experiments.

A Bayesian Markov chain Monte Carlo method was used to extract oscillation parameter constraints at the T2K experiment. These are T2K's most robust measurements to date, and this set of results also includes many notable analysis framework improvements. A new far-detector sample was added [115], as well as expanded near-detector selections [111]. Furthermore, a more robust and physically motivated neutrino interaction uncertainty model was used [120], and NA61/SHINE replica target data was utlised to improve constraints on the neutrino flux [112].

When applying an external constraint on $\sin^2\theta_{13}$ from reactor experiments, CP-conserving values of the CP-violating phase δ_{CP} and the Jarlskog invariant $\mathcal{J}_{\mathrm{CP}}$ are excluded from the 90% credible interval. A slight preference for normal mass ordering and the upper octant of $\sin^2\theta_{23}$ is also found.

When performing alternative model studies to test the flexibility of the interaction model used in the oscillation analysis, a significant bias on Δm^2_{32} was discovered when fitting the predictions of the HF-CRPA model. This bias

approached 100% of the total systematic uncertainty on Δm^2_{32} and prompted additional manual smearing of the Δm^2_{32} credible intervals to account for this bias. The HF-CRPA model predicts a significantly different neutrino cross section at low energy transfer. Consequently, a new set of interaction uncertainty parameters was designed and implemented into the oscillation analysis framework to specifically account for these variations.

When re-performing the HF-CRPA alternative model study with the newly developed interaction uncertainty parameters, the bias on Δm^2_{32} is found to be lower than the criteria for further action to be taken, and half that of the original bias from the previous oscillation analysis. The introduction of new systematic parameters to describe large model variations at low energy transfer has therefore added the necessary flexibility to the interaction model so it can properly describe HF-CRPA model predictions.

The final section of this thesis presents the development of novel neutrino interaction uncertainties specifically designed for next-generation long-baseline experiments such as DUNE. These new parameters modify the nuclear ground state model and are motivated by the low tracking thresholds for charged hadrons in the DUNE near detectors, as well as their ability to use calorimetric information to accurately reconstruct the neutrino energy. It is demonstrated that mis-modelling the nuclear ground state may lead to biases in oscillation parameter measurements.

Measurements at current-generation long-baseline oscillation experiments are limited by statistical uncertainties. However, next-generation experiments such as DUNE and Hyper-K will be limited by systematic uncertainties. With neutrino interaction uncertainties currently representing a significant component of the total systematic uncertainty, further work and additional neutrino cross-section measurements are required to improve our understanding of neutrino interactions if next-generation experiments are to achieve their physics objectives.

Bibliography

[1] A. D. Sakharov. "Violation of CP Invariance, C asymmetry, and baryon asymmetry of the universe". In: *Pisma Zh. Eksp. Teor. Fiz.* 5 (1967), pp. 32–35.

[2] K. Abe et al. "The T2K Experiment". In: *Nucl. Instrum. Meth. A* 659 (2011), pp. 106–135. arXiv: 1106.1238 [physics.ins-det].

[3] Babak Abi et al. "Deep Underground Neutrino Experiment (DUNE), Far Detector Technical Design Report, Volume II: DUNE Physics". In: (Feb. 2020). arXiv: 2002.03005 [hep-ex].

[4] K. Abe et al. "Hyper-Kamiokande Design Report". In: (May 2018). arXiv: 1805.04163 [physics.ins-det].

[5] W. Pauli. "Dear radioactive ladies and gentlemen". In: *Phys. Today* 31N9 (1978), p. 27.

[6] C. L. Cowan et al. "Detection of the free neutrino: A Confirmation". In: *Science* 124 (1956), pp. 103–104.

[7] Y. Fukuda et al. "Evidence for Oscillation of Atmospheric Neutrinos". In: *Phys. Rev. Lett.* 81 (8 1998), pp. 1562–1567. URL: https://link.aps.org/doi/10.1103/PhysRevLett.81.1562.

[8] J Chadwick. "Intensitätsverteilung im magnetischen Spectrum der β-Strahlen von radium B + C". In: *Verhandl. Dtsc. Phys. Ges.* 16 (1914), p. 383. URL: https://cds.cern.ch/record/262756.

[9] E. Fermi. "An attempt of a theory of beta radiation. 1." In: *Z. Phys.* 88 (1934), pp. 161–177.

[10] J. Chadwick. "Possible Existence of a Neutron". In: *Nature* 129 (1932), p. 312.

[11] F. Reines et al. "Detection of the Free Antineutrino". In: *Phys. Rev.* 117 (1 1960), pp. 159–173. URL: https://link.aps.org/doi/10.1103/PhysRev.117.159.

[12] G. T. Danby et al. "Observation of High-Energy Neutrino Reactions and the Existence of Two Kinds of Neutrinos". In: *Physical Review Letters* 9 (1962), pp. 36–44.

[13] B. Pontecorvo. "Electron and Muon Neutrinos". In: *Zh. Eksp. Teor. Fiz.* 37 (1959), pp. 1751–1757.

[14] J. J. Aubert et al. "Experimental Observation of a Heavy Particle J". In: *Phys. Rev. Lett.* 33 (1974), pp. 1404–1406.

[15] J. E. Augustin et al. "Discovery of a Narrow Resonance in e^+e^- Annihilation". In: *Phys. Rev. Lett.* 33 (1974), pp. 1406–1408.

[16] M. L. Perl et al. "Evidence for Anomalous Lepton Production in $e^+ - e^-$ Annihilation". In: *Phys. Rev. Lett.* 35 (22 1975), pp. 1489–1492. URL: https://link.aps.org/doi/10.1103/PhysRevLett.35.1489.

[17] Cush. *Standard Model of Elementary particles*. Online; accessed 18-12-2023. URL: "https://en.m.wikipedia.org/wiki/File:Standard_Model_of_Elementary_Particles.svg".

[18] Georges Aad et al. "Observation of a new particle in the search for the Standard Model Higgs boson with the ATLAS detector at the LHC". In: *Phys. Lett. B* 716 (2012), pp. 1–29. arXiv: 1207.7214 [hep-ex].

[19] S. Schael et al. "Precision electroweak measurements on the Z resonance". In: *Phys. Rept.* 427 (2006), pp. 257–454. arXiv: hep-ex/0509008.

[20] K. Kodama et al. "Observation of tau neutrino interactions". In: *Phys. Lett. B* 504 (2001), pp. 218–224. arXiv: hep-ex/0012035.

[21] Ziro Maki, Masami Nakagawa, and Shoichi Sakata. "Remarks on the unified model of elementary particles". In: *Prog. Theor. Phys.* 28 (1962), pp. 870–880.

[22] Boris Kayser. "Neutrino Oscillation Physics". In: *2011 European School of High-Energy Physics*. 2014, pp. 107–117. arXiv: 1206.4325 [hep-ph].

[23] Boris Kayser. "Neutrino physics". In: *eConf* C040802 (2004). Ed. by Joanne Hewett et al., p. L004. arXiv: hep-ph/0506165.

[24] M. Aker et al. "Direct neutrino-mass measurement with sub-electronvolt sensitivity". In: *Nature Phys.* 18.2 (2022), pp. 160–166. arXiv: 2105.08533 [hep-ex].

[25] Joachim Kopp. "Phenomenology of Three-Flavour Neutrino Oscillations". MA thesis. Technische Universit¨at M¨unchen, 2006.

[26] Boris Kayser. "On the Quantum Mechanics of Neutrino Oscillation". In: *Phys. Rev. D* 24 (1981), p. 110.

[27] P. A. Zyla et al. "Review of Particle Physics". In: *PTEP* 2020.8 (2020), p. 083C01.

[28] Maria Prado Rodriguez. "Neutrino Mass Ordering with IceCube DeepCore". In: *Physical Sciences Forum* 8.1 (2023). URL: https://www.mdpi.com/2673-9984/8/1/7.

[29] L. Wolfenstein. "Neutrino Oscillations in Matter". In: *Phys. Rev. D* 17 (1978), pp. 2369–2374.

[30] S. P. Mikheev and A. Yu. Smirnov. "Resonant amplification of neutrino oscillations in matter and solar neutrino spectroscopy". In: *Nuovo Cim. C* 9 (1986), pp. 17–26.

[31] Carlo Giunti and Chung W. Kim. *Fundamentals of Neutrino Physics and Astrophysics*. 2007.

[32] Roger Wendell. *Prob3++ software for computing three flavour neutrino.* https://github.com/rogerwendell/Prob3plusplus.

[33] Kaoru Hagiwara, Naotoshi Okamura, and Ken-ichi Senda. "The earth matter effects in neutrino oscillation experiments from Tokai to Kamioka and Korea". In: *JHEP* 09 (2011), p. 082. arXiv: 1107.5857 [hep-ph].

[34] V. Barger et al. "Matter effects on three-neutrino oscillations". In: *Phys. Rev. D* 22 (11 1980), pp. 2718–2726. URL: https://link.aps.org/doi/10.1103/PhysRevD.22.2718.

[35] C. Jarlskog. "Commutator of the Quark Mass Matrices in the Standard Electroweak Model and a Measure of Maximal CP Nonconservation". In: *Phys. Rev. Lett.* 55 (1985), p. 1039.

[36] Mark Hartz. https://t2k.org/docs/plotsx/general/oa. 2016.

[37] K. Abe et al. "Measurements of neutrino oscillation parameters from the T2K experiment using 3.6×10^{21} protons on target". In: *Eur. Phys. J. C* 83.9 (2023), p. 782. arXiv: 2303.03222 [hep-ex].

[38] Yoshinari Hayato and Luke Pickering. "The NEUT neutrino interaction simulation program library". In: *Eur. Phys. J. ST* 230.24 (2021), pp. 4469–4481. arXiv: 2106.15809 [hep-ph].

[39] X. G. Lu et al. "Measurement of nuclear effects in neutrino interactions with minimal dependence on neutrino energy". In: *Phys. Rev. C* 94.1 (2016), p. 015503. arXiv: 1512.05748 [nucl-th].

[40] O. Benhar et al. "Spectral function of finite nuclei and scattering of GeV electrons". In: *Nucl. Phys. A* 579 (1994), pp. 493–517.

[41] Ronen Weiss et al. "Energy and momentum dependence of nuclear short-range correlations - Spectral function, exclusive scattering experiments and the contact formalism". In: *Phys. Lett. B* 791 (2019), pp. 242–248. arXiv: 1806.10217 [nucl-th].

[42] Jaafar Chakrani, Margherita Buizza Avanzini, and Stephen Dolan. "Parametrising CCQE uncertainties in the Spectral Function model for neutrino oscillation analyses". In: *PoS* NuFact2021 (2022), p. 235. arXiv: 2202.03219 [hep-ph].

[43] L. Alvarez-Ruso et al. "NuSTEC White Paper: Status and challenges of neutrino–nucleus scattering". In: *Prog. Part. Nucl. Phys.* 100 (2018), pp. 1–68. arXiv: 1706.03621 [hep-ph].

[44] J. N. Bahcall; W.A. Fowler; I. Jr. Iben; R. L. Sears. "Solar Neutrino Flux". In: *Astrophysical Journal* 137 (1963), pp. 344–346.

[45] John N. Bahcall and Carlos Pena-Garay. "Solar models and solar neutrino oscillations". In: *New J. Phys.* 6 (2004), p. 63. arXiv: hep-ph/0404061.

[46] Raymond Davis, Don S. Harmer, and Kenneth C. Hoffman. "Search for Neutrinos from the Sun". In: *Phys. Rev. Lett.* 20 (21 1968), pp. 1205–1209. URL: https://link.aps.org/doi/10.1103/PhysRevLett.20.1205.

[47] K. S. Hirata et al. "Observation of B-8 Solar Neutrinos in the Kamiokande-II Detector". In: *Phys. Rev. Lett.* 63 (1989), p. 16.

[48] M. Cribier. "Results of the whole GALLEX experiment". In: *Nucl. Phys. B Proc. Suppl.* 70 (1999). Ed. by A. Bottino, Alessandra Di Credico, and Piero Monacelli, pp. 284–291.

[49] J. N. Abdurashitov et al. "Solar neutrino flux measurements by the Soviet-American Gallium Experiment (SAGE) for half the 22 year solar cycle". In: *J. Exp. Theor. Phys.* 95 (2002), pp. 181–193. arXiv: astro-ph/0204245.

[50] John N. Bahcall. "Solar models: An Historical overview". In: *AAPPS Bull.* 12.4 (2002). Ed. by F. von Feilitzsch and N. Schmitz, pp. 12–19. arXiv: astro-ph/0209080.

[51] B. Pontecorvo. "Neutrino Experiments and the Problem of Conservation of Leptonic Charge". In: *Zh. Eksp. Teor. Fiz.* 53 (1967), pp. 1717–1725.

[52] Q. R. Ahmad et al. "Direct evidence for neutrino flavor transformation from neutral current interactions in the Sudbury Neutrino Observatory". In: *Phys. Rev. Lett.* 89 (2002), p. 011301. arXiv: nucl-ex/0204008.

[53] John N. Bahcall, M. H. Pinsonneault, and Sarbani Basu. "Solar models: Current epoch and time dependences, neutrinos, and helioseismological properties". In: *Astrophys. J.* 555 (2001), pp. 990–1012. arXiv: astro-ph/0010346.

[54] Mark Thomson. *Modern particle physics*. New York: Cambridge University Press, 2013.

[55] M. P. Decowski. "KamLAND's precision neutrino oscillation measurements". In: *Nucl. Phys. B* 908 (2016), pp. 52–61.

[56] P. F. de Salas et al. "2020 global reassessment of the neutrino oscillation picture". In: *JHEP* 02 (2021), p. 071. arXiv: 2006.11237 [hep-ph].

[57] F. P. An et al. "Precision Measurement of Reactor Antineutrino Oscillation at Kilometer-Scale Baselines by Daya Bay". In: *Phys. Rev. Lett.* 130 (16 2023), p. 161802. URL: https://link.aps.org/doi/10.1103/PhysRevLett.130.161802.

[58] Y. Abe et al. "Measurement of θ_{13} in Double Chooz using neutron captures on hydrogen with novel background rejection techniques". In: *JHEP* 01 (2016), p. 163. arXiv: 1510.08937 [hep-ex].

[59] J. H. Choi et al. "Observation of Energy and Baseline Dependent Reactor Antineutrino Disappearance in the RENO Experiment". In: *Phys. Rev. Lett.* 116.21 (2016), p. 211801. arXiv: 1511.05849 [hep-ex].

[60] Petr Vogel, Liangjian Wen, and Chao Zhang. "Neutrino Oscillation Studies with Reactors". In: *Nature Commun.* 6 (2015), p. 6935. arXiv: 1503.01059 [hep-ex].

[61] T. J. Haines et al. "Calculation of Atmospheric Neutrino Induced Backgrounds in a Nucleon Decay Search". In: *Phys. Rev. Lett.* 57 (1986), pp. 1986–1989.

[62] K.S. Hirata et al. "Observation of a small atmospheric νμ/νe ratio in Kamiokande". In: *Physics Letters B* 280.1 (1992), pp. 146–152. URL: https://www.sciencedirect.com/science/article/pii/0370269392907886.

[63] Takaaki Kajita. "Atmospheric neutrinos". In: *New Journal of Physics* 6.1 (2004), p. 194. URL: https://dx.doi.org/10.1088/1367-2630/6/1/194.

[64] R. Acciarri et al. "A Proposal for a Three Detector Short-Baseline Neutrino Oscillation Program in the Fermilab Booster Neutrino Beam". In: (Mar. 2015). arXiv: 1503.01520 [physics.ins-det].

[65] M. A. Acero et al. "Improved measurement of neutrino oscillation parameters by the NOvA experiment". In: *Phys. Rev. D* 106.3 (2022), p. 032004. arXiv: 2108.08219 [hep-ex].

[66] K. Abe et al. "Atmospheric neutrino oscillation analysis with external constraints in Super-Kamiokande I-IV". In: *Phys. Rev. D* 97.7 (2018), p. 072001. arXiv: 1710.09126 [hep-ex].

[67] K. Yasutome et al. *P-theta 2021 Run 1-10 Joint-fit Analysis with multi-ring sample*. Tech. rep. TN-430. T2K, 2022. eprint: https://t2k.org/docs/technotes/430.

[68] M. G. Aartsen et al. "Measurement of Atmospheric Neutrino Oscillations at 6–56 GeV with IceCube DeepCore". In: *Phys. Rev. Lett.* 120.7 (2018), p. 071801. arXiv: 1707.07081 [hep-ex].

[69] P. Adamson et al. "Precision Constraints for Three-Flavor Neutrino Oscillations from the Full MINOS+ and MINOS Dataset". In: *Phys. Rev. Lett.* 125.13 (2020), p. 131802. arXiv: 2006.15208 [hep-ex].

[70] Babak Abi et al. "Deep Underground Neutrino Experiment (DUNE), Far Detector Technical Design Report, Volume I Introduction to DUNE". In: *JINST* 15.08 (2020), T08008. arXiv: 2002.02967 [physics.ins-det].

[71] Ivan Esteban et al. "The fate of hints: updated global analysis of three-flavor neutrino oscillations". In: *JHEP* 09 (2020), p. 178. arXiv: 2007.14792 [hep-ph].

[72] Ivan Esteban et al. *NuFit 5.2*. http://www.nu-fit.org/. 2022.

[73] C. R. Das et al. "Determination of the θ_{23} octant in long baseline neutrino experiments within and beyond the standard model". In: *Phys. Rev. D* 97.3 (2018), p. 035023. arXiv: 1708.05182 [hep-ph].

[74] T. Sekiguchi et al. "Development and operational experience of magnetic horn system for T2K experiment". In: *Nucl. Instrum. Meth. A* 789 (2015), pp. 57–80. arXiv: 1502.01737 [physics.ins-det].

[75] K. Matsuoka et al. "Design and performance of the muon monitor for the T2K neutrino oscillation experiment". In: *Nucl. Instrum. Meth. A* 624 (2010), pp. 591–600. arXiv: 1008.4077 [physics.ins-det].

[76] The T2K Collaboration. *T2K Official Plots*. https://t2k.org/docs/plots. 2024.

[77] K Abe et al. "Measurements of the T2K neutrino beam properties using the INGRID on-axis near detector". In: *Nuclear Instruments and Methods in Physics Research Section A: Accelerators, Spectrometers, Detectors and Associated Equipment* 694 (2012), pp. 211–223.

[78] K. Abe et al. "Measurement of neutrino and antineutrino oscillations by the T2K experiment including a new additional sample of ν_e interactions at the far detector". In: *Phys. Rev. D* 96.9 (2017). [Erratum: Phys.Rev.D 98, 019902 (2018)], p. 092006. arXiv: 1707.01048 [hep-ex].

[79] S. Assylbekov et al. "The T2K ND280 off-axis pi–zero detector". In: *Nuclear Instruments and Methods in Physics Research Section A: Accelerators, Spectrometers, Detectors and Associated Equipment* 686 (2012), pp. 48–63. URL: https://www.sciencedirect.com/science/article/pii/S0168900212005153.

[80] P. A. Amaudruz et al. "The T2K Fine-Grained Detectors". In: *Nucl. Instrum. Meth. A* 696 (2012), pp. 1–31. arXiv: 1204.3666 [physics.ins-det].

[81] N. Abgrall et al. "Time Projection Chambers for the T2K Near Detectors". In: *Nucl. Instrum. Meth. A* 637 (2011), pp. 25–46. arXiv: 1012.0865 [physics.ins-det].

[82] I. Giomataris et al. “Micromegas in a bulk”. In: *Nuclear Instruments and Methods in Physics Research Section A: Accelerators, Spectrometers, Detectors and Associated Equipment* 560.2 (2006), pp. 405–408.

[83] D. Allan et al. “The Electromagnetic Calorimeter for the T2K Near Detector ND280”. In: *JINST* 8 (2013), P10019. arXiv: 1308.3445 [physics.ins-det].

[84] S. Aoki et al. “The T2K Side Muon Range Detector (SMRD)”. In: *Nucl. Instrum. Meth. A* 698 (2013), pp. 135–146. arXiv: 1206.3553 [physics.ins-det].

[85] K. Abe et al. “T2K ND280 Upgrade - Technical Design Report”. In: (Jan. 2019). arXiv: 1901.03750 [physics.ins-det].

[86] Y. Fukuda et al. “The Super-Kamiokande detector”. In: *Nucl. Instrum. Meth. A* 501 (2003). Ed. by V. A. Ilyin, V. V. Korenkov, and D. Perret-Gallix, pp. 418–462.

[87] Y. Itow et al. “The JHF-Kamioka neutrino project”. In: *3rd Workshop on Neutrino Oscillations and Their Origin (NOON 2001)*. June 2001, pp. 239–248. arXiv: hep-ex/0106019.

[88] J. Nieves, I. Ruiz Simo, and M. J. Vicente Vacas. “The nucleon axial mass and the MiniBooNE Quasielastic Neutrino-Nucleus Scattering problem”. In: *Phys. Lett. B* 707 (2012), pp. 72–75. arXiv: 1106.5374 [hep-ph].

[89] Dieter Rein and Lalit M. Sehgal. “Neutrino Excitation of Baryon Resonances and Single Pion Production”. In: *Annals Phys.* 133 (1981), pp. 79–153.

[90] Krzysztof M. Graczyk and Jan T. Sobczyk. “Form Factors in the Quark Resonance Model”. In: *Phys. Rev. D* 77 (2008). [Erratum: Phys.Rev.D 79, 079903 (2009)], p. 053001. arXiv: 0707.3561 [hep-ph].

[91] Krzysztof M. Graczyk, Jakub Żmuda, and Jan T. Sobczyk. “Electroweak form factors of the Δ(1232) resonance”. In: *Phys. Rev. D* 90.9 (2014), p. 093001. arXiv: 1407.5445 [hep-ph].

[92] A. Bodek and U. K. Yang. “Modeling neutrino and electron scattering cross-sections in the few GeV region with effective LO PDFs”. In: *AIP Conf. Proc.* 670.1 (2003). Ed. by U. Cotti, M. Mondragon, and G. Tavares-Velasco, pp. 110–117. arXiv: hep-ex/0301036.

[93] Arie Bodek and Un-ki Yang. “A Unified model for inelastic e - N and nu - N cross-sections at all Q**2”. In: *AIP Conf. Proc.* 792.1 (2005). Ed. by Wesley H. Smith and Sridhara R. Dasu, pp. 257–260. arXiv: hep-ph/0508007.

[94] L. L. Salcedo et al. “Computer Simulation of Inclusive Pion Nuclear Reactions”. In: *Nucl. Phys. A* 484 (1988), pp. 557–592.

[95] Alfredo Ferrari et al. “FLUKA: A multi-particle transport code (Program version 2005)”. In: (Oct. 2005).

[96] Giuseppe Battistoni et al. “Overview of the FLUKA code”. In: *Annals Nucl. Energy* 82 (2015), pp. 10–18.

[97] René Brun et al. *GEANT: Detector Description and Simulation Tool; Oct 1994*. CERN Program Library. Long Writeup W5013. Geneva: CERN, 1993. URL: https://cds.cern.ch/record/1082634.

[98] C. Zeitnitz and T. A. Gabriel. "The GEANT-CALOR interface and benchmark calculations of ZEUS test calorimeters". In: *Nuclear Instruments and Methods in Physics Research A* 349.1 (Sept. 1994), pp. 106–111.

[99] S. Agostinelli et al. "GEANT4–a simulation toolkit". In: *Nucl. Instrum. Meth. A* 506 (2003), pp. 250–303.

[100] W.R. Gilks, S. Richardson, and D. Spiegelhalter. *Markov Chain Monte Carlo in Practice*. Chapman & Hall/CRC Interdisciplinary Statistics. Taylor & Francis, 1995. URL: http://books.google.com/books?id=TRXrMWY_i2IC.

[101] Steve Brooks et al. *Handbook of Markov Chain Monte Carlo*. CRC press, 2011.

[102] Nicholas Metropolis et al. "Equation of State Calculations by Fast Computing Machines". In: *The Journal of Chemical Physics* 21.6 (June 1953), pp. 1087–1092. eprint: https://pubs.aip.org/aip/jcp/article-pdf/21/6/1087/18802390/1087_1_online.pdf. URL: https://doi.org/10.1063/1.1699114.

[103] W. K. Hastings. "Monte Carlo sampling methods using Markov chains and their applications". In: *Biometrika* 57.1 (Apr. 1970), pp. 97–109. eprint: https://academic.oup.com/biomet/article-pdf/57/1/97/23940249/57-1-97.pdf. URL: https://doi.org/10.1093/biomet/57.1.97.

[104] Robert E. Kass and Adrian E. Raftery. "Bayes Factors". In: *Journal of the American Statistical Association* 90.430 (1995), pp. 773–795. URL: http://www.jstor.org/stable/2291091 (visited on 03/26/2024).

[105] Harold Jeffreys. *The Theory of Probability*. Oxford Classic Texts in the Physical Sciences. 1939.

[106] Kirsty Elizabeth Duffy. *First Measurement of Neutrino and Antineutrino Oscillation at T2K*. Springer Cham, 2017.

[107] T. Holvey et al. *Measuring Oscillation Parameters in a joint ND280+SK analysis using Markov Chain Monte Carlo Methods*. Tech. rep. TN-429. T2K, 2022. eprint: https://t2k.org/docs/technotes/429.

[108] J. S. Conway. "Incorporating Nuisance Parameters in Likelihoods for Multisource Spectra". In: *PHYSTAT 2011*. 2011, pp. 115–120. arXiv: 1103.0354 [physics.data-an].

[109] P. A. Zyla et al. "Review of Particle Physics". In: *PTEP* 2020.8 (2020), p. 083C01.

[110] K. Fusshoeller et al. *Muon antineutrino and neutrino Charged-Current multiple pion selections in antineutrino mode*. Tech. rep. TN-273. T2K, 2020. eprint: https://t2k.org/docs/technotes/273.

[111] T.A. Doyle et al. *ND280 FHC samples with Photon and Proton information for the 2021 Oscillation Analysis*. Tech. rep. TN-421. T2K, 2022. eprint: https://t2k.org/docs/technotes/421.

[112] T. Doyle et al. *Constraining the flux and cross Section models for the 2021 oscillation analysis using ND280 data*. Tech. rep. T2K-TN-423. T2K, 2022. eprint: http://www.t2k.org/docs/technotes/423.

[113] S Berkman et al. *fiTQun: A New Reconstruction Algorithm for Super-K*. Tech. rep. 146. 2013. eprint: http://www.t2k.org/docs/technotes/146.

[114] D. Barrow et al. *Super-Kamiokande Data Quality, MC, and Systematics in Run 10*. Tech. rep. 399. 2020. eprint: http://www.t2k.org/docs/technotes/399.

[115] S. M . Lakshmi et al. *Super-Kamiokande muon neutrino multi-ring samples for the 2021 Oscillation Analysis*. Tech. rep. 447. 2023. eprint: http://www.t2k.org/docs/technotes/447.

[116] T. Yoshida et al. *A study of multi-ring muon-like events at Super-Kamiokande*. Tech. rep. 388. 2020. eprint: http://www.t2k.org/docs/technotes/388.

[117] E.T. Atkin et al. *NIWG model and uncertainties for 2019-2020 oscillation analysis*. Tech. rep. 344. 2019. eprint: http://www.t2k.org/docs/technotes/344.

[118] L. Berns et al. *Flux Prediction and Uncertainty with NA61/SHINE 2010 Replica Target Measurements*. Tech. rep. 401. 2022. eprint: http://www.t2k.org/docs/technotes/401.

[119] N. Abgrall et al. "Measurements of $\pi^{\pm}$, $K^{\pm}$ and proton double differential yields from the surface of the T2K replica target for incoming 31 GeV/c protons with the NA61/SHINE spectrometer at the CERN SPS". In: *Eur. Phys. J. C* 79.2 (2019), p. 100. arXiv: 1808.04927 [hep-ex].

[120] C. Bronner et al. *NIWG model and uncertainties for 2021 oscillation analysis*. Tech. rep. 414. 2021. eprint: http://www.t2k.org/docs/technotes/414.

[121] L. Alvarez-Ruso et al. "NuSTEC White Paper: Status and challenges of neutrino–nucleus scattering". In: *Prog. Part. Nucl. Phys.* 100 (2018), pp. 1–68. arXiv: 1706.03621 [hep-ph].

[122] Veronique Bernard, Latifa Elouadrhiri, and Ulf-G. Meissner. "Axial structure of the nucleon: Topical Review". In: *J. Phys. G* 28 (2002), R1–R35. arXiv: hep-ph/0107088.

[123] E. S. Pinzon Guerra et al. "Using world charged $\pi^{\pm}$–nucleus scattering data to constrain an intranuclear cascade model". In: *Phys. Rev. D* 99.5 (2019), p. 052007. arXiv: 1812.06912 [hep-ex].

[124] Andrew Missert. *Fit to Super-K Atmospheric Neutrino Data for Optimization of the fiTQun Fiducial Volume Cuts and Estimation of Detector Uncertainties*. Tech. rep. 318. 2017. eprint: http://www.t2k.org/docs/technotes/318.

[125] Christophe Bronner on behalf of the T2K collaboration. "Recent Results From T2K". In: ed. by Zenodo. 2022. URL: https://zenodo.org/records/6683821.

[126] Andrew Gelman, Xiao-Li Meng, and Hal Stern. "POSTERIOR PREDICTIVE ASSESSMENT OF MODEL FITNESS VIA REALIZED DISCREPANCIES". In: *Statistica Sinica* 6.4 (1996), pp. 733–760. URL: http://www.jstor.org/stable/24306036 (visited on 04/22/2024).

[127] Clarence V. C. Wret. "Minimising systematic uncertainties in the T2K experiment using near-detector and external data". PhD thesis. Imperial Coll., London, 2018.

[128] Andrew Gelman. "Comment: Fuzzy and Bayesian p-Values and u-Values". In: *Statistical Science* 20.4 (2005), pp. 380 –381. URL: https://doi.org/10.1214/088342305000000368.

[129] Adrian E. Bayer and Uroš Seljak. "The look-elsewhere effect from a unified Bayesian and frequentist perspective". In: *Journal of Cosmology and Astroparticle Physics* 2020.10 (2020), pp. 009–009. URL: https://doi.org/10.1088/1475-7516/2020/10/009.

[130] T. C. Dieminger et al. *Assessing out-of-model cross-section effects with fits to simulated data*. Tech. rep. TN-441. T2K, 2023. eprint: https://t2k.org/docs/technotes/441.

[131] N. Jachowicz et al. "Continuum random phase approximation approach to charged current neutrino nucleus scattering". In: *Phys. Rev. C* 65 (2002), p. 025501.

[132] V. Pandey et al. "Low-energy excitations and quasielastic contribution to electron-nucleus and neutrino-nucleus scattering in the continuum random-phase approximation". In: *Phys. Rev. C* 92.2 (2015), p. 024606. arXiv: 1412.4624 [nucl-th].

[133] S. Dolan et al. "Implementation of the continuum random phase approximation model in the GENIE generator and an analysis of nuclear effects in low-energy transfer neutrino interactions". In: *Phys. Rev. D* 106.7 (2022), p. 073001. arXiv: 2110.14601 [hep-ex].

[134] A. Nikolakopoulos et al. "Mean field approach to reconstructed neutrino energy distributions in accelerator-based experiments". In: *Phys. Rev. C* 98.5 (2018), p. 054603. arXiv: 1808.07520 [nucl-th].

[135] J. Nieves, I. Ruiz Simo, and M. J. Vicente Vacas. "Inclusive Charged–Current Neutrino–Nucleus Reactions". In: *Phys. Rev. C* 83 (2011), p. 045501. arXiv: 1102.2777 [hep-ph].

[136] Artur M. Ankowski, Omar Benhar, and Makoto Sakuda. "Improving the accuracy of neutrino energy reconstruction in charged-current quasielastic scattering off nuclear targets". In: *Phys. Rev. D* 91.3 (2015), p. 033005. arXiv: 1404.5687 [nucl-th].

[137] T. Skyrme. "The effective nuclear potential". In: *Nucl. Phys.* 9 (1959), pp. 615–634.

[138] Lukas Koch. "Post-hoc regularisation of unfolded cross-section measurements". In: *JINST* 17.10 (2022), P10021. arXiv: 2207.02125 [hep-ex].

[139] R. Acciarri et al. "Design and Construction of the MicroBooNE Detector". In: *JINST* 12.02 (2017), P02017. arXiv: 1612.05824 [physics.ins-det].

[140] MicroBooNE Collaboration. *Microboone at work: Event displays*. Online; accessed 5-5-2024. URL: https://microboone-exp.fnal.gov/public/approved_plots/Event_Displays.html.

[141] Costas Andreopoulos et al. "The GENIE Neutrino Monte Carlo Generator: Physics and User Manual". In: (Oct. 2015). arXiv: 1510.05494 [hep-ph].